Coupled Multiphysics Analysis Method for Thin Flexible Piezoelectric Bimorph in Fluid

Doctoral Thesis

COUPLED MULTIPHYSICS ANALYSIS METHOD FOR THIN FLEXIBLE PIEZOELECTRIC BIMORPH IN FLUID

By

PRAKASHA CHIGAHALLI RAMEGOWDA

Department of Mechanical Information Science and Technology

Graduate School of Computer Science and Systems Engineering

KYUSHU INSTITUTE OF TECHNOLOGY, JAPAN

MARCH 2019

ACKNOWLEDGEMENTS

I wish to express my sincere gratitude to my doctoral thesis adviser, Associate Professor Daisuke Ishihara, for his precious help, kind support and patient guidance in supervising this research work and I am grateful to my another adviser Professor Tomoyoshi Horie for his kind support, constant help, guidance, and encouragement during the course of my research. Also, I wish to thank my co-supervisor Associate Professor Tomoya Niho for his invaluable advice and friendly assistance in research. These professors highly contributed to the completion and improvement of this thesis work. I sincerely thank them for their valuable advice during its elaboration.

I would like to express my gratitude for serving on my doctoral thesis examination committee to Kyutech Vice President Professor Akahoshi Yasuhiro, Professor Ito Takahiro, Professor Tomoyoshi Horie, Associate Professor Tomoya Niho, and Associate Professor Daisuke Ishihara. Thank you very much for all the discussions, comments and advice building up this thesis.

My great appreciation also goes to Mr. Yu Sayama for his contribution in developing analysis codes. I would also like to thank Mr. Rei Takata, who have actively participated and contributed to my researches. I personally thank Mr. Masateru Araki, Mr. Naoto Ohira, Mr. Kenji Kubota, and Mr. Naoki Hayashi for their warm hospitality. I am grateful to all my lab–mates for being kind and supportive to me. I am pleased to acknowledge all my friends in India and Japan, who have always supported me and kept me focused.

My deepest and esteemed appreciation goes to my parents Giddama Ramegowda and Chigahalli Ningegowda Ramegowda, brother Kirana Kumara Ramegowda and sister Divya Sathish, and grandparents, whose warm support and blessing was essential for fulfilling this work. I thank my grandfathers Giniyappa Ningegowda Annaiah and Hampanahalli Kalegowda, who were the constant inspiration for my work.

TABLE OF CONTENTS

List of Tables

List of Figures

Figure **Page**

CHAPTER 1

GENERAL INTRODUCTION

1.1 Motivation

Over the past decade, there has been a serious effort aimed at the development of flapping–wing insect–like micro air vehicles (MAV's) using micro–electro–mechanical system (MEMS) fabrication technology. The use of the MEMS technology enable a systematic research in terms of repeatability, miniaturization, size control, weight minimization, usage of smart materials, and integration with electronic circuits. As the characteristic size of the MAV's decreases than their macro–scale counterparts, the challenges for flight mechanism, fluid mechanics, structural design and fabrication, power requirement to lift its own weight, and computational design and analysis of multiphysics involved between interdisciplinary domains is a difficult task that has focused an active research in the last decade. The recent advancement in the mechanics of the flapping flight suggests the use of smart materials to actuate the flexible wings of a flapping–wing insect–like MAV.

In MEMS, there are number of actuation mechanisms are available. The basic actuation mechanisms used in MAV applications are the electrostatic actuation, thermal actuation and piezoelectric actuation. Among them piezoelectric actuation mechanism received a greatest attention, especially in the past decade. The main advantages of piezoelectric materials are their large power densities at the centimeter to micrometer scales, favorable scaling effects as the transducer size is reduced, ease of application and well established fabrication technology. Generally, piezoelectric devices consist of a thin flexible unimorph or bimorph model. In particular, piezoelectric bimorph actuators have been incorporated in various actuator applications.

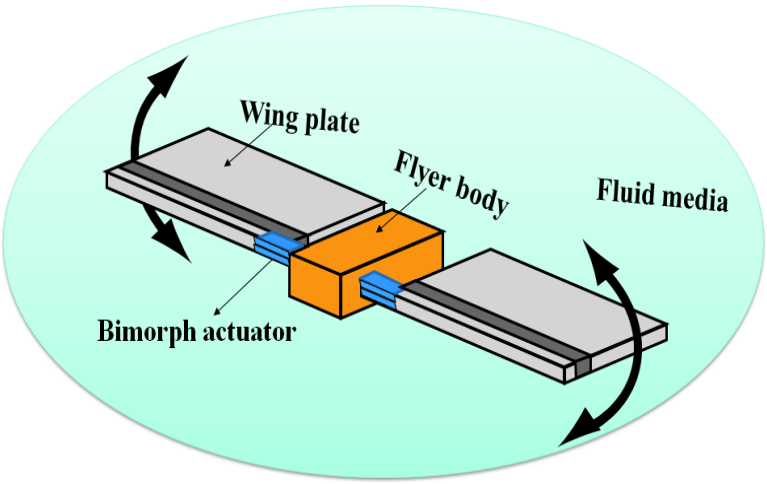

Figure 1.1: Concept sketch of a MEMS flyer

Recently, the flexible wings of insect–like MAV's are actuated by a piezoelectric bimorph actuator [1]. The schematic representation of MAV actuated by a flexible piezoelectric bimorph actuator located at the root of the flapping wing [2] surrounded by the fluid media, shown in Fig. 1.1. These bimorph actuators can produce large deformations when operated near resonance. As shown in Fig. 1.1, the flapping wing actuated by a piezoelectric bimorph actuator at resonance condition is damped significantly due to the fluid viscous force from the surrounding fluid media, the fluid flow is sensitive to the wings motion, and the wing and the actuator interact with each other due to their large deflection which intern has a significant effect on the actuation mechanism.

The large deformation of the flexible piezoelectric bimorph actuator causes the strong interaction with the electric field (piezoelectric effect) and the surrounding fluid, and inversely, these two fields significantly affect the structural behavior of the flexible piezoelectric bimorph and flapping wings. This interdisciplinary coupling effect between the electric field, the surrounding fluid media, and the flexible structure are very significant. Therefore, the triply coupled multiphysics analysis between electric field and fluid–structure interaction (EFSI) is a key design aspect in the modeling and simulation of MAV's. The numerical approach to this triply coupled system of partial differential equations is a challenging task that has attracted an active research in the last five years.

In recent years, with the rise in the demand of energy has attracted research a significant interest in energy harvesting describing the process of generating electrical energy from external sources in the surroundings, such as structural mechanical vibrations, the ocean waves, wind flow and many. The energy harvesting using the thin flexible piezoelectric bimorph devices [3] shown in Fig. 1.2 that converts the mechanical energy such as ocean wave to the electric

energy has attracted greater attention as a next electric generation system due to their strong electro-mechanical convertible characteristics.

In energy harvester, the large deformation of the thin flexible piezoelectric bimorph devices causes the strong interaction with the electric field (piezoelectric effect) and the surrounding fluid, and inversely, these two fields significantly affect on the structural behavior. It is very difficult to analyze such strong interaction using theoretical and experimental methods. It is very important to consider triply coupled multiphysics interaction between the electric field and fluid-structure interaction (EFSI) to obtain maximum power efficiency. There is less effort by commercial software and academic research to treat three fields coupling using finite element method (FEM). A detailed and accurate modeling of EFSI system using FEM will help to achieve maximum power efficiency.

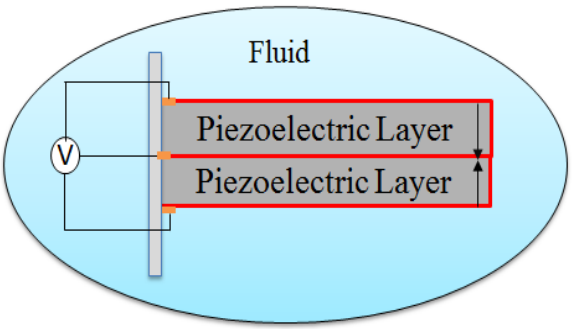

(a) Flexible piezoelectric bimorph sensor in fluid

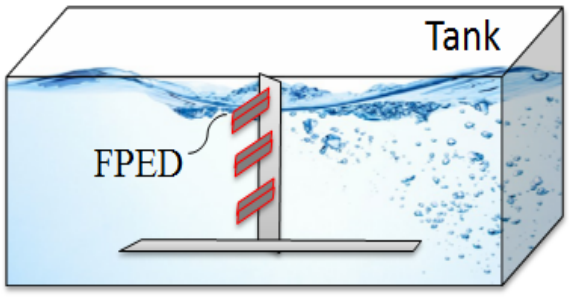

(b) FPED devices used for energy harvesting application

Figure 1.2: Concept sketch of flexible piezoelectric devices used in energy harvesting

As a numerical tool for performing the simulation of multiphysics coupling effects, the finite element method (FEM) has been the standard choice, because of its capabilities to analyze the geometries of complex shapes, detailed analysis of coupled effect, boundary and initial conditions. In general, the MEMS devices have complex geometries, therefore FEM has become an essential computer tool for the design and analysis. In recent years, FEM has been used

in a large number of industrial projects and academic research and resulted in many efficient, both problem specific and general simulation codes. Their simulation is a difficult task which requires the analysis of coupled dependencies that is not studied thoroughly to give enough information, experience, and understanding. The analytical solutions to the model equations of EFSI system are limited in the scope. Therefore, a novel finite element method is required. There has been less study on the development of an efficient and accurate FEM simulation code to analyze EFSI effects. So this thesis is focused on the development of the finite element method for the electric field–fluid–structure interaction of a piezoelectric bimorph actuator in the fluid media and defines objectives to simulate EFSI system.

1.2 Objective of this thesis work

The finite element method to solve the coupled problems can be broadly classified into two algorithms, i.e. the monolithic algorithms and the decomposition algorithm. The decomposition algorithms are computationally efficient, enable the use of different finite elements to solve the different fields as isolated entities which remedies the shortcomings of using the same elements in the monolithic algorithms, and re-usability of various existing algorithms such as parallel computation. On contrary, monolithic methods are computationally expensive, difficult to employ different elements to solve different fields since monolithic algorithms solve all the fields in a single mathematical framework, and therefore it is a challenging task to use advanced parallel computation techniques. In this study, a strongly coupled method for a flexible piezoelectric bimorph actuator in the fluid media is developed based on a finite element method for strongly coupled structure, electric field and fluid using the hierarchal decomposition algorithm. As a theory, the hierarchal decomposition algorithm is superior to the others in terms of application to complicated multiphysics problems.

The objective to solve the EFSI system using the hierarchal decomposition can be divided into a number of sub–objectives:

1. Development of finite element method to analyze the linear electric field–structure interaction describing the piezoelectric effect by partitioning into the electrical field and structural with the use of Gauss–Seidel method and analysis using 3D solid elements of a piezoelectric bimorph actuator.

2. Develop a finite element model for nonlinear structure–electric field interaction using a novel coupling scheme for the nonlinear structure–electric field by using a transformation method between the shell and solid in a thin piezoelectric bimorph actuator and sensor.

3. A triply coupled multiphysics analysis method for the electric field (piezoelectric effect) and fluid–structure interaction (EFSI) of a piezoelectric bimorph in a converging fluid channel based on the hierarchal decomposition.

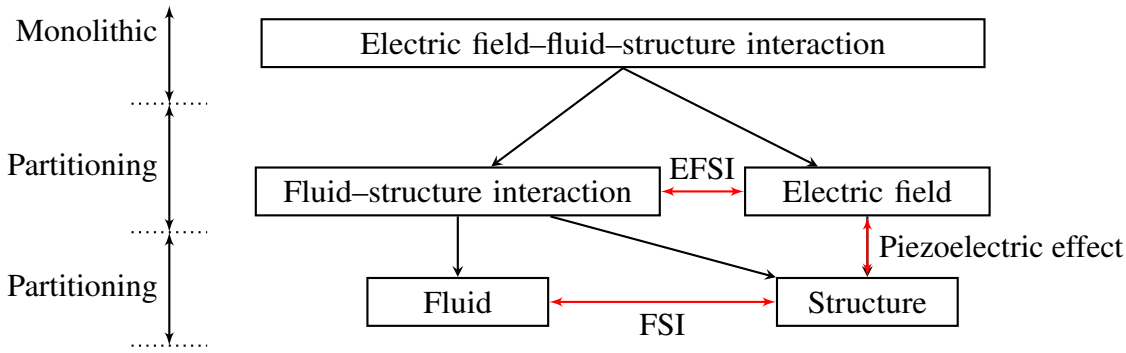

Figure 1.3: Schematic of hierarchal decomposition of EFSI system: Black lines indicates partition and red lines indicates interaction.

Fig. 1.3 shows the schematic representation of the above discussed sub–objectives. As shown here, the monolithic EFSI system is decomposed into subsystems of fluid–structure interaction (FSI) and electric field. Then FSI subsystem is partitioned into sub–subsystem of fluid pressure and fluid–structure velocity using algebraic splitting algorithm. The partitioned electric field and structure are coupled to study the piezoelectric effect of a bimorph actuator. This hierarchal splitting creates a foundation for easy implementation of various existing simulation codes and also easily extendable to other multiphysics problems in a way most suitable for the general application.

1.3 Outline of this thesis

In the present study, a novel triply coupled multiphysics analysis of electric field–fluid–structure interaction of a thin flexible piezoelectric bimorph actuator in the fluid using hierarchal decomposition method is presented, aiming at various engineering applications. An outline of this thesis is organized as follows.

In Chapter 2, a comprehensive and systematic performance evaluation of several finite element coupled algorithms to analyze the electro–mechanical coupling (electric field–structure interaction) in three-dimensional piezoelectric bimorph actuators and a surface acoustic device actuated by piezoelectric actuators are presented based on their accuracy and computational efficiency. The interaction between the electric field and structure is numerically approximated

using FEM for linear piezoelectric effect. Monolithic coupling, partitioned iterative coupling, and non-iterative partitioned coupling schemes are presented to study electric field–structure interaction in a piezoelectric actuator using three–dimensional (3D) solid FE elements. In partitioned iterative coupling schemes, the author employed the block Jacobi and the block Gauss–Seidel methods, which acts as a basis for this thesis work. In this chapter, a comprehensiveness analysis of piezoelectric bimorph actuator with a metal shim and without a metal shim, and a piezoelectric actuator based surface acoustic wave device is demonstrated. Resonance characteristics are very important in MEMS applications. The resonance vibration characteristics of a bimorph actuator are analyzed. At the end of this chapter, an overview of the computational efficiency is given for the dynamic analysis of low frequency and high frequency operating piezoelectric actuators in MEMS.

Chapter 3 presents a novel transformation method to analyze the electro–mechanical coupling in a piezoelectric bimorph actuator and sensor using the shell elements and 3D solid and shell elements to simulate the nonlinear structure and electric field, respectively. In this chapter, the author presents a finite element formulation to transform the induced electric forces in the solid elements to the shell elements, and the resultant displacements in the shell to the solid elements. It is followed by a detailed explanation of how the use of the different elements to analyze two different fields can remedies the shortcoming of using monolithic elements or same FE elements, the originality, coupling approaches, and algorithms. Using the proposed method both the actuation and sensing function of a thin piezoelectric bimorph under several electrical configurations is accurately analyzed.

Chapter 4 presents a triple coupled algorithm to analyze the electric field and fluid–structure interaction of piezoelectric bimorph made of PVDF and PZT–5H material in the viscous fluid media. The electric field–structure interaction and fluid–structure interaction coupled based on the hierarchal decomposition scheme. In this hierarchal decomposition of electric field–fluid–structure interaction system, the induced electric force vector is applied on to the structure domain of the FSI system through the force transformation, then in the nonlinear iteration loop the structural and fluid field is solved by using the projection method in order to evaluate the structural and fluid variables. After the nonlinear iteration loop, the resultant displacements in the shell element is transformed to the solid elements using displacement transformation method. The coupling between the electric field and the fluid–structure interaction is executed using the block Gauss–Seidel method. Piezoelectric bimorph made of PVDF and PZT–5H located in the fluid channel is analyzed using the EFSI method. The resonance frequency of the thin flexible piezoelectric bimorph in the fluid is examined for various electrical configurations and loading conditions. Then the effect of the external ladings on the frequency and vibration

amplitudes are discussed.

Finally some general conclusions are drawn based on the results and discussions and summarized in Chapter 5.

CHAPTER 2

PARTITIONED ITERATIVE COUPLING ALGORITHMS TO STUDY ELECTRO–MECHANICAL COUPLING OF A LINEAR PIEZOELECTRIC EFFECT

2.1 Introduction to piezoelectric effect

The word piezoelectricity is derived from Greek and means electricity resulting from pressure (In Greek Piezo mean pressure). The piezoelectric effect is fundamentally an interaction between electric field and structure discovered in 1880 by Jacques and Pierre Curie [4]. The interaction between electric field and structure is also known as electro-mechanical coupling. Piezoelectric material (PEM) exhibit both the direct and inverse piezoelectric effect, as shown in Fig. 2.1. The direct piezoelectric effect converts the mechanical strain energy of the PEM into electric energy, this direct piezoelectric effect is used in the sensor applications. On the other hand, the inverse piezoelectric effect does the opposite, i.e., the electrical energy is converted into mechanical strain energy, this inverse piezoelectric effect is used in the actuator applications. There fore, the electro-mechanical convertible characteristics of a PEM is widely used for both sensing and actuation applications.

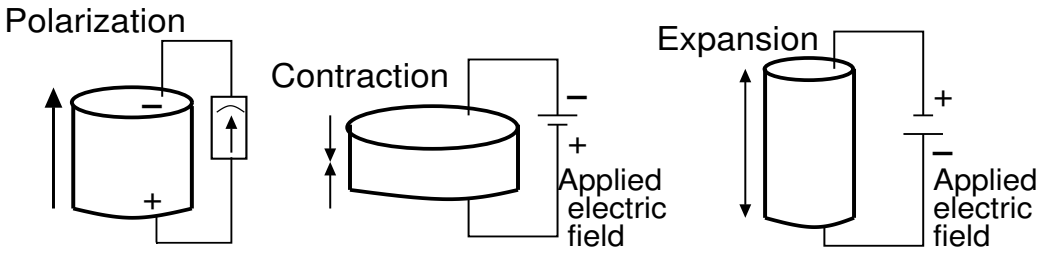

(a) The actuation or inverse piezoelectric effect

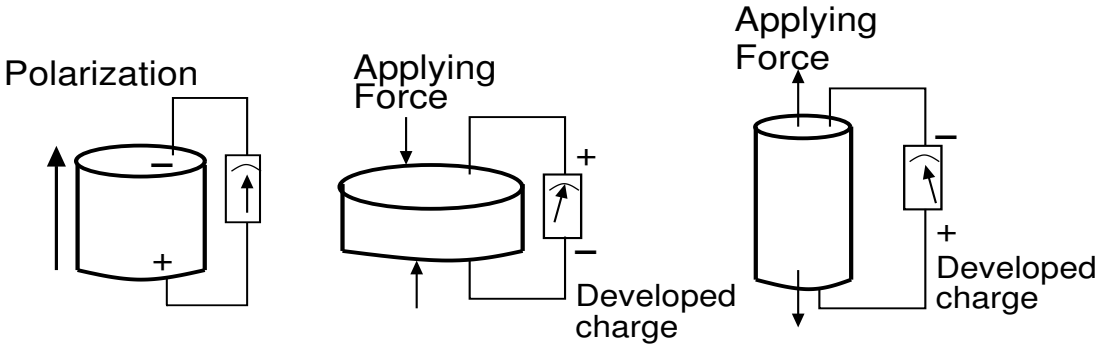

(b) The sensor or direct piezoelectric effect

Figure 2.1: Schematic representation of the piezoelectric effect

Designing piezoelectricity-based sensors and actuators has been an ongoing process over the last few decades. The past decade has seen significant advances in the market growth of MEMS-based piezoelectric products [5], and a wide array of piezoelectric MEMS devices have been developed [6]. Generally, piezoelectric MEMS devices consist of a thin flexible unimorph or bimorph model. In particular, piezoelectric bimorphs cantilvers have been incorporated in various actuator applications [7–9] and sensor applications [10–12]. The piezoelectric sensing effect can also be used for energy harvesting [3, 13, 14]. Recently, the flexible wings of insect-like micro air vehicles [2, 15, 16], which are robotic insects with flexible flapping wings are actuated by a piezoelectric bimorph actuator [1]. Recent advances in the mechanics of flapping flight systems have been presented in Refs.[17–20]. The flexible wing of the MEMS-based MAVs or MEMS flyer is actuated from the root by a piezoelectric bimorph actuator that can produce large deflection at its resonance so that it can produce enough lift force to support its own weight and fly at low speeds [2]. In many practical applications, piezoelectric bimorph actuators with metal shim also known as triple layer actuators are widely used to increase mechanical reliability and strength so that the structure can be maintained even if the ceramics fractures [21]. The constitutive equations and dynamic admittance matrices for piezoelectric bimorph actuators without the metal shim and with metal shim have been presented to study the transmission characteristics between the electrical and mechanical fields, static tip deflection,

and to determine the resonance frequencies in [7, 21–23].

Various micro devices are operated near resonance of the structures to improve their sensitivity because these devices are less sensitive when operated away from their resonance. Resonance frequency, transient dynamic response, dynamic steady state response and static tip deflection are of the primary concern in the design of bimorph actuator and its practical applications. Theoretical solutions to determine the resonance frequency and also static tip deflection are available for bimorph actuators and triple layer actuator [21, 22].

The development of finite element coupled algorithms for piezoelectric interaction to analyze the transient dynamic responses of these piezoelectric bimorph is very important in the design process of piezoelectric actuators and sensor. Experimental study on the vibration characteristics of the triple layer actuators with different configurations has been presented by [24], and they compared the Eigen modal frequencies using commercial CAE tools.

There is an increasing demand and requirement of computer aided engineering (CAE) modeling and simulation of piezoelectric devices because of strong electro-mechanical convertible characteristics, strong coupling effect, applications in miniature devices such as MEMS, and geometric complexity of the device. In recent years, multiphysics modeling and simulation have gained a great attention and some researchers are extensively developing numerical methods using FEM for smart structures [7, 25, 26] and intelligence devices. Zienkiewicz and Taylor [27] have classified interactions in a coupled system into two classes. In class 1, the coupling occurs on domain interfaces, and in class 2, it occurs through the constitutive governing equations of the system. Electromechanical coupling belongs to the latter class. One of the earliest works on developing finite element method for linear piezoelectric interaction analysis was done by Allik and Hughes [28]. A rather comprehensive literature survey on piezoelectric finite elements can track back to [29].

Generally, coupled problems have been simulated using monolithic or partitioned coupling methods. Over the last few decads, many researchers have proposed monolithic coupling algorithms to study the electric field and structure interaction of electro–mechanical coupling in piezoelectric continumm [28, 30–37]. Stability analysis of monolithic coupling and partitioned coupling for both implicit and explicit integration methods was presented for piezo-composites [38], and monolithic coupling with the Newmark's integration was well studied for the linear dynamic response of piezoelectric actuators [39]. Electromagnetic and structural interaction are solved using simultaneous method [40] and staggered method for a cantilever plate in [41, 42]. A finite element model for the static and eigenvalue problems for piezoelectric bimorph actuator without metal shim using a monolithic coupling method can be found in [43]. Although monolithic coupling is available for linear piezoelectric analysis, it is computationally

challenging when performing a nonlinear analysis. On the other hand, partitioned coupling schemes are computationally efficient and can obtain a same level of accuracy with monolithic schemes. Initially, a partitioned algorithm (domain decomposition) was proposed by Fellipa et al. [44] for the analysis of coupled mechanical systems in fluid–structure interaction (FSI) problems. In recent years, this partitioned strategy gained a great deal of attention due to the software modularity and reusable capabilities of existing numerical codes. Shi et al. in Ref [45] had proposed a partitioned method to analyze the structure-electrostatic interaction for MEMS application [45], but the electrostatic phenomena and piezoelectric effect are two completely different interaction problems. Gaudenzi & Bathe in Ref [46] had presented the finite element formulation of the partitioning method for piezoelectric effect. In their work, the comparison of performances of various numerical FE coupled algorithms have not been presented, and also the validation of the algorithm using numerical example is not presented. Nowadays, partitioned iterative methods have gained a great attention because they can enhance the accuracy and robustness in comparison with non-iterative partitioned coupling methods. In partitioned iterative methods, structure and electric interaction are solved separately and iteratively by fixed point iteration at each time step satisfying the convergence criteria [47]. The convergence and robustness of partitioned iterative algorithms for fluid-structure interaction were investigated in [48]. And very recently, Ishihara et al. [49] had proposed hierarchal decomposition for the interaction of structure-fluid-electrostatic interaction, where three fields interactions are studied by partitioning them into fluid-structure interaction and electrostatic fields using an iteratively staggered method, and the structure-fluid interaction is analyzed using algebraic splitting method [50]. It follows from the present literature survey that an implementation and development of partitioned iterative coupling schemes have not addressed to study the electric field–structure interaction and to analyze the steady state, static, and transient dynamic responses of a low–frequency operating piezoelectric bimorph actuators and transient dynamic responses of a high–frequency operating surface acoustic wave problems.

It follows from the previous literature survey that the numerical techniques for static and modal shapes are well established using monolithic coupling method. The transient dynamic responses are very important in the design process and application point of MEMS piezoelectric actuators. Therefore, computational procedures to capture the transient dynamic response of piezoelectric bimorph actuators and also their performance evaluations based on accuracy and computational efficiency must be discussed. The transient dynamic response of piezoelectric actuators was presented using a monolithic coupling with the Newmark's time integration to solve ultrasonic ring motor [39] and partitioned coupling with the Newmark's time integration to solve structure-electrostatic interaction in a microtweezer [45]. Transient response of MEMS

piezoelectric micro-flow sensors using matrix condensation with monolithic coupling and Newmark's time integration shows 5% error in tip deflection of plate [51]. But, in these studies, the comparison of performances of various numerical FE coupled algorithms have not been presented for transient dynamic responses of piezoelectric bimorph actuators.

In this section, a comprehensive and systematic performances evaluation of various numerical coupled algorithms based on accuracy and computational efficiency to study the electric filed and structure interaction is demonstrated. The evaluated linear piezoelectric finite element algorithms are 1) the monolithic coupling with Newmark's time integration, 2) block Jacobi partitioned iterative coupling with Newmark's time integration, 3) block Gauss-Seidel partitioned iterative coupling with Newmark's time integration, 4) non iterative partitioned coupling with central difference time integration. Using these algorithms, the static, dynamic step responses and transient dynamic characteristics of piezoelectric bimorph actuator are predicted accurately. The static and dynamic behaviors of the model from numerical and analytic results are compared with each other. It is shown from these results that the numerical analysis using the proposed algorithms takes into account the interaction of the structure-electric field of the piezoelectric actuator accurately. The performances of the proposed algorithms have been depicted in the present simulation results. The performances of these finite element coupled algorithms are evaluated based on the accuracy of the solution and the computational cost for piezoelectric bimorph actuators without metal shim, bimorph actuators with metal shim (triple layer actuator), and surface acoustic wave devices. Their transient dynamic responses are demonstrated together with the static and steady-state responses.

2.2 Governing equations of piezoelectricity

2.2.1 Piezoelectric constitutive equations

In the actuation and sensing response of piezoelectric body of volume Ω with boundary surface S^B in three-dimensional space, the following mechanical, dynamic and electrostatic equilibrium equations have to be satisfied.
The mechanical equilibrium can be written as

$$\sigma_{ij,j} + f_i^B = \rho \ddot{u}_i, \tag{2.1}$$

where σ_{ij}, f_i^B, ρ and $\ddot{u}_i$ are the stress tensor, the body force vector, the density and the acceleration, respectively. The strain tensor S_{ij} and the mechanical displacement vector u_i are

related as

$$S_{ij} = \frac{1}{2}(u_{i,j} + u_{j,i}), \tag{2.2}$$

The electrostatic equilibrium from Maxwell's equation can be written as

$$D_{i,i} - q = 0, \tag{2.3}$$

where D_i is the electrical displacement vector and q is the electric body charge. The electric field vector E_i and a scalar electric potential $\phi_{,i}$ are related as

$$E_i = -\phi_{,i}. \tag{2.4}$$

The constitutive equations of linear piezoelectricity can be written as

$$\sigma_{ij} = C^E_{ijkl} S_{kl} - e_{kij} E_k, \tag{2.5}$$

$$D_i = e_{ikl} S_{kl} + \varepsilon^S_{ik} E_k, \tag{2.6}$$

where C^E_{ijkl} is the elastic constitutive tensor, S_{kl} the mechanical strain tensor, e_{kij} the piezoelectric coupling coefficient, E_k the electric field vector, and ε^S_{ik} the dielectric permitivity tensor. The superscripts E and S denote that the elastic constants and the dielectric constants are evaluated at constant electric field and constant strain, respectively. The constitutive Eqs.(2.5) and (2.6) for piezoelectric material shows the coupling between electrical and mechanical quantities. The actuation effect also known as inverse piezoelectric effect is described by Eq.(2.5) which shows that when a piezoelectric material is subjected to an electric field produces mechanical strain in the material, shown in Fig. 2.1(a). On the contrary, the sensor effect also known as the direct piezoelectric effect is described by Eq.(2.6), shown in Fig. 2.1(b). It is evident from Eq.(2.6) that an electric field is generated by the applied mechanical stress. To solve Eqs. (2.1)–(2.6) describing the piezoelectric body Ω, the following natural or essential boundary conditions on the boundary surface S^B of the body are prescribed [38, 46]:
Natural mechanical boundary condition on S^B_σ

$$\sigma_{ij} n_j = {f_i}^S. \tag{2.7}$$

Essential mechanical boundary condition on S^B_u

$$u_i = {u_i}^S. \tag{2.8}$$

Natural electrical boundary condition on S^B_q

$$D_i n_i = q^S. \tag{2.9}$$

Essential electrical boundary condition on S_ϕ^B

$$\phi = \phi^S, \tag{2.10}$$

where ${u_i}^S$ and ${f_i}^S$ are the prescribed mechanical displacement and surface force components, respectively; ϕ^S and q^S are the prescribed electric potential and surface charge, respectively; n_i is the outward unit normal vector.

Generally, either piezoelectric polymers (polyvinylidene fluoride (PVDF)) or piezoelectric ceramic (Lead zirconate titanate (PZT), Lithium niobate ($LiNbO_3$), Lithium tantalate ($LiTaO_3$)) are the most commonly used piezoelectric materials. In general, poled piezoceramics and piezopolymers are isotropic materials and exhibits symmetry. Using the symmetrices $C^E_{ijkl} = C^E_{jikl} = C^E_{klij}$, $e_{kij} = e_{kji}$, $\varepsilon^S_{ik} = \varepsilon^S_{ki}$ of the constitutive tensors, and $\sigma_{ij} = \sigma_{ji}$ and $S_{kl} = S_{lk}$ of the second order stress and strain tensors. The expanded form of Eqs.(2.5) and (2.6) can be displayed as follows

$$\left[\begin{array}{c} \sigma_{11} \\ \sigma_{22} \\ \sigma_{33} \\ \sigma_{23} \\ \sigma_{13} \\ \sigma_{12} \\ \hline D_1 \\ D_2 \\ D_3 \end{array}\right] = \left[\begin{array}{ccc|ccc|ccc} C^E_{1111} & C^E_{1122} & C^E_{1133} & 0 & 0 & 0 & 0 & 0 & e_{31} \\ C^E_{2211} & C^E_{2222} & C^E_{2233} & 0 & 0 & 0 & 0 & 0 & e_{33} \\ C^E_{3311} & C^E_{3322} & C^E_{3333} & 0 & 0 & 0 & 0 & 0 & e_{31} \\ 0 & 0 & 0 & C^E_{2323} & 0 & 0 & 0 & e_{15} & 0 \\ 0 & 0 & 0 & 0 & C^E_{1313} & 0 & e_{15} & 0 & 0 \\ 0 & 0 & 0 & 0 & 0 & C^E_{1212} & 0 & 0 & 0 \\ \hline 0 & 0 & 0 & 0 & e_{15} & 0 & -\varepsilon^S_{11} & 0 & 0 \\ 0 & 0 & 0 & e_{15} & 0 & 0 & 0 & -\varepsilon^S_{22} & 0 \\ e_{31} & e_{31} & e_{33} & 0 & 0 & 0 & 0 & 0 & -\varepsilon^S_{33} \end{array}\right] \left[\begin{array}{c} S_{11} \\ S_{22} \\ S_{33} \\ 2S_{23} \\ 2S_{13} \\ 2S_{12} \\ \hline -E_1 \\ -E_2 \\ -E_3 \end{array}\right] \tag{2.11}$$

Using the Voigt's notation, the 3rd order piezoelectric coupling tensor e_{ijk} can represented by 3 x 6 matrix with two subscripts e_{mn} (m=1 to 3 and n= 1 to 6). For the constitutive tensor C^E_{ijkl}, the stress tensor σ_{ij} and the strain tensor S_{kl}, the combined pairs of indices in the matrix notation is as follows: $()_{11} \rightarrow ()_1$, $()_{22} \rightarrow ()_2$, $()_{33} \rightarrow ()_3$, $()_{23} \rightarrow ()_4$, $()_{13} \rightarrow ()_5$, and $()_{12} \rightarrow ()_6$, e.g. $C^E_{1111} = C^E_{11}$, $C^E_{1122} = C^E_{12}$, $C^E_{1133} = C^E_{13}$, $C^E_{2211} = C^E_{21}$, $C^E_{2222} = C^E_{22}$, $C^E_{2233} = C^E_{23}$, $C^E_{3311} = C^E_{31}$, $C^E_{3322} = C^E_{32}$, $C^E_{3333} = C^E_{33}$, $C^E_{2323} = C^E_{44}$, $C^E_{1313} = C^E_{55}$, and $C^E_{1212} = C^E_{66}$.

The constitutive Eqs.(2.5) and (2.6) can be given in matrix form as

$$\left[\begin{array}{c} \boldsymbol{\sigma} \\ \mathbf{D} \end{array}\right] = \left[\begin{array}{cc} \mathbf{C}^{\mathrm{E}} & \mathbf{e} \\ \mathbf{e}^{\mathbf{T}} & -\boldsymbol{\varepsilon}^{\mathrm{S}} \end{array}\right] \left[\begin{array}{c} \mathbf{S} \\ -\mathbf{E} \end{array}\right] \tag{2.12}$$

2.3 Finite element equations of linear piezoelectricity

Finite element method played a significant role in the analysis of electro-mechanical coupling in a piezoelectric material. Using FEM, approximate numerical solutions can be computed for a complex coupled phenomena, complex shapes, and different boundary conditions.

2.3.1 Formulation of variational piezoelectric equations

The variational formulation and basic finite elements equations to derive the stiffness, mass, and electromechanical coupling matrices of piezoelectric system was first presented by Allik and Hughes [28]. The integral form of the mechanical equilibrium and electrostatic equilibrium Eqs.(2.1) and (2.3) can be obtained by employing the principle of virtual work for a piezoelectric medium [28, 29]. For arbitray space-variable and virtual displacements δu_i and virtual electric potential $\delta\phi$, Eqs. (2.1) and (2.3) can be written as,

$$\int_\Omega (\sigma_{ij,j} + f_i - \rho\ddot{u}_i)\delta u_i \, \mathrm{d}\Omega = 0, \tag{2.13}$$

$$\int_\Omega (D_{i,i} - q)\delta\phi \, \mathrm{d}\Omega = 0. \tag{2.14}$$

Using the integration by parts and divergence theorem, Eqs.(2.13) and (2.14) leads to [29],

$$-\int_\Omega \sigma_{ij}\delta u_{i,j}\mathrm{d}\Omega + \int_{S^B} \sigma_{ij} n_j \delta u_i \, \mathrm{d}S^B + \int_\Omega f_i^B \delta u_i \, \mathrm{d}\Omega - \int_\Omega \rho\ddot{u}_i \delta u_i \, \mathrm{d}\Omega = 0, \tag{2.15}$$

$$-\int_\Omega D_i \delta\phi_{,i} \, \mathrm{d}\Omega + \int_{S^B} D_i n_i \delta\phi \, \mathrm{d}S^B - \int_\Omega q\delta\phi \, \mathrm{d}\Omega = 0. \tag{2.16}$$

Substitute the natural mechanical boundary condition Eq.(2.7) and the virtual strain δS_{ij} corresponding to δu_i into Eq.(2.15) give,

$$-\int_\Omega \sigma_{ij}\delta S_{ij} \, \mathrm{d}\Omega + \int_{S^B} f_i^s \delta u_i \, \mathrm{d}S^B + \int_\Omega f_i^B \delta u_i \, \mathrm{d}\Omega - \int_\Omega \rho\ddot{u}_i \delta u_i \, \mathrm{d}\Omega = 0, \tag{2.17}$$

where $\delta S_{ij} = [1/2(\frac{\partial \delta u_i}{\partial x_j} + \frac{\partial \delta u_j}{\partial x_i})]$. Now substitute the natural electrical boundary condition Eq.(2.9) and the virtual electric field $\delta E_i = -\frac{\partial \phi}{\partial x_i}$ corresponding to $\delta\phi$ into Eq.(2.16) gives,

$$\int_\Omega D_i \delta E_i \, \mathrm{d}\Omega + \int_{S^B} q^s \delta\phi \, \mathrm{d}S^B - \int_\Omega q\delta\phi \, \mathrm{d}\Omega = 0. \tag{2.18}$$

By substituting piezoelectric constitutive Eqs.(2.5) and (2.6) into the principle of virtual displcament equation Eq.(2.17) and principle of virtual electrical potential equation Eq.(2.18) the following set of equations is obtained:

$$\int_\Omega [C_{ijkl}^E S_{kl} - e_{kij} E_k]\delta S_{ij} \, \mathrm{d}\Omega + \int_\Omega \rho\ddot{u}_i \delta u_i \, \mathrm{d}\Omega = \int_{S^B} f_i^s \delta u_i \, dS^B + \int_\Omega f_i^B \delta u_i \, \mathrm{d}\Omega, \tag{2.19}$$

$$\int_{\Omega} [e_{ikl} S_{kl} + \varepsilon^{S}_{ik} E_k] \delta E_i \, \mathrm{d}\Omega = \int_{S^B} q^s \delta\phi \, \mathrm{d}S^B - \int_{\Omega} q \delta\phi \, \mathrm{d}\Omega. \tag{2.20}$$

By rearranging above equations give,

$$\int_{\Omega} C^{E}_{ijkl} S_{kl} \delta S_{ij} \, \mathrm{d}\Omega - \int_{\Omega} e_{kij} E_k \delta S_{ij} \, \mathrm{d}\Omega + \int_{\Omega} \rho \ddot{u}_i \delta u_i \, \mathrm{d}\Omega = \int_{S^B} f^s_i \delta u_i \, \mathrm{d}S^B + \int_{\Omega} f^B_i \delta u_i \, \mathrm{d}\Omega, \tag{2.21}$$

$$\int_{\Omega} e_{ikl} S_{kl} \delta E_i \, \mathrm{d}\Omega + \int_{\Omega} \varepsilon^{S}_{ik} E_k \delta E_i \, d\Omega = \int_{S^B} q^s \delta\phi \, \mathrm{d}S^B - \int_{\Omega} q \delta\phi \, \mathrm{d}\Omega. \tag{2.22}$$

In piezoelectric materials, no body density charge is assumed to be present [46], therefore, the last term in Eq.(2.22) is get canceled.

2.3.2 Finite element discritization of piezoelectric equations

Now, by employing the generic finite element discritization with the interpolation functions denoted as $\mathbf{N_u}$ and $\mathbf{N}_\phi$ to evaluate the mechanical displacement vector components $\mathbf{u}$ and electric potential ϕ of an element from its nodal point vectors of corresponding fields by assuming

$$\mathbf{u} = \mathbf{N_u} \hat{\mathbf{u}}, \tag{2.23}$$

$$\phi = \mathbf{N}_\phi \hat{\phi}, \tag{2.24}$$

where $\hat{\mathbf{u}}$ is the vector of the nodal displacement and $\hat{\phi}$ is vector of nodal electric potential of an element. The nodal displacement vector $\hat{\mathbf{u}}$ for a 3D solid element is given as,

$$\hat{\mathbf{u}} = \left\{ \begin{array}{cccccc} u_1 & v_1 & w_1 & \cdots & u_n & v_n & w_n \end{array} \right\}^t. \tag{2.25}$$

Similarly, the nodal electric potential vector $\hat{\phi}$ is given as,

$$\hat{\phi} = \left\{ \begin{array}{cccc} \phi_1 & \phi_2 & \cdots & \phi_n \end{array} \right\}^t, \tag{2.26}$$

where n is maximum nuber of nodes in a 3D solid element. The element strain field vector $\mathbf{S}$ and electric field vector $\mathbf{E}$ are related to its nodal displacement vector $\hat{\mathbf{u}}$ and electric potential vector $\hat{\phi}$ through the shape function derivatives $\mathbf{B_u}$ and $\mathbf{B}_\phi$ as

$$\mathbf{S} = \mathbf{B_u} \hat{\mathbf{u}}, \tag{2.27}$$

$$\mathbf{E} = -\nabla\phi = -\mathbf{B}_\phi \hat{\phi}. \tag{2.28}$$

The expanded form of Eq.(2.27) for a three-dimensional piezoelectric solid elements can be written as

$$\begin{Bmatrix} S_{11} \\ S_{22} \\ S_{33} \\ 2S_{23} \\ 2S_{13} \\ 2S_{12} \end{Bmatrix} = \begin{Bmatrix} \frac{\partial u}{\partial x} \\ \frac{\partial v}{\partial y} \\ \frac{\partial w}{\partial z} \\ \frac{\partial v}{\partial z}+\frac{\partial w}{\partial y} \\ \frac{\partial w}{\partial x}+\frac{\partial u}{\partial z} \\ \frac{\partial u}{\partial y}+\frac{\partial v}{\partial x} \end{Bmatrix} = \begin{bmatrix} \frac{\partial}{\partial x} & 0 & 0 \\ 0 & \frac{\partial}{\partial y} & 0 \\ 0 & 0 & \frac{\partial}{\partial z} \\ 0 & \frac{\partial}{\partial z} & \frac{\partial}{\partial y} \\ \frac{\partial}{\partial z} & 0 & \frac{\partial}{\partial x} \\ \frac{\partial}{\partial y} & \frac{\partial}{\partial x} & 0 \end{bmatrix} \begin{Bmatrix} u \\ v \\ w \end{Bmatrix}$$

$$= \begin{bmatrix} \frac{\partial}{\partial x} & 0 & 0 \\ 0 & \frac{\partial}{\partial y} & 0 \\ 0 & 0 & \frac{\partial}{\partial z} \\ 0 & \frac{\partial}{\partial z} & \frac{\partial}{\partial y} \\ \frac{\partial}{\partial z} & 0 & \frac{\partial}{\partial x} \\ \frac{\partial}{\partial y} & \frac{\partial}{\partial x} & 0 \end{bmatrix} [\mathbf{N}_u]\{\hat{\boldsymbol{u}}\} = [\mathbf{B}_u]\{\hat{\boldsymbol{u}}\} \tag{2.29}$$

Similarly, Eq.(2.28) can be summarized as

$$\begin{Bmatrix} E_1 \\ E_2 \\ E_3 \end{Bmatrix} = -\begin{Bmatrix} \frac{\partial}{\partial x} \\ \frac{\partial}{\partial y} \\ \frac{\partial}{\partial z} \end{Bmatrix} \phi = -\begin{Bmatrix} \frac{\partial}{\partial x} \\ \frac{\partial}{\partial y} \\ \frac{\partial}{\partial z} \end{Bmatrix} [\mathbf{N}_\phi]\, \hat{\phi} = -[\mathbf{B}_\phi]\, \hat{\phi} \tag{2.30}$$

$\mathbf{N_u}$ and $\mathbf{N}_\phi$ are the interpolation function in the isoparemetric coordinate in a 3D solid element [27, 28]. Substitution of relations (2.23) and (2.27) into Eq.(2.21)), and Eqs.(2.24) and (2.28) into Eq.(2.22) give the standard finite element equations of piezoelectricity written as [28, 38]

$$\mathbf{M}\ddot{\mathbf{u}} + \mathbf{K}_{\mathrm{uu}}\mathbf{u} + \mathbf{K}_{\mathrm{u}\phi}\phi = \mathbf{F}, \tag{2.31}$$

$$\mathbf{K}_{\phi\mathrm{u}}\mathbf{u} + \mathbf{K}_{\phi\phi}\phi = \mathbf{q}, \tag{2.32}$$

with

$$\mathbf{M} = \int_\Omega \rho \mathbf{N}_\mathrm{u}^\mathrm{T} \mathbf{N}_\mathrm{u} \mathrm{d}\Omega, \tag{2.33a}$$

$$\mathbf{K}_{\mathrm{uu}} = \int_\Omega \mathbf{B}_\mathrm{u}^\mathrm{T} \mathbf{C} \mathbf{B}_\mathrm{u} \mathrm{d}\Omega, \tag{2.33b}$$

$$\mathbf{K}_{\mathrm{u}\phi} = \int_\Omega \mathbf{B}_\mathrm{u}^\mathrm{T} \mathbf{e} \mathbf{B}_\phi \mathrm{d}\Omega, \quad \mathbf{K}_{\phi\mathrm{u}} = \mathbf{K}_{\mathrm{u}\phi}^\mathrm{T}, \tag{2.33c}$$

$$\mathbf{K}_{\phi\phi} = \int_\Omega \mathbf{B}_\phi^\mathrm{T} \varepsilon \mathbf{B}_\phi \mathrm{d}\Omega, \tag{2.33d}$$

$$\mathbf{F} = \int_\Omega \mathbf{N}_\mathrm{u}^\mathrm{T} \mathbf{f}_i^B \, d\Omega + \int_S \mathbf{N}_\mathrm{u}^\mathrm{T} \mathbf{f}_i^s \, \mathrm{d}S^B, \tag{2.33e}$$

$$\mathbf{q} = \int_S \mathbf{N}_\phi^\mathrm{T} \mathbf{q}^s \mathrm{d}S^B, \tag{2.33f}$$

where $\mathbf{M}$ is the constant mass matrix, $\mathbf{K}_{\mathrm{uu}}$ is the mechanical stiffness matrix, $\mathbf{K}_{\mathrm{u}\phi}$ is the piezoelectric coupling matrix, $\mathbf{K}_{\phi\phi}$ is the dielectric stiffness matrix, $\mathbf{F}$ is the external force vector, and $\mathbf{q}$ is the external electric charge vector. Superscript T stands for transpose matrix. The interpolation functions for $\mathbf{u}$ and ϕ are $\mathbf{N}_\mathrm{u}$ and $\mathbf{N}_\phi$, respectively.

2.4 Time integration for piezoelectric finite element equations

Various implicit and explicit time integration methods are presently in use for piezoelectric analysis [38]. Here the Newmark's integration [52] and the central difference method is used.

2.4.1 Newmark time integration for linear dynamic piezoelectric analysis

In an implicit time integration method (e.g. Newmark's time integration), the solution of accelerations, velocities and displacements at each time increment Δt are evaluated from the equation of motion at time $t + \Delta t$. The piezoelectric finite element Eqs.(2.31) and (2.32) are considered at the time $t + \Delta t$ as

$$\mathbf{M}\, {}^{t+\Delta t}\ddot{\mathbf{u}} + \mathbf{K}_{\mathrm{uu}}\, {}^{t+\Delta t}\mathbf{u} + \mathbf{K}_{\mathrm{u}\phi}\, {}^{t+\Delta t}\phi = {}^{t+\Delta t}\mathbf{F}, \tag{2.34}$$

$$\mathbf{K}_{\phi\mathrm{u}}\, {}^{t+\Delta t}\mathbf{u} + \mathbf{K}_{\phi\phi}\, {}^{t+\Delta t}\phi = {}^{t+\Delta t}\mathbf{q}, \tag{2.35}$$

where ${}^{t+\Delta t}\ddot{\mathbf{u}}$, ${}^{t+\Delta t}\mathbf{u}$ and ${}^{t+\Delta t}\phi$ are the acceleration, displacement and potential solution vectors at time $t + \Delta t$, respectively. In Newmark's time integration [52], the current accelerations and

current velocities in terms of current displacements and past quantities of the same variables can be expressed as [53],

$$^{t+\Delta t}\ddot{\mathbf{u}} = \frac{1}{\beta\Delta t^2}(^{t+\Delta t}\mathbf{u} - {}^{t}\mathbf{u}) + \frac{1}{\beta\Delta t}{}^{t}\dot{\mathbf{u}} - \left(\frac{1}{2\beta} - 1\right){}^{t}\ddot{\mathbf{u}}, \tag{2.36}$$

$$^{t+\Delta t}\dot{\mathbf{u}} = \frac{\gamma}{\beta\Delta t}(^{t+\Delta t}\mathbf{u} - {}^{t}\mathbf{u}) - \left(\frac{\gamma}{\beta} - 1\right){}^{t}\dot{\mathbf{u}} - \Delta t\left(\frac{\gamma}{2\beta} - 1\right){}^{t}\ddot{\mathbf{u}}, \tag{2.37}$$

where β and γ are algorithmic parameters that are used to obtain intended stability and accuracy. Even though Newmark's time integration is unconditionally stable, numerical instability occurs in coupled problems [42]. By substitutingEqs.(2.36) and (2.37) into Eq.(2.34) becomes,

$$\hat{\mathbf{K}}_{\mathbf{uu}}{}^{t+\Delta t}\mathbf{u} + \mathbf{K}_{\mathrm{u}\phi}{}^{t+\Delta t}\phi = {}^{t+\Delta t}\hat{\mathbf{F}}, \tag{2.38}$$

where

$$\hat{\mathbf{K}}_{\mathrm{uu}} = \mathbf{K}_{\mathrm{uu}} + \frac{1}{\beta\Delta t^2}\mathbf{M} + \frac{\gamma}{\beta\Delta t}\mathbf{C}, \tag{2.39}$$

$$^{t+\Delta t}\hat{\mathbf{F}} = {}^{t+\Delta t}\mathbf{F} + \mathbf{M}\left\{\frac{1}{\beta\Delta t^2}{}^{t}\mathbf{u} + \frac{1}{\beta\Delta t}{}^{t}\dot{\mathbf{u}} + \left(\frac{1}{2\beta} - 1\right){}^{t}\ddot{\mathbf{u}})\right\}, \tag{2.40}$$

where $\hat{\mathbf{K}}_{\mathrm{uu}}$, $^{t+\Delta t}\hat{\mathbf{F}}$ and $\mathbf{C}$ are the effective stiffness matrix, the effective force vector at $t+\Delta t$ and the structural damping matrix, respectively. The coefficients of the damping matrix $\mathbf{C}$ will be zero is assumed in subsequent formulation and analysis.

2.4.2 Central difference method for linear dynamic piezoelectric analysis

The linear piezoelectric equation of motion Eq.(2.31) in any explicit time integration method will be at time t is given by,

$$\mathbf{M}{}^{t}\ddot{\mathbf{u}} + \mathbf{K}_{\mathrm{uu}}{}^{t}\mathbf{u} + \mathbf{K}_{\mathrm{u}\phi}{}^{t}\phi = {}^{t}\mathbf{F}. \tag{2.41}$$

The acceleration $\ddot{\mathbf{u}}^{\mathbf{t}}$ and velocity $\dot{\mathbf{u}}^{\mathbf{t}}$ in-terms of current displacement $\mathbf{u}^{\mathbf{t}+\Delta\mathbf{t}}$ is given by [53],

$$\ddot{\mathbf{u}}^{t} = \frac{1}{\Delta t^2}\left\{\mathbf{u}^{t+\Delta t} - 2\mathbf{u}^{t} + \mathbf{u}^{t-\Delta t}\right\} \tag{2.42}$$

$$\dot{\mathbf{u}}^{t} = \frac{1}{2\Delta t}\left\{\mathbf{u}^{(t+\Delta t)} - \mathbf{u}^{t-\Delta t}\right\} \tag{2.43}$$

These two relations for $\ddot{\mathbf{u}}^{t}$ and $\dot{\mathbf{u}}^{t}$ are substituted toEq.(2.41) to solve for $\mathbf{u}^{t+\Delta t}$,

$$^{t+\Delta t}\mathbf{u} = \left[\frac{1}{\Delta t^2}\mathbf{M_L}^{-1}\right]\left\{{}^{t}\mathbf{F} - \mathbf{K}_{\mathrm{u}\phi}{}^{t}\phi - \mathbf{K}_{\mathrm{uu}}{}^{t}\mathbf{u} + 2\,\frac{\mathbf{M_L}}{\Delta t^2}\,{}^{t}\mathbf{u} + {}^{t-\Delta t}\mathbf{u}\right\}, \tag{2.44}$$

where $\mathbf{M}_{\mathrm{L}}$ is a lumped mass matrix. The choice of Δt is an important parameter in central difference method to obtain an accurate and stable solution. $\Delta t < \Delta t_{cr}$ must be satisfied in order to achieve a stable solution, where $\Delta t_{cr} = L/C_v$ is critical time step, L is the effective length of the finite element and $C_v = \sqrt{\frac{E}{\rho}}$ is the wave propagation velocity, E and ρ are Young's modulus and the mass density of the material, respectively.

2.5 Coupled algorithms for electric field-structure interaction in a piezoelectric continuum

In this section, the finite element coupled algorithms to study the interaction between electric field and structure of a linear piezoelectric effect are presented based on the monolithic coupling [38], non iterative partitioned coupling, and partitioned iterative coupling [47, 54].

2.5.1 Monolithic coupling with Newmark's integration (MN)

The monolithic method treats both structural and electric fields in the same mathematical framework as a single computational entity and solve simultaneously [38]. The Eqs.(2.35) and (2.38) can be rearranged in the monolithic form as

$$\begin{bmatrix} \hat{\mathbf{K}}_{\mathrm{uu}} & \mathbf{K}_{\mathrm{u}\phi} \\ \mathbf{K}_{\phi\mathrm{u}} & \mathbf{K}_{\phi\phi} \end{bmatrix} \begin{Bmatrix} {}^{t+\Delta t}\mathbf{u} \\ {}^{t+\Delta t}\phi \end{Bmatrix} = \begin{Bmatrix} {}^{t+\Delta t}\hat{\mathbf{F}} \\ {}^{t+\Delta t}\mathbf{q} \end{Bmatrix}, \tag{2.45}$$

The analysis flow of the MN algorithm is shown in Fig. 2.2. The step by step calculation procedure is that the stiffness matrices $\mathbf{K}_{\mathrm{uu}}$, $\mathbf{K}_{\mathrm{u}\phi}$, $\mathbf{K}_{\phi\phi}$, the effective stiffness matrix $\hat{\mathbf{K}}_{\mathrm{uu}}$ and the consistent mass matrix $\mathbf{M}$ are first calculated and the solution is carried out with the initial values ${}^{0}\mathbf{u}$, ${}^{0}\dot{\mathbf{u}}$, ${}^{0}\ddot{\mathbf{u}}$, ${}^{0}\phi$ and ${}^{0}\mathbf{F}$. The factorization of the stiffness matrices are performed in first time step only. Then the solutions of ${}^{t+\Delta t}\mathbf{u}$, ${}^{t+\Delta t}\phi$, ${}^{t+\Delta t}\dot{\mathbf{u}}$ and ${}^{t+\Delta t}\ddot{\mathbf{u}}$, are calculated using Eq.(2.45)), Eq.(2.36), and Eq.(2.37). This process is repeated following the time marching. The above equations can also be employed for the static analysis of piezoelectric system in a monolithic manner by eliminating the inertial effect and time integration. The schematic of this coupled algorithm is briefly given in Fig. 2.3.

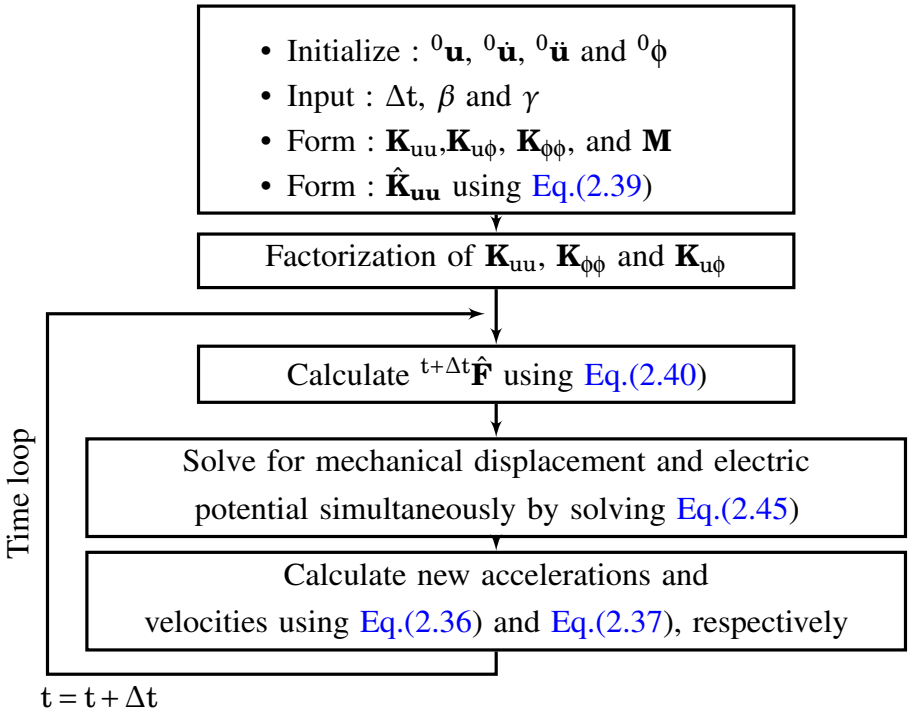

Figure 2.2: Flow chart of the analysis procedure of the MN algorithm

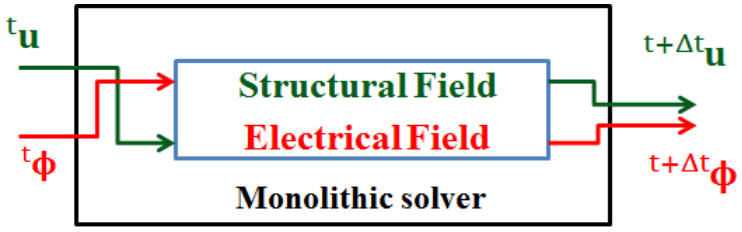

Figure 2.3: Schematic representation of MN algorithm.

2.5.2 Block Jacobi partitioned iterative coupling with Newmark's integration (BJN)

In recent years, decomposition methods a.k.a splitting methods has gained popularity in computational analysis of coupled problems. Splitting methods are computational efficient, allow parallalization techniques, allow different finite elements to solve subsystems independently [55, 56], large scale problems can be solved, and reusability of existing codes. In particular, Jacobi and Gauss–Seidel method has attracted attention for the iteration solution of coupled systems. In the context of coupled systems, the Jacobi and Gauss–Seidel methods are called as block Jacobi (BJ) or block Gauss–Seidel (BGS) methods [57].

In block Jacobi method, the simultaneous system of piezoelectric finite element equations (2.35) and (2.38) are solved separately at each time step iteratively using the solutions obtained from previous iterations until the convergence criteria is satisfied. Applying the block Jacobi iteration method to Eqs.(2.35) and (2.38) leads to the BJN coupled algorithm written as [47],

$$\mathbf{K}_{\phi\phi}\,{}^{t+\Delta t}\phi^{(i)} = {}^{t+\Delta t}\mathbf{q} - \mathbf{K}_{\phi u}\,{}^{t+\Delta t}\mathbf{u}^{(i-1)}, \tag{2.46}$$

$$\hat{\mathbf{K}}_{uu}\,{}^{t+\Delta t}\mathbf{u}^{(i)} = {}^{t+\Delta t}\hat{\mathbf{F}} - \mathbf{K}_{u\phi}\,{}^{t+\Delta t}\phi^{(i-1)}, \tag{2.47}$$

where i indicates the current iteration. The schematic of BJN algorithm is briefly given in Fig. 2.4. The analysis flow of the proposed BJN coupled algorithm is illustrated in Fig. 2.6 where dotted lines indicate iteration process.

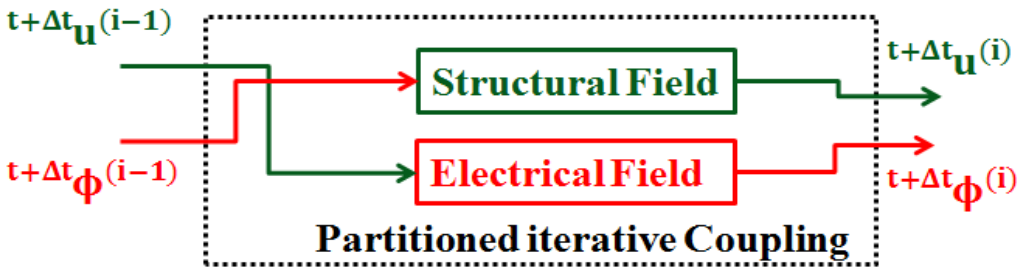

Figure 2.4: Schematic representation of BJN algorithm.

The solution for the current electrical potential ${}^{t+\Delta t}\phi^{(i)}$ will be derived from the previous mechanical displacement ${}^{t+\Delta t}\mathbf{u}^{(i-1)}$. Similarly, the solution for the current mechanical displacement ${}^{t+\Delta t}\mathbf{u}^{(i)}$ will be obtained from the previous electrical potential ${}^{t+\Delta t}\phi^{(i-1)}$. From Eqs.(2.46) and (2.47), it is noted that both electrical potential and mechanical displacement for each iteration in a time step are evaluated from the previous iteration quantities. Since this method does not require the quantities of current iteration to evaluate both electrical potential and mechanical displacement for each iteration makes parallelization of subsystems very easy during the dynamic analysis. The iteration convergence condition is satisfied by comparing the values of electrical potentials and displacements obtained in the current iteration i with those obtained in previous iterations i-1. The tolerance condition for electric potential and mechanical displacement is given as,

$$\frac{\|\phi^i - \phi^{i-1}\|}{\|\phi^i\|} \leq \epsilon, \tag{2.48}$$

$$\frac{\|\mathbf{u}^i - \mathbf{u}^{i-1}\|}{\|\mathbf{u}^i\|} \leq \epsilon, \tag{2.49}$$

where ϵ is a tolerance parameter. It is important to note that, the factorization of stiffness matrices is carried only in the first iteration of the time step. The schematic of this algorithm is briefly given in Fig. 2.4. The equations (2.46) and (2.47) can be used for the static piezoelectric analysis by eliminating the inertial effect and time integration.

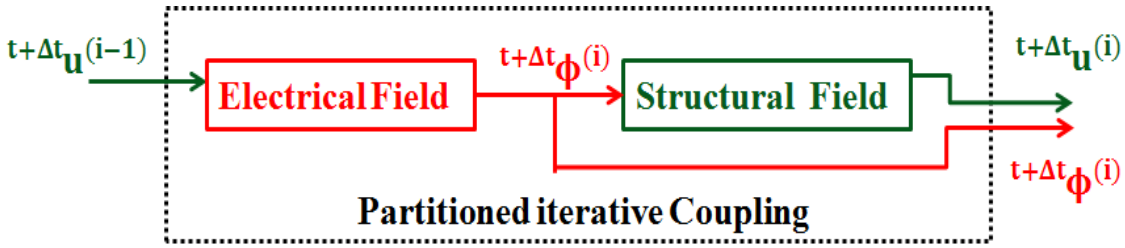

Figure 2.5: Schematic representation of BGSN algorithm.

2.5.3 Block Gauss-Seidel partitioned iterative coupling with Newmark's integration (BGSN)

Block Gauss-Seidel iteration method is one of the widely used partitioned iterative coupling algorithm owing to its simplicity, faster convergence than block Jacobi method. By applying the block Gauss-Seidel partitioned iterations to Eq.(2.35) and Eq.(2.38) leads to the obtain the BGSN coupled algorithm for linear dynamic analysis of piezoelectric effect written as follows,

$$\mathbf{K}_{\phi\phi}{}^{t+\Delta t}\phi^{(i)} = {}^{t+\Delta t}\mathbf{q} - \mathbf{K}_{\phi u}{}^{t+\Delta t}\mathbf{u}^{(i-1)}, \tag{2.50}$$

$$\hat{\mathbf{K}}_{uu}{}^{t+\Delta t}\mathbf{u}^{(i)} = {}^{t+\Delta t}\hat{\mathbf{F}} - \mathbf{K}_{u\phi}{}^{t+\Delta t}\phi^{(i)}. \tag{2.51}$$

The Eqs.(2.46) and (2.50) are the same because the electric potentials are computed using mechanical displacements obtained in the previous iteration. But Eqs.(2.47) and (2.51)) are in contrary to each, where the displacement component is evaluated in each iteration of a time step using the updated/current electric potential obtained in Eq.(2.50). This allows the solutions in BGSN algorithm to converge faster than BJN algorithm, because the physical quantities are computed sequentially in the block Gauss-Seidel partitioned iterative method. This algorithm makes parallelization difficult but tends the solutions to converge faster. The schematic of block Gauss–Seidel coupling of electric field and structure is briefly given in Fig. 2.5. The analysis flow of the proposed BGSN algorithm is illustrated in Fig. 2.6.

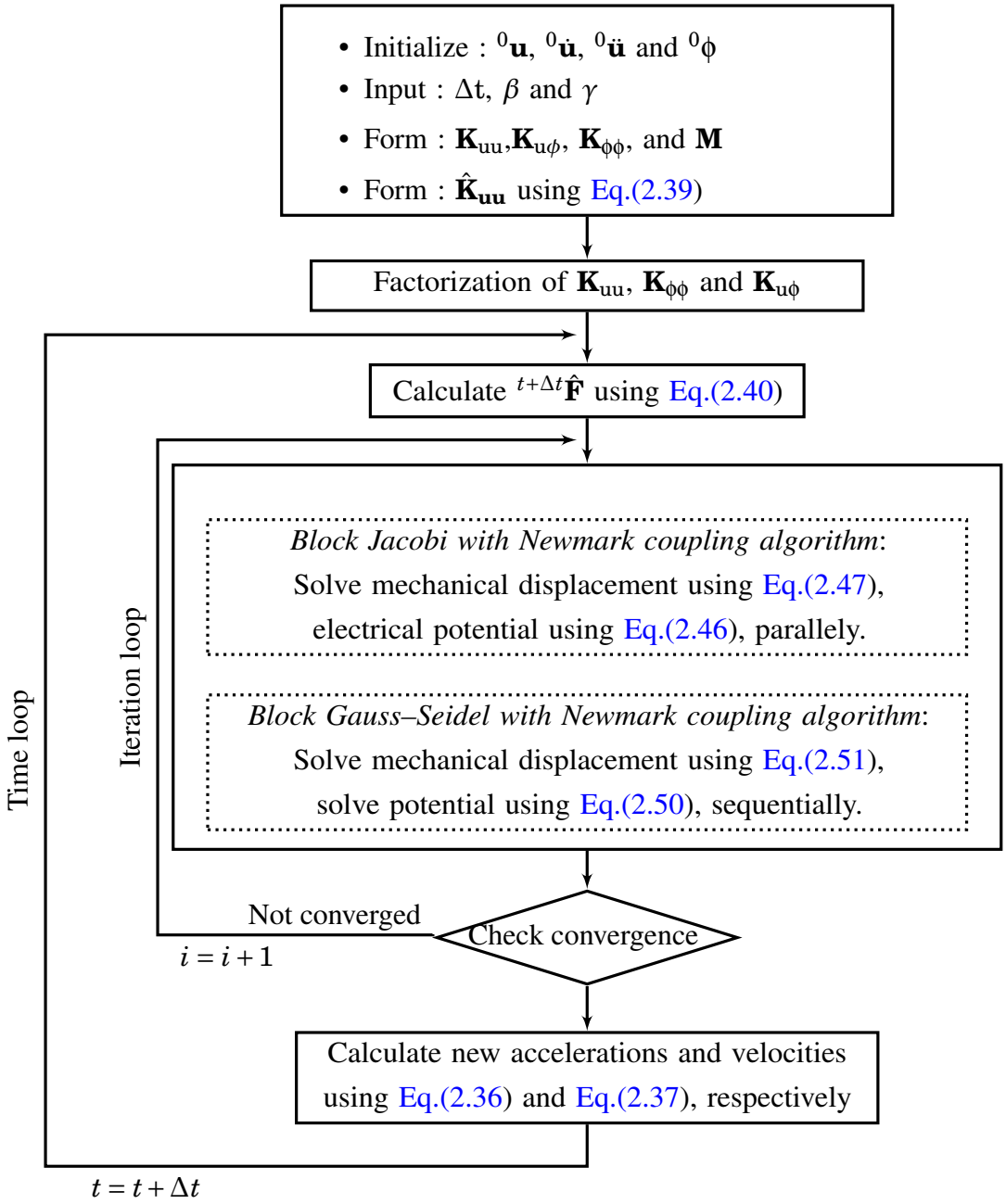

Figure 2.6: Flow of the analysis procedure of the BJN and BGSN algorithms.

2.5.4 Non iterative partitioned coupling algorithm with central difference time integration(PCD)

In general, partitioned methods treat both structure and electric fields as a single computational entity and solves the unknown variables separately by transforming interaction effects between

them. For ease of convenience, rewriting Eqs.(2.35) and (2.44) as,

$$ {}^{t+\Delta t}\mathbf{u} = \left[\frac{1}{\Delta t^2}\mathbf{M_L}^{-1}\right]\left\{{}^{t}\mathbf{F} - \mathbf{K}_{u\phi}{}^{t}\phi - \mathbf{K}_{uu}{}^{t}\mathbf{u} + 2\,\frac{\mathbf{M_L}}{\Delta t^2}\,{}^{t}\mathbf{u} + {}^{t-\Delta t}\mathbf{u}\right\}, \tag{2.52} $$

$$ \mathbf{K}_{\phi\phi}{}^{t+\Delta t}\phi = {}^{t+\Delta t}\mathbf{q} - \mathbf{K}_{\phi u}{}^{t+\Delta t}\mathbf{u}. \tag{2.53} $$

In PCD algorithm the coupling iterations are not performed in each time step. In this algorithm, the mechanical displacement solution at time $t+\Delta t$ is obtained by solving Eq.(2.52) using central difference integration and the electric potential at a time $t+\Delta t$ is solved from Eq.(2.53). The Eqs.(2.52) and (2.53) are solved separately to obtain ${}^{t+\Delta t}\mathbf{u}$ and ${}^{t+\Delta t}\phi$, respectively. ${}^{t+\Delta t}\mathbf{u}$ is used to calculate ${}^{t+\Delta t}\phi$. It is observed in Eq.(2.52) that, the ${}^{t+\Delta t}\mathbf{u}$ is based on previous solutions such as ${}^{t}\mathbf{u}$, ${}^{t-\Delta t}\mathbf{u}$, ${}^{t}\mathbf{F}$ and ${}^{t}\phi$. The schematic of noniterative partitioned coupling of electric field and structure is briefly given in Fig. 2.7. The analysis flow chart is illustrated in Fig. 2.8.

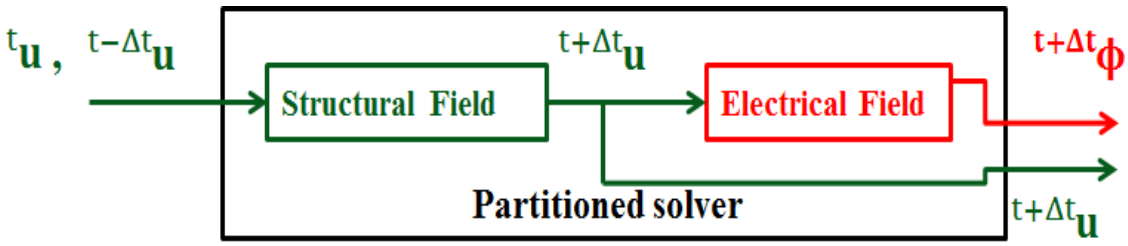

Figure 2.7: Schematic representation of PCD algorithm.

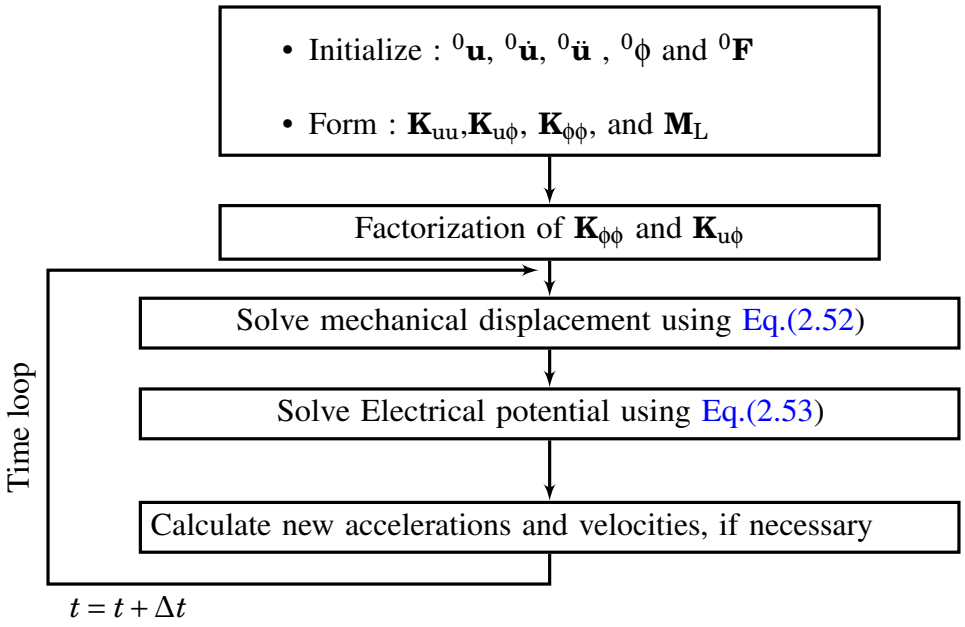

Figure 2.8: Flow chart of the analysis procedure of the PCD algorithm.

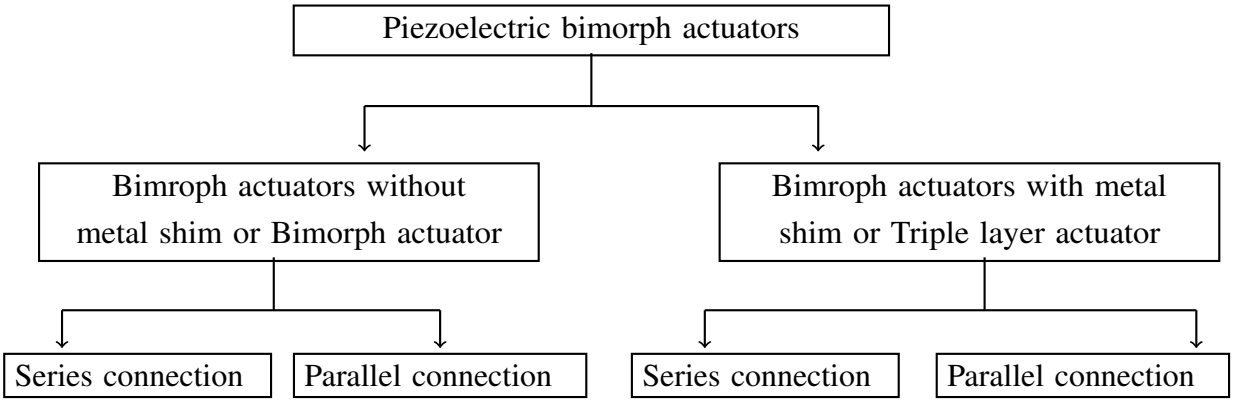

Figure 2.9: Classification of piezoelectric bimorph actuators

2.6 Analysis of piezoelectric bimorph actuators

The numerical results obtained using the proposed finite element coupled algorithms for piezoelectric bimorph actuator is presented here. These piezoelectric bimorph actuators have a very wide area of applications and recently they have are used to actuate the insect-scale robots [2, 15].

The piezoelectric bimorph actuators consist of a double layer of piezoelectric ceramic joined together over their long surfaces. Usually, a metal shim is attached between the two piezoelectric ceramic in-order to enhance the reliability and mechanical strength. This type of the piezoelectric bimorph actuator is called as bimorph actuators with metal shim or triple layer actuator [21]. The classification of piezoelectric bimorph actuators are depicted in Fig. 2.9.

In general, two types of electrical connections are practically used in the configuration of the bimorph actuator shown in Fig. 2.10. One is a series connection, where the piezoelectric layers have opposite polarization directions, and an electric field is applied across the thickness of the bimorph as shown in Figs. 2.10(a) and 2.10(c). The second type of connection is a parallel connection, where the two piezoelectric ceramic layers have a polarization in the same directions, and the electric field is applied across each individual layer with opposite polarity as shown in Figs. 2.10(b) and 2.10(d).

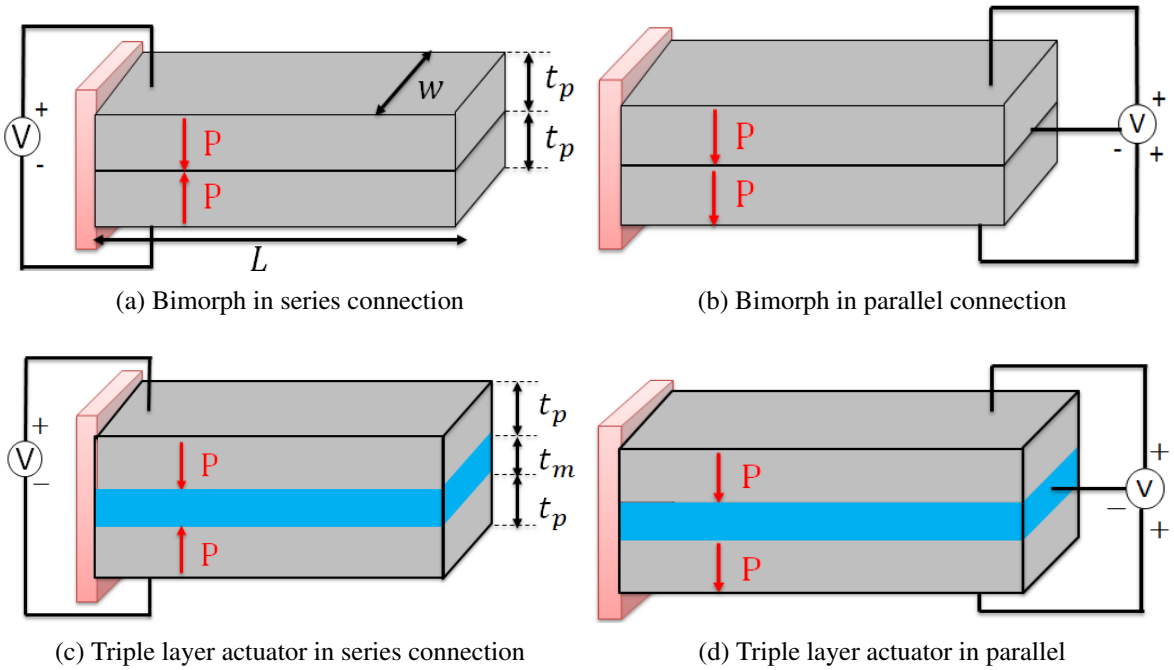

(a) Bimorph in series connection

(b) Bimorph in parallel connection

(c) Triple layer actuator in series connection

(d) Triple layer actuator in parallel

Figure 2.10: Different configurations of cantilever piezoelectric bimorph actuators ▮ :piezoelectric layer (PVDF), ▮ :metal layer (brass), P ↑ : polarization direction.

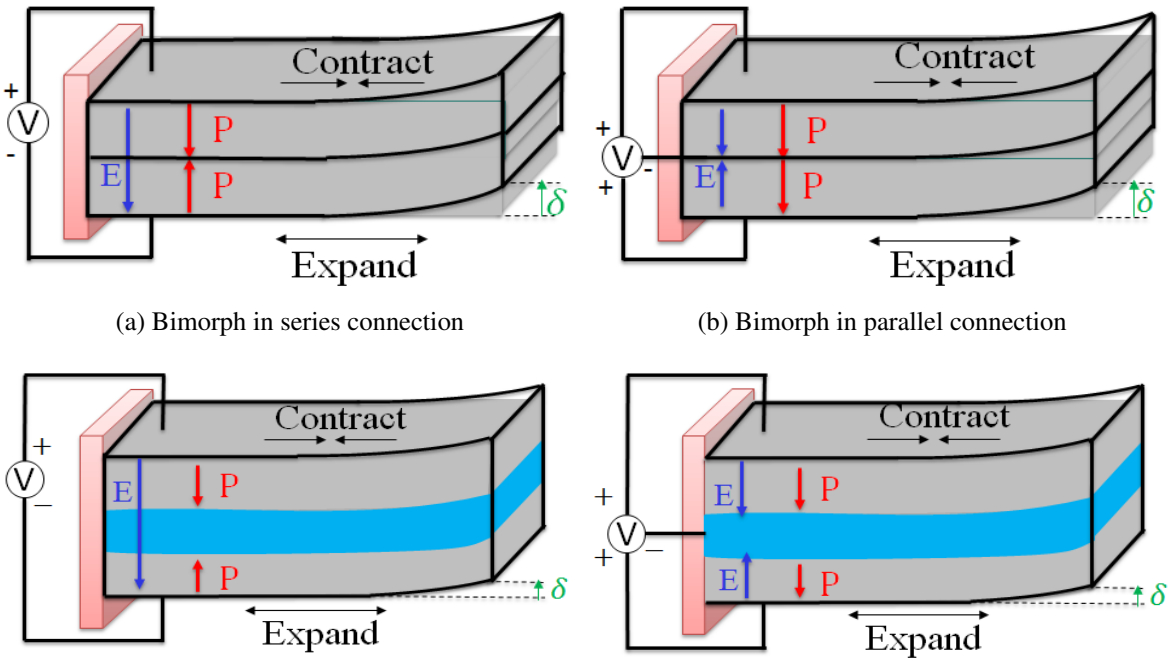

(a) Bimorph in series connection

(b) Bimorph in parallel connection

(c) Triple layer actuator in series connection

(d) Triple layer actuator in parallel

Figure 2.11: Bending in piezoelectric bimorph actuators subjected to external voltages.

Due to the symmetrical structure, in both the series–and parallel–configurations when an electric field is applied to the piezoelectric layers, the induced electric forces in the upper half thickness is canceled by that of the lower half thickness. Hence, for the given configurations in Fig. 2.10 the upper piezoelectric layer contracts and lower piezoelectric layer expands, resulting in a pure bending in the upward direction [21, 22]. Length, width and thickness directions of the bimorph actuator are assigned as X, Y, and Z axes, respectively. Directional parameters of piezoelectric constants are indicated by the subscripts 1,2, and 3, which correspond to X, Y, and Z axes, respectively. The bending effect of piezoelectric bimorph actuator configurations shown in Fig. 2.10 subjected to external voltages is depicted in Fig. 3.9. The material properties used in the numerical simulation and theoretical calculation of piezoelectric bimorph actuators shown in Fig. 2.10 are listed inTable 2.1.

Table 2.1: Material properties used for calculation

materials	Piezoelectric stress constant e_{31}(C/m^2)	Piezoelectric strain constant d_{31}(C/N)	Young's modulus (N/m^2)	Density (kg/m^3)	Poisson's ratio
PVDF	0.046	2.30×10^{-11}	2.0×10^{9}	1800	0.29
Brass	-	-	110×10^{9}	8800	0.35

2.6.1 Bending displacement of piezoelectric bimorph actuators: Theory

The theoretical solutions for the deflection of a piezoelectric bimorph actuator subjected to external voltage for the configuration shown in Figure (2.10) are as follows.

a) Static deflection of a piezoelectric bimorph actuator without metal shim

The transverse deflection u_3 for bimorph actuator without metal shim is given as [7]

$$u_3(X) = \frac{3X^2}{4t_p} d_{31} E_3, \tag{2.54}$$

where d_{31} is piezoelectric strain constant, E_3 is an electric field in the thickness direction and t_p is the thickness of each piezoelectric layers. u_3 reaches the maximum value at $X = L$, where L is the total length of the bimorph actuator. Therefore, the tip deflection of the bimorph actuator in both series and parallel connection [7, 21, 22] is given as

$$u_3(L) = \delta = \frac{3L^2}{4t_p} d_{31} E_3. \tag{2.55}$$

For a series connection the electric field is $E_3 = V/2t_p$ and for parallel connection $E_3 = V/t_p$. Substituting $E_3 = V/2t_p$ into Eq.(2.55), the tip deflection of bimorph actuator in series connection is given as

$$\delta = \frac{3L^2}{8t_p^2} d_{31} V. \tag{2.56}$$

Substituting $E_3 = V/t_p$ into Eq,(2.55), the tip deflection of bimorph actuator in parallel connection is given as

$$\delta = \frac{3L^2}{4t_p^2} d_{31} V, \tag{2.57}$$

From Eqs.(2.56) and (2.57), it is noted that with the same geometrical dimensions and under the same external voltages, the maximum tip deflection which can be achieved in piezoelectric bimorph actuators connected in parallel is twice of that in piezoelectric bimorph actuators connected in series. Therefore, piezoelectric bimorph actuator connected in parallel is competent.

By using Eqs.(2.56) and (2.57), the theoretical solution of static tip deflection for the configuration shown in Figs. 2.10(a) and 2.10(b) and using the material properties given in Table 2.1 for L=100 mm, w=1 mm (width of each layers), t_p=0.5 mm and V=1 V are given in Table 2.2.

Bimorph configuration	Static tip deflection δ (μm)
Bimorph actuator in series connection	0.3450
Bimorph actuator in parallel connection	0.6900

Table 2.2: Analytical solution of tip static deflection (L=100mm, w=1mm, t_p=0.5mm, t_m=0.1mm, V=1V).

b) Static deflection of a piezoelectric bimorph actuator with metal shim

The tip deflection of triple layer piezoelectric actuator is given as [21],

$$\delta = \frac{6E_p d_{31} E_3 (t_m t_p + t_p^2) L^2}{2E_p (3t_m^2 t_p + 6t_m t_p^2 + 4t_p^3) + E_m t_m^3}, \tag{2.58}$$

where E_p is Young's modulus of piezoelectric layer, E_m is Young's modulus of metal layer, t_p is thickness of each piezoelectric layer, t_m is thickness of metal layer and $E_3 = V/2t_p$ for series connection and $E_3 = V/t_p$ for parallel connection. The thickness of the metal layer has significant effect on the performance of the triple layer piezoelectric bimorph actuator. For ease

of convenience, say $A = E_m/E_p$, $B = t_m/2t_p$, $t = t_m/2t_p$ above equation in simplified form as [21],

$$\delta = \frac{3L^2}{2t} \frac{(1+B)(2B+1)}{AB^3+3B^2+3B+1} d_{31}E_3 \tag{2.59}$$

From the Eqs.(2.58) and (2.59), it is evident that as the metal layer thickness increases, tip deflection decreases. As mentioned in [21], the thickness ratio $B = t_m/2t_p = 0.2$ is good enough to reinforce the actuator mechanical strength, resulting a reduction of very small tip deflection. The piezoelectric bimorph cantilever used in this study had the dimensions of the length L=100mm, the width w=1mm, and the thickness of each piezoelectric ceramic layers t_p=0.5mm.

In order to choose the thickness of the metal later, a non-dimensional parameter is defined,

$$\Gamma = \frac{(1+B)(2B+1)}{AB^3+3B^2+3B+1} \tag{2.60}$$

The effect of metal layer on the tip deflection of bimorph actuator can be determined by plotting Γ $vs.$ thickness ratio B by varying the t_m and fixing the values of L and t_p, is shown in Fig. 2.12(a).

It is clear from the Fig. 2.12(a) that when the thickness ration B=0, i.e., t_m=0, t=2t_p, the tip deflection of both series and parallel connections of triple layer piezoelectric actuator is δ=0.345µm and δ=0.690µm respectively, which are in consistent with tip deflection of series connection and parallel connection of bimorph actuator, respectively as show in Table 2.2. Also, when B=0.1, i.e., t_m=0.1, t=t_m+2t_p, the tip deflections is δ=0.29891µm and δ=0.59783µm for series and parallel connections of triple layer piezoelectric actuator, which shows a small reduction in the tip deflection compared with bimorph actuators satisfying the thickness ratio criteria is depicted in Fig. 2.12(b) and Table 2.3.

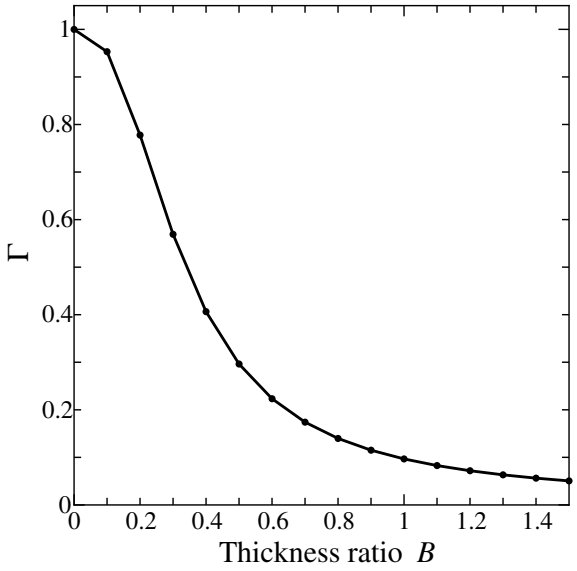

(a) Normalized tip deflection Γ $vs.B$

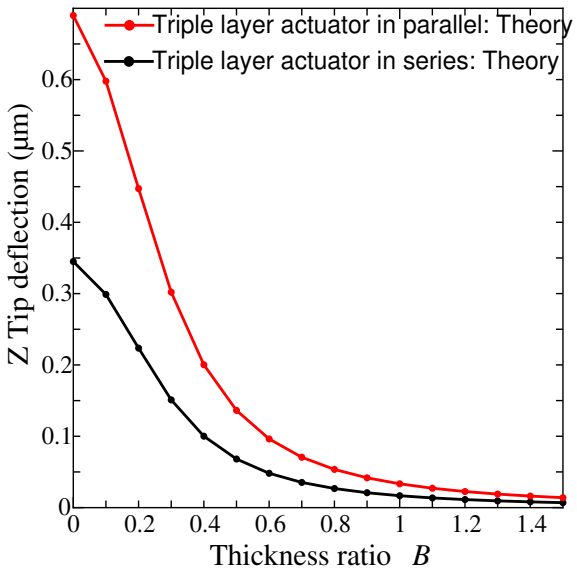

(b) Tip deflection of bimorph actuator with metal shim $vs.B$

Figure 2.12: Effect of metal layer thickness on the tip deflection of bimorph actuators

The metal layer thickness t_m=0.1 mm is considered based on the parametric analysis which satisfy the thickness ratio criteria. By using the Eq.(2.58), the theoretical solution of static tip deflection for the triple layer bimorph actuator shown in Figs. 2.10(c) and 2.10(c) and using material properties given in Table 2.1 for L=100 mm, w=1 mm (width of each layers), t_p=0.5 mm, t_m=0.1 mm and V=1 V are given in Table 2.3.

Triple layer bimorph configuration	Static tip deflection δ (µm)
Triple layer actuator in series connection	0.29891
Triple layer actuator in parallel connection	0.59783

Table 2.3: Analytical solution of tip static deflection (L=100mm, w=1mm, t_p=0.5mm, t_m=0.1mm, V=1V).

c) Dynamic tip deflection of a piezoelectric bimorph actuator driven by a dynamic voltage

The dynamic tip deflection of the piezoelectric bimorph cantilever without metal shim is [22],

$$\delta_{dyn} = \frac{3d_{31}V \sin \varpi L \sinh \varpi L}{4t_{p^2}\varpi^2(1+\cos \varpi L \cosh \varpi L)}, \tag{2.61}$$

where ϖ is the normalized frequency defined as,

$$\varpi = \sqrt{\frac{\omega}{a}}, \tag{2.62}$$

with

$$a = \sqrt{\frac{E_p I}{\rho_p A}}, \tag{2.63}$$

where ω is the frequency of the dynamic voltage, I is the moment of area, ρ_p is the density of piezoelectric material, and A is the cross sectional area. By adding the flexural rigidity and the mass per unit length of the metal layer into the Eq.(2.63) one can obtain theoretical solution for the dynamic tip deflection of a bimorph actuator with metal shim. In Eq.(2.61), when the denominator term $1+\cos \varpi L \cosh \varpi L$ becomes zero, the tip deflection goes to infinity, which indicates the resonance for the bimorph actuator. Moreover, the nominator term $\sin \varpi L \sinh \varpi L$ and the denominator term $1+\cos \varpi L \cosh \varpi L$ never reach zero at the same normalized frequency ϖ. Theoretically, it is well–known fact that for linear systems without damping, resonance refers to the vibration with an infinite amplitude. Therefore, using theoretical calculations it is difficult to capture the resonance amplitudes. However, using Eq.(2.61) one can calculate the dynamic tip displacements at driving voltage frequencies far away from the resonance frequencies. This effect will be demonstrated in Section 2.6.2.

c) Bending resonance of bimorph actuators: Theory

a) Bending resonance of bimorph actuator without metal shim

The first bending resonance $\omega_r^{(1)}$ for bimorph actuator without metal shim in series connection and parallel connection is given as [22],

$$\omega_r^{(1)} = \frac{1.875^2}{L^2}\sqrt{\frac{E_p I}{\rho_p A}}, \tag{2.64}$$

where I is moment of area, A is the cross sectional area, and 1.875 is constant eigenvalue for first bending mode. Using the material properties of PVDF given in Table 2.1 and dimensions L=100mm, w=1mm, t_p=0.5mm into Eq.(3.57) gives the resonance frequency for first bending mode

$$\omega_r^{(1)} = 106.988 \text{ rad/sec.}$$

b) Bending resonance of bimorph actuator without metal shim

The first bending resonance $\omega_r^{(1)}$, for triple layer actuator shown in Fig. 2.10(c) and 2.10(d) is given as [21],

$$\omega_r^{(1)} = \frac{1.875^2 E_p^{1/2}}{2L^2}\sqrt{\frac{2t_p^3 + 6t_p(t_m + t_p)^2 + (E_m/E_p)t_m^3}{3(t_m\rho_m + 2t_p\rho_p)}}. \tag{2.65}$$

Substituting the material properties of PVDF and brass metal given in Table 2.1 into Eq.(2.65) gives the resonance frequency for first bending mode in triple layer actuator

$$\omega_r^{(1)} = 103.30 \text{ rad/sec.}$$

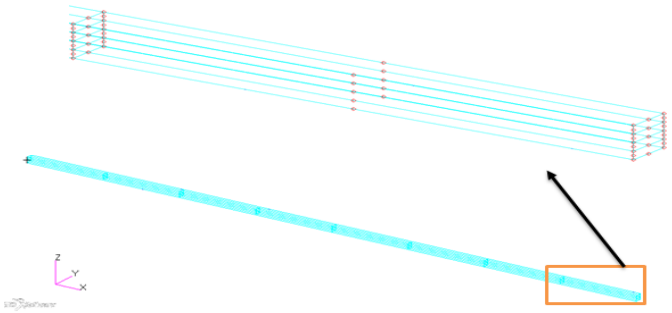

(a) M1: 32 elements and 287 nodes

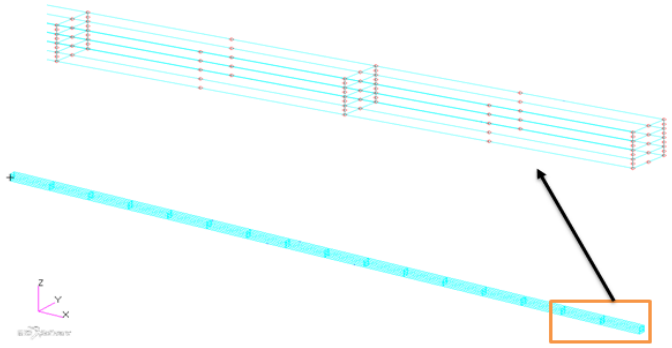

(b) M2: 64 elements and 551 nodes

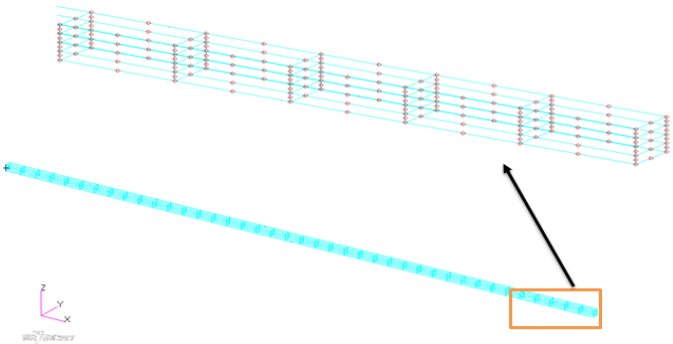

(c) M3: 160 elements and 1343 nodes

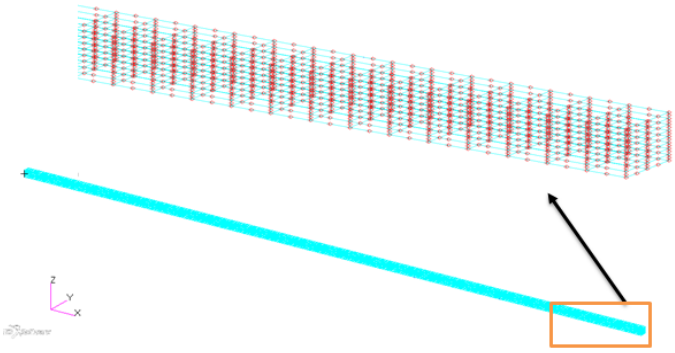

(d) M4: 2560 elements and 15429 nodes

Figure 2.13: Piezoelectric bimorph cantilever Hexa20 FE mesh convergence

2.6.2 Numerical analysis of piezoelectric bimorph actuator

a) Static tip deflection of piezoelectric bimorph actuators without metal shim

The numerical problems shown in Figs. 2.10(a) and 2.10(b) are analyzed here. The monolithic coupling, the block Jacobi (BJ) partitioned iterative coupling [47]and block Gauss-Seidel (BGS) partitioned iterative coupling [47] are employed, where the time integration is not taken into account, by eliminating the inertial and damping effects. At first, the mesh convergence analysis is presented for the shown mesh division in Fig. 2.13 using MN algorithm. The number of elements along length direction (X), width direction (Y), and thickness direction (Z) for the above shown mesh are given in Table 2.4

Table 2.4: Mesh division of piezoelectric bimorph actuator without metal

Bimorph Mesh	Number of Hexa20 elements				Total number of nodes
	X direction	Y direction	Z direction	Total	
M1	8	1	4	32	287
M2	16	1	4	64	551
M3	40	1	4	160	1343
M4	160	2	8	2560	15429

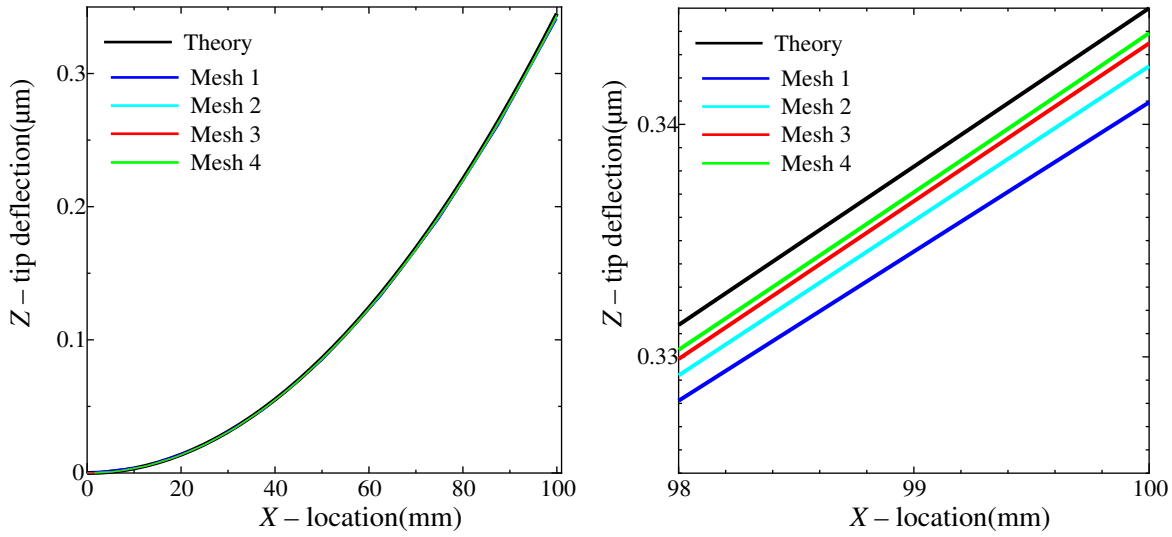

(a) Bimorph actuator deformation along the length (b) Enlarged view near the end (L=98 mm to 100 mm)

Figure 2.14: Bending deformation of the bimorph actuator: Mesh convergence analysis using MN algorithm

Table 2.5: Mesh convergence result: Tip deflection at bias voltage V = 1 V

Mesh	Tip displacement (µm)	Error [%]
M1	0.34095	1.173
M2	0.34250	0.732
M3	0.34349	0.438
M4	0.34392	0.313

Fig. 2.14 and Table 2.5 summarizes the mesh convergence results analyzed using the monolithic coupling algorithm at bias voltage V = 1 V. The tip displacement relative error in Table 2.5 is calculated using the theoretical solution given in Table 2.2 for series connection. The coarse Hexa20 meshes M1 and M2 predicts quite less accurate displacement at the tip of the cantilever compared to that of fine mesh M3 and very fine mesh M4. But the meshes M3 and M4 show a similar results. The mesh convergence results shows that the results are comparable to those from the fine mesh M3 and very fine mesh M4, but the simulation with the fine mesh M3 required considerably less computational time than the analysis with the very fine mesh M4. Based on this mesh convergence study, by using the mesh which consists of 160 elements and 1343 nodes.

Fig. 2.15 show the convergence properties of the block Jacobi and block Gauss-Seidel partitioned iterative algorithms for tip deflection. It follows from these results that, at least 6 iterations are necessary for block Jacobi algorithm and 4 iterations for block Gauss–Seidel algorithm in order to satisfy the convergence condition of displacement relative error given in Eq.(2.49). In general, the Gauss–Seidel iteration method tend to converge faster than the Jacobi iteration method, because Gauss–seidel method uses the most recent solutions of the other subsystems. The tolerance value used is ϵ=1×10^{-5}. Based on the mesh convergence study, 6 iterations in block Jacobi and 4 iterations in block Gauss–Seidel algorithm is used for the static analysis. Table 2.6 shows the static tip deflection accuracy of the monolithic, block Jacobi, and block Gauss–Seidel algorithms compared with the theoretical solution for the numerical problems described in Figs. 2.10(a) and 2.10(b). It follows from these static analyses that the monolithic, block Jacobi, and block Gauss–Seidel algorithms can solve accurately for the static bending deflection of bimorph actuator.

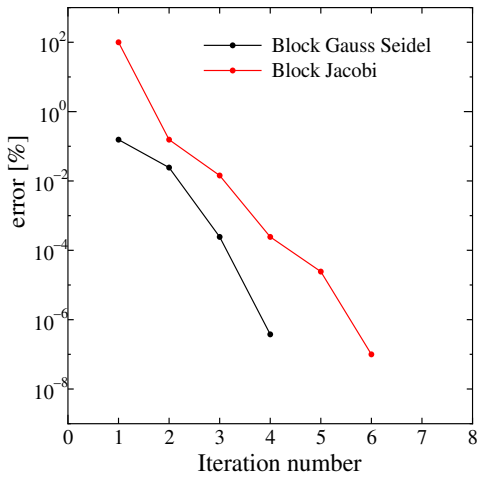

Figure 2.15: Convergence properties of of BJ and BGS algorithms for static bending deflection

Table 2.6: Accuracy of the proposed algorithms: Static tip deflection

Configuration	Tip deflection (μm)			
	Theory	Monolithic	Block Jacobi	Block Gauss–Seidel
Bimorph in series	0.3450	0.34349	0.34487	0.34487
Bimorph in parallel	0.6900	0.68697	0.69202	0.69202

b) Static tip deflection of piezoelectric bimorph actuators with metal shim

In the analysis of triple layer actuator shown in Figs. 2.10(c) and 2.10(d), the piezoelectric coefficient constants of the metal layer which is sandwiched between two piezoelectric polymers are zero because brass is a non-piezoelectric material. Therefore, the metal layer is not polarized, piezoelectric coefficient matrix $\mathbf{e} = 0$ in Eq.(2.33c). It is well-known fact that the electric field inside a metal is zero ($\mathbf{E} = 0$), therefore, a metal is regarded as a medium of infinite dielectric constant ($\varepsilon = \mathbf{D}/\mathbf{E}$) [58]. For metal layer, piezoelectric FE equations (2.31) and (2.32) are reduces to [56],

$$\mathbf{M}\ddot{\mathbf{u}} + \mathbf{K}_{uu}\mathbf{u} + \cancelto{0}{\mathbf{K}_{u\phi}}\phi = \mathbf{F}, \tag{2.66}$$

$$\cancelto{0}{\mathbf{K}_{\phi u}\mathbf{u}} + \mathbf{K}_{\phi\phi}\phi = \mathbf{q}, \tag{2.67}$$

i.e.,

$$\mathbf{M}\ddot{\mathbf{u}} + \mathbf{K}_{uu}\mathbf{u} = \mathbf{F}, \tag{2.68}$$

$$\mathbf{K}_{\phi\phi}\phi = \mathbf{q}, \tag{2.69}$$

The structure and electric mesh of triple layer actuator consists of 1939 nodes and 240 elements. A large value of dielectric constant is used for the metal layer in the computer program. The choice of the dielectric constant of the metal layer in the numerical problems shown in Figs. 2.10(c) and 2.10(d) is based on the parametric study presented in Figure.2.16. It is clear from the Fig. 2.16(a) that when $\varepsilon_{11} = \varepsilon_{22} = \varepsilon_{33} = 10^{15}$ F/m, the tip deflection is close to the theoretical solution. The tip displacement relative error between theoretical solution in Table 2.3 and the numerical solution for $\varepsilon_{11} = \varepsilon_{22} = \varepsilon_{33} = 10^{15}$ F/m is 0.05 %, shown in Fig. 2.16(b). In a 64-bit computer memory, the number of significant digit of double-precision floating-point format is about 15. Therefore, it is sufficient to use the value of the dielectric constant of a metal close to 10^{15} F/m.

Fig. 2.17 shows the static bending deformation of the triple layer actuator connected in series from the theoretical and numerical solutions. The numerical solutions are in good agreement with the theory. Table 2.7 shows the tip deflection in comparison with the numerical solution. It follows from these results that the monolithic and partitioned iterative algorithms (block Jacobi and block Gauss–Seidel) can accurately predict the static characteristics of bimorph actuator and triple layer actuator.

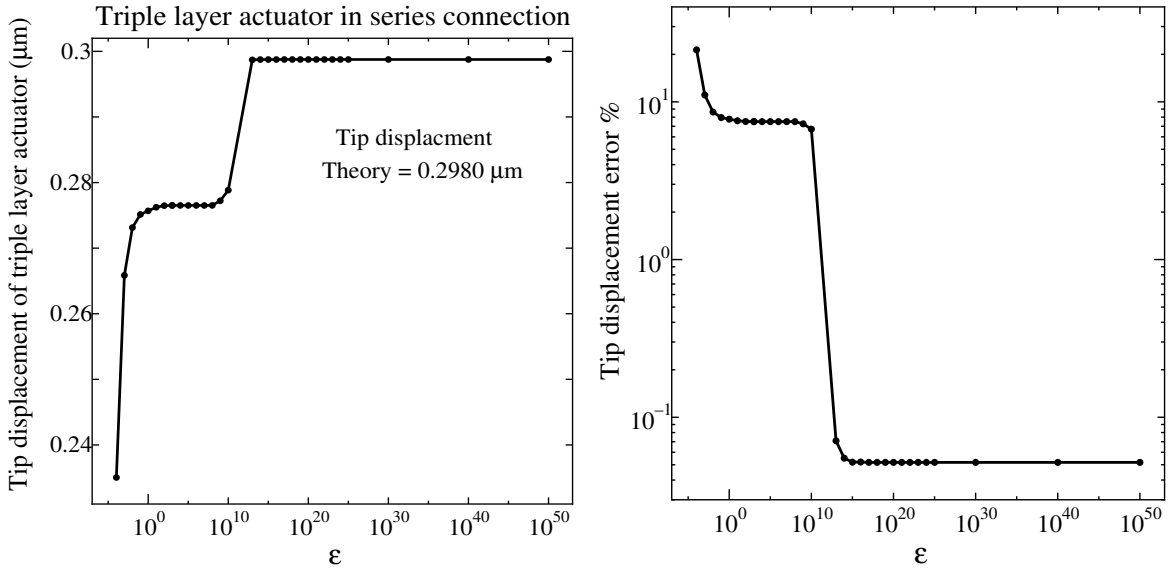

(a) Tip deflection v.s dielectric constant of the metal layer(b) Relative error v.s dielectric constant of the metal layer

Figure 2.16: Vary dielectric constant of metal layer: Parametric study-Triple layer actuator in series connection

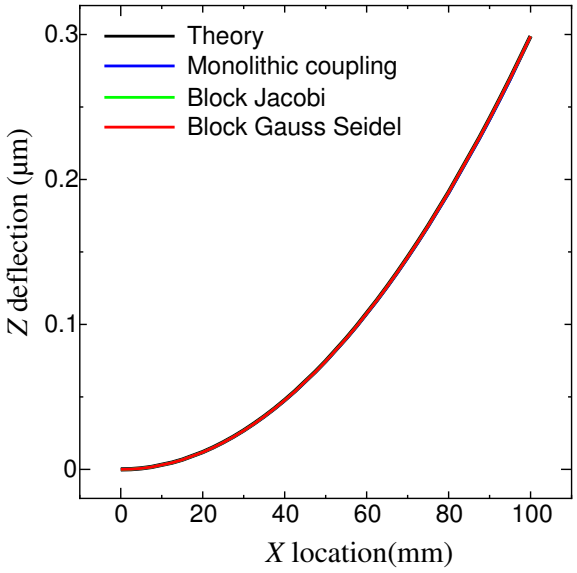

Figure 2.17: Static bending deformation of the triple layer actuator connected in series with bias voltage V = 1 volts

Table 2.7: Static tip deflection of triple layer actuator with L=100mm, w=1mm, t_p=0.5mm, t_m=0.1mm, and bias voltage V = 1V

Configuration	Tip deflection (μm)			
	Theory	Monolithic	Block Jacobi	Block Gauss–Seidel
Triple layer actuator in series	0.29891	0.29871	0.29876	0.29876
Triple layer actuator in parallel	0.59783	0.59421	0.59772	0.59772

c) Dynamic analysis of piezoelectric actuators: Response to AC voltage

In general, the central difference time integration method requires $\Delta t < \Delta t_{cr}$. The critical time step $\Delta t_{cr} = L/C_v$ for the present bimorph cantilever mesh assemblage is 1.18585μs and a scale factor of $0.1\Delta t_{cr}$ would give $\Delta t = 1.18585 \times 10^{-7}$sec. From the theoretical solution, the natural period T_r of the first mode of bimorph actuator without metal shim is about 0.05873 s. When the bimorph cantilever vibrates at its first resonance frequency at least 495,265 steps (step $n^t = \mathrm{T}_r/\Delta t$) are essential in order to capture one period [45], which becomes very expensive computationally [47]. Therefore, all the dynamic analysis of piezoelectric bimorph actuators have been carried out using MN, BJN and BGSN algorithms.

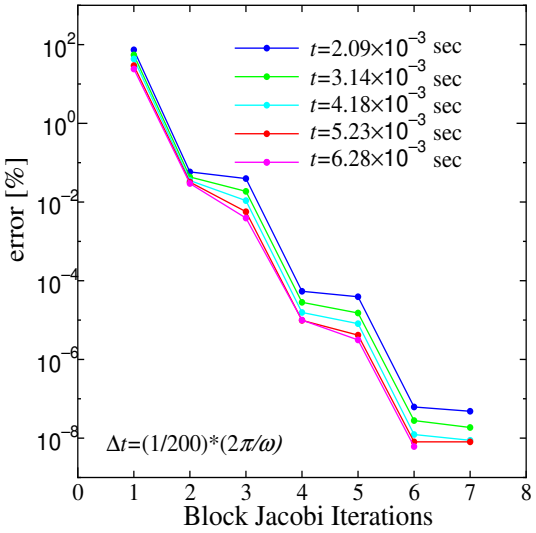

(a) Iteration convergence in BJN algorithm

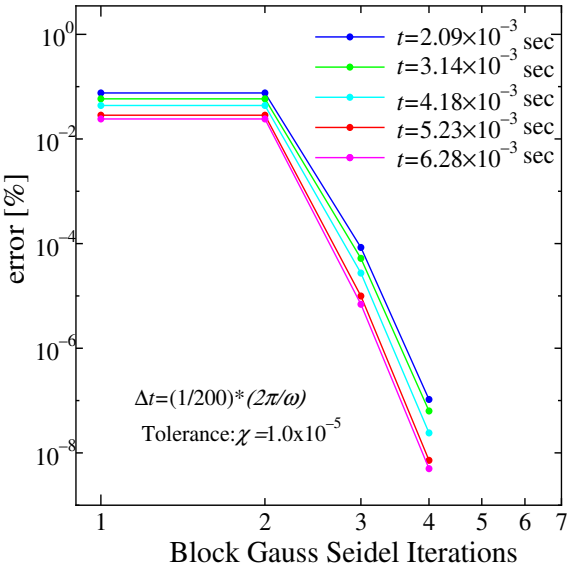

(b) Iteration convergence in BGSN algorithm

Figure 2.18: Convergence results of BJN and BGSN algorithm for dynamic analysis

The dynamic problem of AC type input is examined. When the applied signal to the bimorph cantilever beam is of the AC type, the corresponding charge q will be $V\sin\omega$ t, where V is the amplitude of the signal, and ω is the angular frequency of the charge q. The accuracy of these coupled algorithms is dependent on the choice of time increment Δt. The analysis was carried at an unconditionally stable and numerically undamped condition ($\beta = 0.25$ and $\gamma = 0.5$).

In Fig. 2.18, the convergence properties of the partitioned iterative algorithms (BJN and BGSN algorithms) at different time steps in order to perform dynamic analysis of piezoelectric

bimorph actuators is presented. As can be seen in the Fig. 2.18(a), after 6 iterations for each time increment, the solution is converged satisfying the convergence criteria in BJN algorithm and 4 iterations for each time step in BGSN algorithm. From these results, fixed the number of iterations to 6 in BJN, and 4 in BGSN to compute the response of bimorph actuator at different frequencies.

Fig. 2.19 shows the choice of time increment for dynamic analysis at various input frequencies. These results are analyzed for bimorph actuator without metal shim connected in series, shown in Fig. 2.10(a). The first bending resonance frequency for this numerical example is $\omega_r^{(1)} = 106.988$ rad/sec which is evaluated using theoretical Eq.(3.57)), discussed in Section 2.6.1. When the frequencies of input signals to the bimorph actuator is much smaller or larger than its resonance frequency, the displacement amplitude computed with all the time increment approximately coincide with each other as shown in Figs. 2.19(a) and 2.19(c). It indicates that the influence of time increment Δt on the deflection is not much significant compared to that with the resonance frequency. On contrary, a fine Δt is necessary for input frequency near resonance [47] to obtain converged solutions as shown in Fig. 2.19(b). This is because the deflection is very sensitive to the resonance and a fine time increment is necessary to capture the resonance effect. Therefore, the time increment is chosen as Δt=(1/100)×($2\pi/\omega$) to obtain the converged vibration amplitudes.

Fig. 2.20 shows some of the vibration characteristics of the bimorph actuator in series connection to AC signals with different frequencies for input signal V=1 V with BGSN algorithm. From the results in Fig. 2.20 it is also noted that, for the input frequencies close to resonance points (ω=106.9, 107, 107.1, 107.2 rad/sec), the responses have large amplitudes. In general, the actuators are very sensitive to the input AC signals whose frequencies are close to the structure resonance frequency, shown in Figs. (2.20(b))–(2.20(e)). When the frequencies of input signals to the bimorph actuator is much smaller than its structural resonance frequency (ω=30 rad/sec), the maximum vibration amplitudes of the tip will be approximately equivalent to the tip deflection when the force is applied statically, shown in Fig. 2.20(a). For input voltage frequencies away from the resonance (ω=110 rad/sec) have very less amplitudes than frequencies near to the resonance, shown in Fig. 2.20(f). Also, the vibration characteristics with the BJN algorithm is similar to the BGSN algorithm except the number iterations used in each time step. In Ref [47], author presented the AC responses of the same numerical problem using the MN algorithm. All the algorithms show a good agreement with each other.

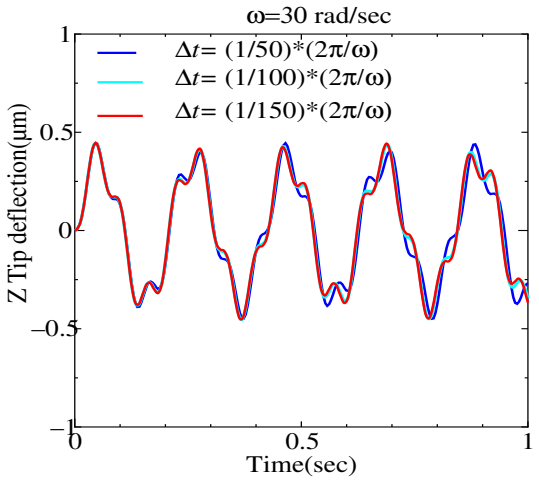

(a) Δt for frequencies much smaller than resonance

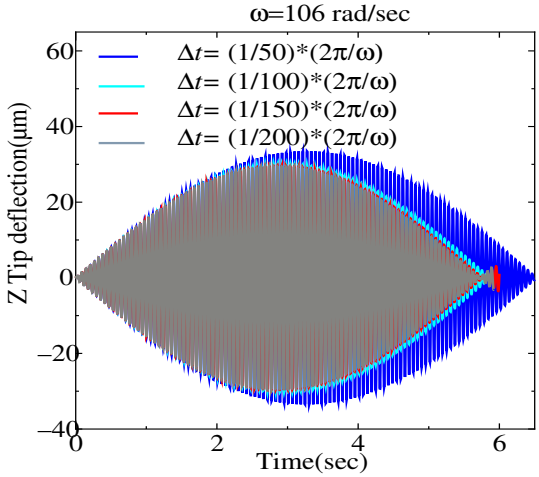

(b) Δt for frequencies very close to resonance

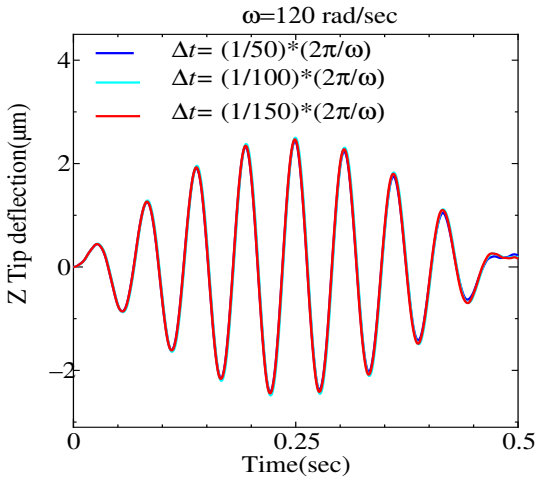

(c) Δt for frequencies much larger than resonance (away from resonance)

Figure 2.19: Time increment for the transient dynamic analysis with the BGSN algorithm

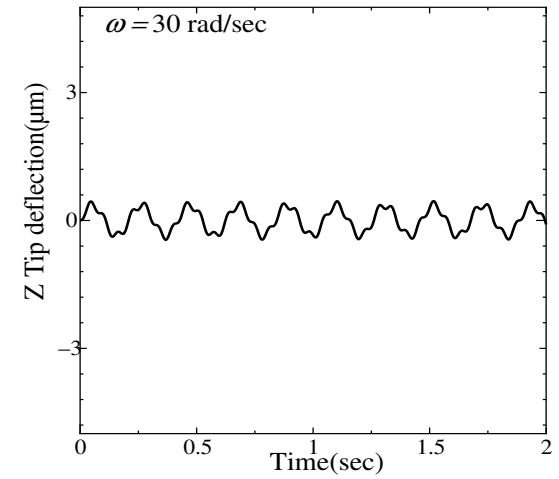

(a) ω=30 rad/sec

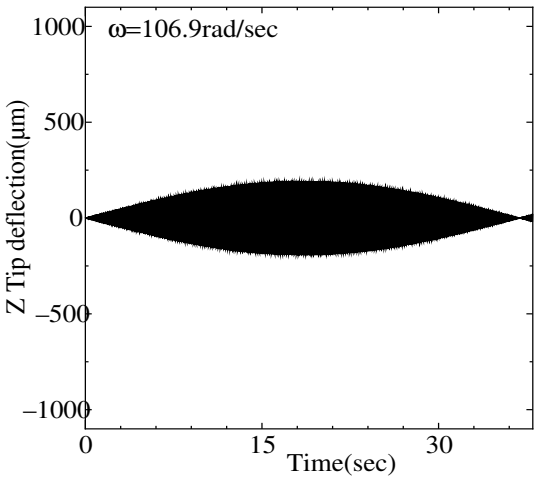

(b) ω=100 rad/sec

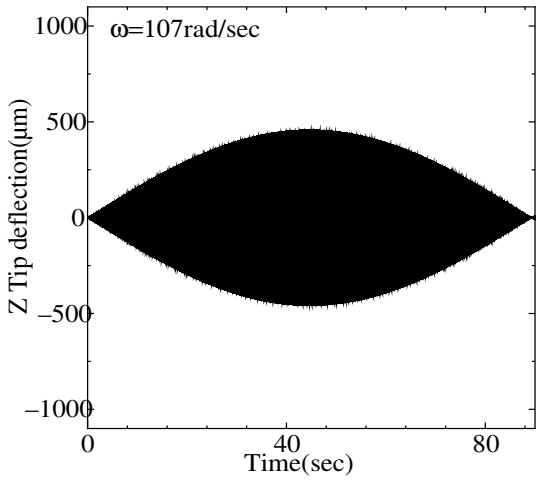

(c) ω=107 rad/sec

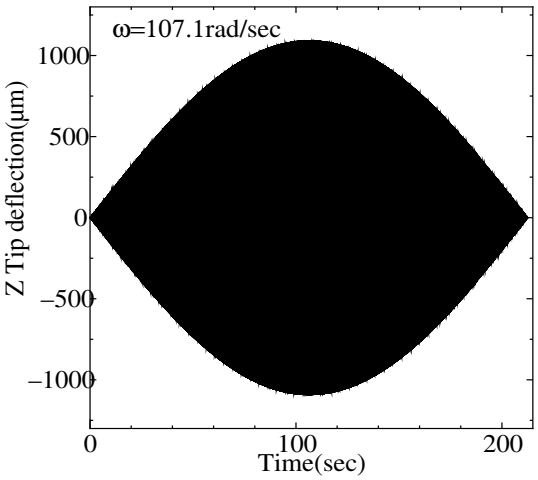

(d) ω=107.1 rad/sec

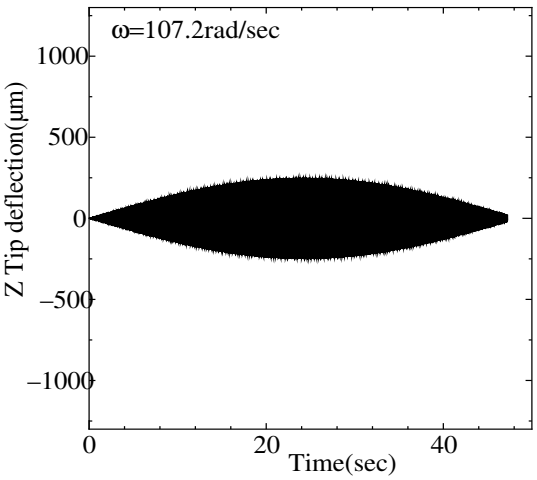

(e) ω=107.2 rad/sec

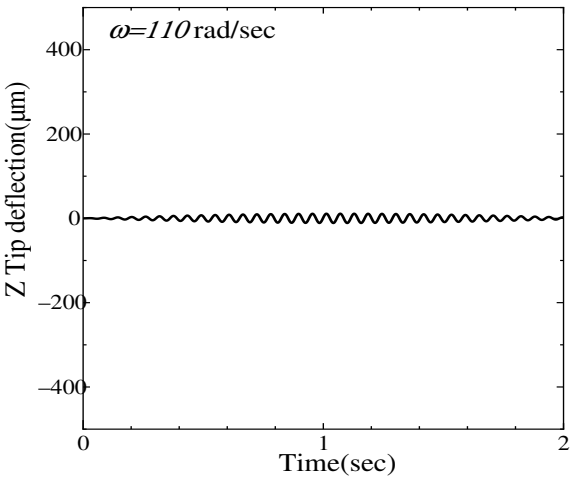

(f) ω=110 rad/sec

Figure 2.20: AC response of the bimorph actuator in series connection at different frequencies with the BGSN algorithm.

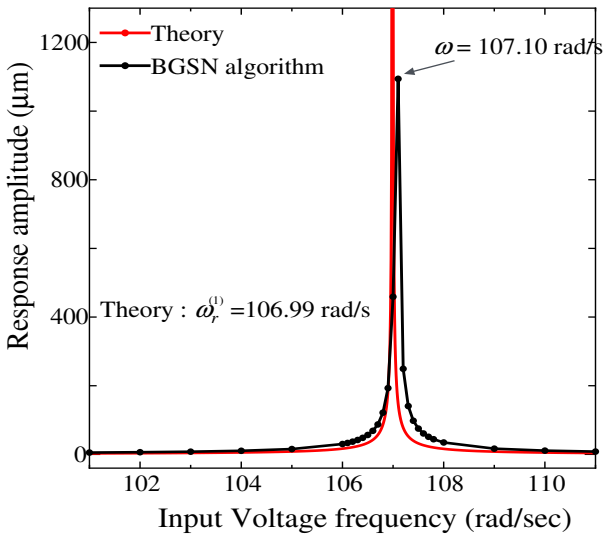

Figure 2.21: Summary of amplitudes of the responses to different input frequencies with the BGSN algorithm and theory for a *bimorph actuator* in series connection

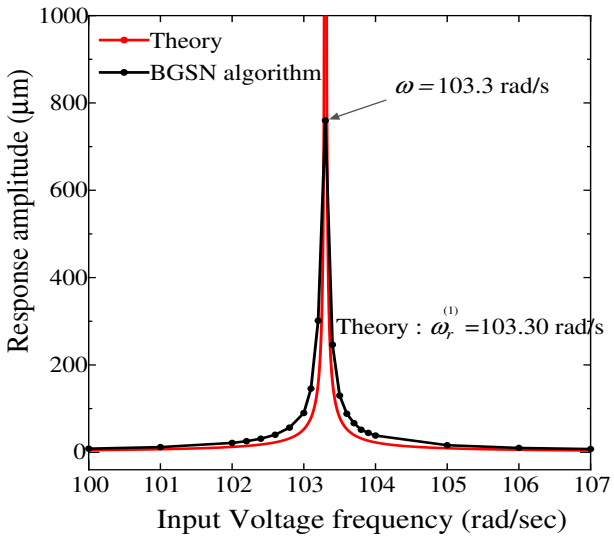

Figure 2.22: Summary of amplitudes of the responses to different input frequencies with the BGSN algorithm and theory for a *triple layer actuator* in series connection

Fig. 2.21 summarizes the amplitudes of the response to the input signals with the different frequencies for the numerical problem in Fig. 2.10(a) analyzed with the BGSN algorithm and compared with the theoretical solution using Eq.(2.61). As described in Section 2.6.1, the theoretical solution calculated using Eq.(2.61) takes infinite amplitude at the resonance $\omega_1^{(r)}$ = 106.99 rad/sec. Using the BGSN algorithm, the peak appears at the input signal frequency

ω=107.1 rad/sec. The increment of frequency used in the numerical solution near resonance points is $\Delta\omega$= 0.1 rad/sec. Good agreement can be seen in the location of resonance frequency and tip peak amplitudes except at resonance points between the numerical solution and theory.Fig. 2.22 shows the profiles of the tip amplitudes of the responses analyzed with BGSN algorithm and theoretical solution for the triple layer actuator described in Fig. 2.10(c). From this response curve, one can see that the larger amplitudes can be found in the location of resonance frequency $\omega_1^{(r)}$ = 103.30 rad/sec. Again, the numerical results and theoretical solution show good agreement with each other.

d) Dynamic analysis of piezoelectric actuators: Response to step voltage

The numerical problems described in Fig. 2.10 dynamic problem are examined. The numerical parameters β and γ in Newmark's time integration method are used to introduce the amount of positive numerical damping into the system.

- For $\gamma = 1/2$ and $\beta = 0.25 \times (\gamma + 0.5)^2 = 0.25$ there is no numerical damping.
- When $\gamma \geq 1/2$ a positive numerical damping is introduced into the system.
  - Example: $\gamma = 0.6$ and $\beta = 0.25 \times (\gamma + 0.5)^2 = 0.3025$.

When a bimorph actuator is actuated introducing positive numerical damping into the system with a step input bias voltage, the steady-state response of the tip deflection is equal to the theoretical solution for the static deflection. The values of β and γ for Newmark's time integration are chosen as $\gamma = 0.6$ and $\beta = 0.25 \times (\gamma + 0.5)^2 = 0.3025$, respectively, to obtain steady state equilibrium after a long time interval. The piezoelectric bimorph actuator described in Fig. 2.10 are driven by a step voltage V=1 V and analyzed using MN, BJN, and BGSN coupled algorithms. The time increment Δt is chosen as 1.0×10^{-3} sec. The number of iterations used for BJN and BGSN algorithm is 6 and 4, respectively, which are determined based on the discussion in Section 2.6.2.

Fig. 2.23 shows the step response of the bimorph actator without metal shim analyzed using MN algorithm with numerical parameters $\gamma = 0.5$ and $\beta = 0.25$, and $\gamma = 0.6$ and $\beta = 0.3025$. As shown in this result, by introducing a positive numerical damping the output tip oscillations reaching a steady-state value, while the undamped condition shows harmonic tip oscillations.

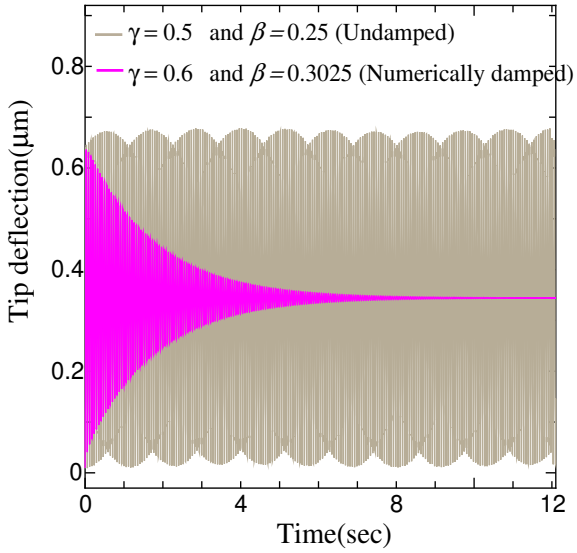

Figure 2.23: Step response of numerical example in Fig. 2.10(a) to input step bias V=1volt under positively damped and undamped condition

Fig. 2.24 shows the step response of numerical problems in Fig. 2.10 to input step bias V=1volt with numerical parameters $\gamma = 0.6$ and $\beta = 0.3025$. The tip deflections in the steady state equilibrium is very close to the theoretical static tip deflection of their respective configurations as shown in Table 2.8. As discussed in Section 2.6.1, the maximum tip deflection which can be achieved in piezoelectric bimorph actuators connected in parallel is twice of that in piezoelectric bimorph actuators connected in series with the same geometrical dimensions and under the same external voltages. This is because the electric field in the parallel connection is twice that of series connection. A same trend can be observed between Figs. 2.24(a) and 2.24(b), and Figs. 2.24(c) and 2.24(d). This indicates that the MN, BJN, and BGSN algorithms accurately capture the step responses of all the numerical examples shown in Fig. 2.10.

Table 2.8: Comparison of steady–state tip deflection with the static tip deflection at bias voltage V = 1V analyzed using BGSN algorithm

Configuration	Step response steady–state tip deflection(μm)	Theory Static tip deflection(μm)	Error[%]
Bimorph in series	0.34436	0.34500	0.184
Bimorph in parallel	0.69201	0.69000	0.293
Triple layer in series	0.29806	0.29891	0.284
Triple layer in parallel	0.59910	0.59783	0.213

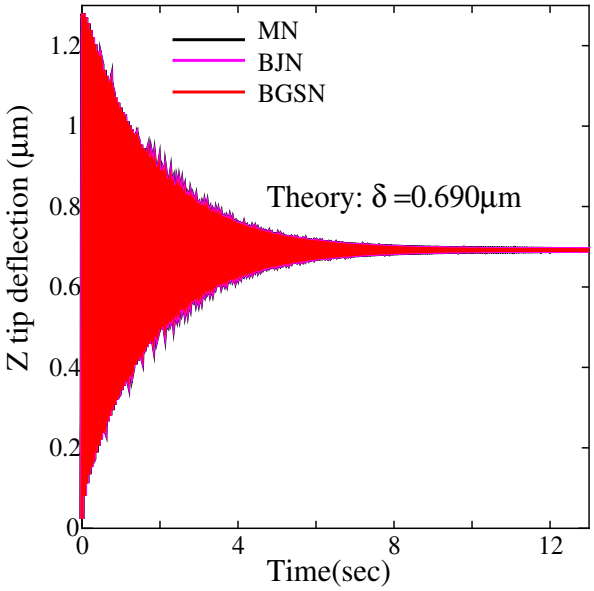

(a) Step response of *bimorph actuator in parallel*

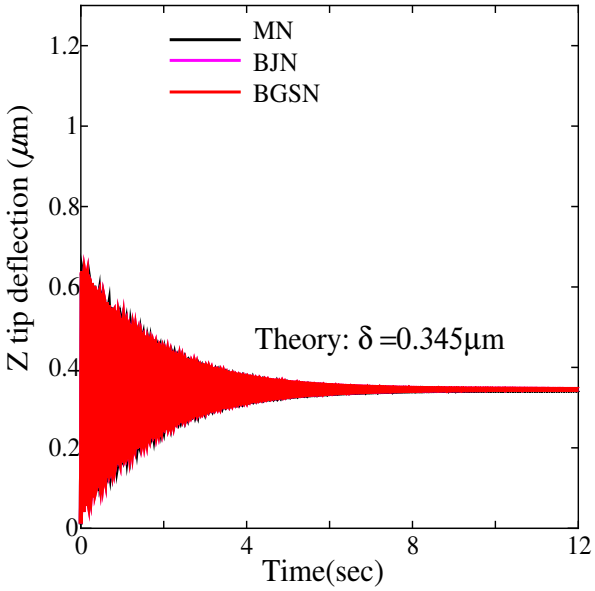

(b) Step response of *bimorph actuator in series*

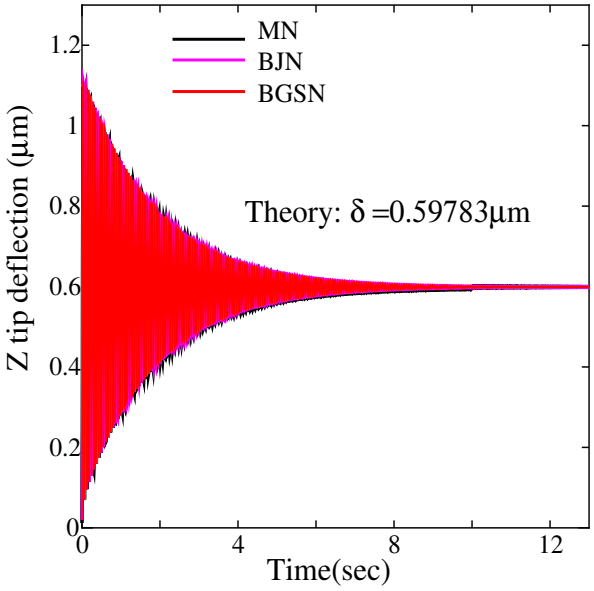

(c) Step response of *triple actuator in parallel*

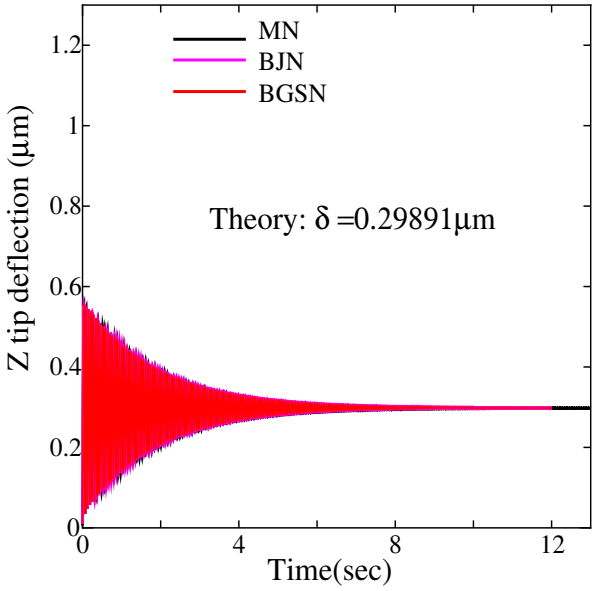

(d) Step response of *triple layer actuator in series*

Figure 2.24: Step response of numerical examples in Fig. 2.10 to input step bias V=1 V under positively damped condition ($\gamma = 0.6$ and $\beta = 0.3025$)

2.7 Analysis of surface acoustic wave (SAW) problem

The purpose of considering surface acoustic wave (SAW) problem is to validate the PCD algorithm with MN, BJN, and BGSN algorithms for high–frequency MEMS applications. Piezoelectricity is also extensively employed in the fabrication of MEMS based surface acoustic wave devices. Wave propagation can be achieved in a beam using piezoelectric actuators and sensors. In general, these SAW devices are operated at resonance condition, at the very high bias voltage. The piezoelectric beam used in this study had the dimensions of the length 5 mm, width 1.5 mm and thickness 1mm. The width and gap between the comb type interdigital transducer (IDT) electrode is 100 µm. The bottom surface and the end near IDT is fixed. The AC bias voltage is applied to the interdigital transducer located at the fixed end of the actuator as shown in Fig. 2.25. The mesh of the beam consists of 3195 nodes and 500 elements where hexahedron elements with 20 nodes were used for simulation. The piezoelectric beam made of Lithium niobate $LiTiO_3$ has Young's modulus E_{LiTiO_3}=200 GPa and mass density of 4700 kg/m^3. Surface acoustic waves can be generated and detected by interdigital transducer (IDT) electrodes located on the plane surface of a piezoelectric beam.

2.7.1 Calculation setup

The critical time increment for the finite element assemblage shown in Fig. 2.25(b) is Δt_{cr}=1.58×10^{-8}sec. The first resonance mode of the problem is $\omega_r^{(1)} = 60.3 \times 10^6$ rad/sec and its natural period is T_r=1.0421×10^{-7} sec. The time increment Δt is chosen as 2.604×10^{-9} sec for all the coupled algorithms, which satisfies the condition $\Delta t < \Delta t_{cr}$. The values of β and γ, appear in MN, BJN, and BGSN algorithms are chosen as $\beta = 0.5$ and $\gamma = 0.25$. The number of iterations required in BJN and BGSN for this problem is 13 and 9, respectively, which satisfies the convergence criteria of relative error. A sinusoidal input AC voltage is applied to these comb-type electrodes. The model is actuated at its resonance frequency ω =60.3×10^6 rad/sec, at an amplitude of input voltage V=125 V for all the coupled algorithms.

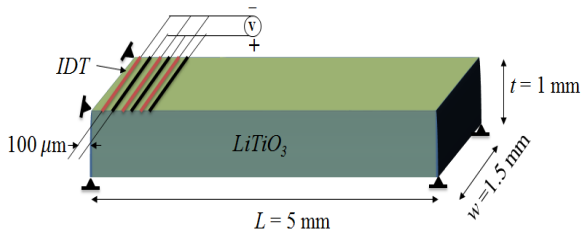

(a) 3D model of SAW numerical problem

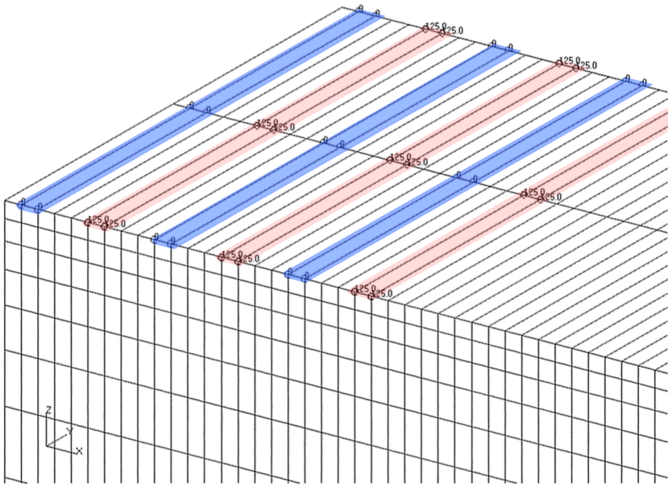

(b) Mesh model:Hexahedron 20 node element

Figure 2.25: Surface acoustic wave (SAW) with Inter-Digital-Transducer (IDT)

2.7.2 Results and discussion

Fig. 2.26 shows the response of the SAW made of a piezoelectric beam for the AC signals. The results obtained are compared in Fig. 2.26 with the response using the MN, BJN, BGSN, and PCD. As can be seen in Fig. 2.26, as the time progress, the amplitude of the displacement increases along the length direction, hence it generates an acoustic wave. The displacements coincide with all the coupled algorithms at the initial time interval as shown in Fig. 2.26(a). The amplitudes with MN, BJN and BGSN algorithms visually coincides at all the time intervals. However, a small difference is seen between partitioned coupling with central difference (PCD) and other algorithms after natural time. The propagation of surface acoustic wave at different time interval is shown in Fig. 2.27 for PCD algorithm. At time t=15.63×10^{-9}sec, the maximum displacement is observed between the length X=0 to 1000 µm, as shown in Fig. 2.27(a). As the time progress, the displacements can be seen along the entire length of the piezoelectric beam. In fact, the computing cost makes PCD more feasible, whereas MN, BJN, and BGSN would be expensive, demonstrated in Section 2.8.2.

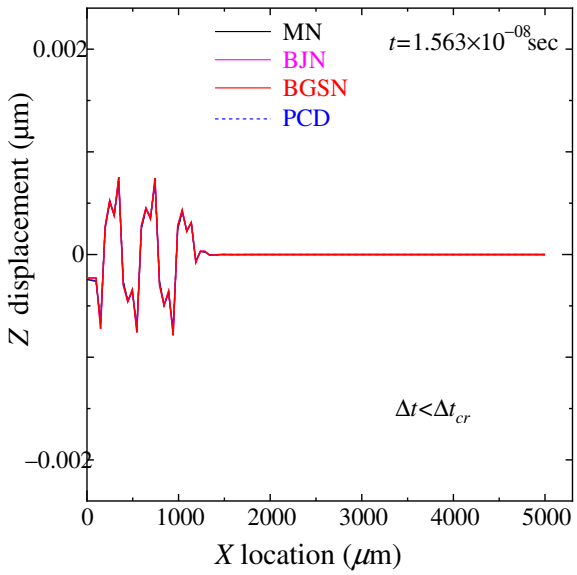

(a) Z displacement at t=15.63 $\times 10^{-9}$sec

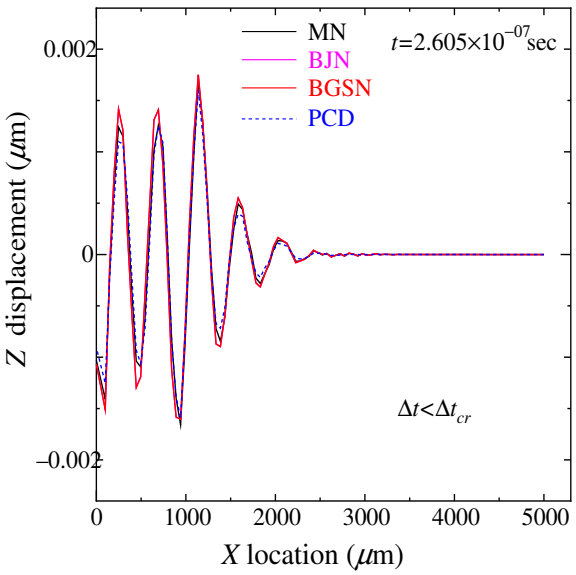

(b) Z displacement at t=260.5 $\times 10^{-9}$sec

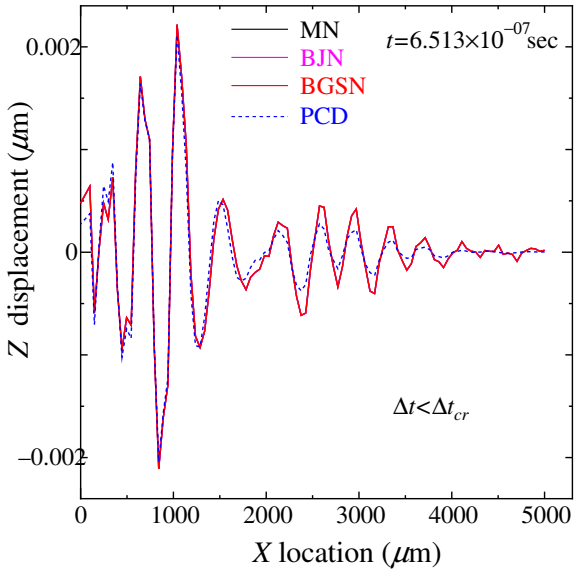

(c) Z displacement at t=651.3 $\times 10^{-9}$sec

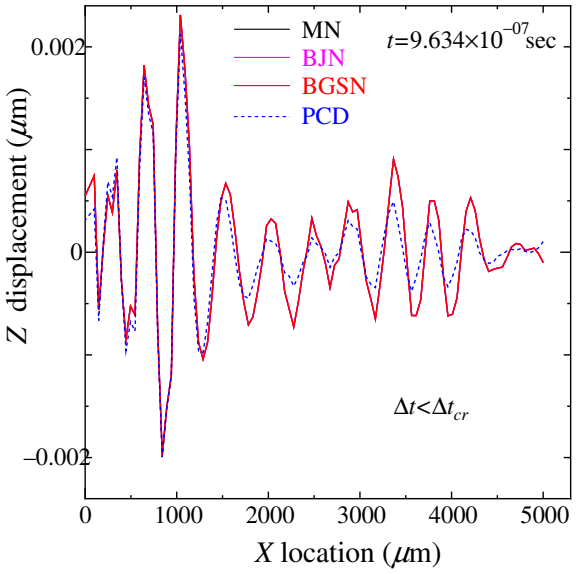

(d) Z displacement at t=963.4 $\times 10^{-9}$sec

Figure 2.26: Excitation of SAW with AC voltage of 125.0 sin 60.3$\times 10^6$ t V

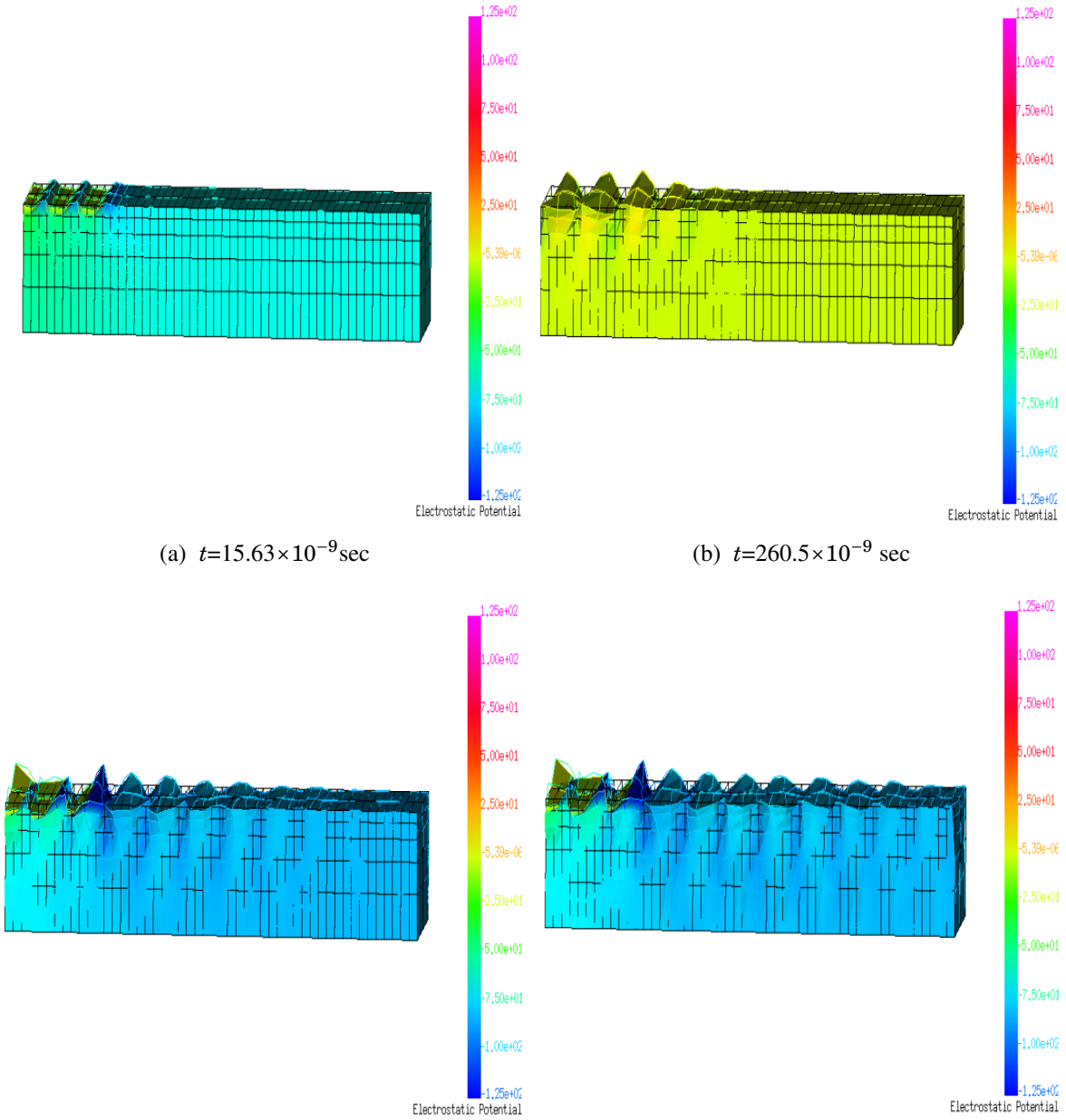

(a) t=15.63×10^{-9}sec

(b) t=260.5×10^{-9} sec

(c) t=651.3×10^{-9} sec

(d) t=963.4×10^{-9} sec

Figure 2.27: Propagation of surface acoustic wave using the PCD algorithm

2.8 Computing cost of the MN, BJN, BGSN and PCD algorithms

2.8.1 Low frequency operating piezoelectric bimorph actuators

The computational efficiency of the numerical finite element coupled algorithms is a great concern from the viewpoint of practical usage during dynamic analysis. Therefore, it is compared based on the numerical results made under the conditions of the time increment Δt satisfying the convergence of the solution. The comparison is made between algorithms employed to perform dynamic analysis of piezoelectric bimorph actuators described in Fig. 2.10(a). This actuator is basically a low–frequency operating MEMS device. The analysis was carried using a computing environment with Intel (R) Xeon(R) 2.33GHz processor.

The results in Table 2.9 indicates that the MN algorithm is computationally expensive than BJN and BGSN at the first time step [47]. This is because in MN algorithm both the structural and the electrical fields are solved in a single mathematical framework simultaneously, but in the case of BJN and BGSN algorithm, the structural and the electrical fields are solved separately thereby reducing the computational cost. As a consequence, the computing time for the first-time step is very high for MN algorithm, but it is very less in BJN and BGSN algorithms. Because of the linear dynamic analysis problem, the factorization of stiffness matrices is performed only for the first iteration of first time step in both of the BJN and BGSN algorithms, whereas in the MN algorithm factorization of stiffness matrices are performed only for the first time. Therefore the computing cost in the first iteration of the first time step in both the BJN and BGSN algorithm is large compared to that of the subsequent iterations. After first time step in MN, and after the first iteration in the first time step in BJN and BGSN, the computational time reduces and posse same computing time as shown in Table 2.9 because the coupled algorithms reuse the factorized stiffness matrices in the case of a linear analysis.

Table 2.9: Computing time for each coupled algorithm at each time step : Piezoelectric bimorph actuators

Time step (n^t)	Computing time(s)				
	MN	BJN		BGSN	
		iteration i=1	$i \geqq 2$	i=1	$i \geqq 2$
n^t=1	47.02	3.93	0.11	3.93	0.11
$n^t \geqq 2$	0.11	0.11	0.11	0.11	0.11

Fig. 2.28 shows the computing time for MN, BJN and BGSN algorithms. BJN and BGSN algorithms cross the MN curve at 0.12 sec and 0.3 sec, respectively, as shown inside the blue dotted circle. Therefore, in the linear dynamic piezoelectric bimorph actuator analysis, MN algorithm is efficient. If only 1 iteration is used for each time step in BJN and BGSN algorithm, the computing time between the MN, BJN and BGSN algorithms would be similar to each other. Using the results in Table 2.9, the computing time for the nonlinear case where the factorization of stiffness matrices is done at each time steps can be estimated. As shown in Fig. 2.28(b), the results indicate that, for nonlinear dynamic analysis of piezoelectric bimorph actuators, BGSN algorithm is most efficient with regard to computational cost.

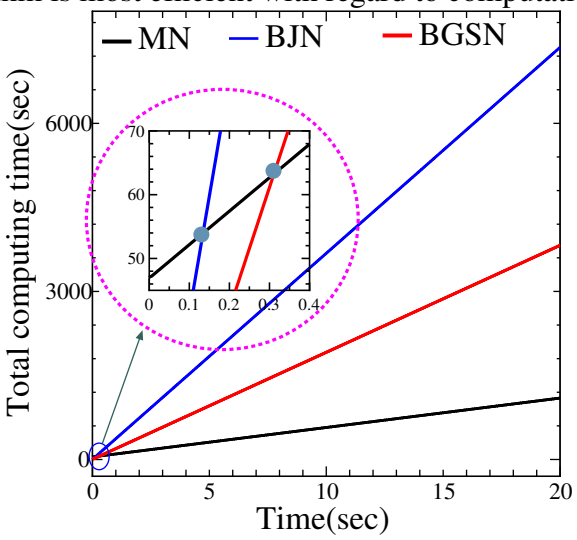

(a) Linear piezoelectric dynamic analysis

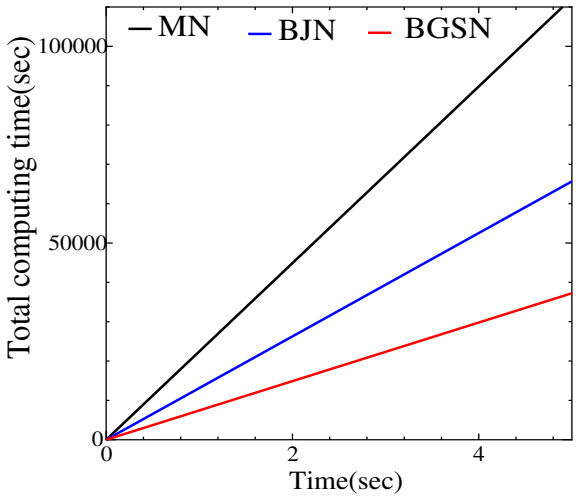

(b) Nonlinear piezoelectric dynamic analysis (estimated)

Figure 2.28: Computing cost of the MN, BJN and BGSN algorithms for analyses of piezoelectric bimorph actuator

2.8.2 High frequency operating SAW device actuated by piezoelectric actuators

Here the computational efficiency of the MN, BJN, BGSN and PCD algorithm for SAW device actuated by piezoelectric actuator is presented. Table 2.10 shows the computational time for each time step for all the MN, BJN, BGSN and PCD algorithm. The computing time in the first time step with MN algorithm is expensive compared to others and also PCD algorithm has the least computing time in the first time step as well as subsequent time steps compared with others. Note that, in PCD algorithm the structural field is solved using central difference time integration, where the factorization of stiffness matrices is not necessary, but electric field is obtained from a simultaneous equation, where the factorization of stiffness matrices is done in the first time step only. Therefore, the computing cost is very less in the PCD algorithm than MN, BJN and BGSN algorithms. In BJN and BGSN algorithms, the computing time is high at the first iteration of a first-time step, after the first iteration of first time steps the cost is same with the MN algorithm. Fig. 2.29 shows the total computing time with all the coupled algorithms. The BJN and BGSN algorithms cross the MN curve because more iterations are necessary to achieve convergence, and PCD is very efficient compared with other algorithms.

From these results, I conclude that the PCD algorithm is computationally efficient than MN, BJN, and BGSN coupled algorithms for linear dynamic analysis of a high–frequency MEMS piezoelectric actuator. These coupled algorithms can be used in high–frequency MEMS piezoelectric actuator applications.

Table 2.10: Computing time for each coupled algorithm at each time step

Time step	Computing time(sec)					
	MN	BJN		BGSN		PCD
		i=1	$i \geqq 2$	i=1	$i \geqq 2$	
n^t=1	594.85	44.8	1.85	44.8	1.85	1.34
$n^t \geqq 2$	1.85	1.85	1.85	1.85	1.85	0.46

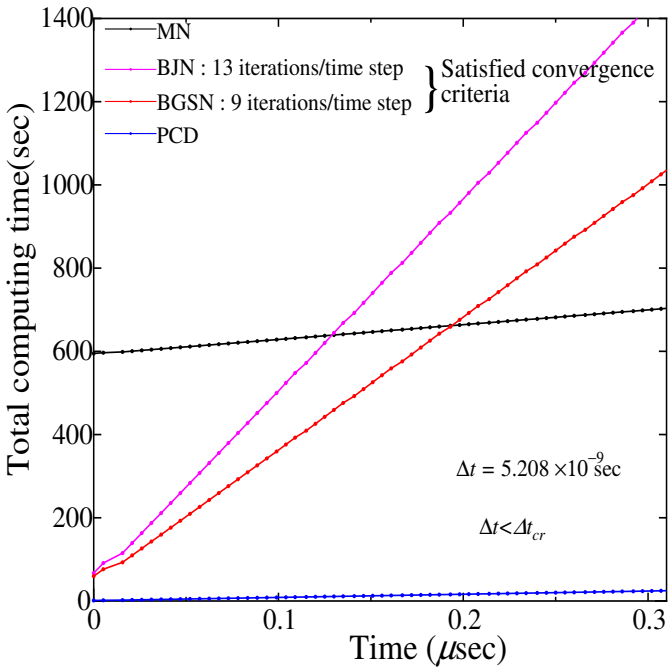

Figure 2.29: Computing cost of MN, BJN , BGSN and PCD algorithms for high–frequency MEMS actuator - SAW

2.9 Conclusions

In this section a detailed and systematic performances evaluation of the MN, BJN, BGSN and PCD numerical finite element coupled algorithms based on their solution accuracy and computational efficiency to analyze the electro–mechanical coupling or structure-electric interaction in piezoelectric bimorph actuators with different configurations and their transient dynamic responses as well as the static and steady state responses are demonstrated. This comprehensive study can be of important for computer aided modeling and analysis of piezoelectric actuators and to assist designers of piezoelectric actuators in resonance MEMS devices of complex geometries.

High accurate solutions are obtained using the proposed linear piezoelectric finite element coupled algorithms to analyze linear structure-electric interaction in a 3D piezoelectric actuator. A same level of accuracy was obtained using the MN, partitioned iterative coupling algorithms (BJN and BGSN) to analyze the static deflection of various piezoelectric bimorph actuators. The step responses and the resonance characteristics of the piezoelectric bimorph actuators is predicted accurately with the MN, BJN, and BGSN algorithms. As shown in the present results, a fine time increment is necessary to obtain converged solutions of transient dynamic responses

for input voltage frequencies near resonance. In the linear dynamic analysis of low–frequency devices such as piezoelectric bimorph actuators, the MN algorithm is computationally efficient than BJN and BGNS algorithm, but in the nonlinear dynamic analysis, BGSN algorithm is most efficient with regard to computational cost and the MN algorithm is very expensive.

In the analysis of high–frequency piezoelectric actuators in surface acoustic wave devices, a same level of accuracy is obtained with the PCD, MN, BJN, and BGSN algorithms. In the linear dynamic analysis of high–frequency actuators, the PCD algorithm is computationally efficient compared with the MN, BJN, and BGSN algorithms.

CHAPTER 3

A NOVEL TRANSFORMATION METHOD TO ANALYZE THE ELECTRIC–STRUCTURE INTERACTION IN A THIN FLEXIBLE PIEZOELECTRIC BIMORPH

3.1 Introduction

Piezoelectric bimorph actuators and sensors generally consist of two or three electrodes at the top, mid-surface (interface between the two piezoelectric layers) and bottom surfaces which are modeled using electric potential variables enabling to apply an electric field or to obtain sensor signals, respectively. These electrodes are conventionally made of the metal coating. Generally, the nodes with the electric degree of freedom (DOF) at the top, bottom and mid-surfaces of a piezoelectric bimorph FE model are regarded as an electrode

In the piezoelectric bimorph actuator function, typically an electric potential is applied between the top, interface and bottom electrodes (see Fig. 3.1(a) and (b)). Thus, the loading is caused by an applied electric potential across the thickness. This results in a pure bending of the structure, where the electric potential varies almost linearly in the thickness direction [37, 43, 59]. Usually, two different electric configurations are used in the piezoelectric actuator application [21, 22, 60]. One is a series connection in which the piezoelectric bimorph layers are usually polarized oppositely and the top electrode has applied a potential while the bottom electrode is set to zero representing grounding, shown in Fig. 3.1(a). The other is a parallel connection in which the piezoelectric layers are polarized parallel and both the top and bottom electrodes have applied a potential while the interface electrode is grounded, shown

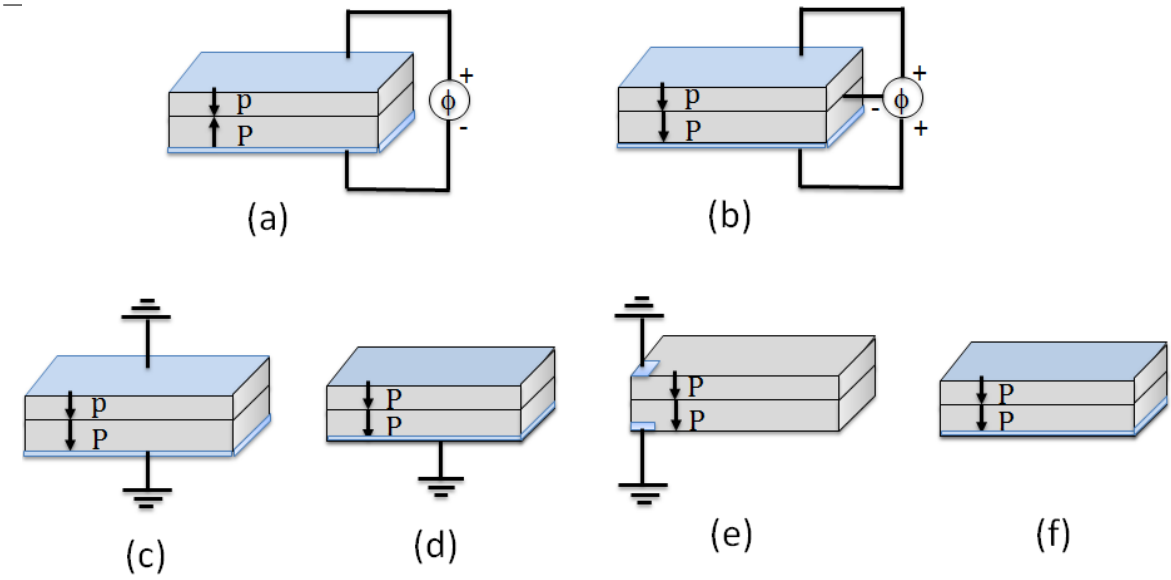

Figure 3.1: Schematic of the electrical configurations of a piezoelectric bimorph cantilever FE model; a) bimorph actuator in a series configuration, b) bimorph actuator in a parallel configuration, c) bimorph sensor in a closed circuit configuration, d) bimorph sensor in a active–sensory mode configuration, e) bimorph sensor in a partial open circuit, f) bimorph sensor in a full open circuit. P refer to polarization.

in Fig. 3.1(b). For the above mentioned electric configurations, the actuator surface becomes equipotential electrodes [61] wherein electric potentials have known prescribed values. This leads to a nearly linear variation of the electric potential across the thickness.

On the other hand, in the piezoelectric sensor mode, when some mechanical force is applied to the piezoelectric continuum, some electric voltage is induced in the piezoelectric material. Commonly, four types of electric configurations are employed, namely, closed circuit, closed and open circuit, partial open circuit, and full open circuit configuration. In the closed circuit configuration, the electric potentials of both the top and bottom electrodes are grounded (electric potentials have known prescribed values at all the nodes of both the top and bottom surfaces as shown in Fig. 3.1(c). In the closed and open circuit configuration, the bottom electrode is grounded while the top electrode is open, this configuration is also known as active–sensory mode connection [61] wherein the electric potentials have known set values at the nodes of the bottom surface while the electric potentials are unknown at the nodes of the top surface as shown in Fig. 3.1(d). In the partial open circuit connection, the piezoelectric surfaces are directly exposed to the mechanical loading, but, to avoid unstable and floating electric potential distribution electrodes are deposited at the end of the piezoelectric layers and connected to the ground as shown in Fig. 3.1(e). In the full open circuit, the electrodes at the top and bottom

surface are open (potentials are unknown at all the nodes of the top and bottom surfaces as shown in Fig. 3.1(f), a typical case in many piezoelectric energy harvesting [3, 13, 14]. Either series or parallel polarization can be used. In the work of Benjeddou [29, 62, 63], Kogle & Bucalem [37, 64], Wang [43], and Fernandes & Pouget [59], it is demonstrated that only a quadratic variation of the electric potential over the thickness can takes into account the potential induced by the bending dominant deformation in a piezoelectric bimorph sensor mode.

There is a growing need for numerical methods to analyze both the actuation and sensing function of electro–mechanical coupling in a piezoelectric continuum using finite element methods. A number of researchers have analyzed piezoelectric bimorph cantilever in MEMS devices using the FEM [7, 9, 12, 47]. It is imperative to develop a finite element formulation which can takes into account both actuator and sensor effect of a thin layered piezoelectric bimorph. At the same time, FE formulation must takes into account almost a linear variation of the electric potential across the thickness in a piezoelectric actuator mode and a nearly quadratic variation of induced electric potential across the thickness in a piezoelectric sensor made of a thin layered piezoelectric bimorph.

The development of finite elements for the analysis of piezoelectric systems was first presented by Allik and Hughes [28]. More details regarding the piezoelectric finite elements, such as piezoelectric solid, shell, plate, and beam elements, can be found in the survey by Benjeddou [29]. This survey discusses a wide range of studies in which different piezoelectric solid elements have been used to analyze electromechanical coupling [8, 28, 30–36, 65, 66]. The electric potential is quadratic in a piezoelectric solid element proposed in Refs. [30, 36, 65, 66] except [28, 31–35] for which it is linear. Multi–layered linear solid elements over the thickness direction can treat a quadratic variation of the electric potential across the thickness. The major advantages of using the 3D piezoelectric solid elements in the analysis of electromechanical coupling are that they can correctly takes into account the electric charge distribution on both the top and bottom surfaces and accurately represent the linear or quadratic variation of the induced electric potential along the thickness direction. Most importantly, all the above discussed electric configurations of both the actuator and sensor functions can be easily achieved with the 3D solid elements. However, the piezoelectric solid finite elements presented therein are inappropriate for the discretization of the structure in thin-layer MEMS actuators and sensors [67–69]. The computing cost of using solid elements to perform the structural analysis is larger.

Since MEMS piezoelectric composites are composed of thin layers and undergo large deformations, shell elements are very well suited for the structural discretization of these structures. Shell elements yield more accurate results than solid elements in terms of the

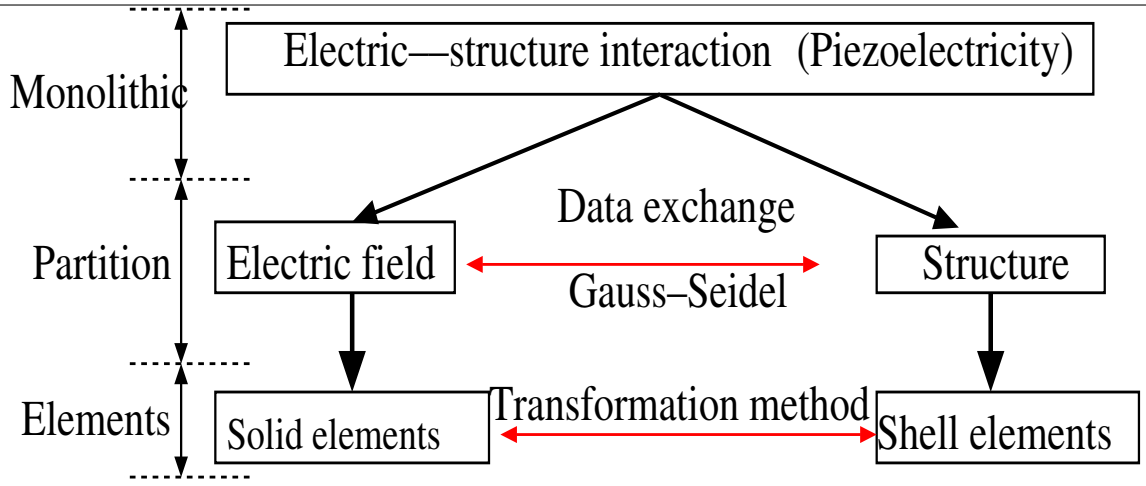

Figure 3.2: Field decomposition of the structure–electric interaction using different types of finite elements.

dominant bending deformation. Furthermore, the computing cost of using shell elements to perform the structural analysis of these composites is much less than that of using solid elements. The finite element formulation of the shell elements for the geometric nonlinear analysis of thin structures is well established [70–72]. Shear locking in the shell can be eliminated by using the mixed interpolation of the natural strains (MITC) approach [71–73]. However, modeling the electric contribution in the discretization procedure is a challenging task when using the conventional formulations of shell elements.

Only a few studies using the piezoelectric shell elements [67, 74, 75] were reported in the survey by Benjeddou [29]. Some recently developed piezoelectric shell elements [37, 63, 76–78] have shown incompatible approximation spaces for the electrical fields, particularly in bending-dominated problems, as discussed in previous reports [79, 80]. Many piezoelectric shell elements are limited to actuator applications (see e.g.[81–83]), so that it can not be used to analyze the piezoelectric sensor function. Numerous piezoelectric shell element formulations [67, 78, 79, 84, 85] assumes a linear variation of the electric potential over the thickness, this limits the applicability of the elements to a certain loading condition only, because the induced electric potential by the bending deformation is quadratic in the piezoelectric sensor mode. Some piezoelectric shell elements [37, 67, 79, 84–86] can be used to model both the actuator and sensor mode, provided one or two equipotential electrodes in the piezoelectric actuator and sensor surfaces. However, they are limited to a certain electric configuration because they require the equipotential electrodes at the top and bottom surfaces. Since the electric potential serves as unknowns in an active–sensory configuration, they are modeled with a linear variation of the electric potential through the thickness [79], which leads to quite a

wrong solution because the electromechanical coupling would be partial and would neglect the induced potential in sensor mode, as discussed in [29].

A few piezoelectric shell elements in Refs. [37, 63, 76, 86] uses a quadratic variation of electric potential over the thickness in the multi–piezoelectric layer structures for both the actuator and sensor analysis, provided at least one equipotential electrode in the piezoelectric actuator and sensor surfaces. In the formulations of Lammering & Mesecke–Rischmann [76], the electrodes located at the laminate interface are assumed to be grounded for both the actuator and sensor modeling, therefore limiting to certain electric configurations. The above-mentioned shortcomings of the piezoelectric shell elements related to the electrical field discretization can be treated using the 3D solid elements.

In this study, the best features of solid and shell elements were combined to analyze the electrical and mechanical fields of the piezoelectric effect in a thin-layer piezoelectric bimorph actuators and sensors. Importantly, the monolithic constitutive equations describing the piezoelectric effect were decomposed into the electrical and structural fields, enabling the use of different elements to solve the different fields. Field decomposition [44] enables the use of solid elements for electrical analysis and shell elements for structural analysis, as shown in Fig. 3.2. Since the electric field is solved using solid elements, the induced electric forces and the moment of these forces must be transformed into externally applied forces acting on to the shell elements to analyze the mechanical field. Conversely, because the structural field is solved using shell elements, the displacements obtained from the structural analysis of the shell elements must be transformed to the solid elements. Therefore, this paper proposes a novel transformation method for the electric force, the moment of the electric force, and the displacement transformation to exchange the variables between solid and shell elements in the piezoelectric analysis.

In the present work, the BGS partitioned iterative coupling scheme [47] was used to apply the two types of finite elements (the solid elements for the electrical analysis and the shell elements for the structural analysis) in the developed transformation method. Two approaches to analyzing the dynamic and static behavior of the piezoelectric continuum are proposed using our transformation method. In the first approach, a full N–R iteration loop is executed inside the BGS loop; therefore, many N–R iterations are executed in each BGS iteration. In contrast, in the second approach, only one N–R iteration is executed in each BGS iteration, i.e., the BGS iteration loop and the full N–R iteration loop are unified in a single loop.

In summary, different from the previous methods, the proposed method can model both the actuator and sensor effect in a thin-layer piezoelectric bimorph beam for any electrical configurations with a quadratic variation of the electric potential across the thickness, a novel

transformation method between the solid and shell elements accurately takes into account the electromechanical coupling for both the actuator and sensor mode and the field decomposition allows users to reuse the existing finite elements and its extensibility for multiphysics problems. The stability and accuracy of the two approaches are presented for a standard series-type and parallel type piezoelectric bimorph actuator. A sensor function is demonstrated for a piezoelectric bimorph with a closed circuit, combination of open and closed circuit, partial open circuit, and fully open circuit configurations.

3.2 Formulation of a nonlinear electric–structure interaction using a transformation method

In this section, the linear finite element equations of the piezoelectric effect given in Section 2.3 are extended to the geometric nonlinear case. The linearized incremental form of the principle of virtual work described by Bathe [53, 87] for the nonlinear analysis of the structure is considered in this section. In Chapter 2, both the electric field and structure are analyzed using solid elements for the linear piezoelectric effect. But here, electric field is analyzed using 3D solid elements and structure using shell elements. By rewriting the linear piezoelectric finite element equations (2.50) and (2.51)

$$\mathbf{K}_{\phi\phi}\,{}^{t+\Delta t}\phi^{(b)} = {}^{t+\Delta t}\mathbf{q} - \mathbf{K}_{\phi u}\,{}^{t+\Delta t}\mathbf{u}^{(b-1)}, \tag{3.1}$$

$$\hat{\mathbf{K}}_{uu}\,{}^{t+\Delta t}\mathbf{u}^{(b)} = {}^{t+\Delta t}\hat{\mathbf{F}} - \mathbf{K}_{u\phi}\,{}^{t+\Delta t}\phi^{(b)}, \tag{3.2}$$

where b indicates the current BGS iteration. In this chapter, index b is used instead of i to indicate the BGS iteration.

The general expressions of the linearized coupled equations for the nonlinear structure–electric interaction in the piezoelectric effect are given as follows.

3.2.1 Discretization of the electric field using 3D solid elements

The electrical field is discretized using solid elements to analyze the nonlinear piezoelectric effect as,

$${}^{t+\Delta t}\mathbf{K}^{(b)}_{\phi\phi}\;{}^{t+\Delta t}\phi^{(b)} = {}^{t+\Delta t}\mathbf{q} - {}^{t+\Delta t}\mathbf{K}^{(b)}_{\phi u}\;{}^{t+\Delta t}\mathbf{u}^{(b-1)}. \tag{3.3}$$

The solution for the electric potential ${}^{t+\Delta t}\phi^{(b)}$ in Eq.(3.3) in each iteration is derived from the mechanical displacements ${}^{t+\Delta t}\mathbf{u}^{(b-1)}$ of the previous iteration. It is important to note that, in the linear dynamic analysis problem the evaluation and factorization of electric stiffness matrix $\mathbf{K}_{\phi\phi}$

and the piezoelectric coupling coefficient matrix $\mathbf{K}_{u\phi}$ is performed only for the first iteration of first time step. But, in the nonlinear dynamic analysis of electric field the evaluation and factorization of electric stiffness matrix $\mathbf{K}_{\phi\phi}$ and the piezoelectric coupling coefficient matrix $\mathbf{K}_{u\phi}$ is performed at every Gauss–Seidel iteration of each time step and given as,

$$ {}^{t+\Delta t}\mathbf{K}_{u\phi} = \int_{\Omega} {}^{t+\Delta t}\mathbf{B}_{u}^{T}\, \mathbf{e}\, {}^{t+\Delta t}\mathbf{B}_{\phi} d\Omega, \tag{3.4a} $$

$$ {}^{t+\Delta t}\mathbf{K}_{\phi\phi} = \int_{\Omega} {}^{t+\Delta t}\mathbf{B}_{\phi}^{T}\, \varepsilon\, {}^{t+\Delta t}\mathbf{B}_{\phi} d\Omega, \tag{3.4b} $$

3.2.2 Discretization of the structure using shell elements

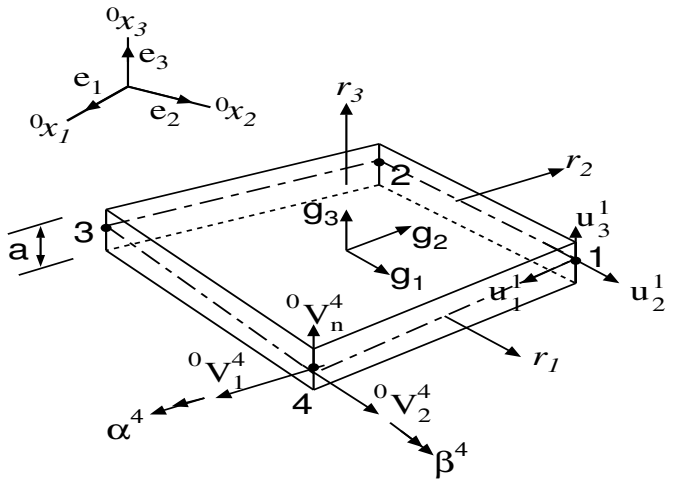

Figure 3.3: Schematic of a four–node shell element

The large deformation formulation to capture the geometric nonlinear effects of the shell element is performed effectively by the use of an incremental formulation of the equations of motion. Here, the geometry of the shell is interpolated at time t using the nodal coordinates, ${}^t x_i^k$, and director vectors ${}^t V_n^k$, at time t given as [71, 72],

$$ {}^t x_i = \sum_{k=1}^{4} h^k\, {}^t x_i^k + \frac{\zeta}{2} \sum_{k=1}^{4} a^k\, h^k {}^t V_{ni}^k, \tag{3.5} $$

with

${}^t x_i$ = Cartesian coordinates of any point in the element at time t.

${}^t x_i^k$ = Cartesian coordinates of nodal point k at time t.

h^k = Two dimensional interpolation functions corresponding at nodal point k.
${}^tV_{ni}^k$ = Director vector at each node k along isoparametric coordinate r_3 at time t.
a^k = Shell thickness at node k along director vector ${}^tV_{ni}^k$. Italic indices k =1, 2, 3, 4 are the nodes in the mid-surface of the shell element.

The displacements, ${}^tu_i$, and incremental displacements, u_i of a material particle in a shell element with natural coordinates (ξ,η,ζ) at time t are given as, [72],

$$ {}^tu_i = \sum_{k=1}^{4} h^k \, {}^tu_i^k + \frac{\zeta}{2}\sum_{k=1}^{4} a^k h^k \, ({}^tV_{ni}^k - {}^0V_{ni}^k), \tag{3.6} $$

$$ u_i = \sum_{k=1}^{4} h^k \, u_i^k + \frac{\zeta}{2}\sum_{k=1}^{4} a^k h^k \, (-{}^tV_{2i}^k\alpha^k + {}^tV_{1i}^k\beta^k), \tag{3.7} $$

with ${}^tu_i$ = The displacements of a particle of the shell element at time t.
${}^tu_i^k$ = Nodal point displacements into the Cartesian coordinate direction at time t.
${}^tu_i$ = The incremental displacements of a particle of the shell at time t.
u_i^k = Nodal point incremental displacements at time t.
${}^tV_1^k, {}^0V_2^k$ = Vector normal's to the director vector ${}^tV_n^k$ at each node at time t.
α^k, β^k = Rotations of the director vector about ${}^tV_1^k$ and ${}^0V_2^k$ respectively. In the framework of the isoparametric concept, the geometry and displacements are interpolated by using same shape functions. In shell elements, the two dimensional bilinear interpolation functions corresponding at nodal point k is given as,

$$ h^k(\xi,\eta) = \frac{1}{4}(1+\xi^k\xi)(1+\eta^k\eta) \tag{3.8} $$

Total Lagrangian (T.L) formulation is employed to solve for the static and kinematic variables of the body at time $t+\Delta t$ where in these variables are referred to the initial configuration at time 0. The principle of virtual work applied to time $t+\Delta t$ is given as[72],

$$ \int_{{}^0\Omega} {}^{t+\Delta t}_{0}\tilde{\sigma}^{ij}\delta\, {}^{t+\Delta t}_{0}\tilde{S}_{ij} \, d^0\Omega = {}^{t+\Delta t}R, \tag{3.9} $$

where ${}^{t+\Delta t}_{0}\tilde{\sigma}^{ij}$ are the contravariant components of the 2nd Piola-Kirchhoff stress tensor at time $t+\Delta t$ but referred to the configuration at time 0 (initial configuration), the ${}^{t+\Delta t}_{0}\tilde{S}_{ij}$ are the covariant components of the Green-Lagrange strain tensor at time $t+\Delta t$ but referred to the configuration at time 0. The 2nd Piola–Kirchhoff stress tensor ${}^{t+\Delta t}_{0}\tilde{\sigma}^{ij}$ and Green–Lagrange strain ${}^{t+\Delta t}_{0}\tilde{S}^{ij}$ of the structure are expressed as [87]:

$$ {}^{t+\Delta t}_{0}\tilde{\sigma}^{ij} = \frac{{}^0\rho}{{}^{t+\Delta t}\rho} {}^{t+\Delta t}_{0}x_{i,m} \, {}^{t+\Delta t}\tau_{mn} \, {}^{t+\Delta t}_{0}x_{j,n} \tag{3.10} $$

$$ {}^{t+\Delta t}_{0}\tilde{S}^{ij} = \frac{1}{2}({}^{t+\Delta t}_{0}u_{i,j} + {}^{t+\Delta t}_{0}u_{j,i} + {}^{t+\Delta t}_{0}u_{k,i} \, {}^{t+\Delta t}_{0}u_{k,j}), \tag{3.11} $$

where x_i is the shell position vector and τ_{ij} is the Cauchy stress tensor. The virtual work of the externally applied loads ${}^{t+\Delta t}R$ at time $t+\Delta t$ given by,

$$ {}^{t+\Delta t}R = \int_{t+\Delta t\Omega}^{t+\Delta t} f_i^B \delta u_i \; {}^{t+\Delta t}d\Omega + \int_{t+\Delta t S^B}^{t+\Delta t} f_i^S \delta u_i^S \; {}^{t+\Delta t}dS^B, \tag{3.12} $$

where ${}^{t+\Delta t}f_i^B$, ${}^{t+\Delta t}f_i^S$ are real body forces over the volume Ω at time $t+\Delta t$ and surface forces over the surface S at time $t+\Delta t$, respectively, δu_i is virtual displacements and δu_i^S is virtual displacements on the surface. By imposing these virtual displacements to the Eq.(3.12) can solve for ${}^{t+\Delta t}R$. The L.H.S of Eq.(3.9) is integrated over a known volume ${}^0\Omega$ and incrementally decomposing ${}^{t+\Delta t}_{0}\tilde{\sigma}^{ij}$ and ${}^{t+\Delta t}_{0}\tilde{S}_{ij}$ as shown in [72] i.e.

$$ {}^{t+\Delta t}_{0}\tilde{\sigma}^{ij} = {}^{t}_{0}\tilde{\sigma}^{ij} + {}_0\,\tilde{\sigma}^{ij} \tag{3.13} $$

$$ {}^{t+\Delta t}_{0}\tilde{S}^{ij} = {}^{t}_{0}\tilde{S}^{ij} + {}_0\,\tilde{S}^{ij} \tag{3.14} $$

where ${}^{t}_{0}\tilde{\sigma}^{ij}$ and ${}^{t}_{0}\tilde{S}^{ij}$ are known 2nd piola-Kirchhoff stress and Green-Lagrange strains, respectively, ${}_0\tilde{\sigma}^{ij}$ and ${}_0\tilde{S}^{ij}$ are unknown incremental 2nd piola-Kirchhoff stress and Green-Lagrange strains, respectively [72]. The term ${}_0\tilde{S}^{ij}$ is given by the combination of linear strain increment ${}_0\tilde{e}_{ij}$ and nonlinear increment strain ${}_0\tilde{\eta}_{ij}$, hence

$$ {}_0\tilde{S}^{ij} = {}_0\,\tilde{e}_{ij} + {}_0\,\tilde{\eta}_{ij} \tag{3.15} $$

By linearizing ${}_0\tilde{\sigma}^{ij}$ gives ${}_0\tilde{\sigma}^{ij} = {}_0\tilde{C}_0^{ijkl}\tilde{e}_{kl}$ and $\delta_0\tilde{S}^{ij} = \delta_0\tilde{e}_{ij}$, where ${}_0\tilde{C}^{ijkl}$ is the contravaiant constitutive tensor in the convicted coordinates. Using these relations and substituting the equations from Eqs.(3.13) and (3.15) into Eq.(3.9) gives a complete linearized equation of motion [72] is given as,

$$ \int_{{}_0\Omega} {}_0\tilde{C}^{ijkl}\,{}_0\tilde{e}_{kl}\delta_0\tilde{e}_{ij}d^0\Omega + \int_{{}_0\Omega} {}^{t}_{0}\tilde{\sigma}^{ij}\delta_0\tilde{\eta}_{ij}d^0\Omega = {}^{t+\Delta t}R - \int_{{}_0\Omega} {}^{t}_{0}\tilde{\sigma}^{ij}\delta_0\tilde{e}_{ij}d^0\Omega. \tag{3.16} $$

Equation (3.16) is the completely linearized equation of motion in T.L formulation and it is the basic equation used for the isoparametric formulation of finite element analysis. The element matrices of the structure are obtained using this equation. Mixed interpolation of tensorial components (MITC) approach [71–73] is used to avoid the shear locking in the shell. Using Eqs. (3.5)–(3.7) the linearized equation of motion Eq.(3.16) becomes,

$$ ({}^{t}_{0}\mathbf{K}_{\mathrm{L}} + {}^{t}_{0}\mathbf{K}_{\mathrm{NL}})\mathbf{u} = {}^{t+\Delta t}\mathbf{R} - {}^{t}_{0}\mathbf{F} \tag{3.17} $$

where $\mathbf{u}$, ${}^{t}_{0}\mathbf{K}_{\mathrm{L}}$, ${}^{t}_{0}\mathbf{K}_{\mathrm{NL}}$ and ${}^{t}_{0}\mathbf{F}$ are incremental displacements, linear incremental stiffness matrix, nonlinear incremental stiffness matrix and incremental of elastic internal force vector, respectively, i.e.

$$ {}^{t}_{0}\mathbf{K}_{\mathrm{L}} = \int_{{}_0\Omega} {}^{t}_{0}\mathbf{B}_{\mathrm{L}}^{\mathrm{T}}\; {}_0\tilde{\mathbf{C}}\; {}^{t}_{0}\mathbf{B}_{\mathrm{L}}\; \mathrm{d}^0\Omega \tag{3.18} $$

$$ {}^{t}_{0}\mathbf{K}_{NL} = \int_{{}_{0}\Omega} {}^{t}_{0}\mathbf{B}^{T}_{NL}\ {}^{t}_{0}\tilde{\sigma}\ {}^{t}_{0}\mathbf{B}_{NL}\ d^{0}\Omega \tag{3.19} $$

$$ {}^{t}_{0}\mathbf{F} = \int_{{}_{0}\Omega} {}^{t}_{0}\mathbf{B}^{T}_{L}\ {}^{t}_{0}\hat{\sigma}\ d^{0}\Omega \tag{3.20} $$

In the above equations, ${}^{t}_{0}\mathbf{B}_{L}$, ${}^{t}_{0}\mathbf{B}_{NL}$, ${}_{0}\tilde{\mathbf{C}}$, ${}^{t}_{0}\tilde{\sigma}$ and ${}^{t}_{0}\hat{\sigma}$ are linear strain–displacement matrix, nonlinear strain displacement matrix, an incremental material constant matrix, 2^{nd} Piola-Kirchhoff stress matrix and vector of stresses, respectively, and all corresponding to the configuration at time t but referred to the initial configuration i.e. time 0. The detailed derivations of the element matrices for the shell elements used in this work can be found in Ref. [87]. In dynamic analysis an inertial term will be added to the equation (3.17) and

$$ ({}^{t}_{0}\mathbf{K}_{L} + {}^{t}_{0}\mathbf{K}_{NL})\mathbf{u} = {}^{t+\Delta t}\mathbf{R} - {}^{t}_{0}\mathbf{F} - \mathbf{M}^{t+\Delta t}\ddot{\mathbf{u}} \tag{3.21} $$

where $\mathbf{M}$ is the consistent mass matrix calculated at time 0 and ${}^{t+\Delta t}\ddot{\mathbf{u}}$ is a vector of the nodal point accelerations at time $t+\Delta t$ and this acceleration will be approximated using Newmark's time integration scheme. Structural damping effect has been ignored in our analysis (matrix $\mathbf{C} = 0$).

The above equation is only an approximation to the principle of virtual work Eq.(3.9) to be solved in each time step. Because of the nonlinearities, the linearization of equation (3.16) may introduce errors resulting in an instability in the solution. For accurate and better solution of nonlinear finite element equation, some forms of Newton-Raphson iteration schemes are used within each load steps [88]. In this study, nonlinear iterations corresponding to a full Newton–Raphson iteration within each load step is used. Newmark's time integration is employed to solve the equation of motion. In a nonlinear analysis at time $t+\Delta t$, the equilibrium equation be to solved is [88],

$$ {}^{t+\Delta t}\tilde{\mathbf{R}}(\mathbf{u}^{*}) - {}^{t+\Delta t}_{0}\mathbf{F}(\mathbf{u}^{*}) = 0, \tag{3.22} $$

where

$$ {}^{t+\Delta t}\tilde{\mathbf{R}}(\mathbf{u}^{*}) = {}^{t+\Delta t}\mathbf{R} - \mathbf{M}^{t+\Delta t}\ddot{\mathbf{u}}^{*} \tag{3.23} $$

In the case of nonlinear static analysis the inertial term will be neglected from above equation. The equilibrium requirement is,

$$ \mathbf{f}(\mathbf{u}^{*}) = 0 \tag{3.24} $$

where

$$ \mathbf{f}(\mathbf{u}^{*}) = {}^{t+\Delta t}\tilde{\mathbf{R}}(\mathbf{u}^{*}) - {}^{t+\Delta t}_{0}\mathbf{F}(\mathbf{u}^{*}) \tag{3.25} $$

In the above equations $\mathbf{u}^*$ is a solution vector and each row in the vector corresponds to each degree of freedom. Using Taylor series of expansion for $\mathbf{f}(\mathbf{u}^*)$ about solution vector $\mathbf{u}^*$ gives,

$$\mathbf{f}(\mathbf{u}^*) = \mathbf{f}({}^{t+\Delta t}\mathbf{u}^{(k-1)}) + \left[\left.\frac{\partial \mathbf{f}}{\partial \mathbf{u}}\right|_{t+\Delta t\mathbf{u}^{(k-1)}}\right]({}^{t+\Delta t}\mathbf{u}^{(k)} - {}^{t+\Delta t}\mathbf{u}^{(k-1)}) + \text{higher order terms} \tag{3.26}$$

where roman indices k = 1,2,3....m are employed to describe the full Newton–Raphson iterations and higher order terms are neglected to obtain a Taylor series approximation. Now define,

$$\Delta\mathbf{u}^{(k)} = {}^{t+\Delta t}\mathbf{u}^{(k)} - {}^{t+\Delta t}\mathbf{u}^{(k-1)}. \tag{3.27}$$

Substituting Eq.(3.25) into Eq.(3.26) and imposing equilibrium condition ($\mathbf{f}(\mathbf{u}^*) = 0$) gives

$${}^{t+\Delta t}\tilde{\mathbf{R}}^{(k-1)} - {}^{t+\Delta t}_{0}\mathbf{F}^{(k-1)} + \left[\left.\frac{\partial {}^{t+\Delta t}\tilde{\mathbf{R}}^{(k-1)}}{\partial \mathbf{u}}\right|_{t+\Delta t\mathbf{u}^{(k-1)}} - \left.\frac{\partial {}^{t+\Delta t}_{0}\mathbf{F}^{(k-1)}}{\partial \mathbf{u}}\right|_{t+\Delta t\mathbf{u}^{(k-1)}}\right]\Delta\mathbf{u}^{(k)} = 0, \tag{3.28}$$

where

$${}^{t+\Delta t}\tilde{\mathbf{R}}^{(k-1)} = {}^{t+\Delta t}\mathbf{R} - \mathbf{M}\,{}^{t+\Delta t}\ddot{\mathbf{u}}^{(k-1)}. \tag{3.29}$$

In equation (3.28) one has to find the partial derivatives of ${}^{t+\Delta t}\tilde{\mathbf{R}}^{(k-1)}$ and ${}^{t+\Delta t}_{0}\mathbf{F}^{(k-1)}$ with respect to $\mathbf{u}$ about ${}^{t+\Delta t}\mathbf{u}^{(k-1)}$. Differentiating equation (3.29) with respect to $\mathbf{u}$ about ${}^{t+\Delta t}\mathbf{u}^{(k-1)}$ to obtain

$$\left.\frac{\partial {}^{t+\Delta t}\tilde{\mathbf{R}}^{(k-1)}}{\partial \mathbf{u}}\right|_{t+\Delta t\mathbf{u}^{(k-1)}} = \cancelto{0}{\left.\frac{\partial {}^{t+\Delta t}\mathbf{R}}{\partial \mathbf{u}}\right|_{t+\Delta t\mathbf{u}^{(k-1)}}} - \mathbf{M}\left.\frac{\partial {}^{t+\Delta t}\ddot{\mathbf{u}}^{(k-1)}}{\partial \mathbf{u}}\right|_{t+\Delta t\mathbf{u}^{(k-1)}}, \tag{3.30}$$

Assuming the loads are deformation-independent and hence the first term in L.H.S of Eq.(3.30) becomes zero. Also, using Newmark's time integration to obtain

$$\left.\frac{\partial {}^{t+\Delta t}\ddot{\mathbf{u}}^{(k-1)}}{\partial \mathbf{u}}\right|_{t+\Delta t\mathbf{u}^{(k-1)}} = \frac{1}{\beta\Delta t^2}, \tag{3.31}$$

where $\beta \geq \frac{1}{4}\left(\gamma + \frac{1}{2}\right)^2$ and $\gamma \geq \frac{1}{2}$ for unconditionally stable system. Substituting Eq.(3.31) into Eq.(3.30) to get

$$\left.\frac{\partial {}^{t+\Delta t}\tilde{\mathbf{R}}^{(k-1)}}{\partial \mathbf{u}}\right|_{t+\Delta t\mathbf{u}^{(k-1)}} = -\mathbf{M}a_0, \tag{3.32}$$

where $a_0 = \frac{1}{\beta\Delta t^2}$ is Newmark's integration constant and by recognizing,

$$\left.\frac{\partial {}^{t+\Delta t}_{0}\mathbf{F}^{(k-1)}}{\partial \mathbf{u}}\right|_{t+\Delta t\mathbf{u}^{(k-1)}} = {}^{t+\Delta t}_{0}\mathbf{K}^{(k-1)}_{uu}, \tag{3.33}$$

where ${}^{t+\Delta t}_{0}\mathbf{K}_{uu}^{(k-1)}$ is the tangent stiffness matrix in Newton-Raphson iteration $(k-1)$. Using Eq.(3.32) and Eq.(3.33) into Eq.(3.28) to obtain

$$\left[\mathbf{M}a_0 + {}^{t+\Delta t}_{0}\mathbf{K}_{uu}^{(k-1)}\right]\Delta\mathbf{u}^{(k)} = {}^{t+\Delta t}\tilde{\mathbf{R}}^{(k-1)} - {}^{t+\Delta t}_{0}\mathbf{F}^{(k-1)}. \tag{3.34}$$

The above equation in compact form is written as,

$${}^{t+\Delta t}_{0}\hat{\mathbf{K}}_{uu}^{(k-1)}\Delta\mathbf{u}^{(k)} = {}^{t+\Delta t}\tilde{\mathbf{R}}^{(k-1)} - {}^{t+\Delta t}_{0}\mathbf{F}^{(k-1)}, \tag{3.35}$$

where

$${}^{t+\Delta t}_{0}\hat{\mathbf{K}}_{uu}^{(k-1)} = \mathbf{M}a_0 + {}^{t+\Delta t}_{0}\mathbf{K}_{uu}^{(k-1)} \tag{3.36}$$

Eq.(3.35) is a set of simultaneous equations, which is used to solve for $\Delta\mathbf{u}^{(k)}$. Then the next displacement approximation is obtained using

$${}^{t+\Delta t}\mathbf{u}^{(k)} = {}^{t+\Delta t}\mathbf{u}^{(k-1)} + \Delta\mathbf{u}^{(k)} \tag{3.37}$$

Hence, the Eqs.(3.35) and (3.37) are important equations which constitutes the full Newton–Raphson equilibrium iteration solution of Eq.(3.24).

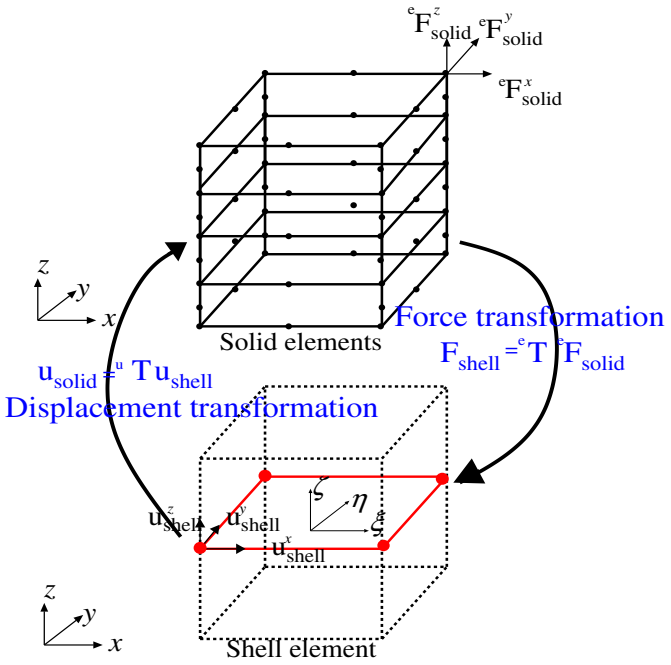

Figure 3.4: Electric force and displacement transformation between the solid and the shell elements.

3.2.3 Transformation method between solid and shell elements

The electric forces induced by the inverse piezoelectric effect in the solid elements must be transformed into forces and moments that are applied externally into the shell elements; similarly, the mechanical displacements must be transformed from the shell elements to the solid elements to evaluate the inverse piezoelectric effect, as shown in the Fig. 3.4. Therefore, a transformation method to exchange the mechanical and the electrical variables between the solid and shell elements is imperative.

A) Electric force and moment transformation from the solid to the shell elements

The standard bimorph actuator shown in Fig. 3.5 consists of a double layer of polyvinylidene difluoride (PVDF) piezoelectric ceramics joined together over their long surfaces with opposing polarization (P). Fig. 3.6 shows the regular grid-type mesh division of the bimorph actuator, and Fig. 3.7 shows the section highlighted by thick black lines in Fig. 3.6, which consists of a block of four solid elements and a shell element. The transformation equation that transforms the electric forces from the solid elements to the shell elements can be generally expressed as [89, 90],

$$\mathbf{F}_{\text{shell}} = {}^{\text{e}}\mathbf{T}\ {}^{\text{e}}\mathbf{F}_{\text{solid}}, \tag{3.38}$$

where $\mathbf{F}_{\text{shell}}$ is the equivalent force vector at the shell elements, ${}^{\text{e}}\mathbf{F}_{\text{solid}}$ is the induced electric force vector in the solid elements, ${}^{\text{e}}\mathbf{T}$ is the transformation matrix, and the left-hand superscript e stand for “electric." As shown in Fig. 3.4, the induced electric forces in the solid elements ${}^{\text{e}}\mathbf{F}_{\text{solid}}$ are transformed as an equivalent force vector $\mathbf{F}_{\text{shell}}$ on to the shell elements. The electric forces induced in the solid elements by the inverse piezoelectric effect are calculated as [89, 90],

$${}^{\text{e}}\mathbf{F}_{\text{solid}} = \mathbf{K}_{\text{u}\phi}\phi. \tag{3.39}$$

Eqs. (3.38) and (3.39) are the general expressions of electric forces transformation from any type of solid elements to shell elements with regular and irregular meshes.

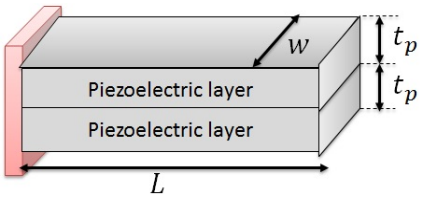

Figure 3.5: Piezoelectric bimorph cantilever.

.

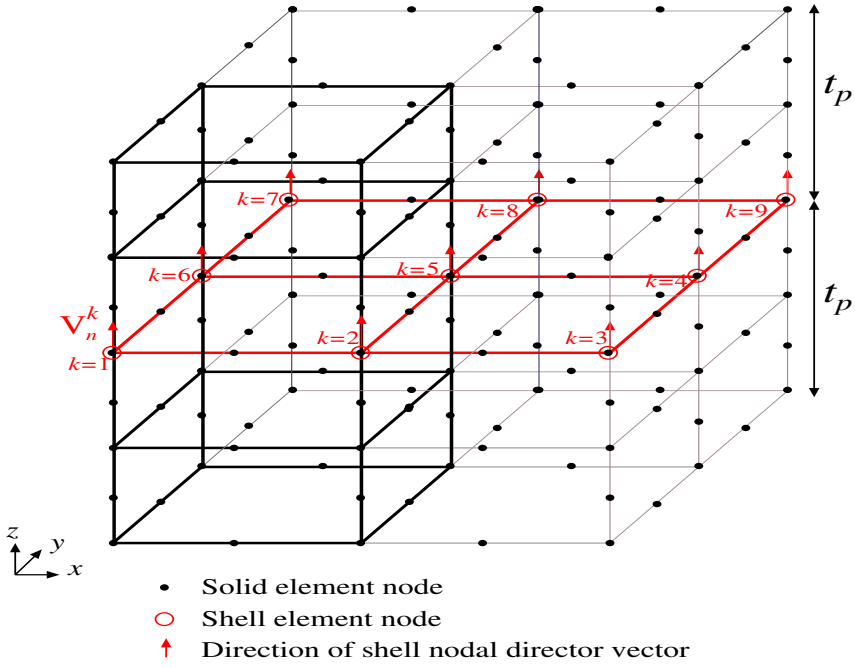

Figure 3.6: Regular grid-type meshing of a piezoelectric bimorph beam.

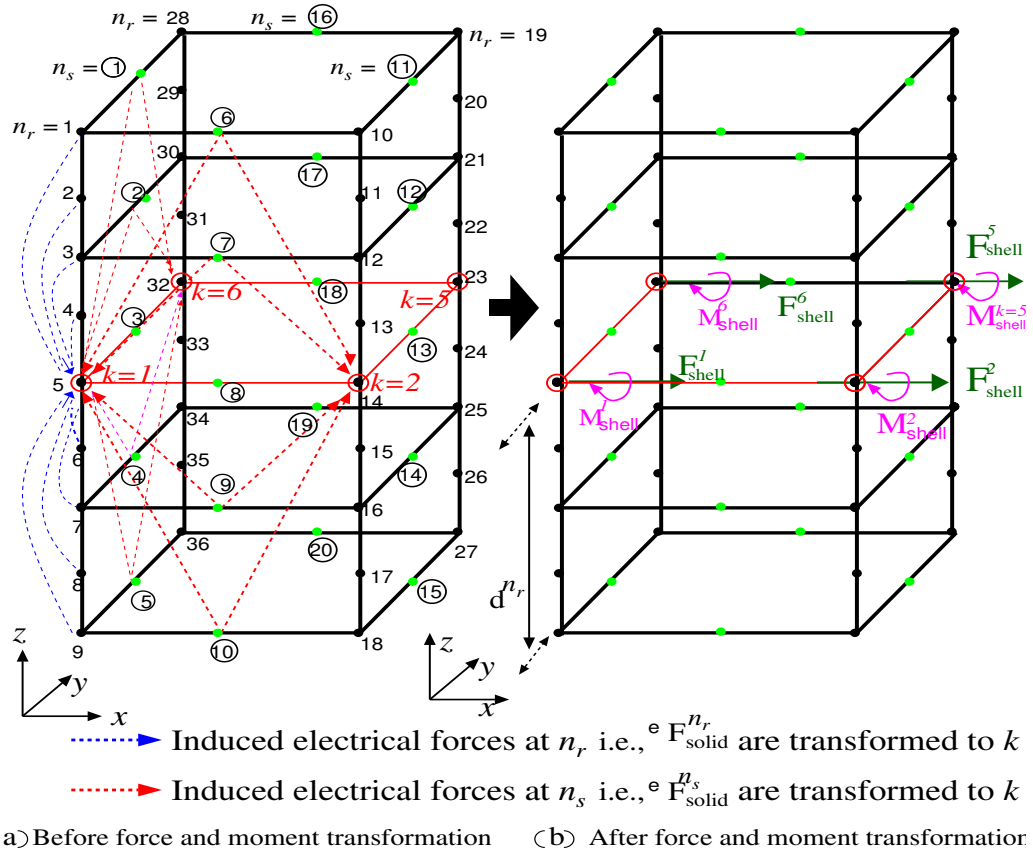

Figure 3.7: Transformation of nodal electric forces and moments from solid to shell elements.

The proposed method is quite general; however, for the purpose of simplicity the following assumptions were made in this study.

1. The top and bottom layers of the bimorph actuator have the same material properties and the same dimensions.

2. A shell midsurface (highlighted in red in Fig. 3.6) is placed at the interface of the two piezoelectric layers, and a regular grid-type mesh was used to discretize the shell midsurface.

The equivalent externally applied forces at the shell node are given as [89, 90],

$$\mathbf{F}^{k}_{\text{shell}} = \sum_{n_r=1}^{N_r} {}^{\text{e}}\mathbf{F}^{n_r}_{\text{solid}} + \sum_{n_s=1}^{N_s} \frac{{}^{\text{e}}\mathbf{F}^{n_s}_{\text{solid}}}{2}, \tag{3.40}$$

where $n_r = 1,\ldots,N_r$ are the indices of the solid element nodes that are located along the considered director vectors $\mathbf{V}^{k}_{n}$ of the shell nodes in the regular grid mesh shown in Fig. 3.6, N_r is the total number of these nodes, and ${}^{\text{e}}\mathbf{F}^{n_r}_{\text{solid}}$ is the induced nodal electric force vector at solid node n_r, as shown in Fig. 3.7. Similarly, $n_s = 1,\ldots,N_s$ are the indices of the solid element nodes that are located not along the considered director vector of the shell nodes but directly adjacent to it (see Fig. 3.7), N_s is the total number of these nodes, and ${}^{\text{e}}\mathbf{F}^{n_s}_{\text{solid}}$ is the induced nodal electric force vector at solid node n_s. The moment ${}^{\text{e}}\mathbf{M}^{k}_{\text{shell}}$ of the electric forces about the shell nodes can be easily calculated as [89, 90],

$${}^{\text{e}}\mathbf{M}^{k}_{\text{shell}} = \sum_{n_r=1}^{N_r} (\mathbf{d}^{n_r} \times {}^{\text{e}}\mathbf{F}^{n_r}_{\text{solid}}) + \sum_{n_s=1}^{N_s} (\mathbf{d}^{n_s} \times \frac{{}^{\text{e}}\mathbf{F}^{n_s}_{\text{solid}}}{2}), \tag{3.41}$$

where $\mathbf{d}^{n_r}$ and $\mathbf{d}^{n_s}$ are the position vectors of the solid element nodes n_r and n_s, respectively, with respect to the shell midsurface nodes. The components of the matrix ${}^{\text{e}}\mathbf{T}$ in Eq.(3.38) are then obtained from the electric force vector Eq.(3.40) and the moment of electric force vector Eq.(3.41).

Eqs. (3.40) and (3.41) correspond to the highlighted block of four solid elements and one shell element shown in Fig. 3.7. These equations should be summed for all other blocks in a regular grid mesh such as that shown in Fig. 3.7. As shown in Figs. 3.6 and 3.7, the shell node $k = 1$, which is located in the corner of the mesh, has $N_r = 9$ solid nodes lying along $\mathbf{V}^{1}_{n}$ and $N_s = 10$ solid nodes adjacent to $\mathbf{V}^{1}_{n}$ contributing to the summations of the first and second terms in Eq.(3.40), respectively. Similarly, the shell node $k = 5$, which is shared among four neighboring shell elements in Fig. 3.6, has $N_r = 9$ and $N_s = 20$, and the shell node $k = 6$, which is located at the junction of two neighboring shell elements, has $N_r = 9$ and $N_s = 15$.

B) Displacement transformation from shell to solid elements

After the electric forces and the moment of the electric forces have been transformed from the solid elements to the shell elements using Eq.(3.38), the nodal displacements and rotations in the shell can be evaluated in the global Cartesian coordinate system. The equation that relates the displacements from the shell elements to the solid elements can be generally expressed as

$$\mathbf{u}_{\text{solid}} = {}^{\text{u}}\mathbf{T}\mathbf{u}_{\text{shell}}, \tag{3.42}$$

where ${}^{\text{u}}\mathbf{T}$ is the displacement transformation matrix.

The displacements of a material particle in a shell element with natural coordinates of (ξ,η,ζ) are transformed into the Cartesian coordinates (x,y,z) of the shell elements in the total Lagrangian (TL) configuration using the interpolation function at time t shown in Eq.(3.6) is rewritten as,

$${}^{t}\mathbf{u}(\xi,\eta,\zeta) = h^{k}(\xi,\eta)\,{}^{t}\mathbf{u}^{k} + \frac{\zeta}{2}a^{k}h^{k}(\xi,\eta)({}^{t}\mathrm{V}_{n}^{k} - {}^{0}\mathrm{V}_{n}^{k}). \tag{3.43}$$

The displacements of a material point in a shell element with natural coordinates of (ξ,η,ζ) at time t in Eq.(3.43) are mapped to the corresponding solid element node at time t. The total number of material points in the shell structure is equal to the total number of nodal points in the solid elements used for the discretization of the electric field. As shown in Fig. 3.7, there are 56 nodes in four solid elements; therefore, 56 material points are considered in the shell structure at the natural coordinate ζ of a material point in a shell element, which corresponds to the Cartesian coordinate z of the corresponding solid element nodal point. The components of the matrix ${}^{\text{u}}\mathbf{T}$ are obtained from the interpolation function given in Eq.(3.43). As illustrated in Fig. 3.4, the resultant displacements in the shell elements $\mathbf{u}_{\text{shell}}$ are transformed to the solid elements.

3.2.4 Coupling of electric field and structure using block Gauss–Seidel iteration and transformation method

The electrical potential is obtained using the mechanical displacement by solving Eq.(3.3) in 3D solid as,

$${}^{t+\Delta t}\mathbf{K}_{\phi\phi}^{(b)}\,{}^{t+\Delta t}\phi^{(b)} = {}^{t+\Delta t}\mathbf{q} - {}^{t+\Delta t}\mathbf{K}_{\phi\text{u}}^{(b)}\,{}^{t+\Delta t}\mathbf{u}^{(b-1)}. \tag{3.44}$$

The mechanical displacements are obtained using the induced electrical force as,

$${}^{t+\Delta t}_{0}\hat{\mathbf{K}}_{\text{uu}}^{(i-1)(b)}\;\Delta\mathbf{u}^{(i)(b)} = \Delta\mathbf{R} - {}^{t+\Delta t}\mathbf{K}_{\text{u}\phi}^{(b)}\,{}^{t+\Delta t}\phi^{(\text{b})}, \tag{3.45}$$

where i indicates the full N–R iteration, $\Delta\mathbf{R}$ is the out-of-balance force vector, and $\Delta\mathbf{u}^{(i)(b)}$ is the incremental displacement at each BGS and N–R iteration in a time step. The last term on the right-hand side of Eq.(3.45) is the 3D electric force vector. The effective stiffness matrix is defined as,

$$ {}^{t+\Delta t}_{0}\hat{\mathbf{K}}_{\mathrm{uu}}^{(i-1)(b)} = \frac{1}{\beta\Delta t^2}\mathbf{M} + {}^{t+\Delta t}_{0}\mathbf{K}_{\mathrm{uu}}^{(i-1)(b)}, \tag{3.46} $$

where ${}^{t+\Delta t}_{0}\mathbf{K}_{\mathrm{uu}}^{(i-1)(b)}$ is the tangent stiffness matrix [71, 72] corresponding to the configuration at time $t+\Delta t$ but measured in the configuration at time 0 during N–R iteration $(i-1)$ and BGS iteration b. The out-of-balance force vector $\Delta\mathbf{R}$ in Eq.(3.45) is defined as,

$$ \Delta\mathbf{R} = {}^{t+\Delta t}\mathbf{R} - \mathbf{M}\Big\{a_0({}^{t+\Delta t}\mathbf{u}^{(i-1)} - {}^{t}\mathbf{u}) - a_1\,{}^{t}\dot{\mathbf{u}} - a_2\,{}^{t}\ddot{\mathbf{u}}\Big\} - {}^{t+\Delta t}_{0}\mathbf{F}^{(i-1)}, \tag{3.47} $$

where ${}^{t+\Delta t}\mathbf{R}$ is the vector of the externally applied nodal point loads at time $t+\Delta t$; ${}^{t+\Delta t}_{0}\mathbf{F}^{(i-1)}$ is the vector of the internal forces corresponding to the configuration at time $t+\Delta t$ but measured in the configuration at time 0; and $a_0 = \frac{1}{\beta\Delta t^2}$, $a_1 = \frac{1}{\beta\Delta t}$, and $a_2 = (\frac{1}{2\beta} - 1)$ are the Newmark constants. The displacement approximation is corrected by,

$$ {}^{t+\Delta t}\mathbf{u}^{(i)(b)} = {}^{t+\Delta t}\mathbf{u}^{(i-1)(b)} + \Delta\mathbf{u}^{(i)(b)}. \tag{3.48} $$

The approximation of the accelerations and velocities in the Newmark time integration is applied as described in Eqs.(2.36) and (2.37) and respectively.

This paper proposes the following two approaches, described in Fig. 3.8, for the nonlinear dynamic analysis of the structure–electric interaction in a piezoelectric actuator:

- Approach 1: BGS iteration with the N–R loop
  In a BGS iteration, full N–R equilibrium iterations are evaluated until the energy tolerance is satisfied [88], and several BGS iterations are executed in each time step until the preassigned relative tolerance criteria is satisfied for displacements and potentials [46]. Eqs. (3.3)–(3.48) correspond to Approach 1. The analysis flow of this approach is illustrated in Fig. 3.8 with the blue note.

- Approach 2: Unified BGS iteration and N–R loop
  In each BGS iteration, only one full N–R iteration is performed, i.e., the number of N–R iterations in each BGS iteration is fixed to one. This approach is also referred to as the unified algorithm. The analysis flow of this approach is illustrated in Fig. 3.8 with the red note. For this approach, Eq.(3.48) is modified as

$$ {}^{t+\Delta t}\mathbf{u}^{(b)} = {}^{t+\Delta t}\mathbf{u}^{(b-1)} + \Delta\mathbf{u}^{(b)}. \tag{3.49} $$

3.2.5 Nonlinear electric field–structure coupling scheme using the proposed transformation method

The model for the nonlinear structure–electric interaction described in the previous section is quite general. Here, the proposed transformation method presented in Section 3.2.3 is applied to the general nonlinear piezoelectric equations given in Section 3.2.4.

Electrical field analyzed in the solid elements: The electrical field in the solid elements is solved using Eq.(3.3) as

$$ {}^{t+\Delta t}\mathbf{K}_{\phi\phi}^{(b)}\ {}^{t+\Delta t}\phi_{\text{solid}}^{(b)} = {}^{t+\Delta t}\mathbf{q} - {}^{t+\Delta t}\mathbf{K}_{\phi u}^{(b)}\ {}^{t+\Delta t}\mathbf{u}_{\text{solid}}^{(b-1)}. \tag{3.50} $$

The displacements ${}^{t+\Delta t}\mathbf{u}_{\text{solid}}^{(b-1)}$ in the solid elements are obtained using the relation given in Eq.(3.42). Substituting Eq.(3.42) into Eq.(3.50) yields the electric potential in the solid elements as

$$ {}^{t+\Delta t}\mathbf{K}_{\phi\phi}^{(b)}\ {}^{t+\Delta t}\phi_{\text{solid}}^{(b)} = {}^{t+\Delta t}\mathbf{q} - {}^{t+\Delta t}\mathbf{K}_{\phi u}^{(b)}\ {}^{u}\mathbf{T}\ {}^{t+\Delta t}\mathbf{u}_{\text{shell}}^{(b-1)}. \tag{3.51} $$

The matrices ${}^{t+\Delta t}\mathbf{K}_{\phi\phi}^{(b)}$, ${}^{t+\Delta t}\mathbf{K}_{u\phi}^{(b)}$, and ${}^{t+\Delta t}\mathbf{K}_{\phi u}^{(b)}$ are evaluated from the solid elements at each BGS iteration in every time step $t+\Delta t$.

Structural field analyzed in the shell elements: The incremental displacements in the shell elements are obtained using Eq.(3.45) as

$$ {}^{t+\Delta t}_{0}\hat{\mathbf{K}}_{uu}^{(i-1)(b)}\Delta\mathbf{u}_{\text{shell}}^{(i)(b)} = \Delta\mathbf{R} - {}^{t+\Delta t}\mathbf{F}_{\text{shell}}^{(i-1)(b)}. \tag{3.52} $$

Substituting the transformation equation given in Eq.(3.38) into Eq.(3.52) yields

$$ {}^{t+\Delta t}_{0}\hat{\mathbf{K}}_{uu}^{(i-1)(b)}\Delta\mathbf{u}_{\text{shell}}^{(i)(b)} = \Delta\mathbf{R} - {}^{e}\mathbf{T}\ {}^{t+\Delta t}\mathbf{F}_{\text{solid}}^{(i-1)(b)}, \tag{3.53} $$

where $\Delta\mathbf{u}_{\text{shell}}^{(i)(b)}$ is the incremental displacement in the shell element. The tangent stiffness matrix ${}^{t+\Delta t}_{0}\mathbf{K}_{uu}^{(i-1)(b)}$ is calculated in the shell elements.

The displacement approximation in the shell elements is corrected using

$$ {}^{t+\Delta t}\mathbf{u}_{\text{shell}}^{(i)(b)} = {}^{t+\Delta t}\mathbf{u}_{\text{shell}}^{(i-1)(b)} + \Delta\mathbf{u}_{\text{shell}}^{(i)(b)}. \tag{3.54} $$

Eqs. (3.52) and (3.54) yield the structure in the shell elements from the electric forces and moments transformed onto the shell elements, which are considered as externally applied equivalent forces, as described in Section 3.2.3.

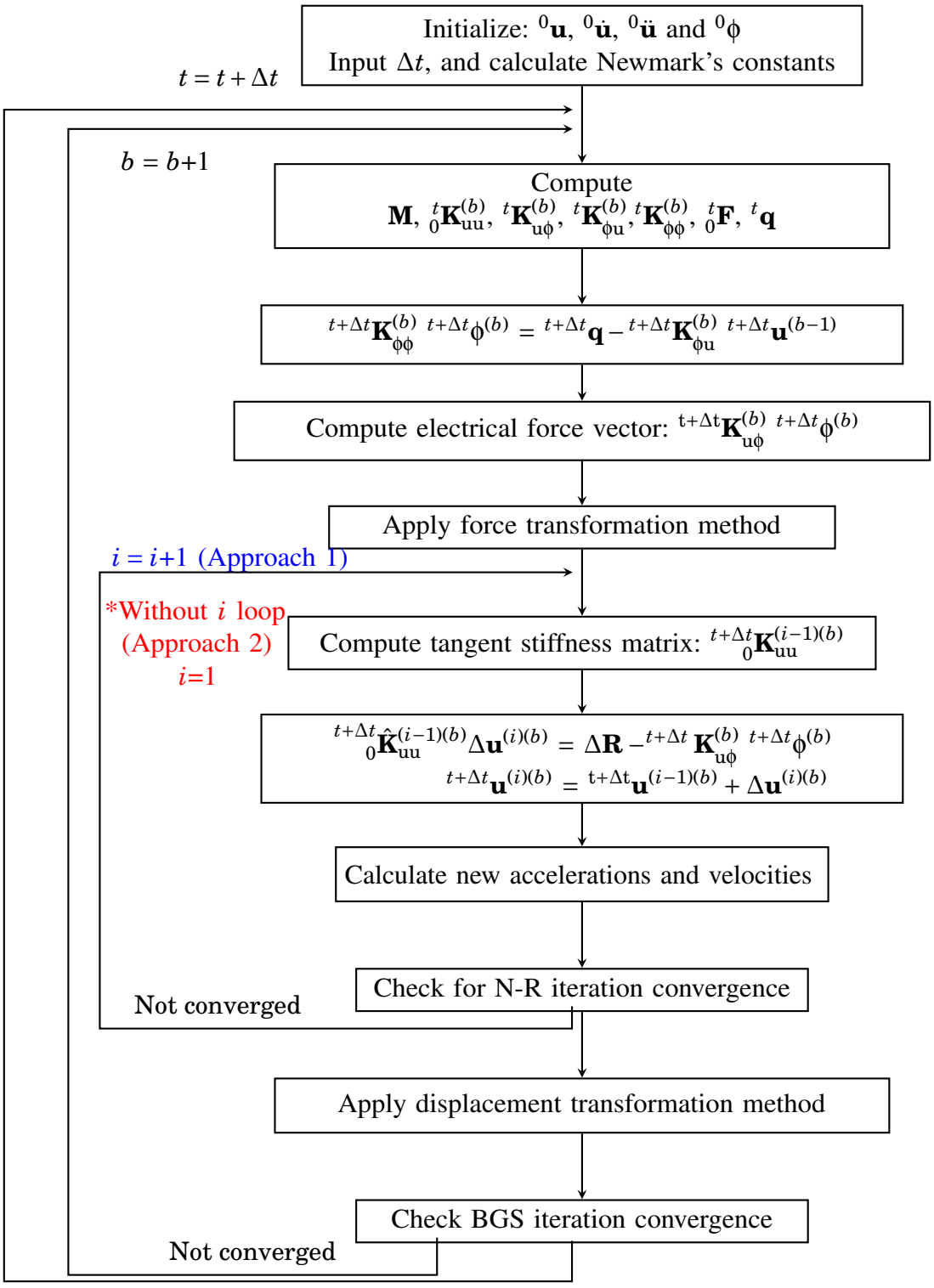

Figure 3.8: Nonlinear dynamic piezoelectric analysis: Approaches 1 and 2.

3.3 Analysis of piezoelectric bimorph actuator

3.3.1 Problem setup

The piezoelectric bimorph actuator shown in Fig. 3.5 consists of two piezoelectric ceramic layers joined together over their long surfaces. The beam has a length of $L = 100$ mm along x-axis, a width of $w = 1$ mm along y-axis, and a thickness of $t_p = 0.5$ mm along z-axis. The beam is fixed at $x = 0$. As shown in Fig. 3.9, two electrical loading cases are analyzed:

1. Series connection: Two layers of PVDF polarized along opposite transverse directions, see Fig. 3.9(a), uniform potential is applied on the top electrode with the bottom electrode being earthed.

2. Parallel connection: Two layers of PVDF polarized along same transverse directions, see Fig. 3.9(b), uniform potential applied on the top and bottom electrodes with the interface electrode being grounded.

For the electric configuration presented in Fig. 3.9, it is observed that under the potential load, the top and bottom layers of the piezoelectric bimorph actuator undergoes, respectively, contraction and expansion, and producing a pure bending in the upward direction.

3.3.2 Numerical setup

The meshes used for the electrical and structural analyses are shown in Fig. 3.10. The mesh for the electric analysis Fig. 3.10(a) consists of 20-node hexahedral elements with the numbers of the nodes and elements totaling 1343 and 160, respectively. The mesh for the structural

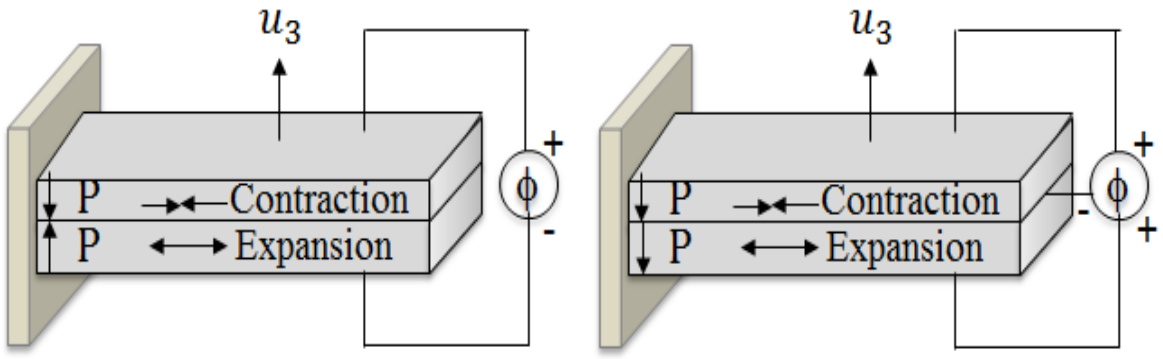

(a) Bimorph actuator in series connection

(b) Bimorph actuator in parallel connection.

Figure 3.9: Piezoelectric bimorph actuators subjected to external voltages .

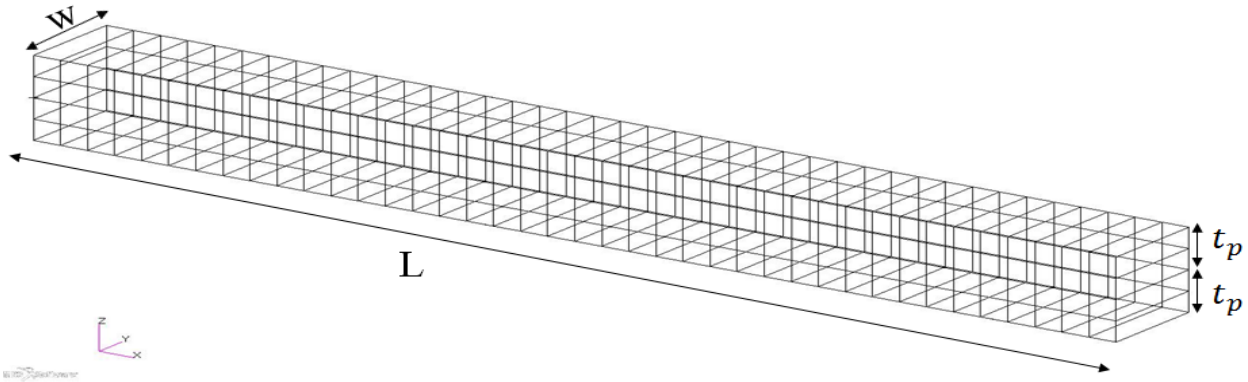

(a) 3D solid mesh for electrical analysis.

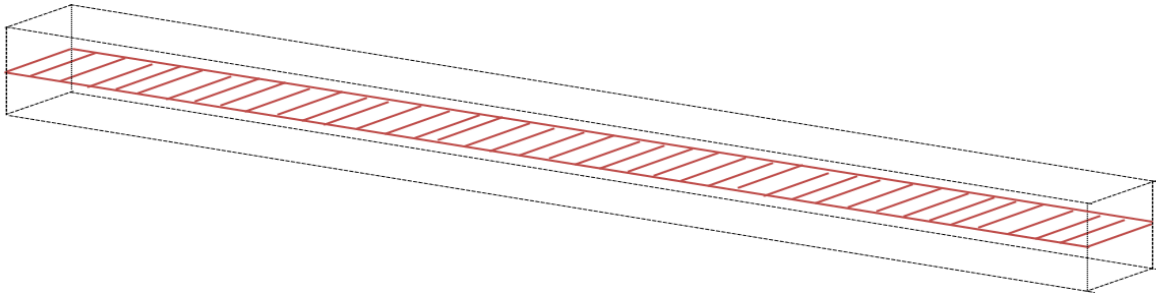

(b) Shell elements for structural analysis.

Figure 3.10: Finite element mesh for the bimorph actuator analysis.

analysis Fig. 3.10(b) consists of MITC4 shell elements [71, 73] with the numbers of nodes and elements totaling 82 and 40, respectively. The shell elements shown in Fig. 3.10(b) are positioned at the interface of the two piezoelectric ceramic layers discretized using 3D solid elements for electrical analysis as shown in Fig. 3.10(a). There are 40 shell elements in the x-direction; this number is consistent with the number of solid elements along the x-direction.

3.3.3 Static analysis of actuator function

A) Theoretical solution

The theoretical solution to the static deflection in thickness direction (z-direction) along length of the bimorph actuator (x-direction) is given as [22]

$$u_3(x) = \frac{3x^2}{4t_p} d_{31} E_3, \tag{3.55}$$

where d_{31} is the piezoelectric strain constant, $E_3 = \phi/2t_p$ is an applied electric filed for a series-type electrical connection and $E_3 = \phi/t_p$ for a parallel-type electrical connection and t_p is the thickness of each piezoelectric layers. Substituting the actuator dimensions and the

material properties of the PVDF given in Table 2.1 into Eq.(3.55) with $x = L$ for $\phi = 1$ V across the thickness yields a static tip deflection of $u_3(L) = 0.3450$ µm for a series-type electrical connection and $u_3(L) = 0.690$ µm for a parallel-type electrical connection.

The theoretical solution for the equivalent bending moment, which is defined as the moment that can produce the same deflection in a piezoelectric bimorph actuator as an applied electric field, can be obtained as [21]

$$M_{eq} = \frac{wh^2 E_p}{4} d_{31} E_3, \tag{3.56}$$

where $h = 2t_p$ is the total thickness of the bimorph. Substituting the actuator dimensions and the material properties given in Table 2.1 into Eq.(3.56) for an applied voltage of $\phi = 1$ V with $E_3 = \phi/2t_p$ across the thickness yields

$$M_{eq} = 1.1500 \times 10^{-8} \text{ Nm}.$$

The first bending resonance $\omega_r^{(1)}$ for a piezoelectric bimorph actuator is given as [22]

$$\omega_r^{(1)} = \frac{1.875^2}{L^2} \sqrt{\frac{E_p I}{\rho_p A}}, \tag{3.57}$$

where I is the second moment of area and A is the cross-sectional area. From Eq.(3.57) and the material properties of PVDF given in Table 2.1, the resonance frequency for the first bending mode was obtained as 107.0 rad/s.

B) Numerical analysis: Convergence and results accuracy for approaches 1 and 2

Here, the static analysis results for both approaches are presented for the case where the time integration of Eq.(3.52) is not taken into account. First, the convergence properties of the two approaches are addressed for a series-type piezoelectric bimorph actuator. Fig. 3.11(a) shows the convergence results for Approach 1, in which the first BGS iteration required three N–R iterations to satisfy the preassigned energy tolerance of $e_{tol} = 1.0 \times 10^{-12}$ and subsequent BGS iterations required two N–R iteration to satisfy this condition. Fig. 3.11(b) shows the relative error of the numerically obtained tip deflection using Approach 1 with respect to the theoretical solution given by Eq.(3.55). At BGS iteration 4, the tip deflection converged to within the set relative tolerance value of $\epsilon = 1 \times 10^{-5}$ in this approach. Similarly, Fig. 3.12 shows the BGS iteration convergence proprieties of Approach 2. By the fifth BGS iterations, the set energy tolerance condition was satisfied. In Approach 2, five BGS iterations with one N–R iteration in each BGS loop were sufficient to perform static analysis for this numerical problem.

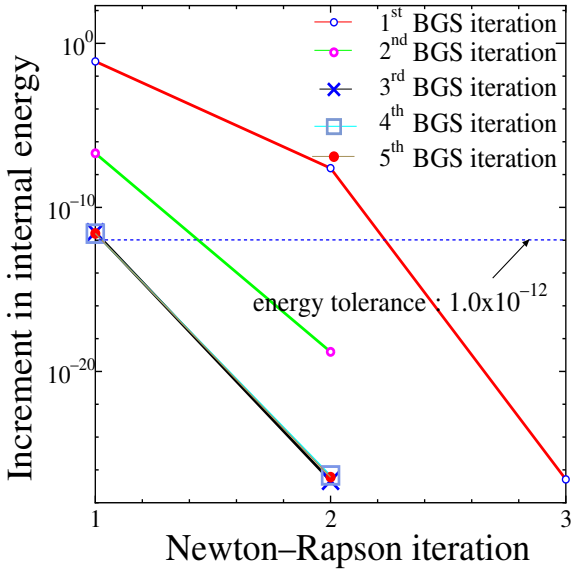

(a) N–R convergence in each BGS iteration.

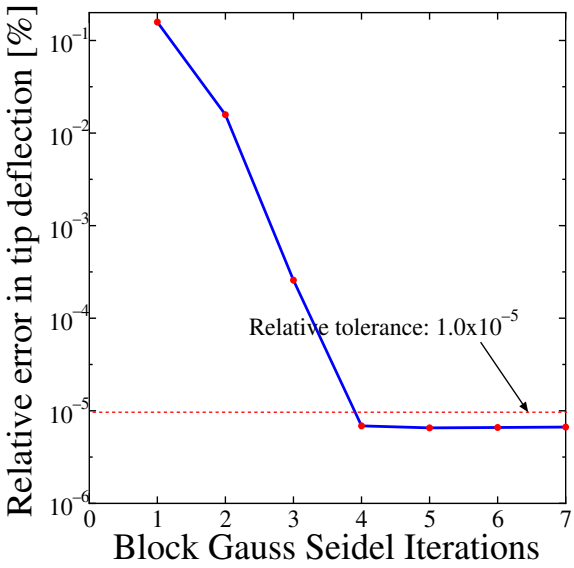

(b) BGS iteration convergence of the tip deflection.

Figure 3.11: Iteration convergence analysis for the static case: Approach 1 (BGS iteration with the N–R loop).

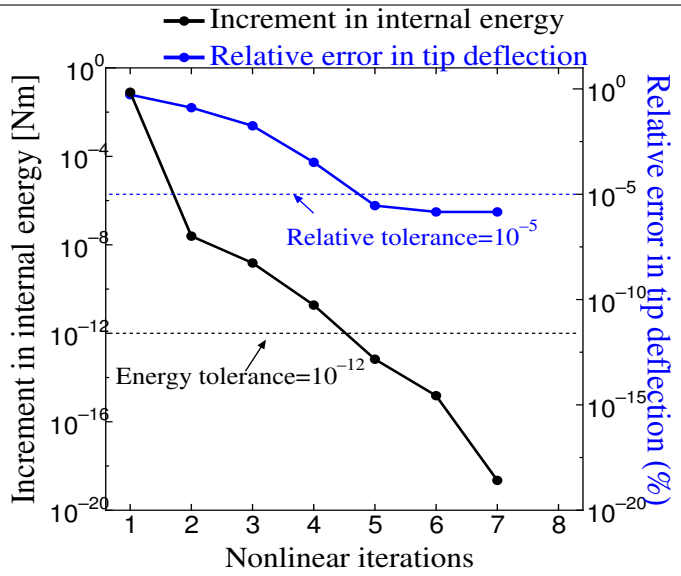

Figure 3.12: Iteration convergence analysis for the static case: Approach 2 (Unified algorithm).

.

Table 3.1: Deflection of the bimorph actuator in series connection (for a unit applied voltage)

Location along the length (mm)	Deflection(μm)				
	Theory[22]	Tseng[8]	Wang[9]	Present	
				Approach 1	Approach 2
20	0.01380	0.01500	0.01390	0.01379	0.01378
40	0.05520	0.05690	0.05470	0.05519	0.05511
60	0.12420	0.13710	0.11350	0.12419	0.12413
80	0.22080	0.23510	0.21980	0.22078	0.22079
100	0.34500	0.35980	0.34160	0.34505	0.34510

Table 3.2: Deflection of the bimorph actuator in parallel connection (for a unit applied voltage)

Location along the length (mm)	Deflection(µm)		
	Theory[22]	Present	
		Approach 1	Approach 2
20	0.0276	0.02746	0.02768
40	0.1104	0.11040	0.11108
60	0.2484	0.24880	0.24947
80	0.4416	0.44268	0.44297
100	0.6900	0.69200	0.69200

Next, the static deflections obtained using Approaches 1 and 2, the theoretical solution using Eq.(3.55), and the deflection at the nodes obtained by Tseng [8] and Wang et al. [9] are listed in Table 3.1 and Table 3.2 for a series and parallel connection, respectively. These cases are all under the condition of a unit input voltage. Tseng [8] modeled the piezoelectric continuum using solid hexahedral elements, which are too thick for the simulation of thin-layered MEMS structures. Wang et al. [9] used a piezoelectric plate element and applied the Guyan reduction method to condense the electric potential vectors.

Fig. 3.13 shows the tip deflection of the bimorph actuator in series analyzed under various applied voltages. The purpose of this analysis is to demonstrate the superiority of the present nonlinear shell–solid method over linear solid–solid [47] and linear theoretical solution [22]. From the current literature review, there are no nonlinear theoretical solutions for the deflection of the piezoelectric bimorph actuator. Therefore, blocking force F_{b} [21] corresponding to the induced electric forces for an applied voltage ϕ in a bimorph actuator is externally applied on to the nonlinear pure shell [71] to perform the structural analysis and the displacement obtained in the nonlinear pure shell is compared with the proposed shell–solid combination. The blocking force can be obtained as [21],

$$F_{\mathrm{b}} = \frac{3wh^2E_p}{8L} d_{31}E_3. \tag{3.58}$$

As shown in Fig. 3.13, at lower input bias voltages, in the elastic regime, the deflections analyzed using present nonlinear shell–solid coincides with linear theory and linear solid–solid. However, at higher voltages, the proposed method shows the large deformation due to geometric nonlinear effect. The solution obtained with the pure shell using the blocking force is very close to that of the proposed method. This indicates that the proposed method accurately takes into account the geometric nonlinear effect in a thin plate–like piezoelectric bimorph.

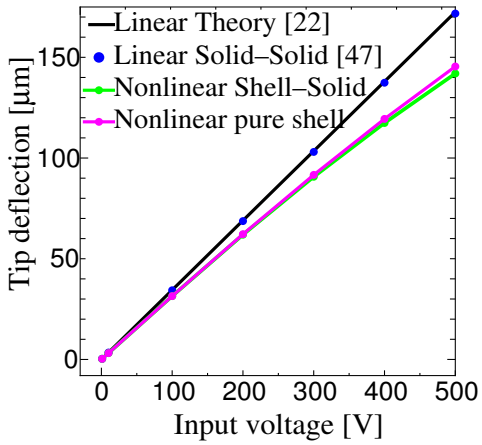

Figure 3.13: Tip deflection of the bimorph actuator at various input voltages.

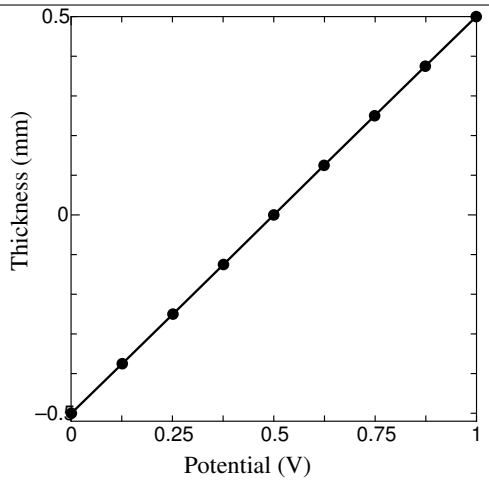

(a) Potential distribution in a piezoelectric bimorph actuator in series connection.

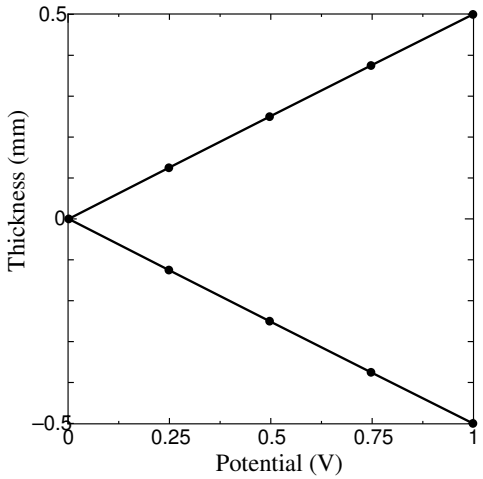

(b) Potential distribution in a piezoelectric bimorph actuator in parallel connection.

Figure 3.14: Variation of the electric potential across the thickness in a piezoelectric bimorph actuator.

Finally, the variation of the electric potential in the solid elements across the thickness direction ($x = L$, $y = w$) for a series and parallel connection are presented in Fig. 3.14. The results confirm clearly that for a piezoelectric actuator mode, the variation of the electric potential varies almost linearly in the thickness direction, as previously discussed in [37, 43, 86]. Kogli & Bucalem in [37, 86] solved a piezoelectric bimorph actuator with a quadratic variation of electric potential over the thickness for a parallel electric configuration, their results clearly show that the electric potential varies almost linearly, because of the three equipotential electrodes at the top, bottom, and interface.

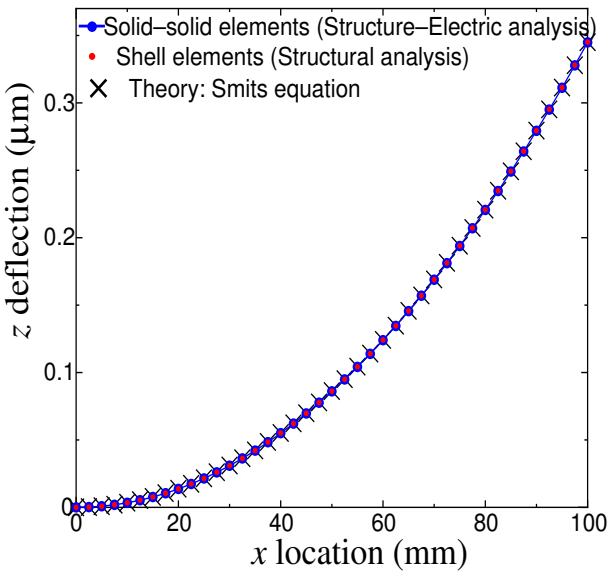

Figure 3.15: Static deflection of the bimorph actuator.

.

C) Validation of electric force and moment transformation

The purpose of this section is to validate the transformation of the electric forces and moments from the solid to the shell elements. The numerical problem described in Fig. 3.9(a) in the case with a unit static input voltage was considered. First, both the structure and electric field were solved using the solid elements to evaluate both the nodal displacements and the electric potential under the BGS coupling scheme [47]. Next, the electric force vector in the solid elements was calculated using Eq.(3.39). Then, the electric forces and moments were applied externally to the shell elements using the proposed force and moment transformation method described in Section 3.2.3 to obtain the mechanical displacements of the shell elements from the displacement interpolation function [70, 72]. Finally, the mechanical displacements of the solid elements due to the piezoelectric effect were compared with the displacements of the shell elements obtained from the transformed electric forces and moments.

Fig. 3.15 shows the static deflection obtained by solving both the electrical and mechanical fields using the solid elements and the static deflection obtained in the shell elements from the electric forces and moments applied externally to the shell elements. These results demonstrate very good agreement among the static deflection from the piezoelectric effect obtained using the solid–solid element analysis, the shell elements for the structural analysis, and the theory Eq.(3.55) [22]. This indicates that the induced electric force and the moment of the electric forces are accurately transformed from the solid elements to the shell elements using the proposed method.

The motional restrictions along the joined surfaces of the two piezoceramic layers creates forces and moments that result in the pure bending of the bimorph actuator [60]. The total moment of the electric forces in the solid elements due to the piezoelectric effect obtained using the BGS algorithm is,

$$M_{eq} = 1.1506 \times 10^{-8} \text{ Nm}.$$

The relative error of the numerical solution with respect to the theoretical solution is 0.052%. The deflection of the bimorph solved using the piezoelectric solid elements [47] and that solved using shell elements show good agreement, demonstrating the accurate transformation of the forces and moments.

3.3.4 Dynamic analysis of bimorph actuator

A) AC response

The bimorph actuator shown in Fig. 3.9 was examined under AC input voltages with $\phi = \phi_0 \sin\omega_\phi t$, where ω_ϕ and ϕ_0 are the frequency and amplitude of the input voltage, respectively. The values of β and γ for the Newmark integration were selected as $\beta = 0.25$ and $\gamma = 0.5$. The time increment was set to $\Delta t = (1/50)(2\pi/\omega_\phi)$ for input frequencies much smaller or larger than the resonance frequency and $\Delta t = (1/200)(2\pi/\omega_\phi)$ for input frequencies near resonance to obtain the converged vibration amplitudes [47]. A finer time resolution was used near resonance because the deflection is very sensitive to changes in the frequency near resonance.

Figs. 3.16 and 3.17 show the iteration convergence properties of the BGS and full N–R iterations in the dynamic analysis using Approach 1 for a bias voltage of $\phi = 1$ V at a frequency of $\omega_\phi = 106$ rad/s and a time increment of $\Delta t = 3.0 \times 10^{-4}$ s. Fig. 3.16 shows the increment in internal energy during each N–R iteration at every BGS iteration. According to Fig. 3.16(a), in the first BGS iteration at every time step, three or four N–R iterations were executed before the preassigned energy tolerance criterion was satisfied. Similarly, in the second and third BGS iterations, only one N–R iteration was required to reach convergence, as shown in Fig. 3.16(b) and (c), respectively. The relative error of the tip deflection at every BGS iteration is shown in Fig. 3.17. As shown in Fig. 3.17(a) and (b), the tip deflection did not converge to the preassigned relative tolerance value in first and second BGS iterations; in contrast, the relative error of the tip deflection satisfied the tolerance criteria at every time step in the third BGS iteration, as shown in Fig. 3.17(c).

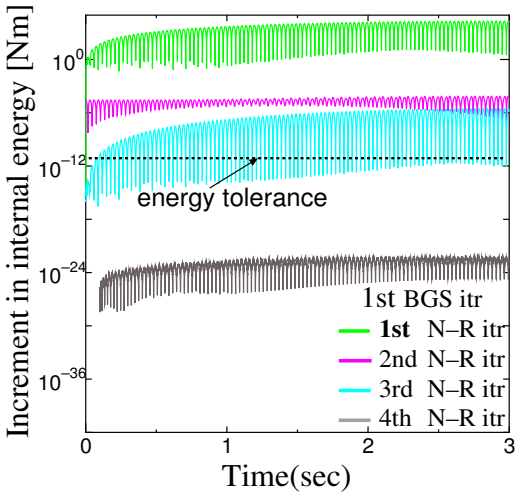

(a) First BGS iteration.

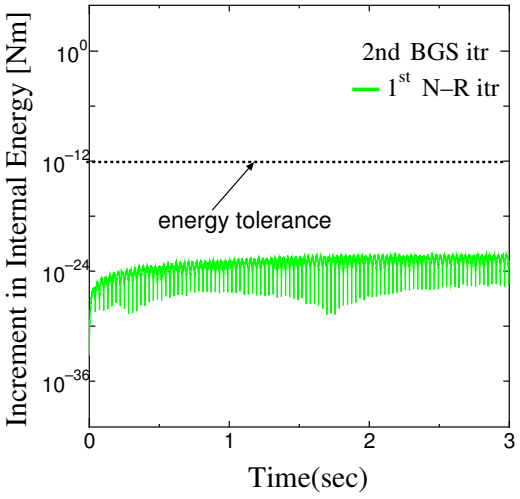

(b) Second BGS iteration.

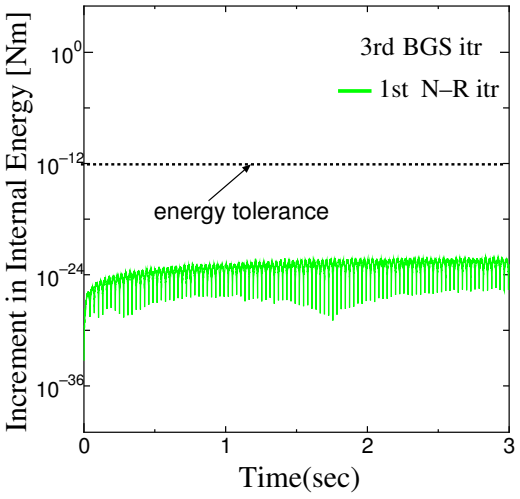

(c) Third BGS iteration.

Figure 3.16: Iteration convergence properties of Approach 1: The increment in internal energy is plotted against the time at each BGS iteration.

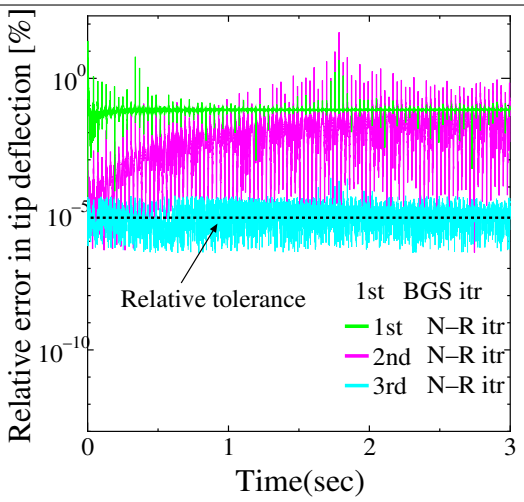

(a) First BGS iteration.

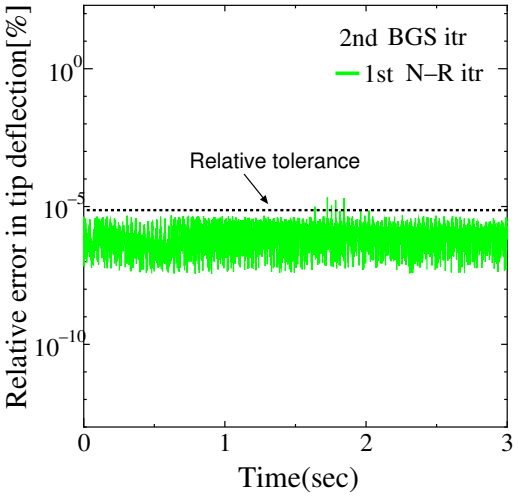

(b) Second BGS iteration.

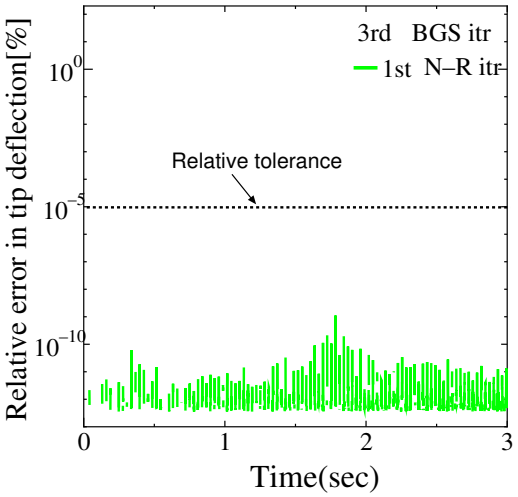

(c) Third BGS iteration.

Figure 3.17: Iteration convergence properties of Approach 1: The relative error of the tip deflection v/s time at each BGS iteration.

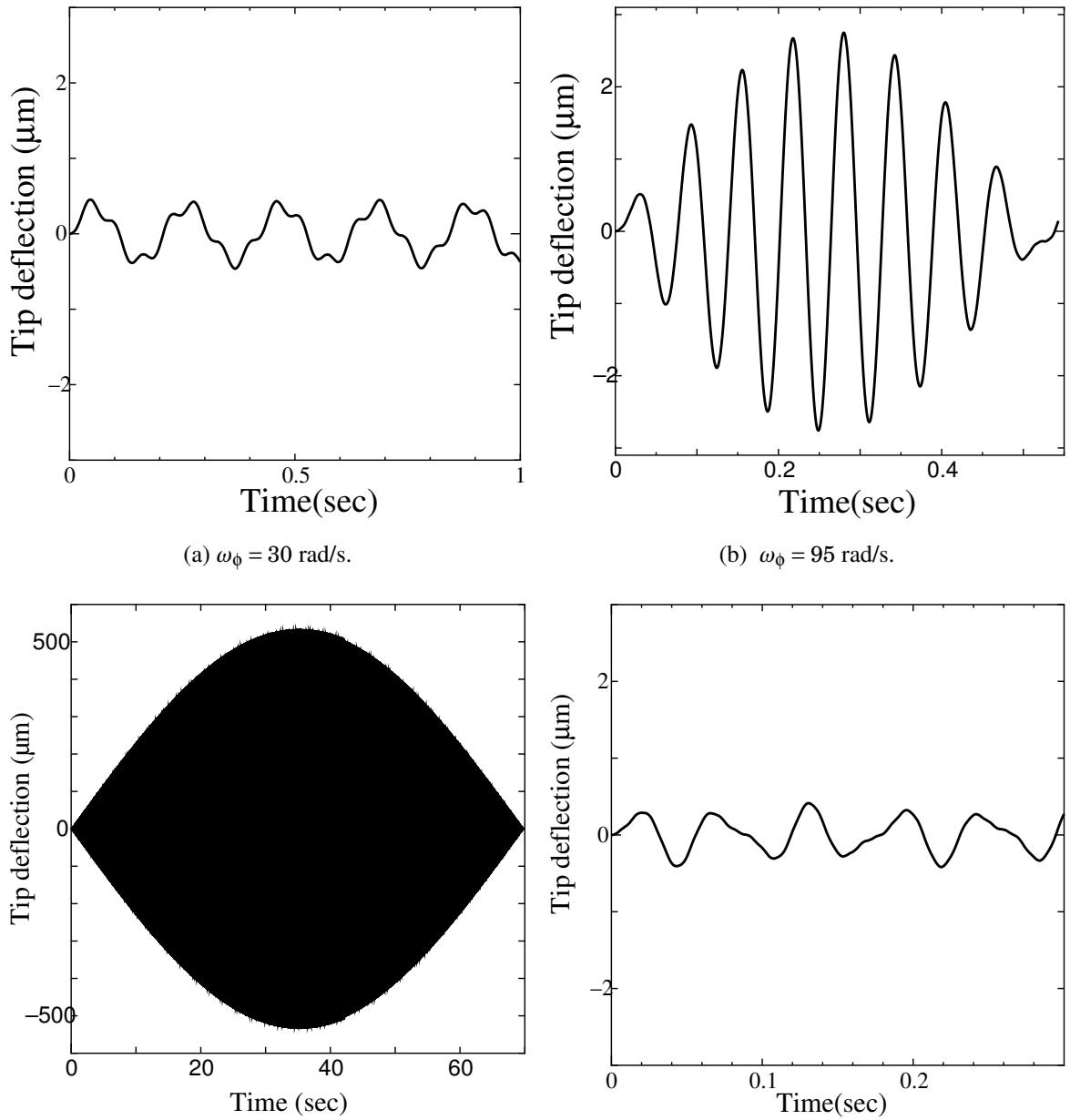

(a) $\omega_\phi = 30$ rad/s.

(b) $\omega_\phi = 95$ rad/s.

(c) $\omega_\phi = 106.9$ rad/s.

(d) $\omega_\phi = 180$ rad/s.

Figure 3.18: AC response of a bimorph actuator in a series connection at different frequencies simulated using Approach 1.

Next, the vibration characteristics of the tip of the piezoelectric bimorph actuator in response to input AC signals with different frequencies and an amplitude of $\phi = 1$ V obtained using Approach 1 are depicted in Fig. 3.18. The peak displacements of the AC responses to the input signals with the different frequencies are summarized in Fig. 3.19. The point of maximum

deflection at the tip of the bimorph actuator indicates when the frequency of the input voltage is equal to the resonance frequency of the actuator. The responses of the actuator at input voltage frequencies of ω_ϕ = 106.8 to 107.2 rad/s, which are close to the structural resonance frequency, had large amplitudes [45], as shown in Fig. 3.19; however, for input voltage frequencies much larger or smaller than the structural resonance frequency, the peak amplitudes of the responses were approximately equivalent to the tip deflection under a static force [45], as shown in Fig. 3.18(a) and (d). The response in Fig. 3.18(c) achieved the largest peak amplitude among the different input frequencies, indicating resonance was achieved at this frequency.

Fig. 3.19 reveals that the simulation results yielded a maximum peak deflection amplitude at an input voltage frequency of ω_ϕ = 106.9 rad/s. The resonance of the piezoelectric bimorph actuator actually occurs at a driving input voltage frequency very close to the theoretical frequency of $\omega_r^{(1)}$ = 107.0 rad/s. Therefore, the numerical and theoretical solutions are in good agreement with each other.

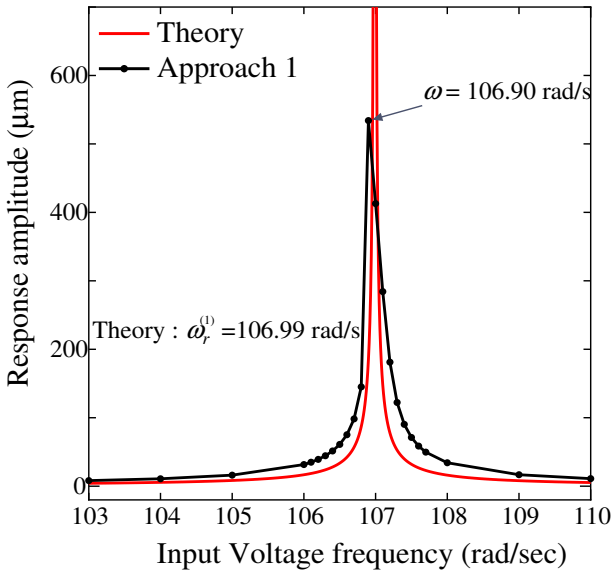

Figure 3.19: Frequency response curve of a bimorph actuator calculated using Approach 1.

The AC response was then simulated using Approach 2. Fig. 3.20(a) shows the vibration characteristics at an input voltage frequency much smaller than the structural resonance frequency of the bimorph actuator. There is an instability in the solution when one BGS iteration is performed in each time step; however, there is no such instability when two or more BGS iterations are used in each time step. Additionally, when the input voltage frequency is close to the structural resonance frequency, an instability arises when one or two BGS iterations are used in each time step, as shown in Fig. 3.20(b). The reason for the instability that arises when the

input voltage frequency is much smaller than the resonance frequency and one BGS iteration is used is delineated in Fig. 3.21. The relative error of the tip deflection approaches infinity when one BGS iteration is used in this case, as shown in Fig. 3.21(a). This is because the energy tolerance in the nonlinear N–R iteration is not satisfied when only one BGS iteration is applied, as shown in Fig. 3.21(b). From this assessment, it is apparent that executing three or four BGS iterations in every time step would yield a converged solution without any instability when Approach 2 is used. The vibration amplitudes at various AC input voltages are approximately equal to those obtained using Approach 1. The same level of accuracy in the simulated tip vibration was achieved in both approaches.

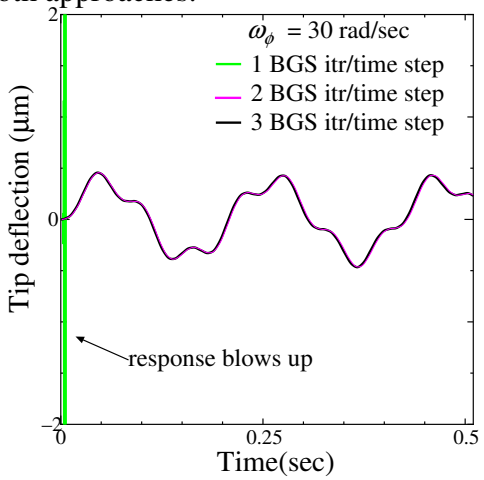

(a) Response for the input frequency far from the resonance frequency.

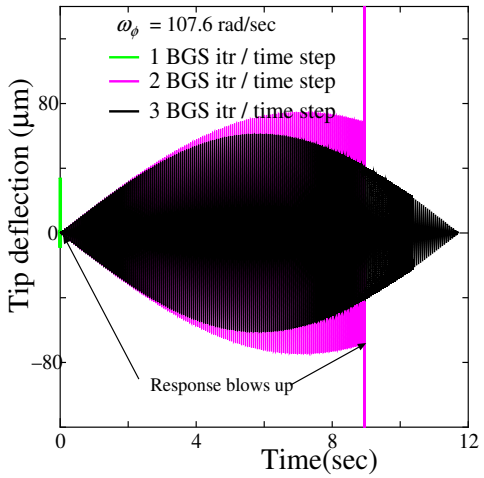

(b) Response for the input frequency near the resonance frequency.

Figure 3.20: AC response of a bimorph actuator in a series connection at different frequencies simulated using Approach 2.

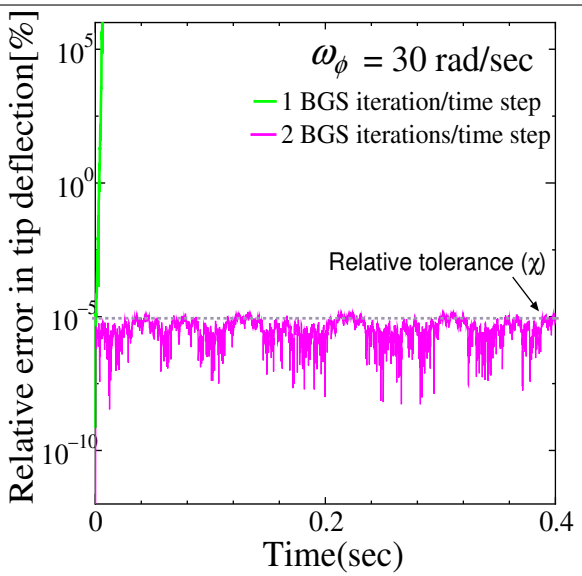

(a) Tip deflection iteration convergence.

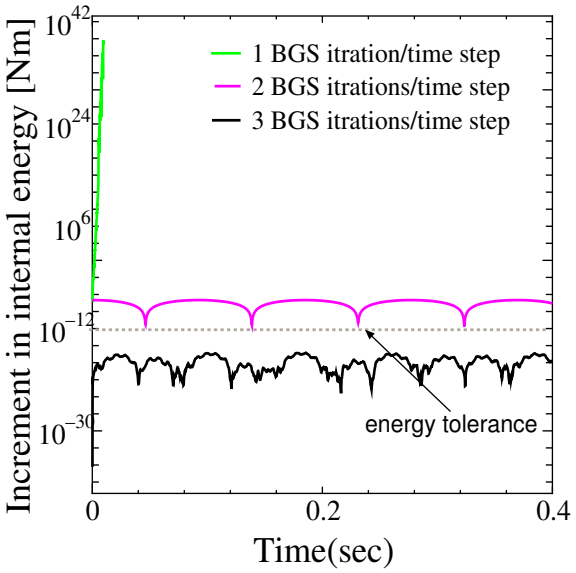

(b) The internal energy increment obtained after N–R and BGS iteration for each time step.

Figure 3.21: Dynamic analysis iteration convergence properties: Approach 2.

B) Step response of a piezoelectric bimorph actuator

The vibration characteristics of the piezoelectric bimorph actuators driven by a step voltage $\phi = 1$ V obtained using Approach 1 are presented here. Newmark [52] presented a numerical damping scheme in which $\beta = 0.25(\gamma + 0.5)^2$ with $\gamma > 0.5$; on the basis of this method, a step input voltage with the Newmark parameters of $\gamma = 0.6$ and $\beta = 0.3025$ was used to obtain

steady-state equilibrium after a long time interval. These parameters were adopted because when a bimorph actuator is actuated with numerically positive damping with a step input bias voltage, the steady-state response of the tip deflection is equal to the theoretical solution for the static deflection. The time increment Δt was chosen as 1.0×10^{-3} s.

Fig. 3.22 shows the step response of the numerical problem in Fig. 3.9. The steady-state tip deflection was obtained as 0.3452 µm as shown in Fig. 3.22(a), whereas the theoretical static tip deflection obtained from Eq.(3.55) is $u_3(L) = 0.3450$ µm. Thus, the relative error of the tip deflection is 0.057%. The exact value of the natural period of vibration ($T_n = 1/f_r$) for this problem is 0.0587 s, where the natural frequency f_r is obtained using Eq.(3.57). The obtained natural period using the numerical analysis is 0.0585 s, shown in Fig. 3.22(b). The natural period of vibration showed good agreement between the numerical and theoretical solution. Highly accurate solutions were obtained using the proposed coupled algorithm. Approach 2 yielded similar results.

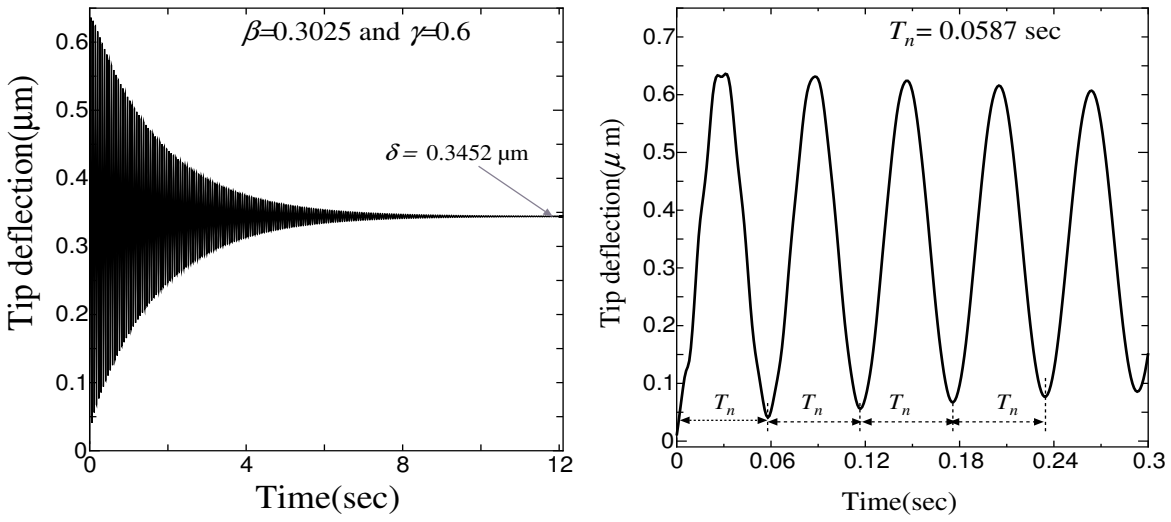

(a) Step response of piezoelectric bimorph actuator (b) Enlarged view to show the natural period of vibration

Figure 3.22: Response of a bimorph actuator to a step input voltage using transformation method: Approach 1

.

3.4 A piezoelectric bimorph sensor mode

3.4.1 Problem setup

In this section, the sensor response of a 3D piezoelectric bimorph cantilever shown in Fig. 3.23 is obtained for a transverse load F at the free end of the shell structure. The nodes with the electric degree of freedom (DOF) at the top, bottom, and mid–surfaces of a piezoelectric bimorph FE model are regarded as an electrode.

Four electrical configurations are analyzed for a transverse load F at the free end of the shell structure Fig. 3.23(a):

1. Closed circuit configuration (active mode): The nodes at the top and bottom surfaces are set to zero electric potential, as shown in Fig. 3.23(b).

2. Closed and open circuit configuration (active–sensory mode): The nodes at the top surface are in an open circuit condition while the bottom surface is earthed, as shown in Fig. 3.23(c).

3. Partial open circuit configuration: In this configuration, a node at the top and bottom surface near the fixed end are grounded while other nodes are in open circuit configuration, as shown in Fig. 3.23(d).

4. Full open circuit configuration (sensory mode): Both the top and bottom surfaces are in an open circuit condition, as shown in Fig. 3.23(e). In energy harvesting application, open surfaces at the bottom and top are general [3, 13, 14].

The piezoelectric bimorph beam shown in Fig. 3.23 has a length of $L = 250$ mm, a width of $w = 20$ mm, and a thickness of each layer $t_p = 2.5$ mm. The piezoelectric layers are polarized in the same direction along the thickness. All the mechanical DOF are fixed at $x = 0$. The mesh for the structural analysis consists of MITC4 shell elements with the numbers of nodes and elements totaling 22 and 10, respectively. The mesh for the electric analysis consists of 20-node hexahedral elements with the numbers of the nodes and elements totaling 353 and 40, respectively.

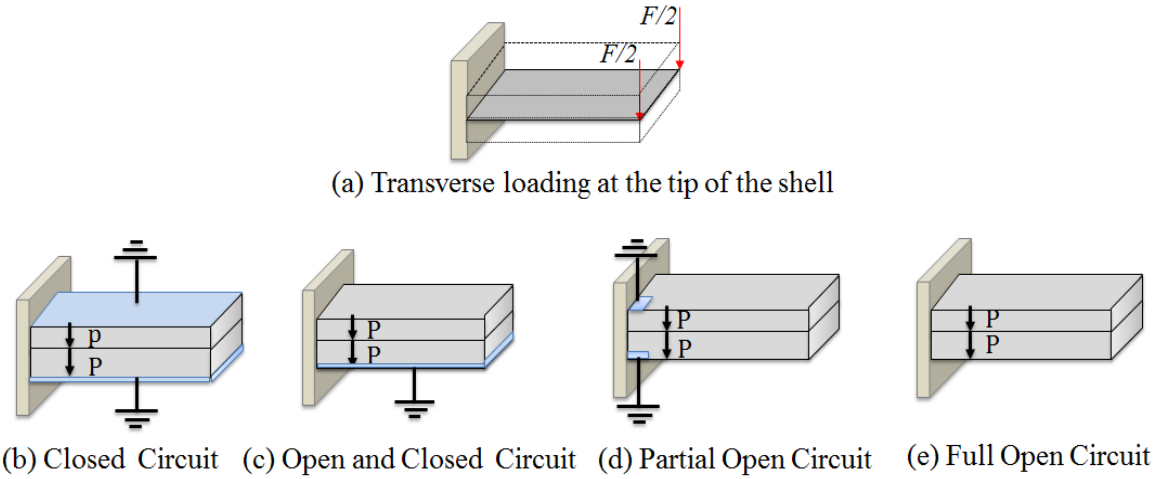

(a) Transverse loading at the tip of the shell

(b) Closed Circuit (c) Open and Closed Circuit (d) Partial Open Circuit (e) Full Open Circuit

Figure 3.23: Piezoelectric bimorph cantilever sensor configuration: a) Tip loading in shell, b) closed circuit configuration in solid, c) closed and open circuit configuration in solid, d) partial open circuit configuration in solid, e) full open circuit configuration in solid

3.4.2 Static analysis of sensor function

The displacement of the tip due to a transverse load F at the free end of the shell structure produces a voltage in the 3D solid of the bimorph cantilever beam. The generated electric potential V of a parallel polarized rectangular piezoelectric layers is given by [91, 92]

$$V = \frac{3}{16} g_{31} E_p \frac{h^2}{L^2} \delta, \tag{3.59}$$

where g is the piezoelectric voltage coefficients, E_p is the Young's modulus of the piezoelectric layer, h is the overall thickness of the bimorph cantilever, L is the length of the bimorph and δ is maximum tip deflection due to pure mechanical transverse loading F at the tip. The piezoelectric voltage constant g_{31} for PVDF material is 0.216 Vm/N. The maximum tip deflection δ for an applied tip load F is obtained using,

$$\delta = \frac{FL^3}{3E_p I}. \tag{3.60}$$

Taking tip load $F = 1 \times 10^{-3}$ N, the numerical results of the distribution of induced electrical potential over the thickness at $x = 0, y = 0$ are presented in Fig. 3.24. It is apparent from Fig. 3.24 that the induced electrical potential obtained with the FE analysis varies, almost quadratically over the thickness. It is easily understood that the potential in the upper and lower surfaces is zero for closed circuit electric configuration, as shown in Fig. 3.24(a). Similarly, there exists

a potential on the top surface while it is zero on the bottom surface for active–sensory mode configuration, as shown in Fig. 3.24(b). The induced electric potential for the third electric configuration of the sensor mode is shown in Fig. 3.24(c). As shown in Fig. 3.24(b), it is clear that for the active–sensory mode configuration, the induced electric potential on both the top surface has a value $V = 0.810$ V for applied tip load $F = 1 \times 10^{-3}$ N, which is very close to that of the theory.

As presented here, the 3D solid elements in the sensor mode can model the electric field under any electric boundary conditions with almost a quadratic variation of the induced electric potential over the thickness.

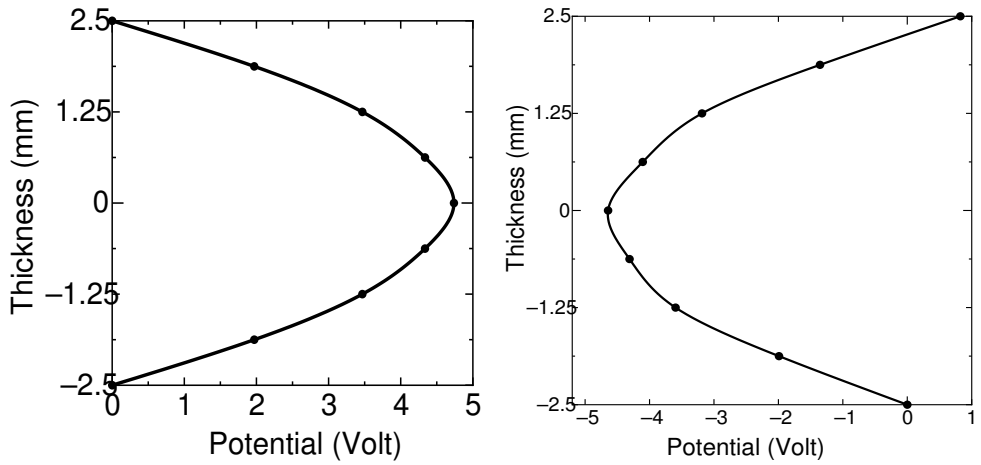

(a) Closed circuit configuration

(b) Active–sensory mode configuration

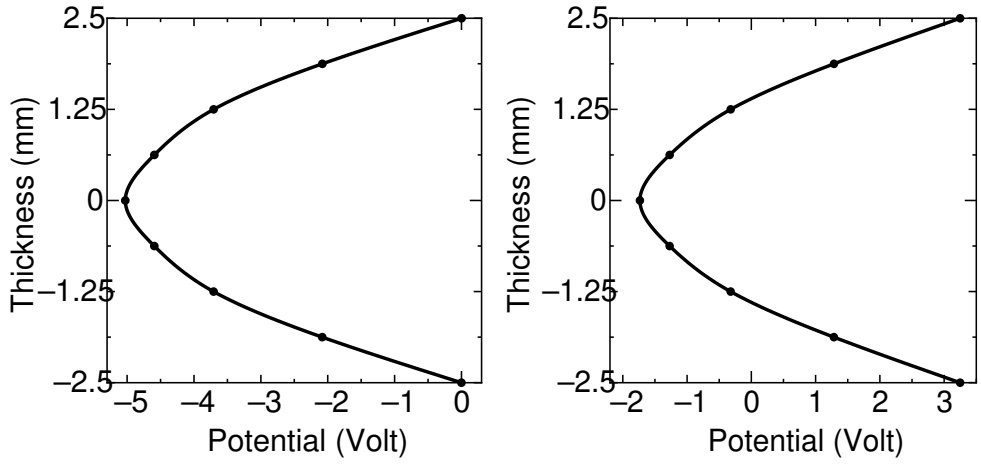

(c) Partial open circuit configuration

(d) Full open circuit configuration

Figure 3.24: Distribution of potential over the thickness of the bimorph cantilever for sensor model under $F = 1 \times 10^{-3}$ N

3.5 Conclusions

A new finite element scheme for the simulation of the piezoelectric interaction between the structure and electrical fields was developed using a combination of both solid and shell elements for the finite element model. The field decomposition employed in this method enables the use of different elements to solve the different fields. A novel method of exchanging the electric force, the moment of the electric force, and the displacement between the electrical field in the solid elements and the mechanical field in the shell elements was developed. The proposed method can be used to analyze both the actuator and sensor function in a thin–layered piezoelectric bimorph cantilever of various electric configurations with both the linear and quadratic variations of the electric potential across the thickness direction.

The geometric nonlinear structure–electric interaction of the piezoelectric effect was analyzed by applying two different approaches. In the first approach, the full N–R iteration loop is executed in every BGS iteration until the convergence criteria are satisfied, and the results were shown to be accurate and stable. In the second approach, on the contrary, only one full N–R iteration is executed in each BGS iteration, but in this approach, stability is not guaranteed when fewer than three BGS iterations are executed.

The proposed coupling scheme is well suited for use in the general–purpose finite element analysis of the thin piezoelectric bimorph. It was shown that using a combination of solid and shell elements to solve the electrical and structural fields, respectively, with the proposed method of transforming the force, moment, and displacement between the two fields allows for the very accurate simulation of the general electromechanical coupling or both the actuation and the sensing that occurs in the piezoelectric effect.

CHAPTER 4

ELECTRIC–FLUID–STRUCTURE INTERACTION ANALYSIS OF A THIN FLEXIBLE PIEZOELECTRIC BIMORPH IN FLUID

4.1 Introduction

The large deformation of a thin flexible piezoelectric bimorph devices due to the external mechanical forces or applied voltages cause a strong coupling between the electric field and structure. This phenomena, known as electric–structure interaction (ESI) or electro–mechanical coupling of a piezoelectric continuum, has gained a great deal of attention in many sciences and engineering fields. In Chapter 2, the author compared various finite element approaches to study linear electric–structure interaction, in Chapter 3, a novel coupling method to study the nonlinear structure-electric field interaction which can be used to analyze both the actuation and sensing characteristics of a thin flexible piezoelectric bimorph without considering the effect of the surrounding fluid is demonstrated. Since the piezoelectric effect is an electric field–structure interaction phenomenon as described above, the piezoelectric materials surrounded by the fluid is basically electric field and fluid–structure interaction problem, as presented schematically in Figs. 4.1 and 4.2.

The triply coupled phenomenon of electric field and fluid–structure interaction (EFSI) has gained a popular research interest in last couple of years due to the significant engineering applications in piezoelectrically actuated flapping wings [15, 93], flapping wing aerodynamics [17–20], piezoelectric based energy harvesting [3, 13, 94], active control by the piezoelectric materials for fluid–structure interaction problems [95, 96], device miniaturization applications

in MEMS [6, 16] and many. In this section, a coupling strategy for multiphysics analysis of electric field (piezoelectric effect) and fluid–structure interaction using finite element method is presented. Fig. 4.1 shows the schematic representation of ESI, FSI, and EFSI for a piezoelectric bimorph driven by fluid flow and external voltage.

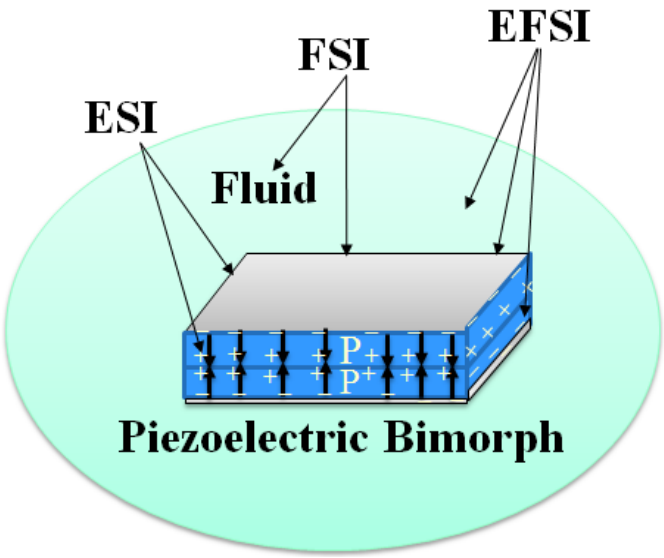

Figure 4.1: Schematic representation a piezoelectric bimorph driven by fluid flow and external voltage.

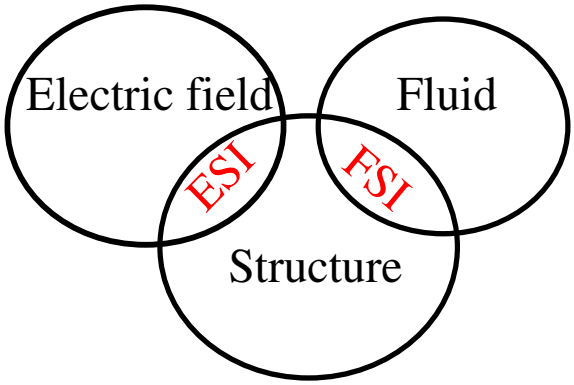

Figure 4.2: Schematic representation a multiphysics coupling of EFSI system

In previous Chapters 2 and 3, coupling analyses of electric field and structure using block Gauss–Seide partitioned iterative method is shown [47, 89]. The implementation of fluid–structure interaction coupling can be done using monolithic approach [97–100] and partitioned approaches [44].

In the monolithic FSI coupling approaches, the fluid and structure equations and the fluid–structure interface conditions (consists of geometrical compatibility and equilibrium conditions on the interface between fluid and structure) are discretized and computed simultaneously. Monolithic approaches for FSI problems are generally known to be robust, accurate and strongly coupled. However, the monolithic approaches are computationally very expensive and monolithic FSI formulation can lead to an ill–conditioned equation system.

In the partitioned FSI coupling approaches, the fluid and structure analyses are conducted separately, and they are coupled via the transformation of their solution variables on the interface. The generally used transformation algorithms are the Dirichlet–Neumann algorithms, wherein the Dirichlet and Neumann boundary conditions (bc's) are imposed on the interface for the fluid and structure, respectively. Furthermore, partitioned approaches are easy for the implementation, easy to reuse existing fluid and structure codes and are appropriate for parallel computation. This is the main reason why partitioned coupling approaches are so popular in FSI analysis.

The partitioned FSI coupling approaches are generally known to be weakly coupled when the interface conditions are not exactly satisfied. Several coupled iteration methods have been widely studied for the partitioned method of the FSI system to enforce the interface conditions. This approach, called as a partitioned iterative approach has been widely investigated to solve fluid–structure interaction problem [48, 101, 102]. In this partitioned iterative approach, the analyses composing of fluid and structure are performed separately and iteratively until the interface condition between the fluid and structure are satisfied in every time step. With this coupled iteration process, the coupling interaction between fluid and structure is expected to be very strong as similar with monolithic approaches. Therefore, partitioned iterative approaches are regarded as strongly coupled methods.

In Ref [50], Ishihara and Horie have proposed a partitioned and splitting algorithm for an incompressible fluid and a structure using a new algebraic splitting method, wherein the monolithic equation system is split into the equilibrium equations and the pressure Poisson equation (PPE) algebraically using the intermediate variables. This is method is also known as the algebraic splitting method or the projection method. The projection method is very popular in fluid analysis and has been successfully used in an incompressible fluid analysis. Therefore, in this study, a projection method [50] to solve fluid–structure interaction coupling is employed. In their study, the projection method for the FSI system is applied for a converging fluid channel with a flexible structure [103, 104], which is one the typical benchmark problem used by many researchers to test the FSI mesh sensitivity, accuracy and convergence properties, and the computational efficiencies of the FSI algorithms [50, 105–107].

Electromagnetic and structure couple problems using monolithic and partitioned algorithms can be found in Refs. [40, 42, 108–110]. These studies were conducted in–order to understand the coupling effect between the electric field and deflections of thin structures in a magnetic damped vibration, which is one type of electromagnetic and structure coupled problem [42]. Triply coupled analysis of elasto–plastic contact, electric current and thermal conduction during resistance spot welding using FEM can be found in [111–114]. There is a large difference between electromagnetic effect, triply coupled phenomenon in resistance spot welding, and the piezoelectric effect in–terms of governing equations and multiphysics theory. These studies cannot solve for direct and inverse piezoelectric effect with fluid–structure interaction.

Several algorithms have been proposed to solve electrostatic–fluid–structure interaction problems using a monolithic approach [115, 116]. The hierarchal decomposed analysis for the electrostatic–fluid–structure interaction was proposed by Ishihara et al. [49]. All these studies were basically intended to solve the electrostatic, fluid, and structure interactions in–order to study micro electrostatic actuation effect in micro–electro–mechanical systems rather than direct and inverse piezoelectric effect in a piezoelectric material. Again, there is a fundamental difference of multiphysics theory and governing equations between electrostatic and the piezoelectric phenomenon. These studies can not solve electro–mechanical coupling in the piezoelectric materials. A few studies for the electrostatic–structure interaction without fluid in MEMS application can be found in [117, 118]. In their studies, a monolithic approach is used. Initially a partitioned approach without coupled iterations was proposed to solve the electrostatic–structure interaction [45] by neglecting the surrounding fluid in MEMS micro electrostatic actuator application.

A few research work on the triply coupled finite element analysis of EFSI system can be found in [94, 95]. In Ref [95], the quadrilateral finite element is used to analyze both the structure and electrostatic field. These elements are not well–suited for the thin structure analysis of the piezoelectric bimorph sensors and actuator. Ravi and Zilian in [94] proposed a monolithic method to solve electric field and fluid–structure interaction of a bimorph beam driven by fluid flow. Although monolithic schemes are strongly coupled by the formulation itself, but are computationally expensive, lead to ill–conditioned monolithic system and produce Schur complement inevitably during fluid–structure interaction problem. In their analysis, they used 3D solid elements to analyze both the structure and electric fields. However, solid elements presented therein are inappropriate for the discretization of the structure in thin–layered MEMS and energy harvesting applications [67, 68, 74]. On the other hand, our proposed method can treat thin–layered structure using shell elements, quadratic electric potential distribution across thickness for any given electric configuration using 3D solid elements to overcome the

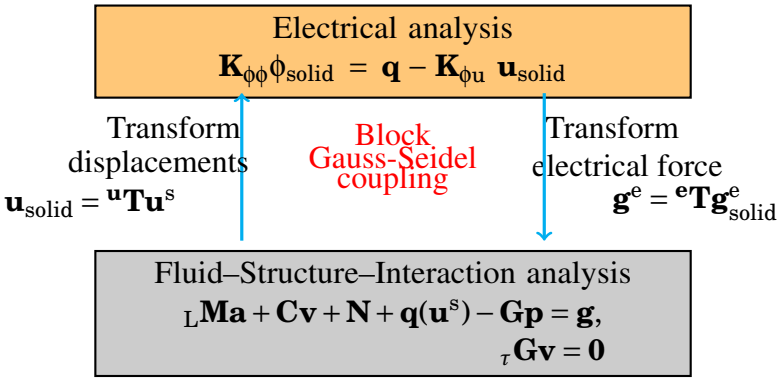

Figure 4.3: Symbolical presentation of Electric field–fluid–structure interaction using Gauss–Seidel coupling

drawbacks of using a same finite element presented in [94, 95].

In this study, a hierarchal decomposition algorithm is proposed to solve for the electric field and fluid–structure interaction. The hierarchal decomposition [49] as the theory is superior to the others in terms of the application to complicated multiphysics problems. In the hierarchal decomposition or partitioned iterative approach, the EFSI system is partitioned into fluid–structure interaction (FSI) and electric field, and then the fluid–structure interaction is partitioned into the fluid–structure velocity field and the pressure field using an algebraic splitting or projection method for FSI system [50], the fluid–structure velocity field is partitioned into fluid velocity field and structure velocity field, and finally the structure and electric field are coupled using block Gauss–Seidel partitioned iterative method for the ESI system. This is the reason why this type of partitioning and the splitting of the EFSI system in a hierarchical way is termed as hierarchal decomposition. The coupling between the electric field and the fluid–structure interaction is executed using the block Gauss–Seidel method is shown schematically in Fig. 4.3.

In the case of large deformation analysis using the Lagrangian description for the structural mechanics, the displacement of the structure changes the domain of the fluid causing large distortion of the computation mesh. The fluid equations have to follow the motion to be able to deal with moving domains. Therefore, Eulerian description is very popular in fluid mechanics. The combination of the Lagrangian and Eulerian description, respectively, for the structure and fluid mechanics, known as arbitrary Lagrangian–Eulerian (ALE) description [119] is used in the present formulation.

The proposed strongly coupled hierarchal decomposition of EFSI system is implemented using finite element method and it is applied to a converging fluid channel with a flexible bimorph actuator. Here, the flexible piezoelectric bimorph flap is made of PVDF or PZT-5H materials and three electric configurations (actuator setup, closed circuit sensor setup, and open

circuit sensor setup) along with the inlet fluid velocity boundary condition in a converging channel as defined in [50, 103, 104] are studied. The simulation results were compared with the reference solution [50]. It follows from the comparisons among the present solution with the reference solution that the proposed strongly coupled method takes into account the full interaction. The simulated frequency responses and vibration amplitudes of a thin flexible piezoelectric bimorphs analyzed using the proposed EFSI method shows a good agreement with the previous studies. The shift in the resonance frequency upon the connected electric resistive load matched well with the theoretical approximations.

4.2 Formulation of the electric field and fluid–structure interaction

In this section, the coupled EFSI equation system from the governing equations of the existing formulation FSI system based on [50] and the piezoelectric equations given inChapter 3 is derived. Basically, the piezoelectric equation are inserted into the FSI coupled system as follows.

4.2.1 Governing equations for the fluid, structure and electric fields

A) Governing equations for the fluid

Let the fluid be an incompressible viscous Newtonian fluid. The fluid flow is governed by the Navier–Stokes equations for incompressible fluids. The arbitrary Lagrangian–Eulerian formulation is employed to describe the incompressible viscous fluid motion in the deformable domain. The ALE description of the incompressible Navier–Stokes equations as the governing equations of the fluid motion [120]:

$$\rho^{\mathrm{f}}\frac{\partial v_i^{\mathrm{f}}}{\partial t}+\rho^{\mathrm{f}}(v_j^{\mathrm{f}}-\hat{v}_j^{\mathrm{f}})\frac{\partial v_i^{\mathrm{f}}}{\partial x_j}=\frac{\partial \sigma_{ji}^{\mathrm{f}}}{\partial x_j}+\rho^{\mathrm{f}}g_i^{\mathrm{f}},\quad \text{in } {}^{t}\Omega^{\mathrm{f}}, \tag{4.1}$$

under the incompressibility constraint

$$\frac{\partial v_i^{\mathrm{f}}}{\partial x_i}=0,\quad \text{in } {}^{t}\Omega^{\mathrm{f}}, \tag{4.2}$$

where superscript f indicates the fluid components, ${}^{t}\Omega^{\mathrm{f}}$ is the spatial fluid domain at time t, ρ^{f} is the density of the fluid, v_i^{f} is the fluid velocity vector, $\hat{v}_i^{\mathrm{f}}$ is the velocity vector of the mesh

deformation in ALE co–ordinate, g_i^{f} is the body force vector acting on the fluid, and σ_{ij}^{f} is the stress tensor of the fluid. The stress tensor σ_{ij}^{f} of Newtonian fluid can be written as

$$\sigma_{ij}^{\mathrm{f}} = -p^{\mathrm{f}}\delta_{ij} + \mu\Big(\frac{\partial v_i^{\mathrm{f}}}{\partial x_j} + \frac{\partial v_j^{\mathrm{f}}}{\partial x_i}\Big), \quad \text{in } {}^t\Omega^{\mathrm{f}}, \tag{4.3}$$

where p^{f} is the pressure, μ is the dynamic viscosity, and δ_{ij} is the Kronecker delta. The Eq.(4.3) relates the fluid stress components to the fluid velocity. To solve for the equilibrium fluid equation Eq.(4.1), one has to specify the essential and natural boundary conditions on the closed boundary of the fluid domain ${}^t\Gamma^{\mathrm{f}}$. The essential or Dirichlet and the natural or Neumann boundary conditions could be imposed at different segments of the boundary ${}^t\Gamma^{\mathrm{f}}$:

$$v_i^{\mathrm{f}} = \bar{v}_i^{\mathrm{f}}, \quad \text{on } \Gamma_{\mathrm{E}}^{\mathrm{f}}, \tag{4.4}$$

$$\sigma_{ij}^{\mathrm{f}}.n_j^{\mathrm{f}} = \tau_i^{\mathrm{f}}, \quad \text{on } \Gamma_{\mathrm{N}}^{\mathrm{f}}, \tag{4.5}$$

where $\Gamma_{\mathrm{E}}^{\mathrm{f}}$ and $\Gamma_{\mathrm{N}}^{\mathrm{f}}$ are complementary subsets of ${}^t\Gamma^{\mathrm{f}}$ corresponding to the Dirichlet– and Neumann–type boundary conditions at time t, $\bar{v}_i^{\mathrm{f}}$ and τ_i^{f} are the prescribed fluid velocity and traction values on the complementary subset of ${}^t\Gamma^{\mathrm{f}}$.

B) Governing equations for the structure

The equilibrium equation of the structure can be written as

$$\rho^{\mathrm{s}}\frac{\mathrm{d}^2 u_i^{\mathrm{s}}}{\mathrm{d}t^2} = \frac{\partial \sigma_{ji}^{\mathrm{s}}}{\partial x_j} + \rho^{\mathrm{s}} g_i^{\mathrm{s}}, \quad \text{on } {}^t\Omega^{\mathrm{s}}, \tag{4.6}$$

where ${}^t\Omega^{\mathrm{s}}$ is the spatial domain of a structure at time t, ρ^{s} is the density of the structure, u_i^{s} is the structural displacement vector, $\dfrac{\mathrm{d}}{\mathrm{d}t}$ is the so–called material derivative, g_i^{s} is the body force vector acting on the structure, and σ_{ij}^{s} is the stress tensor of the structure. While the structure undergoes large deformations causing to geometric nonlinearities, the strains are assumed to be small, thus a materially linear elastic model is assumed. The 2nd Piola–Kirchhoff stress tensor σ_{ij}^{s} of the structure is expressed using the constitutive relation as follows:

$$\sigma_{ij}^{\mathrm{s}} = \lambda\delta_{ij}\frac{\partial u_k^{\mathrm{s}}}{\partial x_k} + G\Big(\frac{\partial u_i^{\mathrm{s}}}{\partial x_j} + \frac{\partial u_j^{\mathrm{s}}}{\partial x_i}\Big), \quad \text{in } {}^t\Omega^{\mathrm{s}}, \tag{4.7}$$

where superscript s indicates components of the elastic structure, λ and G are the Lame constants and u_i^{s} is the structure displacement. In this study, the large deformation formulation of the elastic structure is based on the total Lagrangian framework shown in Chapter 2 which

is based on the derivation given in Ref [71, 72, 87]. For the elastic body, the Dirichlet– and Neumann–type boundary conditions are given by

$$v_i^{\mathrm{s}} = \bar{v}_i^{\mathrm{s}}, \quad \text{on } \Gamma_{\mathrm{E}}^{\mathrm{s}}, \tag{4.8}$$

$$\sigma_{ij}^{\mathrm{s}}.n_j^{\mathrm{s}} = \tau_i^{\mathrm{s}}, \quad \text{on } \Gamma_{\mathrm{N}}^{\mathrm{s}}. \tag{4.9}$$

C) Governing equations of piezoelectricity

The direct and inverse piezoelectric effect of a piezoelectric material is governed by the mechanical and electric equilibrium equations described in Chapter 2. The structural part of the piezoelectric material is solved using equilibrium equation of the structure given in Eq.(4.6) and the electric part is solved using Maxwell's equation of equilibrium for the quasi–static electric field given in Eq.(2.3). By rewriting those equations again as

$$\rho^{\mathrm{p}} \frac{\mathrm{d}^2 u_i^{\mathrm{p}}}{\mathrm{d}t^2} = \frac{\partial \sigma_{ji}^{\mathrm{p}}}{\partial x_j} + \rho^{\mathrm{p}} g_i^{\mathrm{p}}, \quad \text{on } {}^t\Omega^{\mathrm{p}} \tag{4.10}$$

$$\frac{\partial D_i^{\mathrm{p}}}{\partial x_i} = q^{\mathrm{p}}, \quad \text{on } {}^t\Omega^{\mathrm{p}} \tag{4.11}$$

where superscripts p and p stands for the piezoelectric field, D_i^{p} is the electrical displacement vector and q^{p} is the electric body charge. The electric field vector E_i^{p} and a scalar electric potential $\phi_{,i}^{\mathrm{p}}$ are related as

$$E_i^{\mathrm{p}} = -\phi_{,i}^{\mathrm{p}}. \tag{4.12}$$

The constitutive equations of linear piezoelectricity can be written as

$$\sigma_{ij}^{\mathrm{p}} = C_{ijkl}^{E} S_{kl} - e_{kij} E_k^{\mathrm{p}}, \tag{4.13}$$

$$D_i^{\mathrm{p}} = e_{ikl} S_{kl} + \varepsilon_{ik}^{S} E_k^{\mathrm{p}}, \tag{4.14}$$

where C_{ijkl}^{E} is the elastic constitutive tensor, S_{kl} the mechanical strain tensor, e_{kij} the piezoelectric coupling coefficient, E_k the electric field vector, and ε_{ik}^{S} the dielectric permittivity tensor. The superscripts E and S denote that the elastic constants and the dielectric constants are evaluated at a constant electric field and constant strain, respectively. The essential and natural boundary conditions related to the mechanical filed of the piezoelectricity is given in Eqs.(4.8) and (4.9), and similarly, the electrical boundary conditions are written as

$$\phi^{\mathrm{p}} = \bar{\phi}^{\mathrm{p}}, \quad \text{on } \Gamma_{\mathrm{E}}^{\mathrm{p}} \tag{4.15}$$

$$D_i^{\mathrm{p}} n_i = \bar{q}^{\mathrm{p}}, \quad \text{on } \Gamma_{\mathrm{N}}^{\mathrm{p}} \tag{4.16}$$

where $\bar{\phi}^{\mathrm{p}}$ and $\bar{q}^{\mathrm{p}}$ are the prescribed electric potential and surface charge on the piezoelectric boundary corresponding to the Dirichlet– and Neumann–type, respectively; n_i is the outward unit normal vector.

D) Interface conditions

The interaction conditions on the interface between the fluid and the structure are imposed using the following geometric compatibility and equilibrium conditions:

$$v_i^{\mathrm{f}} = v_i^{\mathrm{s}} \equiv v_i^{\mathrm{fs}}, \quad \text{on } \Gamma^{\mathrm{fs}}, \tag{4.17}$$

$$\sigma_{ij}^{\mathrm{f}}.n_j^{\mathrm{f}} + \sigma_{ij}^{\mathrm{s}}.n_j^{\mathrm{s}} = \tau_i^{fs}, \quad \text{on } \Gamma^{\mathrm{fs}}, \tag{4.18}$$

where superscript fs indicates the components of fluid–structure interface, v_i^{fs} is the fluid–structure interface velocity vector, and τ_i^{fs} is the surface force vector acting on the fluid–structure interface. Eq.(4.17), the geometric compatibility, equates the velocity of the fluid with that of the structure velocity at the fluid–structure interface. Eq.(4.18), the equilibrium condition is exactly the continuity of the traction vector at the fluid–structure interface. In the present formulation $v_i^{\mathrm{s}} = v_i^{\mathrm{p}}$, since the structural filed of the piezoelectric effect is solve using the shell elements.

4.2.2 FE formulation of electric–fluid–structure interaction system

In this section, at first, the variational formulations for an incompressible fluid, finite element coupling equations for fluid–structure interaction, finite element coupling equations for nonlinear structure–electric interaction, and final the coupling of FSI system with the piezoelectric electric is presented.

A) FE formulations of fluid–structure interaction using the projection method

A.1) Discretization of fluid

Now, Eqs.(4.1) and (4.2) are discretized to obtain the weak formulation by transforming them into a variational problem. At first, the weak form of incompressible Navier–Stokes equations by using the residual method is obtained. To derive weak form, following the standard procedure, by multiplying the momentum equation Eq.(4.1) with the velocity weight function w_i and the incompressibility constrain Eq.(4.2) is weighted with the pressure weighting function q,

integrate over ${}^t\Omega^{\mathrm{f}}$ to obtain

$$\int_{{}^t\Omega^{\mathrm{f}}} w_i\left(\rho^{\mathrm{f}}\frac{\partial v_i^{\mathrm{f}}}{\partial t}+\rho^{\mathrm{f}}(v_j^{\mathrm{f}}-\hat{v}_j^{\mathrm{f}})\frac{\partial v_i^{\mathrm{f}}}{\partial x_j}-\frac{\partial \sigma_{ji}^{\mathrm{f}}}{\partial x_j}-\rho^{\mathrm{f}}g_i^{\mathrm{f}}\right)\mathrm{d}\Omega^{\mathrm{f}}=0, \tag{4.19}$$

$$\int_{{}^t\Omega^{\mathrm{f}}} q\frac{\partial v_i^{\mathrm{f}}}{\partial x_i}\mathrm{d}\Omega^{\mathrm{f}}=0, \tag{4.20}$$

Rearranging Eq.(4.19) to get

$$\rho^{\mathrm{f}}\int_{{}^t\Omega^{\mathrm{f}}} w_i\frac{\partial v_i^{\mathrm{f}}}{\partial t}\,\mathrm{d}\Omega^{\mathrm{f}}+\rho^{\mathrm{f}}\int_{{}^t\Omega^{\mathrm{f}}} w_i\overset{*}{v}{}_j^{\mathrm{f}}\frac{\partial v_i^{\mathrm{f}}}{\partial x_j}\,\mathrm{d}\Omega^{\mathrm{f}}-\int_{{}^t\Omega^{\mathrm{f}}} w_i\frac{\partial \sigma_{ji}^{\mathrm{f}}}{\partial x_j}\,\mathrm{d}\Omega^{\mathrm{f}}-\rho^{\mathrm{f}}\int_{{}^t\Omega^{\mathrm{f}}} w_i g_i^{\mathrm{f}}\,\mathrm{d}\Omega^{\mathrm{f}}=0, \tag{4.21}$$

where $v_i^{\mathrm{f}}-\hat{v}_i^{\mathrm{f}}=\overset{*}{v}{}_i^{\mathrm{f}}$. The Cauchy stress tensor σ_{ij}^{f} in Eq.(4.21) can be simplified using integration by parts written as

$$\int_{{}^t\Omega^{\mathrm{f}}} w_i\frac{\partial \sigma_{ij}^{\mathrm{f}}}{\partial x_j}\,\mathrm{d}\Omega^{\mathrm{f}}=-\int_{{}^t\Omega^{\mathrm{f}}}\sigma_{ij}^{\mathrm{f}}\frac{\partial w_i}{x_j}\,\mathrm{d}\Omega^{\mathrm{f}}+\int_{{}^t\Gamma^{\mathrm{f}}} w_i\sigma_{ij}^{\mathrm{f}}n_j^{\mathrm{f}}\,\mathrm{d}\Gamma^{\mathrm{f}}. \tag{4.22}$$

Apply the natural boundary condition given in Eq.(4.5) to the last term in the above equation to obtain

$$\int_{{}^t\Omega^{\mathrm{f}}} w_i\frac{\partial \sigma_{ij}^{\mathrm{f}}}{\partial x_j}\,\mathrm{d}\Omega^{\mathrm{f}}=-\int_{{}^t\Omega^{\mathrm{f}}}\sigma_{ij}^{\mathrm{f}}\frac{\partial w_i}{x_j}\,\mathrm{d}\Omega^{\mathrm{f}}+\int_{{}^t\Gamma_{\mathrm{N}}^{\mathrm{f}}} w_i\tau_i^{\mathrm{f}}\,\mathrm{d}\Gamma^{\mathrm{f}}. \tag{4.23}$$

Now substitute Eq.(4.23) into Eq.(4.21) to obtain

$$\rho^{\mathrm{f}}\int_{{}^t\Omega^{\mathrm{f}}} w_i\frac{\partial v_i^{\mathrm{f}}}{\partial t}\,\mathrm{d}\Omega^{\mathrm{f}}+\rho^{\mathrm{f}}\int_{{}^t\Omega^{\mathrm{f}}} w_i\overset{*}{v}{}_j^{\mathrm{f}}\frac{\partial v_i^{\mathrm{f}}}{\partial x_j}\,\mathrm{d}\Omega^{\mathrm{f}}+\int_{{}^t\Omega^{\mathrm{f}}}\sigma_{ij}^{\mathrm{f}}\frac{\partial w_i}{x_j}\,\mathrm{d}\Omega^{\mathrm{f}}-\int_{{}^t\Gamma_{\mathrm{N}}^{\mathrm{f}}} w_i\tau_i^{\mathrm{f}}\,\mathrm{d}\Gamma^{\mathrm{f}}-\rho^{\mathrm{f}}\int_{{}^t\Omega^{\mathrm{f}}} w_i g_i^{\mathrm{f}}\,\mathrm{d}\Omega^{\mathrm{f}}=0, \tag{4.24}$$

Introducing the fluid stress tensor σ_{ij}^{f} given in Eq.(4.3) into the above equation gives

$$\rho^{\mathrm{f}}\int_{{}^t\Omega^{\mathrm{f}}} w_i\frac{\partial v_i^{\mathrm{f}}}{\partial t}\,\mathrm{d}\Omega^{\mathrm{f}}+\rho^{\mathrm{f}}\int_{{}^t\Omega^{\mathrm{f}}} w_i\overset{*}{v}{}_j^{\mathrm{f}}\frac{\partial v_i^{\mathrm{f}}}{\partial x_j}\,\mathrm{d}\Omega^{\mathrm{f}}+\int_{{}^t\Omega^{\mathrm{f}}}\left\{-p^{\mathrm{f}}\delta_{ij}+\mu\left(\frac{\partial v_i^{\mathrm{f}}}{\partial x_j}+\frac{\partial v_j^{\mathrm{f}}}{\partial x_i}\right)\right\}\frac{\partial w_i}{x_j}\,\mathrm{d}\Omega^{\mathrm{f}}$$
$$=\int_{{}^t\Gamma_{\mathrm{N}}^{\mathrm{f}}} w_i\tau_i^{\mathrm{f}}\,\mathrm{d}\Gamma^{\mathrm{f}}+\rho^{\mathrm{f}}\int_{{}^t\Omega^{\mathrm{f}}} w_i g_i^{\mathrm{f}}\,\mathrm{d}\Omega^{\mathrm{f}}, \tag{4.25}$$

Rearranging the above equation gives

$$\rho^{\mathrm{f}} \int_{{}^{t}\Omega^{\mathrm{f}}} w_i \frac{\partial v_i^{\mathrm{f}}}{\partial t}\,\mathrm{d}\Omega^{\mathrm{f}} + \rho^{\mathrm{f}} \int_{{}^{t}\Omega^{\mathrm{f}}} w_i \overset{*}{v}{}_j^{\mathrm{f}} \frac{\partial v_i^{\mathrm{f}}}{\partial x_j}\,\mathrm{d}\Omega^{\mathrm{f}} - \int_{{}^{t}\Omega^{\mathrm{f}}} \frac{\partial w_i^{\mathrm{f}}}{\partial x_j} p^{\mathrm{f}} \delta_{ij}\,\mathrm{d}\Omega^{\mathrm{f}}$$
$$+ \mu\left\{\left(\int_{{}^{t}\Omega^{\mathrm{f}}} \frac{\partial w_i^{\mathrm{f}}}{\partial x_j}\frac{\partial v_i^{\mathrm{f}}}{\partial x_j}\,\mathrm{d}\Omega^{\mathrm{f}}\right) + \left(\int_{{}^{t}\Omega^{\mathrm{f}}} \frac{\partial w_i^{\mathrm{f}}}{\partial x_j}\frac{\partial v_j^{\mathrm{f}}}{\partial x_i}\,\mathrm{d}\Omega^{\mathrm{f}}\right)\right\} = \int_{{}^{t}\Gamma_{\mathrm{N}}^{\mathrm{f}}} w_i \tau_i^{\mathrm{f}}\,\mathrm{d}\Gamma^{\mathrm{f}} + \rho^{\mathrm{f}} \int_{{}^{t}\Omega^{\mathrm{f}}} w_i g_i^{\mathrm{f}}\,\mathrm{d}\Omega^{\mathrm{f}}, \quad (4.26)$$

Eqs.(4.20) and (4.26) provides the basis for the finite element formulation of the incompressible Navier–Stokes equations. The approximation solutions for the fluid velocity and pressure will now be defined using the finite element procedure. The usual assumptions to approximate the weak variational equation using the finite element method is a discretization of the weak formulation. In general, the continuous fluid domain Ω^{f} is discretized into a number of elements forming a union $\bar{\Omega}^{\mathrm{f}}$ of elements $\Omega_{\mathrm{e}}^{\mathrm{f}}$

$$\Omega^{\mathrm{f}} \approx \bar{\Omega}^{\mathrm{f}} = \bigcup_{\mathrm{e}} \Omega_{\mathrm{e}}^{\mathrm{f}}, \quad (4.27)$$

where $\bar{\Omega}^{\mathrm{f}}$ is an approximation of Ω^{f}, and the sum over e is taken over the total number of elements. In FEM, the approximation solution is expressed as a function of a set of interpolation functions. Let us now introduce the standard FE interpolation of the fluid velocity and pressure fields given as

$$v_i^{\mathrm{f}} = \sum_{\alpha=1}^{n} N_\alpha v_{\alpha i}^{\mathrm{f}}), \quad (4.28)$$

$$p^{\mathrm{f}} = \sum_{\alpha=1}^{m} M_\alpha p_\alpha^{\mathrm{f}}, \quad (4.29)$$

where N_α and M_α are the shape functions interpolating the fluid velocities v_i^{f} and pressure p^{f} within each element, v_i^{f} and p_α denotes the nodal velocity and pressure, respectively. The summing is carried out over the total number of fluid velocity nodes n and the total number of pressure nodes m. By substituting the approximations Eqs.(4.28) and (4.29) into the weak form of fluid momentum equation Eq.(4.26) and continuity equation Eq.(4.20), respectively to obtain

$$\rho^{\mathrm{f}}\left(\int_{{}^{t}\Omega^{\mathrm{f}}} w_i N_\beta \mathrm{d}\Omega^{\mathrm{f}}\right)\frac{\partial v_{\beta i}^{\mathrm{f}}}{\partial t} + \rho^{\mathrm{f}}\left(\int_{{}^{t}\Omega^{\mathrm{f}}} w_i N_\beta \frac{\partial N_\gamma}{\partial x_j}\mathrm{d}\Omega^{\mathrm{f}}\right)\overset{*}{v}{}_{\beta j}^{\mathrm{f}} v_{\gamma i}^{\mathrm{f}} - \left(\int_{{}^{t}\Omega^{\mathrm{f}}} \frac{\partial w_i}{\partial x_j} M_\beta \delta_{ij}\mathrm{d}\Omega^{\mathrm{f}}\right)p_\beta^{\mathrm{f}}$$
$$+ \left[\mu\left(\int_{{}^{t}\Omega^{\mathrm{f}}} \frac{\partial w_i}{\partial x_j}\frac{\partial N_\beta}{\partial x_j}\mathrm{d}\Omega^{\mathrm{f}}\right)v_{\beta i}^{\mathrm{f}} + \mu\left(\int_{{}^{t}\Omega^{\mathrm{f}}} \frac{\partial w_i}{\partial x_j}\frac{\partial N_\gamma}{\partial x_i}\mathrm{d}\Omega^{\mathrm{f}}\right)v_{\gamma j}^{\mathrm{f}}\right] = \int_{{}^{t}\Gamma_{\mathrm{N}}^{\mathrm{f}}} w_i \tau_i^{\mathrm{f}}\mathrm{d}\Gamma^{\mathrm{f}} + \rho^{\mathrm{f}}\int_{{}^{t}\Omega^{\mathrm{f}}} w_i g_i^{\mathrm{f}}\mathrm{d}\Omega^{\mathrm{f}}, \quad (4.30)$$

$$\left(\int_{{}^{t}\Omega^{\mathrm{f}}} q\frac{\partial N_\beta}{\partial x_i}\mathrm{d}\Omega^{\mathrm{f}}\right)v_{\beta i}^{\mathrm{f}} = 0, \quad (4.31)$$

Using the standard Galerkin method, the weighting functions are chosen to be the same as the shape functions interpolating the fluid velocity and pressure with $w_i = N_\alpha$ and $q = M_\alpha$, respectively. By summing over all the elements leads to the following finite element equation system

$$\sum_e \rho^{\mathrm{f}}\left(\int_{{}^t\Omega_e^{\mathrm{f}}} N_\alpha N_\beta \mathrm{d}\Omega^{\mathrm{f}}\right)\frac{\partial v_{\beta i}^{\mathrm{f}}}{\partial t} + \sum_e \rho^{\mathrm{f}}\left(\int_{{}^t\Omega_e^{\mathrm{f}}} N_\alpha N_\beta \frac{\partial N_\gamma}{\partial x_j}\mathrm{d}\Omega^{\mathrm{f}}\right)\overset{*}{v}{}_{\beta j}^{\mathrm{f}} v_{\gamma i}^{\mathrm{f}} + \sum_e \left[\mu\left(\int_{{}^t\Omega_e^{\mathrm{f}}} \frac{\partial N_\alpha}{\partial x_j}\frac{\partial N_\beta}{\partial x_j}\mathrm{d}\Omega^{\mathrm{f}}\right)v_{\beta i}^{\mathrm{f}} + \mu\left(\int_{{}^t\Omega_e^{\mathrm{f}}} \frac{\partial N_\alpha}{\partial x_j}\frac{\partial N_\gamma}{\partial x_i}\mathrm{d}\Omega^{\mathrm{f}}\right)v_{\gamma j}^{\mathrm{f}}\right] - \sum_e\left(\int_{{}^t\Omega_e^{\mathrm{f}}} \frac{\partial N_\alpha}{\partial x_j} M_\beta \delta_{ij}\mathrm{d}\Omega^{\mathrm{f}}\right)p_\beta^{\mathrm{f}} = \int_{{}^t\Gamma_{\mathrm{N}}^{\mathrm{f}}} N_\alpha \tau_i^{\mathrm{f}}\mathrm{d}\Gamma^{\mathrm{f}} + \int_{{}^t\Omega^{\mathrm{f}}} N_\alpha b_i^{\mathrm{f}}\mathrm{d}\Omega^{\mathrm{f}}, \tag{4.32}$$

$$\left(\int_{{}^t\Omega_e^{\mathrm{f}}} M_\alpha \frac{\partial N_\beta}{\partial x_i}\mathrm{d}\Omega^{\mathrm{f}}\right)v_{\beta i}^{\mathrm{f}} = 0, \tag{4.33}$$

Eqs.(4.32) and (4.33) can be written in index form as

$$M_{\alpha\beta}^{\mathrm{f}}\frac{\partial v_{\beta i}^{\mathrm{f}}}{\partial t} + N_{\alpha\beta\gamma j}^{\mathrm{f}}\overset{*}{v}{}_{\beta j}^{\mathrm{f}} v_{\gamma i}^{\mathrm{f}} + \left[C_{\alpha\beta}^{\mathrm{f}} v_{\beta i}^{f} + C_{\alpha\beta j i}^{\mathrm{f}} v_{\gamma j}^{\mathrm{f}}\right] - G_{\alpha\beta i}^{\mathrm{f}} = g_{\alpha i}^{\mathrm{f}}, \tag{4.34}$$

$$G_{\beta\alpha}^{i} v_{\beta i}^{\mathrm{f}} = 0, \tag{4.35}$$

with

$$M_{\alpha\beta}^{\mathrm{f}} = \sum_e \rho^{\mathrm{f}}\int_{{}^t\Omega_e^{\mathrm{f}}} N_\alpha N_\beta \mathrm{d}\Omega^{\mathrm{f}} \tag{4.36a}$$

$$N_{\alpha\beta\gamma j}^{\mathrm{f}} = \sum_e \rho^{\mathrm{f}}\int_{{}^t\Omega_e^{\mathrm{f}}} N_\alpha N_\beta \frac{\partial N_\gamma}{\partial x_j}\mathrm{d}\Omega^{\mathrm{f}} \tag{4.36b}$$

$$C_{\alpha\beta}^{\mathrm{f}} = \sum_e \mu\int_{{}^t\Omega_e^{\mathrm{f}}} \frac{\partial N_\alpha}{\partial x_j}\frac{\partial N_\beta}{\partial x_j}\mathrm{d}\Omega^{\mathrm{f}} \tag{4.36c}$$

$$C_{\alpha\beta j i}^{\mathrm{f}} = \sum_e \mu\int_{{}^t\Omega_e^{\mathrm{f}}} \frac{\partial N_\alpha}{\partial x_j}\frac{\partial N_\gamma}{\partial x_i}\mathrm{d}\Omega^{\mathrm{f}} \tag{4.36d}$$

$$G_{\alpha\beta i}^{\mathrm{f}} = \sum_e \int_{{}^t\Omega_e^{\mathrm{f}}} \frac{\partial N_\alpha}{\partial x_j} M_\beta \delta_{ij}\mathrm{d}\Omega^{\mathrm{f}} \tag{4.36e}$$

$$G_{\beta\alpha}^{i} = \int_{{}^t\Omega^{\mathrm{f}}} M_\alpha \frac{\partial N_\beta}{\partial x_i}\mathrm{d}\Omega^{\mathrm{f}} \tag{4.36f}$$

$$g^{\mathrm{f}}_{\alpha i} = \int_{{}^{t}\Gamma^{\mathrm{f}}_{\mathrm{N}}} N_\alpha \tau^{\mathrm{f}}_i \mathrm{d}\Gamma^{\mathrm{f}} + \int_{{}^{t}\Omega^{\mathrm{f}}} N_\alpha b^{\mathrm{f}}_i \mathrm{d}\Omega^{\mathrm{f}} \tag{4.36g}$$

Eqs.(4.32) and (4.33) can be expressed in global finite element matrices[50]:

$$\mathbf{Q}^{\mathrm{f}} \equiv_{\mathrm{L}} \mathbf{M}^{\mathrm{f}}\mathbf{a}^{\mathrm{f}} + \mathbf{N}^{\mathrm{f}} + \mathbf{C}^{\mathrm{f}}\mathbf{v}^{\mathrm{f}} + \mathbf{V}^{\mathrm{f}} - \mathbf{G}^{\mathrm{f}}\mathbf{P}^{\mathrm{f}} = \mathbf{g}^{\mathrm{f}}, \tag{4.37}$$

$${}_{\mathrm{T}}\mathbf{G}^{\mathrm{f}}\mathbf{v}^{\mathrm{f}} = \mathbf{0}, \tag{4.38}$$

where $\mathbf{M}^{\mathrm{f}}$ is the mass matrix of the fluid, $\mathbf{N}^{\mathrm{f}}$ is the convective term vector of the fluid, $\mathbf{C}^{\mathrm{f}}$ is the diffusion matrix of the fluid, $\mathbf{G}^{\mathrm{f}}$ is the divergence operator matrix of the fluid, $\mathbf{a}^{\mathrm{f}}$ is the acceleration vector of the fluid, $\mathbf{v}^{\mathrm{f}}$ is the velocity vector of the fluid, $\mathbf{P}^{\mathrm{f}}$ is the pressure vector of the fluid, $\mathbf{g}^{\mathrm{f}}$ is the external force vector acting on the fluid, $\mathbf{Q}^{\mathrm{f}}$ is the equivalent internal force vector including all effects of the fluid, the subscript L stands for lumping of the matrix, and the subscript T stands for transpose of the matrix. In ALE formulation, the fluid convective term $\mathbf{N}^{\mathrm{f}}$ is expressed as $\mathbf{N}^{\mathrm{f}}(\mathbf{v}^{\mathrm{f}} - \hat{\mathbf{v}}^{\mathrm{f}})\mathbf{v}^{\mathrm{f}}$. In this study, a continuous linear velocity and pressure (P1P1) element is used for incompressible fluid analysis. The stabilization formulation streamline–upwind/Petrov–Galerkin (SUPG) formulations [121] and the pressure–stabilizing/Petrov–Galerkin (PSPG) [122, 123] for incompressible flows are adopted to avoid numerical stability due to the fluid convection and the P1P1 element. These stabilization formulations bring numerical stability in the computation of high Reynolds fluid flow problems and improve the convergence rate in iterative solution of coupled nonlinear equation systems.

A.2) Discretization of the structure

The FE equations for the structure to the total Lagrangian formulation of the Eq.(4.6) is presented in Section 3.2.2 for the shell element using mixed interpolation of tensorial components (MITC) approach [71–73]. The linearized equation of motion for the structure in T.L formulation [72] is given as

$$\int_{{}_0\Omega} {}_0\tilde{C}^{ijkl}\, {}_0\tilde{e}_{kl}\delta\, {}_0\tilde{e}_{ij} d^0\Omega + \int_{{}_0\Omega} {}^{t}_0\tilde{\sigma}^{ij}\delta\, {}_0\tilde{\eta}_{ij} d^0\Omega = {}^{t+\Delta t}R - \int_{{}_0\Omega} {}^{t}_0\tilde{\sigma}^{ij}\delta\, {}_0\tilde{e}_{ij} d^0\Omega. \tag{4.39}$$

Equation (4.39) is the completely linearized equation of motion in T.L formulation and it is the basic equation used for the isoparametric formulation of finite element analysis of the structure. The equilibrium equation of the structure in matrix form using finite element formulation can be written as follows.

$$\mathbf{Q}^{\mathrm{s}} \equiv_{\mathrm{L}} \mathbf{M}^{\mathrm{s}}\mathbf{a}^{\mathrm{s}} + \mathbf{q}^{\mathrm{s}}(\mathbf{u}^{\mathrm{s}}) = \mathbf{g}^{\mathrm{s}}, \tag{4.40}$$

where $\mathbf{M}^{\mathrm{s}}$ is the mass matrix of the structure, $\mathbf{q}^{\mathrm{s}}$ is the internal force vector, $\mathbf{a}^{\mathrm{s}}$ is the acceleration vector of the structure, $\mathbf{u}^{\mathrm{s}}$ is the displacement vector of the structure, $\mathbf{g}^{\mathrm{s}}$ is the external force vector applied to the structure, $\mathbf{Q}^{\mathrm{s}}$ is the equivalent internal force vector including all effects of the structure. In this work, the thin flexible structure is solved using the shell finite element. As the MEMS structures usually are quite thin and undergo large deformations, shell elements are very well suited for the structural discretization.

A.3) FE equations of interface conditions

The geometric compatibility condition Eq.(4.17) and equilibrium condition Eq.(4.18) on the fluid–structure interaction can be written in vector form, respectively, as

$$\mathbf{v}_{\mathrm{c}}^{fs} \equiv \mathbf{v}_{\mathrm{c}}^{\mathrm{f}} = \mathbf{v}_{\mathrm{c}}^{\mathrm{s}}, \tag{4.41}$$

and

$$\mathbf{Q}_{\mathrm{c}}^{\mathrm{f}} = \mathbf{Q}_{\mathrm{c}}^{\mathrm{s}} \equiv \mathbf{g}_{\mathrm{c}}^{fs}, \tag{4.42}$$

where subscript $\mathbf{c}$ indicates the coupled degrees of freedoms.

A.4) Coupled fluid–structure interaction equation system: Projection method

The spatially discretized Navier–Stokes fluid Eqs.(4.37) and (4.38), and structural equilibrium Eq.(4.40) can be written as the following monolithic system[50]:

$$\mathbf{Q} \equiv {}_{\mathrm{L}}\mathbf{M}\mathbf{a} + \mathbf{C}\mathbf{v} + \mathbf{N} + \mathbf{q}(\mathbf{u}) - \mathbf{G}\mathbf{p} = \mathbf{g}, \tag{4.43}$$

$${}_{\mathrm{T}}\mathbf{G}\mathbf{v} = 0. \tag{4.44}$$

The definition of each of the matrices and the vectors appearing in Eqs.(4.43) and (4.44) are defined as

$${}_{\mathrm{L}}\mathbf{M} \equiv \begin{bmatrix} {}_{\mathrm{L}}\mathbf{M}_{dd}^{\mathrm{f}} & 0 & 0 \\ 0 & {}_{\mathrm{L}}\mathbf{M}_{cc}^{\mathrm{fs}} & 0 \\ 0 & 0 & {}_{\mathrm{L}}\mathbf{M}_{dd}^{\mathrm{s}} \end{bmatrix}, \quad \mathbf{C} \equiv \begin{bmatrix} \mathbf{C}_{dd}^{\mathrm{f}} & \mathbf{C}_{dc}^{\mathrm{f}} & 0 \\ \mathbf{C}_{cd}^{\mathrm{f}} & \mathbf{C}_{cc}^{\mathrm{f}} & 0 \\ 0 & 0 & \mathbf{C}_{dd}^{\mathrm{s}} \end{bmatrix}, \quad \mathbf{G} \equiv \begin{bmatrix} \mathbf{G}_{d}^{\mathrm{f}} \\ \mathbf{G}_{c}^{\mathrm{f}} \\ 0 \end{bmatrix},$$

$$\mathbf{q}(\mathbf{u}) \equiv \begin{Bmatrix} 0 \\ \mathbf{q}_{c}^{\mathrm{s}}(\mathbf{u}^{\mathrm{s}}) \\ \mathbf{q}_{d}^{\mathrm{s}}(\mathbf{u}^{\mathrm{s}}) \end{Bmatrix}, \quad \mathbf{N} \equiv \begin{Bmatrix} \mathbf{N}_{d}^{\mathrm{f}} \\ \mathbf{N}_{c}^{\mathrm{f}} \\ 0 \end{Bmatrix}, \quad \mathbf{g} \equiv \begin{Bmatrix} \mathbf{g}_{d}^{\mathrm{f}} \\ \mathbf{g}_{c}^{\mathrm{fs}} \\ \mathbf{g}_{d}^{\mathrm{s}} \end{Bmatrix},$$

$$\mathbf{a} \equiv \begin{Bmatrix} \mathbf{a}_d^{\mathrm{f}} \\ \mathbf{a}_c^{\mathrm{fs}} \\ \mathbf{a}_d^{\mathrm{s}} \end{Bmatrix}, \quad \mathbf{v} \equiv \begin{Bmatrix} \mathbf{v}_d^{\mathrm{f}} \\ \mathbf{v}_c^{\mathrm{fs}} \\ \mathbf{v}_d^{\mathrm{s}} \end{Bmatrix}, \quad \mathbf{u} \equiv \begin{Bmatrix} * \\ \mathbf{u}_c^{\mathrm{fs}} \\ \mathbf{u}_d^{\mathrm{s}} \end{Bmatrix},$$
$$\mathbf{p} \equiv \mathbf{p}^{\mathrm{f}}, \quad {}_{\mathrm{L}}\mathbf{M}_{cc}^{\mathrm{fs}} \equiv {}_{\mathrm{L}}\mathbf{M}_{cc}^{\mathrm{f}} + {}_{\mathrm{L}}\mathbf{M}_{cc}^{\mathrm{s}}, \tag{4.45a–k}$$

where subscript d indicates uncoupled degrees of freedoms. The time integration of the incompressible finite element fluid–structure interaction system is based on the predictor–multi–corrector algorithm (PMA)[120, 121]. The PMA is based on the Newmark' β method. Let us consider the nonlinear iteration for the Eqs.(4.43) and (4.44) at the current time $t + \Delta t$ as

$${}_{\mathrm{L}}\mathbf{M}\ {}^{t+\Delta t}\mathbf{a}^{(k)} + \mathbf{C}\ {}^{t+\Delta t}\mathbf{v}^{(k)} + \mathbf{N} + \mathbf{q}\left({}^{t+\Delta t}\mathbf{u}^{(k)}\right) - \mathbf{G}\ {}^{t+\Delta t}\mathbf{p}^{(k)} = \mathbf{g}, \tag{4.46a}$$
$${}_{\mathrm{T}}\mathbf{G}\ {}^{t+\Delta t}\mathbf{v}^{(k)} = \mathbf{0}. \tag{4.46b}$$

During the predictor stage of the PMA, the acceleration, velocity, displacement and pressure at time $t + \Delta t$ are first predicted using those at time t, respectively, as

$${}^{t+\Delta t}\mathbf{a}^{(0)} = 0, \tag{4.47a}$$
$${}^{t+\Delta t}\mathbf{v}^{(0)} = {}^{t}\mathbf{v} + \Delta t(1-\gamma)\ {}^{t}\mathbf{a}, \tag{4.47b}$$
$${}^{t+\Delta t}\mathbf{u}^{(0)} = {}^{t}\mathbf{u} + \Delta t\ {}^{t}\mathbf{v} + \Delta t^2(1/2-\beta)\ {}^{t}\mathbf{a}, \tag{4.47c}$$
$${}^{t+\Delta t}\mathbf{p}^{(0)} = {}^{t}\mathbf{p}, \tag{4.47d}$$

where ${}^{t}\mathbf{a}$, ${}^{t}\mathbf{v}$, ${}^{t}\mathbf{u}$, and ${}^{t}\mathbf{p}$ are the known acceleration, velocity, displacement, and pressure which are obtained from the last time step t, β and γ are the Newmark's parameters that can be chosen so as to obtain numerical stability and integration accuracy, and Δt is the time increment.

The monolithic FSI equation system shown in Eqs.(4.46a) and (4.46b) at time $t + \Delta$ are nonlinear equations. These nonlinear equation system can be linearized using the increments of the accelerations $\Delta\mathbf{a}$, velocity $\Delta\mathbf{v}$, displacement $\Delta\mathbf{u}$, and pressure $\Delta\mathbf{p}$. These increments are obtained from the state variables from the previous nonlinear iteration $k-1$ to the current iteration k during the corrector stage of the PMA method defined as [50],

$${}^{t+\Delta t}\mathbf{a}^{(k)} = {}^{t+\Delta t}\mathbf{a}^{(k-1)} + \Delta\mathbf{a}, \tag{4.48a}$$
$${}^{t+\Delta t}\mathbf{v}^{(k)} = {}^{t+\Delta t}\mathbf{v}^{(k-1)} + \Delta\mathbf{v} = {}^{t+\Delta t}\mathbf{v}^{(k-1)} + \gamma\Delta t\Delta\mathbf{a}, \tag{4.48b}$$
$${}^{t+\Delta t}\mathbf{u}^{(k)} = {}^{t+\Delta t}\mathbf{u}^{(k-1)} + \Delta\mathbf{u} = {}^{t+\Delta t}\mathbf{v}^{(k-1)} + \beta\Delta t^2\Delta\mathbf{a}, \tag{4.48c}$$
$${}^{t+\Delta t}\mathbf{p}^{(k)} = {}^{t+\Delta t}\mathbf{p}^{(k-1)} + \Delta\mathbf{p}. \tag{4.48d}$$

Substituting Eqs. (4.48a)–(4.48d) into Eq.(4.46), the following linearized equations in residual form are obtained

$$\mathbf{M}^{*}\Delta\mathbf{a} - \mathbf{G}\Delta\mathbf{p} = \Delta\mathbf{g}, \tag{4.49a}$$

$$\gamma\Delta t\ {}_{\mathrm{T}}\mathbf{G}\Delta\mathbf{a} + \mathbf{G}_{\varepsilon}\Delta\mathbf{p} = \Delta\mathbf{h}. \tag{4.49b}$$

where $\mathbf{M}^{*}$ is the generalized mass matrix , $\Delta\mathbf{g}$ and $\Delta\mathbf{h}$ are the residual force vectors, Δ indicates the increment, and $\mathbf{G}_{\varepsilon}$ is come from the pressure stabilization term of the pressure–stabilizing/Petrov–Galerkin (PSPG) [122, 123] for incompressible flows. The definition of $\mathbf{M}^{*}$ for the implicit, explicit, and implicit and explicit treatment of the fluid convection term $\mathbf{N}$ and the fluid diffusion term $\mathbf{C}$ can be found in Ref [50, 99].

If the fluid convection and diffusion terms are treated implicitly then

$$\mathbf{M}^{*} \equiv_{\mathrm{L}} \mathbf{M} + \gamma\Delta t(\tilde{\mathbf{N}} + \mathbf{C}) + \beta\Delta^{2}\mathbf{K}. \tag{4.50}$$

In case the fluid convection and diffusion terms are treated explicitly then

$$\mathbf{M}^{*} \equiv_{\mathrm{L}} \mathbf{M} + \beta\Delta^{2}\mathbf{K}. \tag{4.51}$$

If the fluid convection term is treated explicitly, and the fluid diffusion term is treated implicitly then

$$\mathbf{M}^{*} \equiv_{\mathrm{L}} \mathbf{M} + \gamma\Delta t\mathbf{C} + \beta\Delta^{2}\mathbf{K}. \tag{4.52}$$

The FSI monolithic system Eq.(4.49) is very strongly coupled method. However, the monolithic approach is computationally expensive and monolithic formulations can lead to ill–conditioned equation system [99, 100]. But in the projection method, the monolithic equation systems for the FSI system is split into its subsystems algebraically [50]. In the algebraic splitting method proposed by Ishihara and Horie [50], the fluid–structure interaction is split into the fluid–structure velocity field and the fluid pressure field. This method is computationally efficient and avoids Schur complement without loss of robustness. This method has been successfully used for fluid–structure interaction analysis in the flapping flexible wing analysis [2, 20] and hierarchal decomposition of the structure–fluid–electrostatic interaction in a MEMS micro cantilever [49]. Therefore, in this study, the projection method proposed in Ref. [50] is used. The summary of the projection method is as follows:

From the fluid–structure interaction equilibrium Eq.(4.46a), the state variables is predicted as the intermediate state variables for the known fluid pressure ${}^{t+\Delta t}\mathbf{p}^{(k-1)}$. Then, Eq.(4.46a) is linearized as

$$\mathbf{M}^{*}\Delta\hat{\mathbf{a}} = \Delta\mathbf{g}, \tag{4.53}$$

where the intermediate state variables and their increments are described as

$$^{t+\Delta t}\hat{\mathbf{a}}^{(k)} = {}^{t+\Delta t}\mathbf{a}^{(k-1)} + \Delta\hat{\mathbf{a}}, \tag{4.54a}$$

$$^{t+\Delta t}\hat{\mathbf{v}}^{(k)} = {}^{t+\Delta t}\mathbf{v}^{(k-1)} + \Delta\hat{\mathbf{v}} = {}^{t+\Delta t}\mathbf{v}^{(k-1)} + \gamma\Delta t\Delta\hat{\mathbf{a}}, \tag{4.54b}$$

$$^{t+\Delta t}\hat{\mathbf{u}}^{(k)} = {}^{t+\Delta t}\mathbf{u}^{(k-1)} + \Delta\hat{\mathbf{u}} = {}^{t+\Delta t}\mathbf{v}^{(k-1)} + \beta\Delta t^{2}\Delta\hat{\mathbf{a}}, \tag{4.54c}$$

where $^{t+\Delta t}\hat{\mathbf{a}}^{(k)}$, $^{t+\Delta t}\hat{\mathbf{v}}^{(k)}$ and $^{t+\Delta t}\hat{\mathbf{u}}^{(k)}$ are the intermediate or predicted acceleration, velocity and displacement, respectively. Subtracting both sides of Eq.(4.53) from Eq.(4.49a), after suitable arrangement,

$$\gamma\Delta t\mathbf{G}\Delta\mathbf{p} = \mathbf{M}^{*}\left({}^{t+\Delta t}\mathbf{v}^{(k)} - {}^{t+\Delta t}\hat{\mathbf{v}}^{(k)}\right). \tag{4.55}$$

By left multiplying both sides of Eq.(4.55) with ${}_{\mathrm{T}}\mathbf{G}_{\mathrm{L}}\mathbf{M}^{-1}$ to obtain,

$$\gamma\Delta t\ {}_{\mathrm{T}}\mathbf{G}_{\mathrm{L}}\mathbf{M}^{-1}\mathbf{G}\Delta\mathbf{p} = {}_{\mathrm{T}}\mathbf{G}^{t+\Delta t}\mathbf{v}^{(k)} - {}_{\mathrm{T}}\mathbf{G}^{t+\Delta t}\hat{\mathbf{v}}^{(k)} + {}_{\mathrm{T}}\mathbf{G}_{\mathrm{L}}\mathbf{M}^{-1}\overline{\mathbf{M}}^{*}\left({}^{t+\Delta t}\mathbf{v}^{(k)} - {}^{t+\Delta t}\hat{\mathbf{v}}^{(k)}\right), \tag{4.56}$$

where $\overline{\mathbf{M}}^{*} = \mathbf{M}^{*} - {}_{\mathrm{L}}\mathbf{M}$. If the following pressure Poisson equation (PPE),

$$\gamma\Delta t\ {}_{\mathrm{T}}\mathbf{G}_{\mathrm{L}}\mathbf{M}^{-1}\mathbf{G}\Delta\mathbf{p} = -{}_{\mathrm{T}}\mathbf{G}^{t+\Delta t}\hat{\mathbf{v}}^{(k)}, \tag{4.57}$$

is solved, then Eq.(4.56) is reduced as

$${}_{\mathrm{T}}\mathbf{G}^{t+\Delta t}\mathbf{v}^{(k)} + {}_{\mathrm{T}}\mathbf{G}_{\mathrm{L}}\mathbf{M}^{-1}\overline{\mathbf{M}}^{*}\left({}^{t+\Delta t}\mathbf{v}^{(k)} - {}^{t+\Delta t}\hat{\mathbf{v}}^{(k)}\right) = \mathbf{0}. \tag{4.58}$$

When the nonlinear iterations are convergent, the predicted velocity $^{t+\Delta t}\hat{\mathbf{v}}^{(k)}$ agrees with $^{t+\Delta t}\mathbf{v}^{(k)}$ asymptotically as

$$\left|\ {}^{t+\Delta t}\mathbf{v}^{(k)} - {}^{t+\Delta t}\hat{\mathbf{v}}^{(k)}\ \right| \to 0 \qquad \text{as} \qquad k \to \mathbf{0} \tag{4.59}$$

The second term of the Eq.(4.58) will vanish asymptotically in the nonlinear iterations, and the incompressibility constraint for the current fluid velocity $^{t+\Delta t}\mathbf{v}^{(k)}$ is satisfied as

$${}_{\mathrm{T}}\mathbf{G}^{t+\Delta t}\mathbf{v}^{(k)} = \mathbf{0}. \tag{4.60}$$

In summary, Eq.(4.53) is solved to determine the increment of the intermediate acceleration $\Delta\hat{\mathbf{a}}$ for the previous pressure. Once $\Delta\hat{\mathbf{a}}$ is evaluated, then the intermediate velocity $^{t+\Delta t}\hat{\mathbf{v}}^{(k)}$ is solved using Eq.(4.54b). After that, the pressure increment $\Delta\mathbf{P}$ is obtained solving Eq.(4.57). Next the acceleration increment $\Delta\mathbf{a}$ is solved using Eq.(4.49b), and Eq.(4.48) is solved to derive the acceleration $^{t+\Delta t}\hat{\mathbf{a}}^{(k)}$, the velocity $^{t+\Delta t}\hat{\mathbf{v}}^{(k)}$, and the displacement $^{t+\Delta t}\hat{\mathbf{u}}^{(k)}$.

B) Finite element formulations of nonlinear electric field–structure interaction

The finite element formulations of a nonlinear electric field–structure interaction (ESI) based on a novel transformation algorithm between shell elements for the structural field and 3D solid elements for the electric field is described in Section 3.2.5. The general equations to solve electric filed–structure interaction is given as follows: The electrical potential is obtained using the mechanical displacement by solving

$$^{t+\Delta t}\mathbf{K}_{\phi\phi}^{(b)}\ {}^{t+\Delta t}\phi^{(b)} = {}^{t+\Delta t}\mathbf{q} - {}^{t+\Delta t}\mathbf{K}_{\phi u}^{(b)}\ {}^{t+\Delta t}\mathbf{u}^{(b-1)}. \tag{4.61}$$

The mechanical displacements are obtained using the induced electrical force as

$$^{t+\Delta t}_{0}\hat{\mathbf{K}}_{uu}^{(i-1)(b)}\ \Delta\mathbf{u}^{(i)(b)} = \Delta\mathbf{g}^{s} - {}^{t+\Delta t}\mathbf{K}_{u\phi}^{(b)}\ {}^{t+\Delta t}\phi^{(b)}. \tag{4.62}$$

where $\Delta\mathbf{g}^{s}$ is the residual vector of the structure and superscript s indicates structure. When the electric field is solved using 3D solid elements then Eq.(4.61) can be written as

$$^{t+\Delta t}\mathbf{K}_{\phi\phi}^{(i)}\ {}^{t+\Delta t}\phi^{(i)} = {}^{t+\Delta t}\mathbf{q} - {}^{t+\Delta t}\mathbf{K}_{\phi u}^{(i)}\ {}^{t+\Delta t}\mathbf{u}_{\text{solid}}^{(i-1)}. \tag{4.63}$$

where i indicates the current block Gauss–Seidel iteration between electric field and structure. The displacements ${}^{t+\Delta t}\mathbf{u}_{\text{solid}}^{(i-1)}$ in the solid elements are obtained using

$$\mathbf{u}_{\text{solid}} = {}^{u}\mathbf{T}\mathbf{u}^{s}, \tag{4.64}$$

where ${}^{u}\mathbf{T}$ is the displacement transformation matrix and $\mathbf{u}^{s}$ is the shell structure displacement.

The transformation equation that transforms the electric forces from the solid elements to the shell elements can be generally expressed as

$$\mathbf{g}^{e} = {}^{e}\mathbf{T}\ \mathbf{g}_{\text{solid}}^{e}, \tag{4.65}$$

where $\mathbf{g}^{e}$ has the dofs of the shell element and $\mathbf{g}_{\text{solid}}^{e}$ has the dofs of the 3D solid element. The displacement approximation (incremental form) in the shell elements is corrected using

$$\mathbf{u}^{s} = \mathbf{u}^{s} + \Delta\mathbf{u}^{s}. \tag{4.66}$$

Eq.(4.66) solves the structure in the shell elements from the electric forces and moments transformed onto the shell elements, which are considered as externally applied equivalent forces, as described in Section 3.2.3.

C) Coupling of the electric field and fluid–structure interaction

The strongly coupled nonlinear electric–structure interaction system which is based on the partitioned iteration method and transformation method, and strongly coupled fluid–structure interaction system derived that are based on the projection method for the monolithic FSI system are combined to analyze the electric field and fluid–structure interaction using block Gauss–Seidel coupling scheme and transformation method [124] as shown in Fig. 4.4. The analysis of the EFSI is as follows: First, the electric potentials are derived in the 3D solid elements are derived from the structural displacements solved in shell elements using the following equation:

$$\mathbf{K}_{\phi\phi}\ \phi_{\text{solid}} = \mathbf{q} - \mathbf{K}_{\phi u}{}^{\text{u}}\mathbf{T}\ \mathbf{u}^{\text{s}}. \tag{4.67}$$

Next, the electric force vector $\mathbf{g}^{\text{e}}_{\text{solid}}$ is derived

$$\mathbf{g}^{\text{e}}_{\text{solid}} = \mathbf{K}_{u\phi}\phi. \tag{4.68}$$

where $\mathbf{K}_{u\phi}$ is the piezoelectric coupling coefficient matrix and ϕ is the electric potentials. The $\mathbf{K}_{u\phi}$ is defined as

$$\mathbf{K}_{u\phi} = \int_{t\Omega^{\text{p}}} \mathbf{B}_{\text{u}}^{\text{T}}\mathbf{e}\mathbf{B}_{\phi}\,\text{d}\Omega^{\text{p}}, \tag{4.69}$$

where $\mathbf{B}_{\text{u}}$, $\mathbf{B}_{\phi}$, $\mathbf{e}$ are the strain–displacement matrix, the electric field–potential matrix, and the piezoelectric–stress coefficient matrix, respectively. In the nonlinear analysis problem, the piezoelectric coupling coefficient matrix $\mathbf{K}_{u\phi}$ is evaluated and factorization is performed at every time step.

The induced electric force vector $\mathbf{g}^{\text{e}}_{\text{solid}}$ is now applied on to the structural domain of the FSI system through the force transformation relation given in Eq.(4.65), which gives $\mathbf{g}^{\text{e}}$. After the force transformation, the external force vector $\mathbf{g}$ in the monolithic fluid–structure interaction system given in Eq.(4.43) becomes

$$\mathbf{g} \equiv \begin{Bmatrix} \mathbf{g}^{\text{f}}_{d} \\ \mathbf{g}^{\text{fs}}_{c} \\ \mathbf{g}^{\text{s}}_{d} \end{Bmatrix} \Longrightarrow \mathbf{g} \equiv \begin{Bmatrix} \mathbf{g}^{\text{f}}_{d} \\ \mathbf{g}^{\text{fs}}_{c} + \mathbf{g}^{\text{e}}_{c} \\ \mathbf{g}^{\text{s}}_{d} + \mathbf{g}^{\text{e}}_{d} \end{Bmatrix}, \tag{4.70}$$

where $\mathbf{g}^{\text{e}} = [\mathbf{g}^{\text{e}}_{c}, \mathbf{g}^{\text{e}}_{d}]^{\text{T}}$, and $\mathbf{g}^{\text{e}}_{c}$ is the external force or transnational force acting on the shell and $\mathbf{g}^{\text{e}}_{d}$ is the external electric moment of force or rotational force acting on the shell. Therefore, the expression for $\mathbf{g}$ in Eq. 4.45(f) changes to Eq.(4.70). After that, in the nonlinear iteration k,

the increment of the intermediate acceleration $\Delta\hat{\mathbf{a}}$ is obtained by solving Eq.(4.53) and then the intermediate velocity ${}^{t+\Delta t}\hat{\mathbf{v}}^{(k)}$ is obtained using Eq.(4.54b), Eq.(4.57) is solved to obtain the pressure increments $\Delta\mathbf{P}$, Eq.(4.49b) is solved to determine the acceleration increment $\Delta\mathbf{a}$, and Eq.(4.48) is solved to derive the acceleration ${}^{t+\Delta t}\hat{\mathbf{a}}^{(k)}$, the velocity ${}^{t+\Delta t}\hat{\mathbf{v}}^{(k)}$, and the displacement ${}^{t+\Delta t}\hat{\mathbf{u}}^{(k)}$. After the nonlinear iterations, the resultant displacements in the shell element is transformed to the solid elements using Eq.(4.64) inside the block Gauss–Seidel iteration loop. The coupling strategy of the EFSI system is symbolically represented using the model equation system including the degrees of freedoms (dofs) of fluid, structure and electric fields as shown in Fig. 4.4. The analysis flow of the proposed triply coupling method to solve for the electric field and fluid–structure interaction algorithm is illustrated in Fig. 4.5

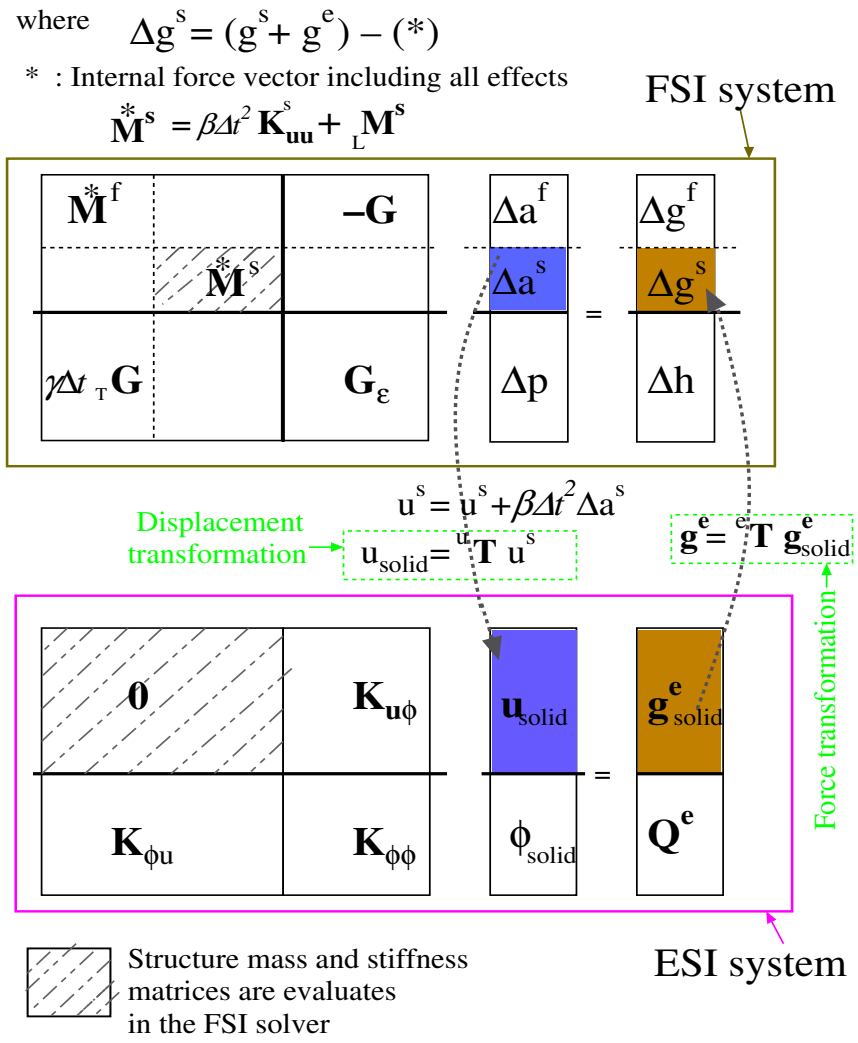

Figure 4.4: EFSI coupling: Data flow between FSI and ESI system.

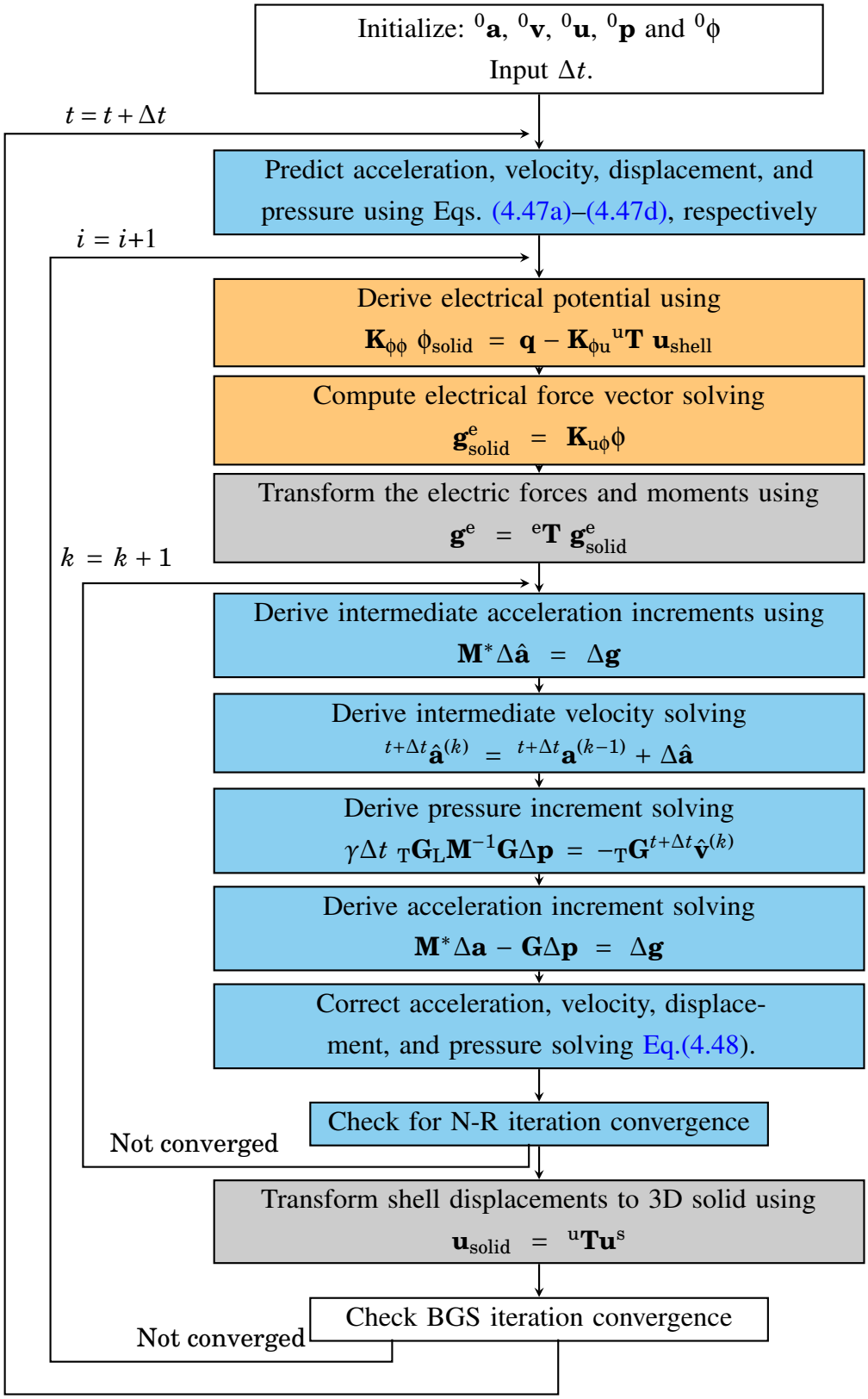

Figure 4.5: Solution procedure of the proposed EFSI analysis
Electric solver, FSI solver, force and displacement transformation.

Table 4.1: Material properties of PVDF and PZT-5H used in the numerical analysis of a piezoelectric bimorph in converging fluid channel (the absolute permitivity $\varepsilon_0 = 8.854$ pF/m)

	PVDF[9]	PZT–5H [125]
Young's Modulus (GPa)		
E_{11}	2.0	62.0
E_{33}	2.0	50.0
Constant electric field Elastic stiffness (GPa)		
C_{11}	2.62	115.0
C_{12}	1.07	68.5
C_{13}	1.07	68.9
C_{33}	2.62	101.5
C_{44}	0.775	20.3
C_{66}	0.775	23.3
Density (kg/m^3)		
ρ_p	1800	7360
Poission's ratio		
v_p	0.29	0.30
Piezoelectric stress constants (C/m^2)		
e_{31}	0.046	-5.01
e_{33}	-	24.0
e_{15}	-	14.7
Piezoelectric strain constants (pC/N)		
d_{31}	23.0	-262
d_{33}	-	518
d_{15}	-	726
Relative permitivity ($\varepsilon^r = \varepsilon/\varepsilon_0$)		
ε^r_{11}	12.0	2778
ε^r_{33}	12.0	3170
Constant strain Absolute permitivity ($\times 10^{-10}$ F/m)		
ε_{11}	1.06	245.9
ε_{33}	1.06	280.6
Electromechanical coupling factor		
k_{31}	0.12	-0.386
k_{33}	-	0.683
k_{15}	-	0.660

4.3 Analysis of a flexible piezoelectric bimorph in channel

4.3.1 Problem setup

A flexible flap in fluid channel shown in Fig. 4.6 is one of the benchmark problem proposed by Mok and Wall [103] in order to demonstrate the convergence properties, computational efficiencies, mesh sensitivity, stability performances of partitioned FSI algorithms, and to check the strong coupling between fluid and structure [50, 103–107]. Ishihara and Horie in Ref.[50] had analyzed the same problem to discuss the convergence properties, computational efficiency and stability performances of the projection method. Their results are close to the solutions from the literature (Mok et al. [103] and Neumann et al. [104]). In the above mentioned references, the flexible solid beam shown in Fig. 4.6 is made of a rubber material with the material density $\rho^{\mathrm{s}} = 1500$ kg/m^3, Young's modulus $E^{\mathrm{s}} = 2.3$MPa, and a Poisson's ratio $v^{\mathrm{s}} = 0.45$. The fluid is a silicone oil. The mass density and the viscosity of silicone oil used in the analysis are $\rho^{\mathrm{f}} = 956$ kg/m^3 and $\mu^{\mathrm{f}} = 0.145$kg/(m.s). The inflow velocity of the fluid has a parabolic shape. The fluid velocity at the top v_{in} varies as $V_{in}(1-\cos 2\pi f t)$ until 10 sec and V_{in} after 10 sec. The value of V_{in} is 0.06067 m/s and $f = 0.05$Hz.

In this study, a piezoelectric bimorph is used instead of rubber. Two separate piezoelectric materials are studies. One is Polyvinylidene fluoride (PVDF), and the other one is lead zirconate titanate (PZT). The mechanical and electric properties of these piezoelectric materials that are used in the analysis are given in Table 4.1. As shown in the Table 4.1, the piezoelectric stress constants, piezoelectric strain constants, and electromechanical coupling factor of PZT-5H material is very high compared to that of PVDF. The reason why these two piezoelectric materials are used is that they have a different mechanical, electrical and electromechanical properties. The piezoelectric ceramic PZT–5H has very strong direct and inverse piezoelectric coupling effect than that of the piezoelectric polymer PVDF.

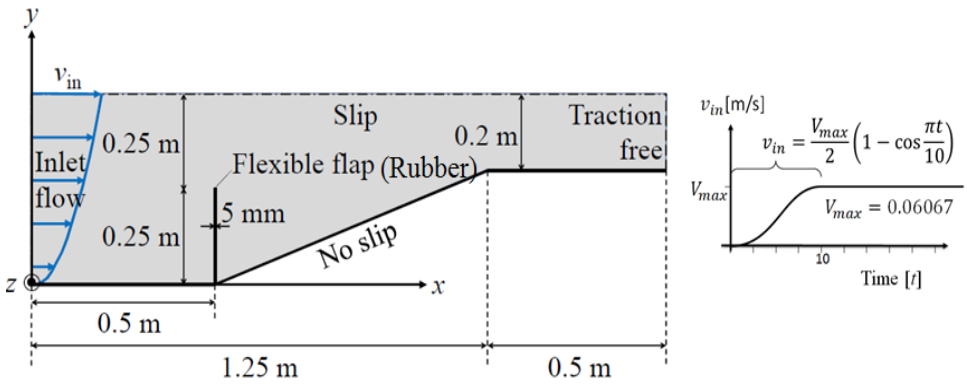

Figure 4.6: A flexible flap in the converging fluid channel

Four test cases involving different loading conditions and electric configurations are investigated.

1. In case 1, *actuator setup* is used for the piezoelectric bimorph where a uniform potential is applied onto the top surface of the bimorph while the bottom surface being earthed as shown in Fig. 4.7(a). The bimorph is subjected to an applied AC voltage $V_\phi = V_{\phi_0} \sin\omega_\phi t$.

2. In case 2, *closed or short circuit sensor setup* is used for a piezoelectric bimorph where the top and bottom surfaces of the bimorph are set to zero electric potential and a transverse mechanical force or block force F_{ext} [21] which is equivalent to the induced electric force in the actuator problem (case 1) is applied to the free end of the shell structure made of the piezoelectric material as shown in Fig. 4.7(b) .

3. In case 3, *open circuit sensor setup* is used for a piezoelectric bimorph where the top and bottom surfaces of the bimorph are in an open circuit condition and a transverse mechanical force which is equivalent to the induced electric force in the actuator problem (case 1) is applied to the free end of the shell structure made of the piezoelectric material as shown in Fig. 4.7(c).

4. In case 4, the pure FSI analysis is performed for the structural properties of a piezoelectric material with sinusoidal external mechanical force which is equivalent to the induced electric force in the actuator problem (case 1) is applied to the tip of the flap as shown in Fig. 4.7(d).

For all these cases, the inlet fluid velocity boundary condition in a converging channel follows the setup shown in Fig. 4.6. The fluid domain of the channel is modeled using P1P1 elements (12,012 nodes and 33,600 elements) shown in Fig. 4.8(a), the structural mesh of the piezoelectric cantilever beam is modeled using shell elements(42 nodes and 20 elements) shown in Fig. 4.8(b) and the electrical field is analyzed using 3D solid elements (20 node hexahedron element) shown in Fig. 4.8(c) consists of 683 nodes and 80 elements. Both the fluid and structural meshes have single division along the z–direction as shown in Figs. 4.8(a) and 4.8(b), while the electrical mesh has 4 divisions along z–direction as shown in Fig. 4.8(c).

Results computed with [50, 103–107] show the maximum velocity at time t = 10s and after maximum velocity is reached, the flap starts retracting until its steady–state position. In this study, a harmonic oscillation is expected about the reference solutions when an AC input voltage source or sinusoidal external mechanical force is applied to the reference setup in [50].

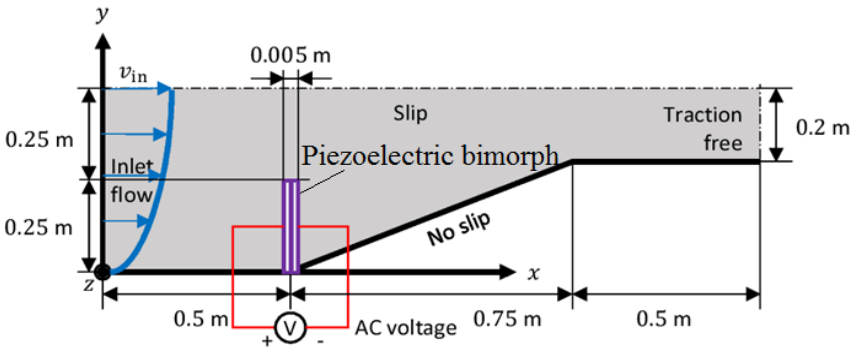

(a) Bimorph actuator in the fluid: AC bias voltage is applied to the bimorph

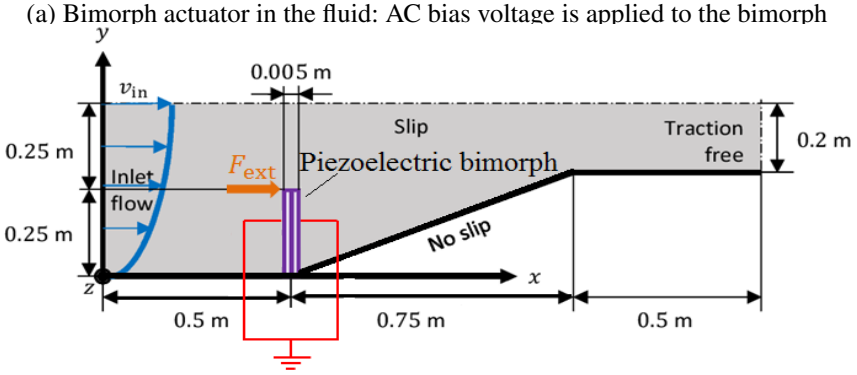

(b) Closed circuit bimorph sensor configuration in the fluid: Bimorph electrodes are grounded and a sinusoidal blocking force is applied to the tip

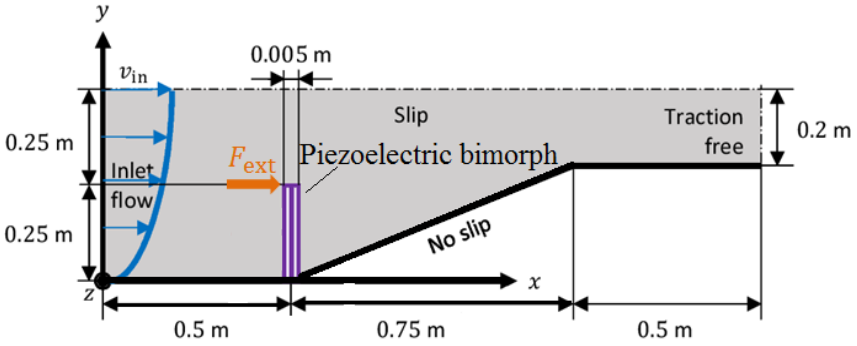

(c) Open circuit bimorph sensor configuration in the fluid: Bimorph electrodes are in open circuit condition and a sinusoidal blocking force is applied to the tip

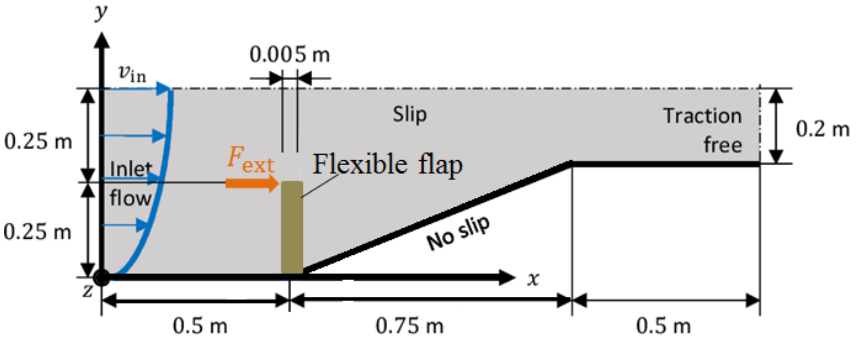

(d) A flap with external force in the fluid: The structure is applied a sinusoidal equivalent or blocking force at the tip

Figure 4.7: EFSI problem description, dimensions, external loading and electric configurations.

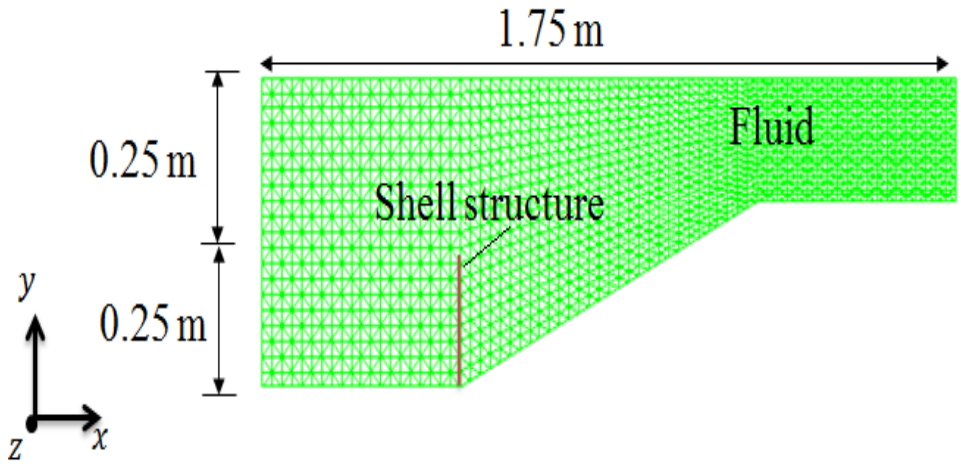

(a)

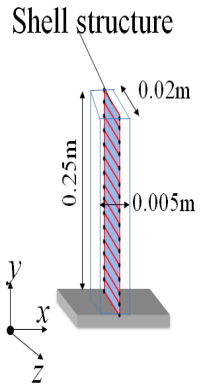

(b)

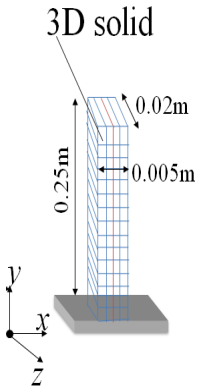

(c)

Figure 4.8: The finite element meshes: a) P1P1 elements for the fluid, b) shell for the thin structure, c) 3D solid elements for electric field (the graphics is enlarged in thickness x–direction for better visibility)

4.3.2 Results and discussions

The theoretical solution for the resonance frequency of the bimorph cantilever beam immersed in the fluids is given as [126]

$$\omega_{\text{fld}}^{(n)} = \omega_{\text{vac}}^{(n)}\left[1 + \frac{\pi\rho^{\text{f}}w}{4\rho^{\text{s}}h}\Gamma_{\text{f}}(m)\right]^{-1/2}, \tag{4.71}$$

where ρ^{f} and ρ^{s} are the density of the fluid and the structure, respectively, w and h are the width and the thickness of the structure, m is the normalized mode numbers given as

$$m = \alpha_n \frac{w}{L}, \tag{4.72}$$

$\Gamma_{\text{f}}(m)$ which is dependent on the normalized mode number m is given as [126]

$$\Gamma_{\text{f}}(m) = \frac{1 + 0.74273m + 0.14862m^2}{1 + 0.74273m + 0.35004m^2 + 0.058364m^3}, \tag{4.73}$$

and $\omega_{\text{vac}}^{(n)}$ is the n^{th} resonant frequency in vacuum given as

$$\omega_{\text{vac}}^{(n)} = \frac{\alpha_n^2}{L^2}\sqrt{\frac{E^s I}{m^s}}, \tag{4.74}$$

where $\alpha_1 = 1.875$ corresponds to the fundamental flexural mode, I is cross-sectional area moment of inertia and m^s is the mass per unit of length. The transverse resonant frequency of the PVDF bimorph in the vacuum using the material properties given in Table 4.1 with the geometric dimensions $L = 0.25\text{m}$, $w = 0.02\text{m}$ and $h = 0.005\text{m}$ is $\omega_{\text{vac}}^{(1)} = 85.58$ rad/s. Similarly, the damped transverse resonance frequency of the bimorph cantilever in the fluid media (silicone oil) is $\omega_{\text{fld}}^{(1)} = 52.45$ rad/s. For the given geometry, the difference between the undamped $\omega_{\text{vac}}^{(1)}$ and damped $\omega_{\text{fld}}^{(1)}$ transverse resonance is 38.71%. Similarly, the transverse resonant frequency of the PZT–5H bimorph in the vacuum with the same geometric dimensions is $\omega_{\text{vac}}^{(1)} = 235.64$ rad/s and the damped resonance frequency in fluid is $\omega_{\text{fld}}^{(1)} = 198.69$ rad/s.

In general, the 1st bending resonance frequency of the cantilever beam operating transversely, laterally, or torsionally in viscous liquid media is found to shift to a lower value compared to that in the vacuum or air [127]. According to the results presented in [126–128], the predicted resonance frequency drop of the 1st transverse mode range from 30–50%, or larger for longer beams [128]. This is however not the cases for the cantilever beams vibrating laterally. The 1st lateral resonance frequencies of the same beam only drop by a value of up to 10% while the 1st torsional frequencies drop within 32% [127].

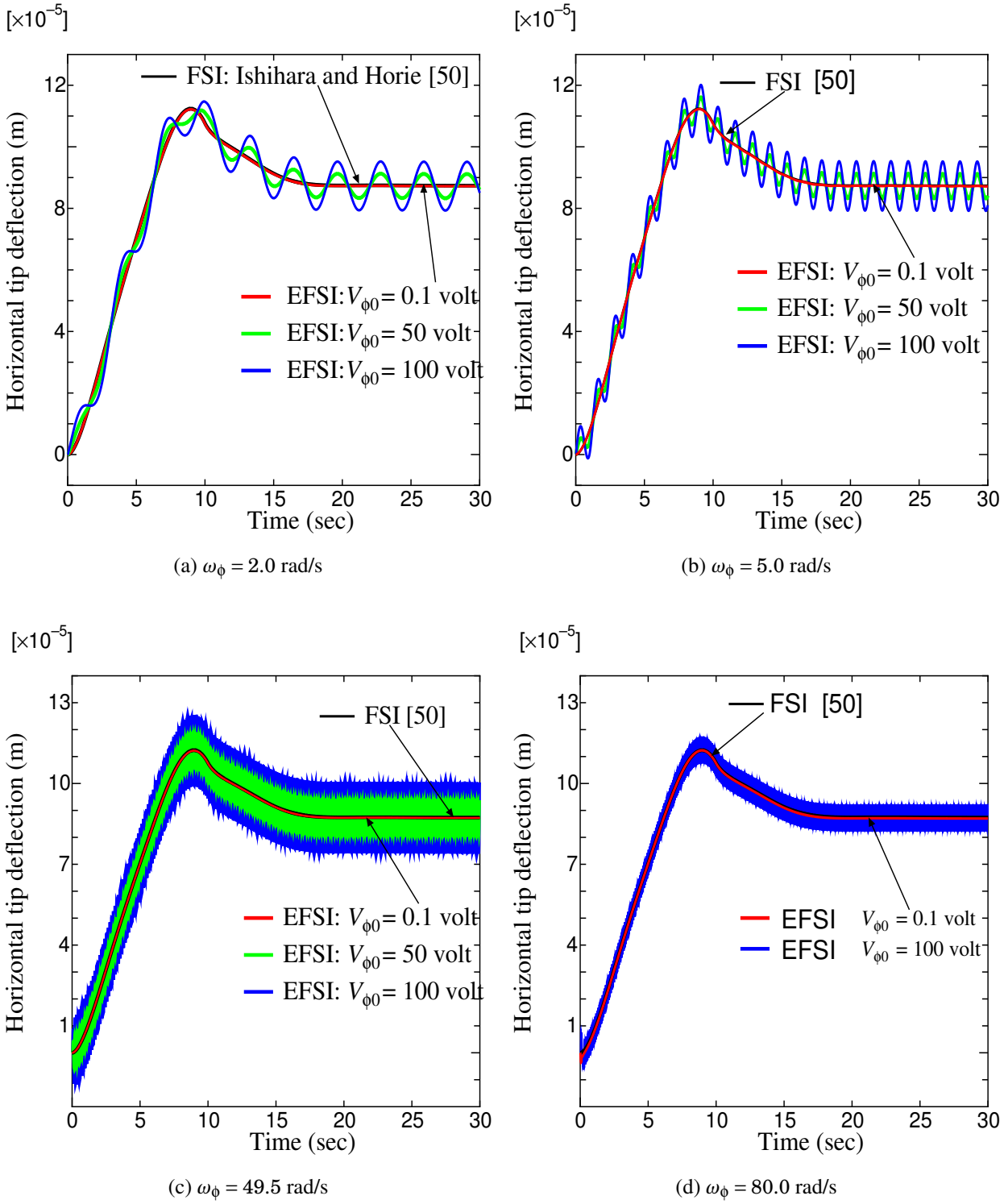

(a) $\omega_\phi = 2.0$ rad/s

(b) $\omega_\phi = 5.0$ rad/s

(c) $\omega_\phi = 49.5$ rad/s

(d) $\omega_\phi = 80.0$ rad/s

Figure 4.9: Horizontal displacement of the bimorph actuator at tip at various input voltage frequency and various bias voltage

Now the EFSI analysis results for the case 1 shown in Fig. 4.7(a) is presented. Since the FSI benchmark problem has no analytical solution or experimental data, a reference FSI solution obtained using Ishihara and Horie [50] was taken as the exact solution for PVDF/PZT–5H material instead of rubber in a silicone oil. Piezoelectric bimorph actuator layers are polarized in series type. The number of block Gauss–Seidel iterations are fixed to 8 and time increment Δt is fixed to 0.005 sec.

Fig. 4.9 shows the vibration characteristics of the tip of the bimorph actuator in response to various input AC signals with different input voltage frequencies. One can see in Fig. 4.9 that, the response for input voltage $V_{\phi_0} = 0.1$volt with frequencies $\omega_\phi = 2, 5, 49.5$ and 80 rad/s, the curve coincides with that of the reference solution [50]. This is because the electric forces induced by the inverse piezoelectric effect in the solid elements acting on the shell elements as an externally applied force is very close that of the applied fluid forces on to shell structure in Ishihara and Horie [50]. This indicates that the coupling between electric and fluid–structure interaction is very similar to the fluid–structure interaction. The shape of the present EFSI curve at $V_{\phi_0} = 0.1$V is identical to those from the numerical solutions of Mok et al. [103], Neumann et al. [104] and Ishihara and Horie [50]. As the input voltage is increased, the coupling between the electric and fluid–structure interaction becomes significantly strong and increases the induced electric force. Therefore, harmonic oscillations occur around the quasi–state phase of the reference solution, as shown in Fig. 4.9 for $V_{\phi_0} = 50$ and100 volt.

Fig. 4.10 shows the frequency response of the bimorph actuator (case 1) in a converging channel for the imposed fluid velocity boundary conditions at a bias voltage $V_{\phi_0} = 100$V for various input voltage frequency ω_ϕ. From the Fig. 4.10 it is evident that the harmonic oscillations for $\omega_\phi = 5$ rad/s, 49.5 rad/s, 80 rad/s are about the reference FSI solution for all the input voltage frequency. Also, the response in $\omega_\phi = 49.5$ rad/s achieved the largest peak amplitude among the different input voltage frequencies, indicating the resonance at this voltage frequency.

Fig. 4.11 is the summary of the maximum horizontal tip displacement after the time $t = 25$s with the input signals at the different frequencies ω_ϕ. It reveals that the EFSI simulation results yielded a maximum displacement at an input voltage frequency $\omega_\phi = 49.50$rad/s.

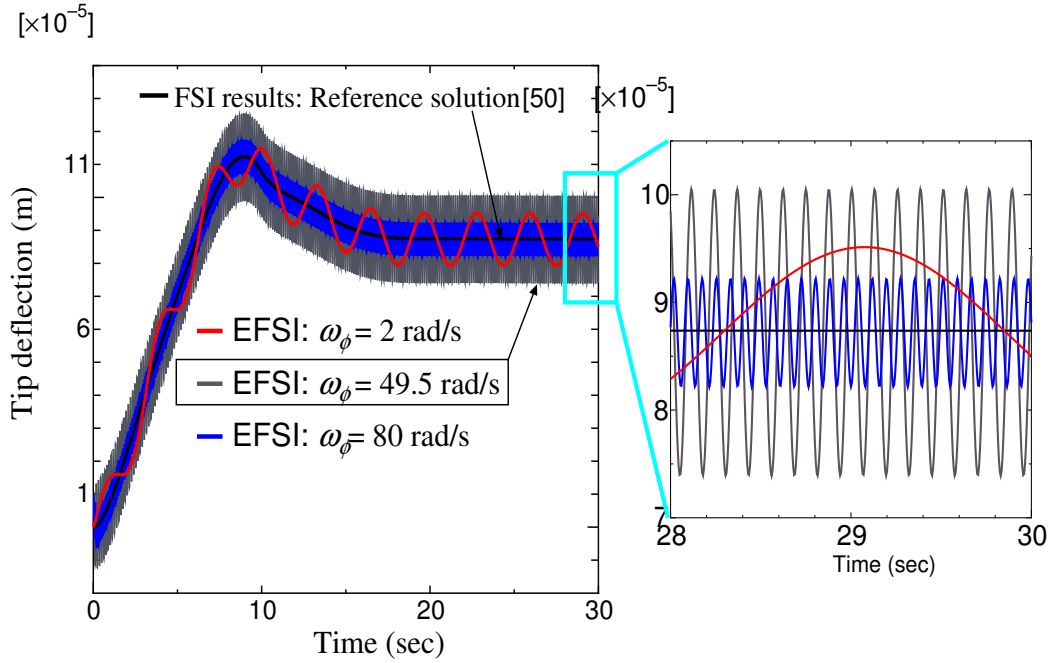

Figure 4.10: AC response of a piezoelectric bimorph actuator in the converging fluid channel at $V_{\phi 0} = 100$V, $V_{in} = 0.06067$ m/s and $f = 0.05$Hz ($v_{in} = V_{in}(1 - \cos 2\pi f t)$).

.

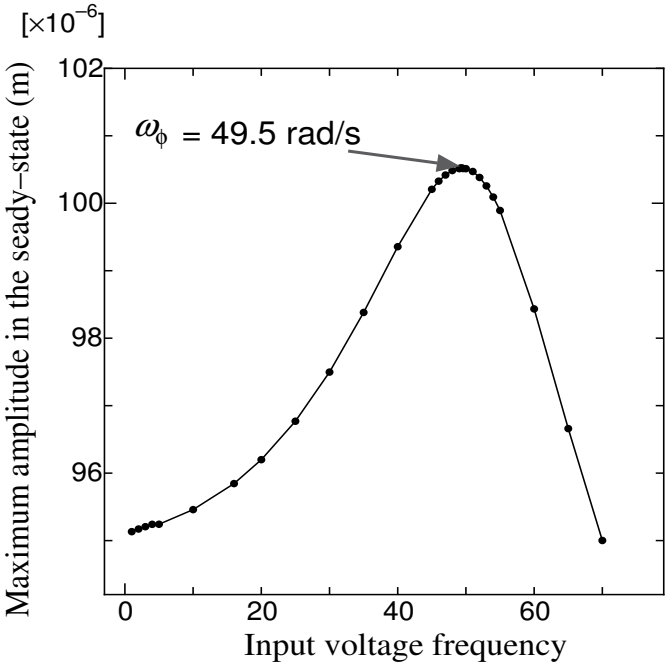

Figure 4.11: Frequency response curve of a piezoelectric bimorph actuator in the converging fluid channel at $V_{\phi 0} = 100$V, $V_{in} = 0.06067$ m/s and $f = 0.05$Hz.

.

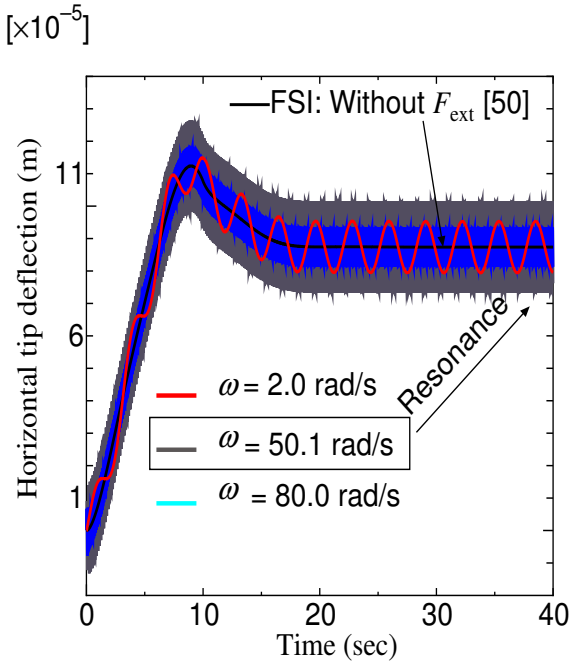

(a) Case 2: Time histories of tip deflection

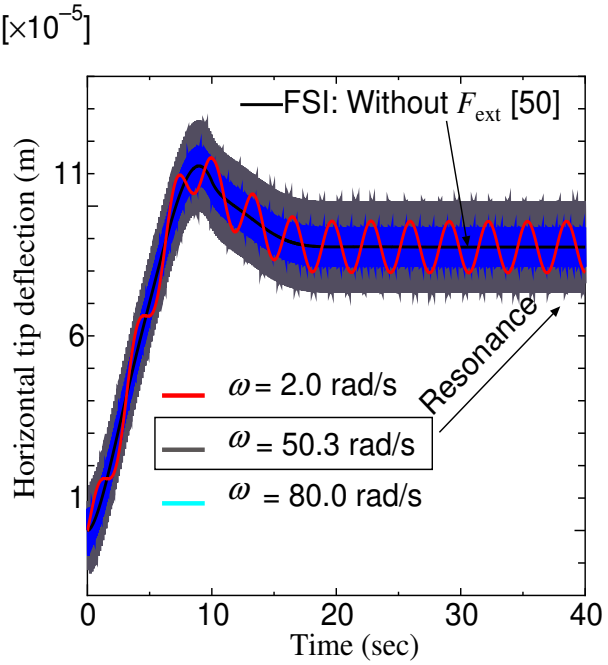

(b) Case 3: Time histories of tip deflection

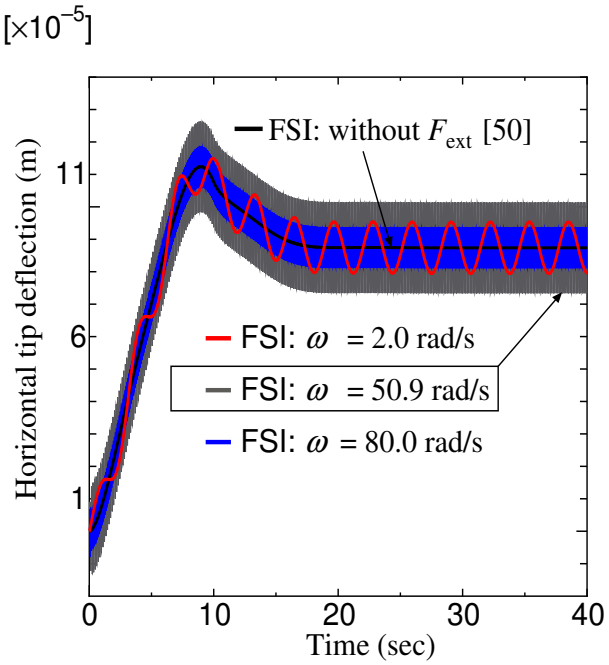

(c) Case 4: Time histories of tip deflection

Figure 4.12: Horizontal displacement of the bimorph for various input external mechanical force frequency ω with $F_{\text{ext0}} = 6.90 \times 10^{-4}$N, $V_{in} = 0.06067$ m/s and $f = 0.05$Hz ($v_{in} = V_{in}(1 - \cos 2\pi f t)$)

.

Next, the results obtained for case 2, 3, and 4 are presented. For these cases studies, the equivalent external force F_{ext_0} corresponding to the induced electric forces in a static piezoelectric bimorph actuator problem is applied dynamically as $F_{\text{ext}} = F_{\text{ext}_0}\sin\omega t$ at the tip of the shell structure, where ω is the input frequency of the external equivalent forces. An external equivalent force or blocking force corresponding to the induced electric forces in the piezoelectric bimorph actuator can be obtained using[21]

$$F_{\text{ext}_0} = \frac{3wh^2E^s}{8L}d_{31}E_3, \tag{4.75}$$

where d_{31} is the piezoelectric strain constant and E_3 is the applied electric field in the thickness direction of the piezoelectric actuator connected in series type, E^s is the Young's modulus of the structure or piezoelectric layers, w is the width of the structure, and L is the length of the structure. For an applied input static voltage of V_{ϕ_0} = 100 V to a piezoelectric bimorph actuator, the estimated blocking force F_{ext_0} using Eq.(4.75) is 6.90×10^{-4} N. Fig. 4.12 shows the the dynamic response of a piezoelectric bimorph in the converging fluid channel with $F_{\text{ext0}} = 6.90\times10^{-4}$N, V_{in} = 0.06067 m/s and f = 0.05Hz ($v_{in} = V_{in}(1-\cos2\pi ft)$ for cases 2, 3, and 4.

Fig. 4.13 is the summary of the peak amplitude of the response within time t = 25 to 40 sec for input force F_{ext} with various frequencies ω. In–order to find the true peak in the frequency response curve Fig. 4.13, the step of 0.1 rad/sec is used in the simulation near the resonance for obtaining a fine–enough resolution in the peak amplitude values. The shift between the open– and closed–circuit resonance frequencies in sensor modes and actuator modes are negligible for the low electro–mechanical coupling factor k_{31} the piezoelectric bimorphs such as PVDF material [129]. This is however not the cases for the piezoelectric bimorphs made of PZT materials since it has high electro–mechanical coupling factor. It is known that the resonance frequency of the piezoelectric bimorph beam under closed circuit and open circuit configuration are co–related as Eq.(4.76) [129, 130],

$$f_{closed} = f_{open}\sqrt{1-k_{31}^2}, \tag{4.76}$$

where k_{31} is the electro–mechanical coupling factor of a piezoelectric material, f_{closed} is the resonance frequency of the piezoelectric bimorph in the closed or short circuit configuration, and f_{open} is the resonance frequency of the open circuit configuration. The value of k_{31} for PVDF is about 0.12, therefore the difference between f_{closed} and f_{open} is within 1%.

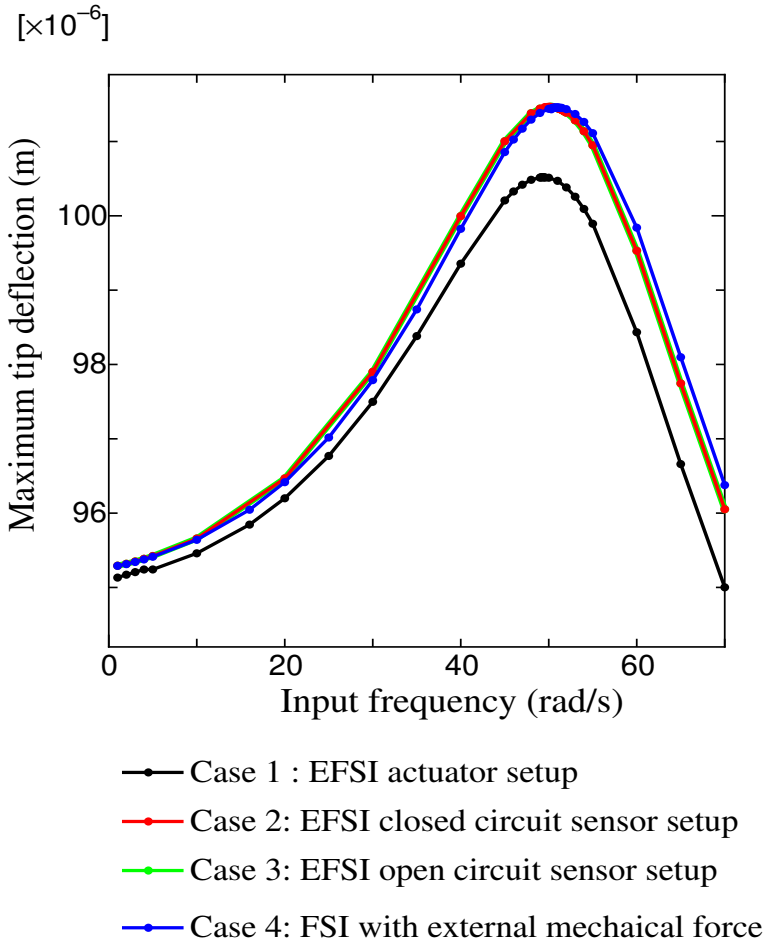

Figure 4.13: Frequency response curve of the piezoelectric bimorph made of PVDF material in the fluid channel

.

As k_{31} of PZT–5H is about 0.4, the difference between f_{closed} and f_{open} is approximately within 10%, as shown the studies of Zhu et al. [131]. In their study, harmonic analysis of the piezoelectric bimorph based on ceramic PZT–5H are performed with different external resistive load values R. The schematic of the external resistive load connected to the piezoelectric bimorph is shown in Fig. 4.14. They demonstrated how an externally connected resistive load R causes the shift in the resonance frequency the of piezoelectric bimorphs. The value of the external resistive load for different electric configurations according to Zhu et al. [131, 132] are as follows: 1) open circuit configuration has external resistive load value R = ∞, 2) closed or short circuit has value R = 0, and 3) a circuit connected wherein an electric potential is applied to the electrodes of the piezoelectric bimorphs has value R = $R_{opt} = \frac{1}{\omega_r C_p}$, where $C_p = n\frac{\varepsilon_0 \varepsilon_r w L}{h}$ is the capacitance of the piezoelectric layers placed between electrodes. In

accordance with this explanation, it should be noted that in the actuator setup (case1) has external resistive load value $R = R_{opt}$ since a uniform potential is applied at the top of the electrode with the bottom electrode being grounded. Therefore, the resonance frequency of the actuator mode $f_{res \to R=R_{opt}}$ is different from that of the resonance of the open circuit $f_{res \to R=\infty}$ and closed circuit $f_{res \to R=0}$ [131, 132]. Also, the shift in the resonance frequencies in PVDF based piezoelectric bimorphs upon the electrical connections are negligible, unlike the case of PZT–5H based piezoelectric bimorphs of which the resonance frequency shows a noticeable shift upon the electric configuration (connection to the external resistive load R).

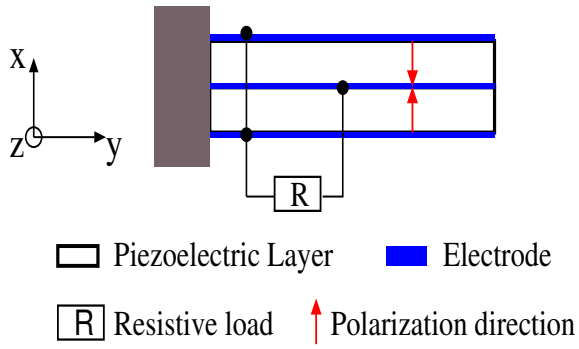

Figure 4.14: Schematic of external electrica resistive load connected to the piezoelectric bimorph.

.

Theoretical damped resonance frequency $\omega_{fld}^{(1)}$ of the bimorph cantilever made of PVDF material with length $L = 0.25$m, width $w = 0.02$ m and thickness $h = 0.005$ m obtained using Eq.(4.71) is 52.45 rad/s. As shown in Fig. 4.13, the resonance appears when the input frequency of the external source (bias voltage for actuator problem case 1or blocking force for cases 2–4) is $\omega_\phi = 49.5$, $\omega = 50.1$ rad/sec, $\omega = 50.3$ rad/sec, and $\omega = 50.9$ rad/sec for case 1, 2, 3, and 4, respectively. Here, cases 1–3 are EFSI setup and their resonance frequency difference with each other is nearly 1%, thus justifying the approximation given in Eq.(4.76). Also, the frequency response curve shown in Fig. 4.13 follows a same trend of tip deflection and resonance point with the results in [130]. The vibration amplitudes of the case 1 in Fig. 4.13 which is an actuator problem setup with $R = R_{opt}$ have less amplitudes compared to that under the closed–circuit sensor configuration (case 2), the open–circuit sensor configurations (case 3) and FSI (case 4), as the inverse piezoelectric effect counter plays with the mechanical excitation [130]. Also, the resonance obtained with the FSI algorithm in case 4 [50] shows a good agreement with the theoretical damped natural frequency i.e. the difference between the theoretical damped natural frequency and the simulated results in case 4 which is pure FSI problem is 2.8%. Now,

by taking the FSI solution as an absolute solution, then the difference between the FSI (case 1) and EFSI problem (cases 1–3) is within 1.5%. This indicates that the proposed EFSI algorithm takes into account a small shift in the resonance frequency of piezoelectric bimorph made of PVDF which has a negligible shift in the frequency upon the external resitive loading, which also appeared in the works of Song et al. [130]. Also, the simulation vibration amplitudes in actuator setup (case 1) decreases a bit (approximately <10%) with optimum resistance load compared to that under closed circuit (case 2), open–circuit (case 3), and the FSI setup (case 4), as the inverse piezoelectric effect counter plays with the mechanical vibration [130] and also the connected optimum resistive load has an obvious damping effect on the vibration amplitude, demonstrated in [131, 132]. This vibration amplitude decrease (about 10%) in PVDF bimorph actuator problem (case 1) shows similarities with the results presented by Song et al. [130].

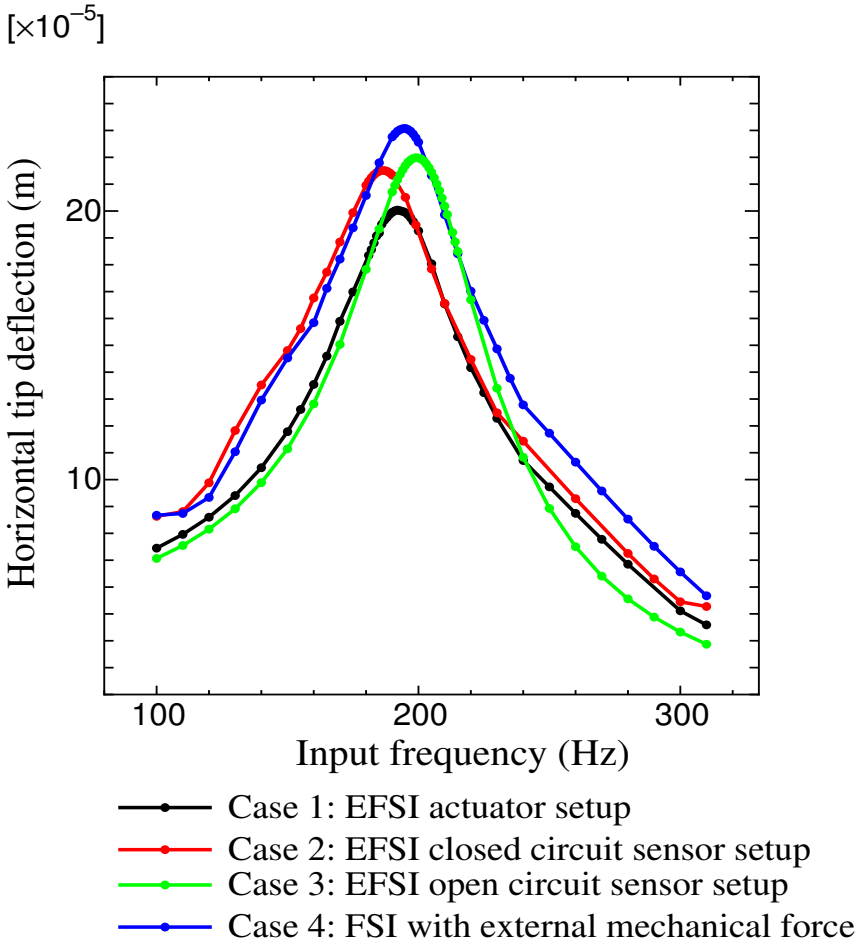

Figure 4.15: Frequency response curve of piezoelectric bimorph made of PZT–5H material in the fluid channel

.

Now the response of the piezoelectric bimorph made of PZT–5H in the fluid channel for the numerical setup described in Fig. 4.7 to demonstrate the noticeable shift in the resonance upon the electrical connection is shown. The material properties of PZT–5H that are used in the theoretical calculations and numerical analysis are given in Table 4.1. The undamped resonance frequency of the 1st transverse mode of vibration of the piezoelectric bimorph made of PZT–5H of length $L = 0.25$m, width $w = 0.02$ m and thickness $h = 0.005$ m is $\omega_{\text{vac}}^{(1)} = 235.64$ rad/s and the damped natural frequency $\omega_{\text{fld}}^{(1)} = 198.69$ rad/s. Fig. 4.15 shows the simulated frequency response of the PZT–5h based piezoelectric bimorph in the fluid channel using EFSI algorithm for cases 1–3 and FSI algorithm [50] with external force F_{ext} is used for the analysis of case 4. The external force F_{ext0} corresponding to $V_{\phi 0} = 100$ V is calculated using the relation given in Eq.(4.75). The value of F_{ext0} used for the case studies of 2–4 is 0.0786N. The piezoelectric bimorph layers are polarized parallel. Time increment Δt is fixed to 0.0005 sec, while the BGS iterations are fixed to 8 satisfying the convergence criteria.

The simulated results depicted in Fig. 4.15 for PZT–5H material shows the resonance when the input frequency of the input bias voltage or the frequency of the equivalent external mechanical force is $\omega_{\phi} = 192$ rad/sec, $\omega = 186$ rad/sec, $\omega = 199$ rad/sec, and $\omega = 195$ rad/sec for case 1, 2, 3, and 4, respectively. The difference between open– and closed–circuit resonance frequency is 6.5%, thus justifying the relation given Eq.(4.76) for PZT–5H material. The simulation results in [131] also shows 5% difference between the open– and closed–circuit configuration for the piezoelectric bimorph based on PZT–5H material. Therefore, the simulated results using the EFSI algorithm follow the same trends upon the shift in the resonance. Also, the resonance obtained with the FSI algorithm [50] shows a good agreement with the theoretical damped natural frequency. The vibration amplitudes of the PZT–5H piezoelectric bimorph in case 1, 2, and 3 shows a dependency on the connected external resistive load. The connected external resistive load decrease the vibration amplitude a bit (by less than 10% [130]) compared to the pure FSI results (case 4) as the inverse piezoelectric effect counter plays the mechanical vibrations. This amplitude dependency upon the external resistive load in PZT–5H piezoelectric bimorph also follows the results presented by Zhu et al. [131].

4.4 Conclusions

In this chapter, a triple coupled algorithm is proposed to analyze the electric field and fluid–structure interaction of a piezoelectric bimorph made of PVDF and PZT–5H material in the viscous fluid media. The proposed EFSI method takes into account the triple coupled interaction phenomena. The method is a combination of the electric field–structure interaction

and fluid–structure interaction coupled based on the hierarchal decomposition scheme. As a fundamental validation, when the bimorph actuator is excited at very low bias voltage and low input frequencies far away from the device resonance operated in the fluid channel with the inlet fluid velocity, horizontal tip displacement of the bimorph actuator coincides with the reference FSI solutions. At higher bias voltages, harmonic oscillation appears about the reference solution, indicates a strong inverse piezoelectric coupling in the fluid.

The resonance frequency of a thin flexible piezoelectric bimorph in the fluid agrees well with the theoretical solutions. Also, the shift in the resonance frequency upon the connected electric resistive load due to the electric boundary conditions is matched well with the theoretical approximations. It is shown that the resonance frequency difference between the open–and closed–circuit sensor mode electric configurations in PVDF piezoelectric bimorphs has negligible shift. However, a noticeably shift upon the connected external electric resistive load can be seen in PZT–5H piezoelectric bimorphs. The simulated frequency responses and vibration amplitudes of the thin flexible piezoelectric bimorphs analyzed using the proposed EFSI method shows a good agreement with the previous studies.

CHAPTER 5

GENERAL CONCLUSIONS

The objective of the present study was to develop a coupled multiphysics analysis method to analyze the sensor and actuator function of a thin flexible piezoelectric bimorph in vacuum and viscous fluid conditions using FEM. In essence, this work is determined to provide an accurate and efficient FE multiphysics coupling method implemented in the computer environment based on an advanced computational mechanics techniques to analyze the electric–structure interaction (ESI) and the electric–fluid–structure interaction (EFSI).

In this thesis work, the following sub–objectives were proposed to achieve the main objective:

1. Development of finite element method to analyze the linear electric field–structure interaction describing the piezoelectric effect by partitioning into the electrical field and structural with the use of Gauss–Seidel method and analysis using 3D solid elements of a piezoelectric bimorph for various configurations, demonstrated in Chapter 2.

2. Develop a finite element model for nonlinear structure–electric field interaction using a novel coupling scheme for the nonlinear structure–electric field by using a transformation method between the shell and solid in a thin piezoelectric bimorph actuator and sensor for various electric configurations, presented in Chapter 3.

3. A triply coupled multiphysics analysis of electric field–fluid–structure interaction of the piezoelectric bimorphs which was based on the combination of the electric field–structure interaction and fluid–structure interaction, shown in Chapter 4.

These sub–objectives have been achieved to meet the aim of this thesis work. The following are the details.

In Chapter 2, a detailed and systematic performances evaluation of the various finite element coupled algorithms to analyze a linear electric field–structure interaction using a monolithic coupling (MN), partitioning coupling (PCD), and partitioned iterative coupling methods (BJN and BGSN) is demonstrated. The comparison of these algorithms were presented based on their solution accuracy and computational efficiency to analyze the electric–structure interaction in piezoelectric bimorph actuators with different configurations and their transient dynamic responses as well as the static and steady state responses. A same level of accuracy was obtained using the MN, partitioned iterative coupling algorithms (BJN and BGSN) to analyze the static deflection of various piezoelectric bimorph actuators. The step responses and the resonance characteristics of the piezoelectric bimorph actuators is predicted accurately with the MN, BJN, and BGSN algorithms. In the linear dynamic analysis of low–frequency devices such as piezoelectric bimorph actuators, the MN algorithm is computationally efficient than BJN and BGNS algorithm, but in the nonlinear dynamic analysis, BGSN algorithm is most efficient with regard to computational cost and the MN algorithm is very expensive. In the analysis of high–frequency piezoelectric actuators in surface acoustic wave devices, a same level of accuracy is obtained with the PCD, MN, BJN, and BGSN algorithms. In the linear dynamic analysis of high–frequency actuators, the PCD algorithm is computationally efficient compared with the MN, BJN, and BGSN algorithms. This comprehensive study can be of important for computer aided modeling and analysis of piezoelectric actuators and to assist designers of piezoelectric actuators.

In Chapter 3, a detailed literature survey to confirm the statement and the novelty of the 2nd sub–objective. It was found that the proposed method can treat various electric configurations of a thin–piezoelectric bimorph actuator and sensor with a linear or quadratic distribution of electric potential across the thickness, whereas the piezoelectric shell elements which were well suited for thin bimorph can not treat various electric configurations and piezoelectric solid elements which were well–suited for electric potential analysis can not treat thin flexible piezoelectric bimorph. Furthermore, to the best of the author's knowledge, there has been no published work, that solves the electric field–structure interaction describing the piezoelectric effect by decomposing into the electrical and structural fields with the use of different elements to solve the different fields to analyze both the actuation and sensing function of piezoelectric bimorph. The results of comparison of actuator and sensor function of thin flexible piezoelectric bimorph presented in Chapter 3 for various electric configurations show a good agreement between the theoretical results and the simulated results.

In Chapter 4, a triple coupling of the electric field–fluid–structure interaction based on the combination of the electric field–structure interaction and fluid–structure interaction was presented using the hierarchal decomposition method. A benchmark problem was analyzed to test the accuracy of the simulated results. The result of comparison shows that the method developed in this thesis has very good agreements between the simulated results and the reference solution. The proposed EFSI method takes into account the electric field–fluid–structure interaction. The damped vibrations of the piezoelectric bimorph analyzed using the proposed EFSI algorithm coincides with that of the FSI solution when the actuator is excited at very low input bias voltage. Also, the damped natural frequencies of the piezoelectric bimorph made of PVDF and PZT–5H are very close to the theoretical damped natural frequency. The shift in the resonance frequency and the vibration amplitudes of the piezoelectric bimorphs upon the connected external resistive loading through the electrical boundary conditions coincides with the previous studies.

In summary, the main contributions of this thesis are outlined below:

1. A comprehensive and detailed analysis of different coupling strategies for a linear electric–structure interaction was presented based on the accuracy and computational efficiency shown in Chapter 2.

2. An accurate coupling of the electric field–structure interaction is achieved based on the decomposition and transformation methods by employing different finite elements to solve the electric field and structure separately. The method presented here is used to analyze both the actuation and sensing mode in the piezoelectric bimorph, shown in Chapter 3.

3. The proposed method in Chapter 3 can treat various electric configurations of a thin–piezoelectric bimorph with a linear or quadratic distribution of the electric potential across the thickness.

4. A finite element approach to compute the complicated triply coupling of the electric field–fluid–structure interaction which can treat both the actuation and sensing of piezoelectric bimorph in the fluid was developed in Chapter 4.

5. The proposed EFSI algorithm based on the hierarchal decomposition was implemented as the computer program, it has been solving the problems, which cannot be solved by the conventional methods.

It follows from these contributions that the proposed multiphysics FE coupling algorithm will serve as a base for an efficient and accurate analysis of ESI and EFSI system for a thin–piezoelectric bimorphs.

BIBLIOGRAPHY

[1] M. Karpelson, G.Y. Wei, R.J. Wood, "A review of actuation and power electronics options for flapping-wing robotic insects," *IEEE International Conference on Robotics and Automation*, vol. 11, pp. 19–23, 2008.

[2] D. Ishihara, N. Ohira, M. Takagi, T. Horie, "Fluid-structure interaction design of insect-like micro flapping wing," *Proceeding of the VII International Conference on Computational Methods for Coupled Problems in Science and Engineering(COUPLED PROBLEMS 2017), Greece*, pp. 870–875, 2017.

[3] Y. Tanaka, T. Oko. H. Mutsuda, A.A. Popov, R. Patel, S.M. William, "Forced vibration experiments on flexible piezoelectric devices operating in air and water environments," *International Journal of Applied Electromagnetics and Mechanics*, vol. 45, pp. 573–580, 2014.

[4] J.Curie, P. Curie, "Development via compression of electric polarization in hemihedral crystals with inclined faces," *Bull Soc Mineral*, pp. 90–93, 1880.

[5] K. Uchino, "Piezoelectric actuators/ ultrasonic motors – their developments and markets," *Proceeding of 1994 IEEE Int Symp Appl Ferroelectr*, pp. 319–324, 1995.

[6] C.B. Eom, S. Trolier-McKinstry, "Thin-film piezoelectric mems," *Material Research Society Bulletin*, vol. 37, no. 11, pp. 1007–1017, 2012.

[7] H.S. Tzou, "Development of a light-weight robot end-effector using polymeric piezoelectric bimorph," *proceedings of IEEE international conference on robotics and automation*, vol. 3, pp. 1704–1709, 1989.

[8] C.I. Tseng, "Electromechanical dynamics of a coupled piezoelectric/mechanical systems applied to vibration control and distributed sensing," *Ph.D Dissertation, Univ. of Kentucky, Lexington, Ky. July*, 1989.

[9] Z. Wang, S. Chen, W. Han, "The static shape control for intelligent structures," *Finite Elements in Analysis & Design*, vol. 26, no. 4, pp. 303–314, 1997.

[10] T. Itoh, T. Suga, "Force sensing microcantilever using sputtered zinc oxide films," *Applied Physics Letter*, vol. 64, pp. 37–39, 1994.

[11] C. Lee, T. Itoh, T. Suga, "Micromachined piezoelectric force sensors based on pzt thin films," *IEEE Transactions on Ultrasonics, Ferroelectrics, and Frequency*, vol. 43, pp. 553–559, 1996.

[12] T. Shibata, K. Unno, E. Makino, S. Shimada, "Fabrication and characterization of diamond afm probe integrated with pzt thin film sensor and actuator," *Sensors & Actuators A: Physical*, vol. 114, no. 2–3, pp. :398–405, 2004.

[13] A. Erturk, D.J. Inman, "An experimental validated bimorph cantilever model for piezoelectric energy harvesting from base excitation," *Smart Materials and Structures*, vol. 18, 025009, 15 pages, 2009.

[14] S. Rafique, P. Bonello, "Experimental validation of a distributed parameter piezoelectric bimorph cantilever energy harvester," *Smart Materials and Structures*, vol. 19, 094008,15 pages, 2010.

[15] R.J. Wood, B. Finio, M. Karpelson, K. Ma, N.O. Perez-Arancibia, P.S. Sreetharan, H. Tanaka H, J.P Whitney, "Progress on pico air vehicles," *The International Journal of Robotics Research*, vol. 31, no. 11, pp. 1292–1302, 2012.

[16] J.R. Bronson, J.S. Pulskamp, R.G. Polcawich, C.M. Kroninger, E.D. Wetzel, "Pzt mems actuated flapping wings for insect-inspired robotics," *IEEE International Conference on Microelectromechanical systems (mems)*, pp. 1047–1050, 2009.

[17] D. Ishihara, T. Horie, M. Denda, "A two dimensional computational study on fluid-structure interaction cause of wing pitch changes in dipteran flapping flight," *Journal of Experimental Biology*, vol. 212, pp. 1–10, 2009.

[18] D. Ishihara, T. Horie, T. Niho, "An experimental and three-dimensional computational study on the aerodynamic contribution to the passive pitching motion of the flapping wings in hovering flies," *Bioinspiration & Biomimetics*, vol. 9, no. 4, 046009,23 pages, 2014.

[19] D. Ishihara, T. Horie, "Passive mechanism of pitch recoil in flapping insect wings," *Bioinspiration & Biomimetics*, vol. 12, 016008, 16 pages, 2012.

[20] D. Ishihara, "Role of fluid-structure interaction in generating the characteristic tip path of a flapping flexible wing," *Physical Review E*, vol. 98, 032411, 19 pages, 2018.

[21] Q.M. Wang, L.E. Cross, "Performance analysis of piezoelectric cantilever bending actuator," *Ferroelectrics*, vol. 215, no. 1, pp. 187–213, 1998.

[22] J.G. Smits, A. Ballato, "Dynamic admittance matrix of piezoelectric cantilever bimorphs," *Journal of Microelectromechanical Systems*, vol. 3, no. 3, pp. 105 – 112, 1994.

[23] Q.M. Wang, L.E. Cross, "Constitutive equations of symmetrical triple layer piezoelectric benders," *IEEE Transactions on Ultrasonics, Ferroelectrics, and Frequency Control*, vol. 46, pp. 1343–1351, 1999.

[24] H. J. Kim, W. S. Yang, K. S. No, "The vibrational characteristics of the triple-layered multimorph ceramics for performance piezoelectric acoustic actuators," *Journal of Electroceramics 2014;*, vol. 33, pp. 53–63, 2014.

[25] Q. Nguyen, L. Tong, "Coupled algorithms for piezoelectric actuator design optimization for shape control of smart structures," *International Journal of Computational Methods*, vol. 6, no. 4, pp. 501–519, 2009.

[26] S. Valliyappan, C. K. Chee, "Numerical analysis of smart structures with uncertainites," *International Journal of Computational Methods*, vol. 1, no. 2, pp. 227–239, 2004.

[27] O.Z. Zienkiewicz, R.L. Taylor, "The finite element method, fifth edition, volume 1 : The basis," *Butterworth-Heinemann*, 2000.

[28] H. Allik, T.J.R. Hughes, "Finite element method for piezoelectric vibration," *International Journal for Numerical Methods in Engineering*, vol. 2, pp. 151–157, 1970.

[29] A. Benjeddou, "Advances in piezoelectric finite element modeling of adaptive structural elements: a survey," *Computers & Structures*, vol. 76, no. 1–3, pp. 347–363, 2000.

[30] H. Allik, M.W. Kenneth, T.H. John, "Vibrational response of sonar transducer using piezoelectric finite elements," *The Journal of the Acoustical Society of America*, vol. 56, pp. 1782–91, 1974.

[31] H.S. Tzou, C.I. Tseng, "Distributed piezoelectric sensor/actuator design for dynamic measurement/control of distributed parameter systems: a piezoelectric finite element approach," *Journal of Sound and Vibration*, vol. 138, no. 1, pp. 17–34, 1990.

[32] H.S. Tzou, C.I. Tseng, H. Bahrami, "A piezoelectric hexahedron finite element applied to design a smart continua," *Finite Elements in Analysis & Design,*, vol. 16:, pp. 27–42, 1994.

[33] L.C. Chin, V.V. Varadan, V.K. Naradan, "Hybrid finite element formulation for periodic piezoelectric arrays subjected to fluid loading," *International Journal for Numerical Methods in Engineering*, vol. 37, no. 1, pp. 2987–3003, 1994.

[34] K. Ghandi, N.W. Hagood, "Nonlinear finite element modeing of phase transitions in electro-mechanically coupled material. in: Varadan vv, chandra j, editors," *Proceeding of SPIE 2715, Smart Structures and Materials 1996: Mathematics and Control in Smart Structures*, vol. 2715, pp. 121–140, 1996.

[35] K. Ghandi, N.W. Hagood, "A hybrid finite element modelfor phase transition in nonlinear electro-mechanically coupled material. in: Varadan vv, chandra j, editors," *Proceeding of SPIE 3039, Smart Structures and Materials 1997: Mathematics and Control in Smart Structures,*, vol. 3039, pp. 97–112, 1997.

[36] S.K. Ha, C. Keilers, F.K. Chang, "Finite element analysis of composite structures containing distributed piezoelectric sensors and actuators," *AIAA Journal*, vol. 30, pp. 772–780, 1992.

[37] M. Kogli, M.L. Bucalem, "Analysis of smart laminates using piezoelectric mitc plate and shell elements," *Computers & Structures*, vol. 83, no. 15–16, pp. 1153–1163, 2005.

[38] J. Fish, W. Chen, "Modeling and simulation of piezocomposites," *Computer Methods in Applied Mechanics and Engineering*, vol. 192, no. 28–30, pp. 3211 – 3232, 2003.

[39] Y. Kagawa, T. Tsuchiya, T. Kataoka, "Finite element simulation of dynamic response of piezoelectric actuators," *Journal of Sounds and Vibration*, vol. 191, no. 4, pp. 519–538, 1996.

[40] T. Horie, T. Niho, "Electromganetic and structural coupled analysis with the effect of large deflection," *IEEE Transactions on Magnetics*, vol. 33, pp. 1658–1667, 1997.

[41] T. Niho, T. Horie, Y. Tanaka, "Numerical instability of magnetic damping problem of elastic plate," *IEEE Transactions on Magnetics*, vol. 36, no. 4, pp. 1373–1376, 2000.

[42] T. Niho, T. Horie, J. Uefhji, D. Ishihara, "Stability analysis and evaluation of staggered coupled analysis methods for electromagnetic and structural coupled finite element analysis," *Computers & Structures*, vol. 178, pp. 129–142, 2017.

[43] S.Y. Wang, "A finite element model for the static and dynamic analysis of a piezoelectric," *International Journal of Solids and Structures*, vol. 41, no. 15, pp. 4075–4095, 2003.

[44] C.A. Felippa, K.C. Park, C. Farhat, "Partitioned analysis of coupled mechanical system," *Computer Methods in Applied Mechanics and Engineering*, vol. 190, pp. 3247–3270, 2001.

[45] F. Shi, P. Ramesh, S. Mukherjee, "Dynamic analysis of micro electro mechanical systems," *International Journal for Numerical Methods in Engineering*, vol. 39, no. 24, pp. 4119–4139, 1996.

[46] P. Gaudenzi, K.J. Bathe, "An iterative finite element procedure for the analysis of piezoelectric continua," *Journal of Intelligent Material Systems and Structures*, vol. 6, no. 2, pp. 226–273, 1995.

[47] P.C. Ramegowda, D. Ishihara, T. Niho, T. Horie, "Performance evaluation of numerical finite element coupled algorithms for structure-electric interaction analysis of mems piezoelectric actuator," *International Journal of Computational Methods*, vol. 15, no. 3, 1850106, 28 pages, 2018.

[48] S. Minami, S. Yoshimura, "Performance evaluation of nonlinear algorithms with line search for partitioned coupling technique for fluid-structure interactions," *International Journal for Numerical Methods in Fluids*, vol. 64, pp. : 1129–1147, 2010.

[49] D. Ishihara, T. Horie, T. Niho, T. Baba, "Hierarchal decomposition for the structure-fluid-electrostatic interaction in a microelectromechanical system," *Computer Modeling in Engineering and Sciences*, vol. 108, no. 6, pp. 429–452, 2015.

[50] D.Ishihara, T. Horie, "A projection method for the monolithic interaction system of an incompressible fluid and a structure using a new algebraic splitting," *Computer Modeling in Engineering and Sciences*, vol. 101, no. 6, pp. 421–440, 2014.

[51] Y. H.lim, V. V. Vasundara, K. V. Vijay, "Finite element modeling of the transient response of mems sensors," *Smart Materials and Structures*, vol. 6, pp. 53–61, 1997.

[52] N.M. Newmark, "A method of computation for structural dynamics," *Journal of the engineering mechanics division*, vol. 85, no. 3, pp. 67–94, 1959.

[53] K.J. Bathe, "Finite element procedures," *Prentice-Hall,*, 2006.

[54] P.C. Ramegowda, D. Ishihara, T. Niho, T. Horie, "Performance evaluation of finite element coupled algorithms for structure–electric interaction analysis of mems actuator," *Proceeding of the 12th World Congress on Computational Mechanics & the 6th Asia–Pacific Congress on Computational Mechanics (12th WCCM 2006),Seoul*, pp. 1137–1150, 2006.

[55] P.C. Ramegowda, D. Ishihara, T. Niho, T. Horie, "A finite element approach for a coupled numerical simulation of fluid -structure-electric interaction in mems," *Proceeding of the VII International Conference Computational Methods for Coupled Problems In Science and Engineering (Coupled Problems 2017), Greece*, pp. 999–1007, 2017.

[56] R. Takata, P.C. Ramegowda, D. Ishihara, T. Niho, T. Horie, "Partitioned iterative method for composite piezoelectric bimorph using shell and electric solid elements," *Proceedings of 31st computational mechanics division, 4 pages*, 2018.

[57] F. Ebert, "Convergence of relaxation methods for coupled systems of odes and daes," *Technical Report. 200. MATHEON, 32 pages*, 2004.

[58] W. Scharfer, M. Wegner, "Semiconductor optics and trasnport phenomena," *Springer-Verlag*, 2007.

[59] A. Fernandes, J. Pouget, "Analytical and numerical approaches to piezoelectric bimorph," *International Journal of Solids and Structures*, vol. 40, pp. 4331–4352, 2003.

[60] J.G. Smits, S.I. Dalke, T.K. Cooney, "The constitutive equations of piezoelectric bimorphs," *Sensors & Actuators A: Physical*, vol. 28, no. 1, pp. 41–61, 1991.

[61] S. Kapuria, P. Hangedorn, "Unified efficient layerwise theory for smart beams with segmented extensio/shear mode, piezoelectric actuators and sensors," *Journal of Mechanics of Materials and Structures*, vol. 2, no. 7, pp. 1267–1298, 2007.

[62] A. Benjeddou, J. Deu, S. Letombe, "Free vibrations of simply–supported piezoelectric adaptive plates: An exact sandwich formulation," *Thin–Walled Struct*, vol. 40, pp. 573–593, 2002.

[63] W. Zouari, B. Zineb, A. Benjeddou, "A fsdt-mitc piezoelectric shell finite element with ferroelectric non-linearity," *Journal of Intelligent Material Systems and Structures*, vol. 20, no. 17, pp. 2055–2075, 2009.

[64] M. Kogli, M.L. Bucalem, "A family of piezoelectric mitc plate elements," *Computers & Structures*, vol. 83, pp. 1277–1297, 2005.

[65] R. MacNeal, R. Harder, "A proposed standard set of problems to test finite element accuracy," *Finite Elements in Analysis & Design*, vol. 1, pp. 3–20, 1985.

[66] I.S. KoKo, I.R. Orisamolu, M.J. Smith, U.O. Alepan, "Finite element based design tool for smart composite structures," *Smart Struct Mater.Washington:SPIE*, vol. 3039, pp. 125–134, 1997.

[67] R. Lammering, "The appllicaton of a finite shell element for composites containing piezoelectric polymer in vibration control," *Computers & Structures*, vol. 41, no. 5, pp. 1101 – 1109, 1991.

[68] T.A. Quentin, D.J. Brian, L.L. Howell, "Geometrically non-linear analysis of thin-film compliant mems via shell and solid elements," *Finite Elements in Analysis & Design*, vol. 49, pp. 70–77, 2012.

[69] W.S. Hwang, H.C. Park, "Finite element modeling of piezoelectric sensors and actuators," *AIAA Journal*, vol. 31, no. 5, pp. 930–9937, 2013.

[70] S. Ahmad, B.M. Irons, O.C. Zienkiewicz, "Analysis of thick and thin shell structures by curved finite elements," *International Journal for Numerical Methods in Engineering*, vol. 2, no. 3, pp. 419–451, 1970.

[71] H. Noguchi, T. Hisada, "Sensitivity analysis in post buckling problems of shell structures," *Computers & Structures*, vol. 47, no. 4-5, pp. 699–710, 1993.

[72] E.N. Dvorkin, K.J. Bathe, "A continuum mechanics based four-node shell element for general nonlinear analysis," *Engineering Computation*, vol. 1, no. 1, pp. 77–88, 1984.

[73] K.J. Bathe, E.N. Dvorkin, "A formulation of general shell elements-the use of mixed interpolation of tensorial components," *International Journal for Numerical Methods in Engineering*, vol. 22, no. 3, pp. 697–722, 1986.

[74] V.V. Varadan, L.C. Chin, V.K. Naradan, "Finite element modeling of flextensional electroacoustic transducers," *Smart Materials and Structures*, vol. 2, no. 4, pp. 201–207, 1993.

[75] N. Guo, P. Cawley, D. Hitchings, "The finite element analysis of the vibration characteristics of piezoelectric discs," *Journal of Sound and Vibration*, vol. 159, no. 1, pp. 115–138, 1992.

[76] R. Lammering, R.S. Mesecke, "Multi-field variational formulations and related finite elements for piezoelectric shells," *Smart Materials and Structures*, vol. 12, no. 12, pp. 904–913, 2003.

[77] V.D. Varelis, D.A. Saravanos, "Coupled mechanics and finite element for non-linear laminated piezoelectric shallow shells undergoing large displacements and rotations," *International Journal for Numerical Methods in Engineering*, vol. 66, no. 8, pp. 1211–1233, 2006.

[78] R. Zemcik, R. Rolfes, M. Rose, J. Tessmer, "High-performance four-node shell element with piezoelectric coupling for the analysis of smart laminated structures," *International Journal for Numerical Methods in Engineering*, vol. 70, no. 8, pp. 934–961, 2007.

[79] D. Lenger, S. Klinkel, W. Wagner, "An advanced finite element formulation for piezoelectric shell structures," *International Journal for Numerical Methods in Engineering*, vol. 95, no. 11, pp. 901– 927, 2013.

[80] X. Wang, Y. Wang, "On non-linear behaviour of spherical shallow shells bonded with piezoelectric actuators by the differential quadrature element method (dqem)," *International Journal for Numerical Methods in Engineering*, vol. 53, no. 6, pp. 1477–1490, 2002.

[81] D.H. Robbins, J.N. Reddy, "Analysis of piezoelectrically actuated beams using a layerwise displacement theory," *Computers & Structures*, vol. 41, no. 2, pp. 265– 279, 1991.

[82] R. Iozzi, P. Gaudenzi, "Effective shear deformable shell elements for adaptive laminate structures," *Journal of Intelligent Material Systems and Structures*, vol. 12, no. 6, pp. 415–422, 2001.

[83] A. Zallo, P. Gaudenzi, "Finite element models for laminated shells with actuation capability," *Computers & Structures*, vol. 81, pp. 1059– 1069, 2003.

[84] V. Balamurugan, S. Narayanan, "Shell finite element for smart piezoelectric composite plate/shell structures and its application to the study of active vibration control," *Finite Elements in Analysis & Design*, vol. 37, pp. 713–738, 2001.

[85] D.A. Saravanos, "Mixed laminate theory and finite element for smart piezoelectric composite shell structures," *AIAA Journal*, vol. 35, no. 8, pp. 1327–1333, 1997.

[86] M. Kogli, M.L. Bucalem, "Locking free piezoelectric shell elements. in bathe kj editor," *Computational Fluid and Solid Mechanics. Elsevier*, no. 15–16, pp. 392–395, 2003.

[87] K.J.Bathe, E.Ramm, E.L.Wilson, "Finite element formulation for large deformation dynamics analysis," *Computer Methods in Applied Mechanics and Engineering*, vol. 9, no. 2, pp. 353–386, 1975.

[88] K.J.Bathe, A.P.Cimento, "Some practical procedures for the solution of nonlinear finite element equations," *Computer Methods in Applied Mechanics and Engineering*, vol. 22, no. 1, pp. 59–85, 1980.

[89] P.C. Ramegowda, D. Ishihara, T. Niho, T. Horie, "A novel coupled algorithm for shell structure-electric interaction analysis in mems piezoelectric actuator," *Proceeding of the 35th JSST Annual Conference International Conference on Simulation Technology, Kyoto*, pp. 332–339, 2016.

[90] P.C. Ramegowda, D. Ishihara, T. Niho, T. Horie, "A novel coupling scheme for the electric field–structure interaction using a transformation method between solid and shell elements in a thin piezoelectric bimorph actuator and sensor analysis," *Finite Elements in Analysis & Design, Submitted*, 2018.

[91] C.P. Germano, "Flexural mode piezoelectric transducers," *IEEE Transactions on Audio Elecroacoustics*, vol. 19, pp. 6–12, 1971.

[92] P. Kielzynski, W. Pajewski, M. Szalewski, "Piezoelectric sensors for investigations of microstructures," *Sensors & Actuators A: Physical*, vol. 65, pp. 13–18, 1998.

[93] B.M. Finio, R.J. Wood, "Distributed power and control actuation in the thoracic mechanics of a robotic insect," *Bioinspiration & Biomimetics*, vol. 4, 045006,12 pages, pp. 1292–1302, 2012.

[94] S. Ravi, A. Zilian, "Numerical modeling of flow driven piezoelectric energy," *Computational Methods for Solids and Fluids:Springer International Publishing*, vol. 41, pp. 399–426, 2016.

[95] S. Kaneko , G. Hong, N. Mitsume, T. Yamada, S. Yoshimura, "Numerical study of active control by piezoelectric materials for fluid–structure interaction problems," *Journal of Sound and Vibration*, vol. 435, pp. 23–35, 2018.

[96] S. Raja, A. Upadhya, "Active control of wing flutter using piezoactuated surface," *Journal of Aircraft*, vol. 41, no. 1, pp. 71–80, 2007.

[97] Q. Zhang, T. Hisada, "Analysis of fluid–structure interaction problems with structural buckling and large domain changes by ale finite element method," *Computer Methods in Applied Mechanics and Engineering*, vol. 190, no. 48, pp. 6341–6357, 2001.

[98] B. Hubner, E. Walhorn, D. Dinkler, "A monolithic approach to fluid–structure interaction using space–time finite elements," *Computer Methods in Applied Mechanics and Engineering*, vol. 193, no. 23–26, pp. 2087–2104, 2004.

[99] D.Ishihara, S. Yoshimura, "A monolithic approach for interaction of incompressible viscous fluid and an elastic body based on fluid pressure poisson equation," *International Journal for Numerical Methods in Engineering*, vol. 64, pp. 167–203, 2015.

[100] S. Rugonyi, K.J. Bathe, "On finite element analysis of fluid flows fully coupled with structural interactions," *Computer Modeling in Engineering and Science*, vol. 2, pp. 195–212, 2004.

[101] T. Yamada, S. Yoshimura, "Line search partitioned approach for fluid–structure interaction analysis of flapping wing," *Computer Modeling in Engineering and Science*, vol. 24, pp. 51–60, 2008.

[102] H.G. Matthies, J. Steindorf, "Partitioned strong coupling algorithms for fluid–structure interaction," *Computer & Structures*, vol. 81, pp. 805–812, 2003.

[103] Mok, D. P.; Wall, W. A., "Partitioned analysis schemes for the transient interaction of incompressible flows and nonlinear flexible structures," *Trends in Computational Structural Mechanics. CIMNE: Barcelona*, pp. 689–698, 2001.

[104] M. Neumann, S.R. Tiyyagura, W.A. Wall, "Robustness and efficiency aspects for computational fluid structure interaction," *Computational Science and High Performance Computing II*, vol. 91, pp. 99–114, 2006.

[105] S.R. Idelsohn, F. Del Pin, R. Rossi, E. Onate, "Fluid-structure interaction problems with strong added-mass effect," *International Journal for Numerical Methods in Engineering*, vol. 80, pp. 1261–1294, 2009.

[106] J. Degroote, K.J. Bathe, J. Vierendeels , "Performance of a new partitioned procedure versus a monolithic procedure in fluid,Äìstructure interaction," *Computer & Structures*, vol. 87, pp. 793–801, 2009.

[107] Y. Carretta, R. Boman, J. Bech, N. Legrand , M. Laugier, J.P. Ponthot, "Numerical modelling of microscopic lubricant flow in sheet metal forming. application to plane strip drawing," *International Journal for Numerical Methods in Engineering*, vol. 112, pp. 203–237, 2017.

[108] T. Horie, T. Niho, "Electromganetic and mechanical interaction analysis of a think shell structure vibrating in an electromagnetic field," *International Journal of Applied Electromagnetics in Materials*, vol. 4, pp. 363–368, 1994.

[109] T. Horie, H. Kuramae, T. Niho, "Parallel electromagnetic-mechanical coupled analysis using combined decomposition method," *IEEE Transactions on Magnetics*, vol. 33, pp. 1792–1795, 1997.

[110] Y. Tanaka, T. Horie, T. Niho, E. Shintaku, Y. Fujimoto, "Stability of augmented staggered method for electromagnetic and structure couple problem," *IEEE Transactions on Magnetics*, vol. 40, pp. 1792–1795, 2004.

[111] T. Niho, T. Horie, D. Ishihara, T. Morita, D. Yamakawa, S. Momii, "Elasto–plastic contact, electric current and thermal conduction triply coupled analysis model for resistance spot welding," *Quarterly Journal of the Japan Welding Society*, vol. 33, pp. 271–282, 2017.

[112] T. Horie, T. Niho, N. Hayashi, D. Ishihara, "Mechanisms of elasto-plastic contact, electric current and thermal conduction triply coupled phenomena during resistance spot welding," *Proceedings of 10th International Conference on Trends in Welding Research & 9th International Welding Symposium of Japan Welding Society*, pp. 329–332, 2016.

[113] T. Niho, T. Horie,K. Ikegami, D. Ishihara, K. Matsunaga, T. Shu, "Triply coupled effect of elasto–plastic contact deformation, electric current and thermal conduction of steel sheets interfaces for three sheets resistance spot welding," *Quarterly Journal of the Japan Welding Society*, vol. 35, no. 2, pp. 63–72, 2017.

[114] T. Niho, K. Kubota, H. Aramaki, H. Kuramae, D. Ishihara, T. Horie, "Microscale electrical contact resistance analysis for resistance spot welding," *Proceeding of the VII International Conference on Computational Methods for Coupled Problems in Science and Engineering(COUPLED PROBLEMS 2017), Greece*, vol. 33, pp. 1152–1158, 2017.

[115] S.K. De, N. R. Aluru, "Coupling of hierarchical fluid models with electrostatic and mechanical models for the dynamic analysis of mems," *Journal for Micromechanics and Microengineering*, vol. 16, pp. 1705–1719, 2006.

[116] V. Rochus, S. Gutschmidt, A. Cardona, C. Geuzaine, "Electro–mechano–fluid modeling of microsystems using finite elements," *IEEE Transactions on Magnetics*, vol. 48, no. 2, pp. 355–358, 2012.

[117] V. Rochus, D.J. Rixen, J.C. Golivnal, "Non-conforming element for accurate modelling of mems," *Finite Elements in Analysis & Design*, vol. 43, pp. 749–756, 2007.

[118] V. Rochus, C. Geuzaine, "A primal/dual approach for the accurate evaluation of the electromechanical coupling in mems," *Finite Elements in Analysis & Design*, vol. 49, pp. 19–27, 2012.

[119] T.J.R. Hughes, W. K. Liu, T. K. Zimmerman, "Lagrangian–eulerian finite element formulation for incompressible viscous flows," *Computer Methods in Applied Mechanics and Engineering*, vol. 29, no. 3, pp. 329–349, 1981.

[120] T. Nomura, T.J.R. Hughes, "An arbitrary lagrangian–eulerian finite element formulation for interaction of fluid and a rigid body," *Computer Methods in Applied Mechanics and Engineering*, vol. 95, no. 1, pp. 115–138, 1992.

[121] TA. Brooks, T.J.R. Hughes, "Streamline upwind/petrov,Äìgalerkin formulations for convection dominated flows with particular emphasis on the incompressible navier,Äìstokes equation," *Computer Methods in Applied Mechanics and Engineering*, vol. 32, no. 1, pp. 199–259, 1982.

[122] T. E. Tezduyar, "Stabilized finite element formulations for incompressible flow computations," *Advances in Applied Mechanics*, vol. 28, pp. 1–44, 1992.

[123] T.E. Tezduyar, S. Mittal, S. Ray, R. Shih, "Incompressible flow computations with stabilized bilinear and linear equal-order-interpolation velocity-pressure elements,"

Computer Methods in Applied Mechanics and Engineering, vol. 95, pp. 221–242, 1992.

[124] P.C. Ramegowda, D. Ishihara, R. Takata, T. Niho, T. Horie, "Fluid–structure and electric interaction analysis of piezoelectric flap in a channel using a strongly coupled fem scheme," *Proceeding of the 6th European Conference on Computational Mechanics (ECCM 6 2018), Glasgow*, pp. ,12 pages, 2018.

[125] S. Zhu, B. Jiang, W. Cao , "Characterization of piezoelectric materials using ultrasonic and resonant techniques," *Proceeding of SPIE, Medical Imaging:Ultrasonic Transducer Engineering*, vol. 3341, pp. 154–162, 1998.

[126] C.A.Van Eysden, J.E. Sader , "Resonance frequencies of a cantilever beam immersed in a fluid," *Journal of Applied Physics*, vol. 100, no. 114916, 8 pages, 2006.

[127] T. Cai, "Theoretical analysis of torsionally vibrating microcantilevers for chemical sensor applications in viscous liquids," *Ph.D Dissertation, Marquette University*, 2009.

[128] R. Cox, F. Josse, S.M. Heinrich, O. Brand, I. Dufour, "Characteristics of laterally vibrating resonant microcantilevers in viscous liquid media," *Journal of Applied Physics*, vol. 111, no. 014907, 14 pages, 2012.

[129] M. Renaud, R. Elfrink, M. Jambunathan, C. de Nooijier, Z. Wang, M. Rovers, R. Vullers, R. V. Schaijk, "Optimum power and efficiency of piezoelectric vibration energy harvesters with sinusoidal and random vibrations," *Journal of Micromachanics and Microengineering*, vol. 22, no. 105030, 13 pages, 2012.

[130] J. Song, G. Zhao, B. Li, J. Wang, "Design optimization of pvdf–based piezoelectric energy harvesters," *Heliyon*, vol. 3, no. e00377, 18 pages, 2017.

[131] M. Zhu, E. Worthington, J. Njuguna, "Analysis of power output of piezoelectric energy harvesting devices directly connected to a resistive load using a coupled piezoelectric circuit finite element method," *IEEE Transactions on Ultrasonics, Ferroelectrics, and Frequency Control*, vol. 56, no. 7, pp. 1309–1317, 2009.

[132] M. Zhu, E. Worthington, A. Tiwari, "Design study of piezoelectric energy harvesting devices for generation of higher electrical power using a coupled piezoelectric–circuit finite element method," *IEEE Transactions on Ultrasonics, Ferroelectrics, and Frequency Control*, vol. 57, no. 2, pp. 427–437, 2010.